Millisecond Pulsars: Decoding Magnetospheres

by

Shauna Michele Sallmen

B.Sc. (University of Toronto, Canada) 1990
M.A. (University of California at Berkeley) 1992

A dissertation submitted in partial satisfaction of the
requirements for the degree of

Doctor of Philosophy
in
Astronomy

in the
GRADUATE DIVISION
of the
UNIVERSITY of CALIFORNIA at BERKELEY

Committee in charge:

Professor Donald C. Backer, Chair
Professor Jonathan A. Arons
Professor Robert Lin

Spring 1998

Millisecond Pulsars:
Decoding Magnetospheres

by Shauna Michele Sallmen

[REPLACE THIS PAGE WITH A COPY OF]
[YOUR SIGNED APPROVAL PAGE]

Abstract

Millisecond Pulsars:
Decoding Magnetospheres

by

Shauna Michele Sallmen

Doctor of Philosophy in Astronomy
University of California at Berkeley

Professor Donald C. Backer, Chair

A hollow-cone model explains the pulse profile morphology and polarization properties of long-period (1 second) pulsars. The radio emission originates in the open-field line region above the polar cap, which is larger in millisecond pulsars. The emission in these rapidly rotating objects may occur at altitudes which rotate at a speed closer to that of light. Relativistic effects and magnetic field distortions may therefore be more important. Pulse profile studies of millisecond pulsars indicate that the long-period pulsar classification system fails to account for the properties of these objects.

Multi-frequency polarization observations with high temporal resolution are presented for several millisecond pulsars. Secure classification of the pulse profile morphology remains elusive for many objects. Pulse components are narrower than expected, and the spectral behaviour makes core and cone component identification uncertain. The fractional polarization of these objects remains relatively constant with frequency, in contrast to the behaviour of slow pulsars. The polarization position angle curves are similar at all frequencies, suggesting that they are geometric in origin. Their small slopes can be reconciled with the results for long-period pulsars by a simple period-scaling of the pulsar magnetosphere. Long-term variations in the intensity and polarization profiles are observed; polarization variations are seen more frequently in millisecond pulsars than in slow pulsars.

Single pulses studies of normal pulsars revealed the phenomenon of microstructure - radio emission on very short time scales. This modulation may be due to either an angular or a temporal effect. In the former case, it would be expected to scale with

pulse period. Giant pulses in the Crab pulsar dominate the emission at some radio frequencies. Simultaneous dual-frequency observations of these pulses reveal that the emission mechanism must be broadband. Both temporal and angular models can account for the modulation. Giant pulses are also seen in PSR B1937+21. These are unexpectedly delayed relative to the average pulse peaks, and are difficult to explain in an angular model. Single-pulse observations of PSR B1534+12 also reveal no evidence for microstructure which scales with pulse period, although an angular beaming origin for the intensity modulation cannot be ruled out.

This dissertation is dedicated to

John Sallmen
Gertrude Sallmen

Lawrence Bostwick
Irene Bostwick

Acknowledgements

'Cause you know that -
People like you help people like me go on, go on
People like you help people like me go on, go on
People like you help people like me go on, go on, go on

"People Like You" by Bob Bossin

There are many people to thank, and it is hard to know where to begin. Except that this thesis could not have been completed without the cooperation, encouragement, and candy-making of my husband Steve, who takes me as I am.

Who I am today results from my family and my past. So I would like to thank my parents for encouraging me to always do my best, and Mrs. Buchwitz, for her patience with capricious five-year-olds. My brother Mark showed me that a thesis can take a long time, but still be done! All my aunts, uncles, and cousins bring warm memories to mind, while the courage of my grandparents gives me strength. Meanwhile Sarah keeps me tied to my roots, and encourages freedom in life.

There are many in my "other life", the one outside astronomy, that deserve mention. I would like to thank Cavan for being the best housemate imaginable, and for willingly feeding Steve and I at a moment's notice. And my Trinity family, for being themselves: Odette, for her gracious calm whenever I needed it, despite her chaotic life; Chuckie, for wonderful massages; Amelia, for entertaining my lonely husband while I was away, and for being generous with her horse; Dolly, for being silly on the trail; and Deborah, for losing her coffee virginity with us. Betsy and Voices for Change kept me sane when I most needed it, and reminded me how to live a life. Thanks to Aimee, for dancing with my husband, but having lunch with me, and Emilie, for being an excellent observing partner in the cold dome in Toronto. Margaret's joy and silliness have been a source of great pleasure, and her advice and support have been greatly appreciated. The members of the Society of the Great Round One know what they have done. Bonnie helped me get through this. And I cannot stop without thanking: Stinky, for being a staunch mascot of the GBPP; Woofie, for his watchful eye on my computer; Robin, for her company on many observing trips; Bruce Moose, for being so squishable; Roberta, for her comforting sounds, Tess, for keeping the others under control, and all the rest of the menagerie, for their cheerful attitudes.

Within the astronomy department, there are many people not directly involved with my research who should be thanked. Jay was a wonderful office mate, and lunches with Charles were always interesting. I appreciated Eric's company during thesis ups and downs, and am grateful to Rosa for proving a thesis *could* be finished when I needed to see that. Paquito's company in I-House was welcome.

The staff in the astronomy department here at UC Berkeley have been incredibly helpful, especially Joyce Wong & Robi Carmack for help with travel, Graduate Assistants Mary Brunn, Beverly Skinner, and Kim Patton (and recently Juliane Monroe) for always knowing who I needed to see, and Patrice for help with the ever-important payroll.

My advisor Don Backer is responsible for getting me hooked on pulsars. The original motivation of studying a gravitational wave background via pulsar timing gave way to an insatiable curiousity about the objects themselves, which he cheerfully encouraged. His knowledge, guidance, and support have made this research interesting, challenging, and enjoyable. Berkeley pulsar post-docs Alex Zepka and Andy Fruchter, and fellow pulsar students Tony and Andrea kept me in touch with aspects of pulsar research other than those contained in this dissertation. Jon Arons clarified complicated magnetospheric theories, allowing this observer to have a clue.

Matt Dexter and his expertise with BPPs made the bulk of the observations in this thesis possible. I especially appreciated his long hours of long-distance assistance during my observations at the Effelsberg 100-m telescope in Germany. The entire pulsar group at Bonn made me feel welcome, but without Axel Jessner the EBPP would not have been usable. Michael Kramer was a wonderful host during that observing trip, and his enthusiasm for millisecond pulsars is infectious. Although I have not met her, e-mail discussions with Kiriaki Xilouris about millisecond pulsar polarization were invaluable.

Alex Wolszczan's technical assistance at Arecibo made the observations for Chapter 6 possible.

The staff at the Green Bank observatory have been very friendly and helpful. My many trips to Wild, Wonderful West Virginia were always enjoyable. Becky Warner, in concert with the Charlottesville, VA NRAO staff, made sure I always got there and had a place to stay. The cafeteria and housekeeping staff saved me spinach salad on request, and let me back into my room after I locked myself out. My thanks to the drivers who occasionally transported me back to Charlottesville on the return journey, for diverting conversation. The 85-3 operators have always been helpful and responsive, helping to track ethernet cables across the ceiling, as well as monitoring the telescope and GBPP when we were absent. George Liptak made sure the GBPP moved from the 85-3 and back again on cue, and the movers

were careful when driving over the potholes, so the system remained operational. Bill Shank responded to requests for filters, feed changes, power meters, amplifiers, and correlated calibration signals with good humour, and kept the radio signals coming. Ed Childers kept the GBPP PC connected to the ethernet, and Preston provided extra cables on request. The 140-foot operators kept an eye on it all, and let me catch a little sleep on occasion. Jay Lockman snagged me for the weekly science talk more than once, but always signed my travel forms and made sure I had all the help I needed. Mark Clark and Rick Fisher kept the spectral processor going during the timing runs, allowing me to concentrate on the GBPP. Pulsar discussions with Mark McKinnon were always enlightening, and he also taught me the basics of polarization calibration. The Minters and Langstons welcomed me to their homes for dinner more than once.

My thanks go to Tim Hankins, Dave Moffett, and Scott Lundgren, for making the simultaneous giant pulse observations of Chapter 5 possible, and for stimulating discussions on the outcome. I am also grateful to the observatory staff at Green Bank and at the VLA for minimizing internet traffic during the two hours of that experiment.

Many members of the pulsar community, encountered at conferences large and small, have been welcoming and helpful. These are too numerous to mention, but Green Bank encounters with David Nice, Scott Lundgren, and Zaven Arzoumanian taught me a great deal about pulsars and observing. Dan Stinebring was especially helpful in clarifying my understanding of polarization calibration using pulsars, during one summer session there.

Finally, I must again thank my beloved Moose, for his patience, support, and calm in my storms.

It's teamwork
I couldn't make it on my own
It takes teamwork...
"Teamwork" by Tamarack

Contents

List of Tables

List of Figures

The beginning is now and will always be
"Another Train" by Pete Morton

Chapter 1

Introduction

1.1 Historical Background and Overview

As far back as 1934, Baade and Zwicky predicted the existence of dense, compact objects called neutron stars, forming as the result of the supernova explosion of massive stars, and supported only by neutron degeneracy. These objects were not observed until pulsars were discovered by chance in 1967 (Hewish *et al.* 1968), when Jocelyn Bell found a pulsating radio source with an astonishingly regular period.

The first pulsar discovered, PSR B1919+21[1], had a period of 1.337 seconds. This period meant that pulsars could have been associated with white dwarfs, but the detection of the Crab pulsar by Staelin and Reifenstein (1968), with a period of 33 milliseconds, confirmed the identification of pulsars as neutron stars, as they are the only objects capable of rotating at the required frequency. If the pulsations reflected an orbital period, then the 33 millisecond orbit of the Crab pulsar would be very small. Gravitational radiation from the system would then predict a period decrease, while the observed period increases. Radial oscillations of neutron stars cannot explain the long period pulsars, while radial oscillations of white dwarfs cannot explain periods shorter than about a second. In addition, in these cases we expect that the period should be proportional to $\sqrt{\rho}$. The star's density ρ would then have to span many orders of magnitude to explain the observed range of periods. Thus pulsars must be associated with rotating neutron stars. The Crab pulsar is located in the Crab nebula, which is the site of the supernova explosion observed in 1054 AD by Chinese astronomers. Several other pulsars are associated with supernova remnants (cf. Figure 1.1), supporting the theory that pulsars form in supernovae. Interestingly, Pacini (1967) predicted that a rotating magnetized neutron star might be the energy source required to explain the observed radiation from the Crab nebula.

[1]Pulsar names give the location of the object in the sky, and take one of two forms. B$hhmm+dd$ gives the hours and minutes of the right ascension, and degrees of declination, in the B1950.0 coordinate system. J$hhmm+ddmm$ gives the hours and minutes of right ascension, and degrees and arcminutes of declination, in the J2000.0 coordinate system.

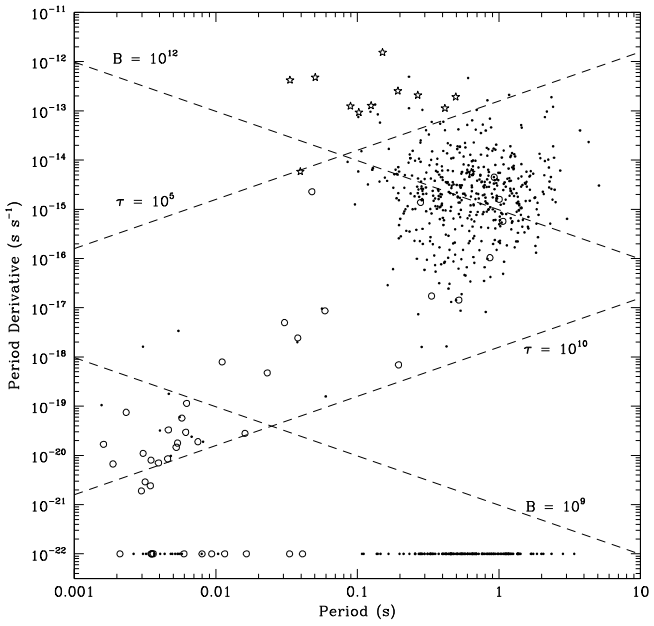

Fig. 1.1.— The observed $P - \dot{P}$ distribution for the pulsars in the current pulsar catalog. Isolated pulsars are designated by single dots, those in binary systems by open circles, and those associated with supernova remnants by stars. Those with $\dot{P} \leq 0$ (either unmeasured, or presumably contaminated by dynamical effects) lie at the bottom of the plot. The dashed lines represent characteristic ages τ of 10^5 and 10^{10} years, and magnetic fields B of 10^{12} and 10^9 Gauss (cf. section 1.5).

A pulsar is therefore a rotating neutron star, which packs 1.4 times the mass of our sun into a sphere only 20 km across and spins once around in less than 5 seconds. One cubic centimeter of its material would weigh about 1 billion metric tonnes on Earth. The radio pulses originate because an emission beam inclined relative to the rotation axis sweeps around like a lighthouse, producing pulses whenever it crosses the line of sight of the observer. In most models, this emission beam is associated with the poles of the strong magnetic field believed to be associated with the neutron star.

More than 700 radio pulsars are currently known with periods from 1.56 ms to 5.09s. All are slowing down due to energy loss. Figure 1.1 displays the period P and period derivative $\dot{P}$ values of the current population. The data were taken from the pulsar catalog publicly available from Princeton (Taylor, *et al.* 1995). Typical "garden variety" pulsars have periods of 100 ms to 2 s (the mean is 0.7 s), and magnetic fields of 10^{12} Gauss (for comparison, the magnetic field of the Earth is of order 1 Gauss). The *spectral index* of the radiation q, is defined by $S_{\nu_1} = S_{\nu_2}(v_1/v_2)^q$, where S_ν is the radio flux. Pulsars have steep radio spectra, with $\bar{q} = -1.6$. As can be seen in Figure 1.1, the period distribution of pulsars is bimodal, and there are two

separate populations of pulsars. The Crab pulsar was the fastest pulsar known until the discovery of the population of millisecond pulsars in 1982 (Backer *et al.* 1982). The first such object discovered, PSR B1937+21, has a period of 1.56 ms, and is still the fastest known pulsar. It rotates an astonishing 640 times a second. There are currently about 60 millisecond pulsars known with periods less than $\sim$ 50 ms. The short-period edge of this population is not defined, due to selection effects in pulsar searches. These have typical magnetic fields of $10^8 - 10^9$ Gauss, and are among the oldest pulsars (cf. Figure 1.1). The fraction of millisecond pulsars with binary companions is much larger than that for the slower pulsars. This leads to the theory that they are "recycled" pulsars, spun up due to the accretion of mass from their companions (see reviews in Bhattacharya 1996, van den Heuvel 1995).

Millisecond pulsars are an apparently distinct population, yet their emission properties are in many ways similar to those of their more sedate relatives (the "slow" pulsars). We know surprisingly little about the source of that emission, even 30 years after the discovery of pulsars. The radio emission contains a tiny fraction of the total available spin-down energy. This fact hinders complete understanding of the emission process, which must produce radiation for periods and magnetic fields each spanning 3 orders of magnitude. This is possible because the two classes of objects have similar accelerating voltages B/P^2 (cf. Section 1.5). Despite the similarities, this newer class of pulsars probes new aspects of the radiation emission beam and region. It is hoped that by relating the properties of millisecond pulsars to the models of pulsar emission based on the slower objects, we may improve our understanding of these models. The remainder of this chapter is devoted to summarizing our current knowledge of normal pulsars, then discussing the motivation behind this study of millisecond pulsars.

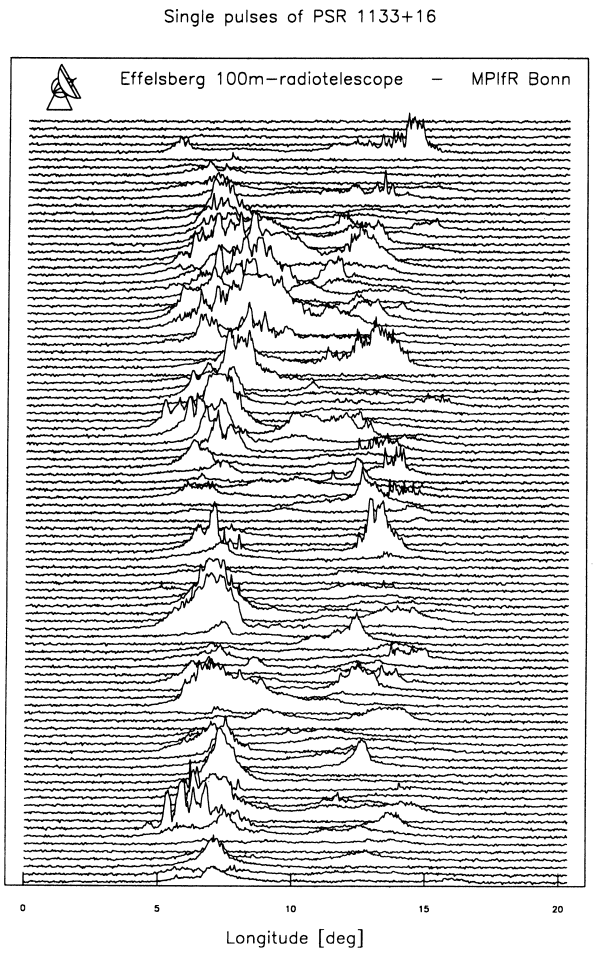

Fig. 1.2.— The measured intensity versus pulse longitude is shown for 100 consecutive single pulses from PSR B1133+16 at 1.41 GHz. One rotation period corresponds to 360° longitude. Both subpulses and microstructure are visible. Taken from Kramer (1995).

1.2 Single Pulses

The first pulsar was originally discovered by observations of individual pulses. Studying the single pulses of many pulsars has told us much about pulsar emission. Figure 1.2 displays a sample of individual pulses from the pulsar B1133+16 at 1.41 GHz.

It is customary to plot the intensity of the radiation versus pulse phase, which is usually quoted in degrees of longitude. One rotation of the pulsar corresponds to one pulse period and 360° of longitude. Individual pulses display a large variety in shape, intensity, and exact location within the pulse. Several bursts of emission are often present in a single pulse. These *sub-pulses* are of order 1 ms – 100 ms for typical pulsars. The range of longitudes where emission is observed for a given pulse reflects the location of instantaneous emission within the pulsar magnetosphere. In some

pulsars, the location of the sub-pulses drifts systematically from one period to the next (*e.g.,* Backer, Rankin & Campbell 1975). This phenomenon is termed *drifting sub-pulses*.

In addition to the sub-pulses, the single pulse intensities are modulated by *microstructure*, which has a characteristic time scale of 1 μs to several hundred μs for slow pulsars.Both sub-pulses and microstructure are visible in Figure 1.2. Microstructure is sometimes quasiperiodic (*e.g.,* Cordes, Weisberg & Hankins 1990), exhibiting a preferred spacing between micropulses. The phenomenon is broadband, occurring across a wide range of frequencies (Rickett, Hankins & Cordes 1975, Boriakoff & Ferguson 1981), although it does not appear to correlate above and below 1.2 GHz (Boriakoff 1992). The longitude of micropulses does not seem to vary with radio frequency, apart from the dispersive effects due to propagation through the interstellar medium (cf. section 1.8). This contrasts with the sub-pulses whose location in longitude changes with the observing frequency (Boriakoff & Ferguson 1981, Boriakoff 1983), similar to the behaviour of the average pulse profiles (cf. section 1.3).

The pulse intensity changes from one pulse period to the next. One measure of this is the *modulation index*

$$m = \sqrt{\frac{\sigma^2_{E_{on}} - \sigma^2_{E_{off}}}{\bar{E}_{on} - \bar{E}_{off}}}, \tag{1.1}$$

where E_{on} is the pulse energy in the pulse window and E_{off} is the pulse energy at a longitude where there is no pulsed emission. This is 1 for 100% modulation of the time series of pulse energies. In a few pulsars, sometimes the change in intensity from pulse to pulse is extreme. The Crab pulsar was discovered by the detection of its very strong individual pulses, dubbed *giant pulses*. These provide a unique probe of the emission from this pulsar. Until recently, this phenomenon was limited to the Crab pulsar, but the fastest millisecond pulsar, PSR B1937+21, has also been shown to possess giant pulses (Backer 1995, Cognard *et al.* 1996).

The pulsed emission sometimes switches off entirely. This *nulling* behaviour typically lasts from a few pulses to hundreds or thousands of periods. In extreme cases a pulsar may be in the null state well over half of the time (*e.g.,* PSR B0826-34, Durdin *et al.* 1979). Nulling is generally a broadband phenomenon, but does not always occur simultaneously at well separated frequencies (Davies *et al.* 1984, Bartel *et al.* 1982, Bartel *et al.* 1981). Nulling behaviour is correlated primarily with the pulse period (Biggs 1992), indicating that it may be due to a faltering emission mechanism. In pulsars exhibiting both nulling and drifting sub-pulses, the drift rate of the sub-pulses has been seen to change during a null, then relax to the pre-null rate (Lyne & Ashworth 1983). Hence there is some "memory" in the system even while the emission is turned off.

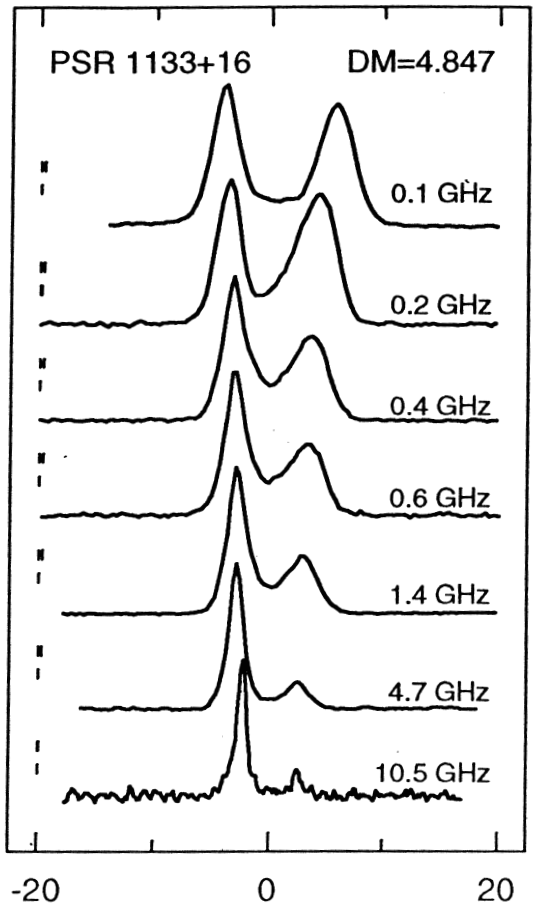

Fig. 1.3.— Average profile of PSR B1133+16 at various radio frequencies. The two components separate with decreasing radio frequency. Taken from Kuzmin *et al.* (1998).

1.3 Properties of Average Profiles: Emission Region

Averaging over hundreds or thousands of pulses leads to an average pulse profile which is remarkably stable for a given pulsar at a given frequency, given the variations in individual pulses. These average profiles stabilize within a few hundred or thousand pulse periods (Helfand, Manchester & Taylor 1975, Rathnasree & Rankin 1995). Figure 1.3 displays the average intensity profile for PSR B1133+16 at several radio frequencies, as a function of pulse longitude. At any given frequency, the average profile has two main components whose longitudes are generally the preferential longitudes of the individual sub-pulses. The average profile is a reflection of the time average of the location of the emission region. The presence of double components in

the profiles of many pulsars suggested a *hollow cone* model of emission (Komesaroff 1970). The existence of triple profiles required the addition of a narrow central pencil beam (Backer 1976). This has come to be known as the *core* emission (Rankin 1983a).

The accuracy of pulsar timing depends on the stability of the average profile over long time scales. Since these measurements are made by comparing the arrival of pulses against a standard template of the pulse profile, unidentified changes in the average pulse shape could introduce systematic errors into the results (see Backer 1989, Backer 1996, Kaspi 1995, Taylor 1994, Taylor 1995,Taylor 1996 for pulsar timing reviews). However average profiles are found to be stable over time scales of years. Blaskiewicz (1991) found that only 2 of 14 pulsars showed any profile shape variations over a time scale of 14.5 years. This indicates that the emission beam location remains constant within the pulsar magnetosphere, which itself maintains (on average), a constant configuration. This is undoubtedly due to the presence of the very strong magnetic field. However, some pulsars display an unusual behaviour known as *moding*, in which the pulsar changes its profile by a large amount, into a new stable configuration (eg. Rankin 1986, Bartel *et al.* 1982). This new profile lasts for a few periods to hundreds of periods, then the profile returns to another mode. Moding is a broadband phenomenon, occurring simultaneously in PSR B0329+54 at both 1.4 and 9.0 GHz (Bartel *et al.* 1982). Mode changes usually affect the average profile mainly by varying the intensity ratios of the components, and through small shifts in component separations. The polarization properties are also changed during a mode change. Bartel *et al.* (1982) suggest that the nulling, moding, and drifting-subpulse phenomena may all be related. A comprehensive list of pulsars exhibiting these phenomena may be found in Rankin (1986).

Based on the above observations, the basic pulsar model is believed to be that of a highly magnetized, rapidly rotating neutron star. The dipolar magnetic field is frozen into the crust and corotates with the pulsar out to the distance of the *light cylinder*, r_{LC}, where the speed associated with rotation reaches the speed of light. The light cylinder for a 1 s pulsar is $\sim$ 48000 km. The region in which the magnetic field lines do not close within the light cylinder is called the *open field region*. On the surface of the neutron star, the *polar cap* is defined by the open field lines. The emission beam is assumed to be a hollow cone with a central component, centered on the magnetic dipole axis, and confined to the open field region above the polar cap. A schematic diagram of the pulsar system for a generic polar cap model is shown in Figure 1.4.

Figure 1.5 shows the possible profiles resulting from various lines of sight across the beam, from a point of view above the polar cap. A line of sight grazing the edge of the emission cone results in a single component profile; a line of sight closer to

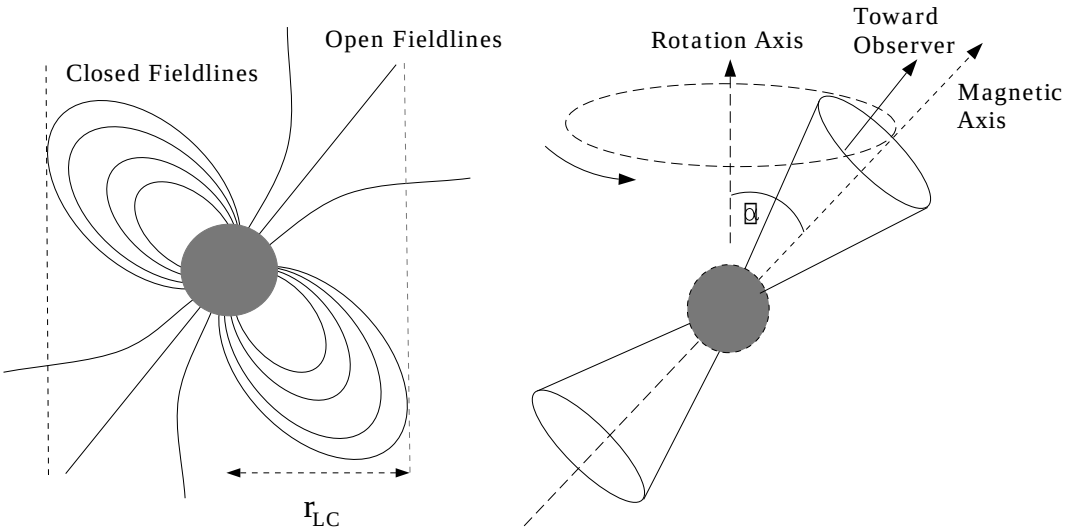

Fig. 1.4.— A schematic diagram of the pulsar configuration. The light cylinder distance r_{LC} is the distance beyond which the corotation velocity would exceed the speed of light. The emission is generated above the polar cap, which is defined on the neutron star surface by the magnetic field lines which do not close within the light cylinder. A hollow cone emission beam is therefore centered on the magnetic axis, which is inclined relative to the rotation axis by an angle α. This sweeps past the observer like a lighthouse beam, resulting in the radio pulse. Adapted from Kramer (1995).

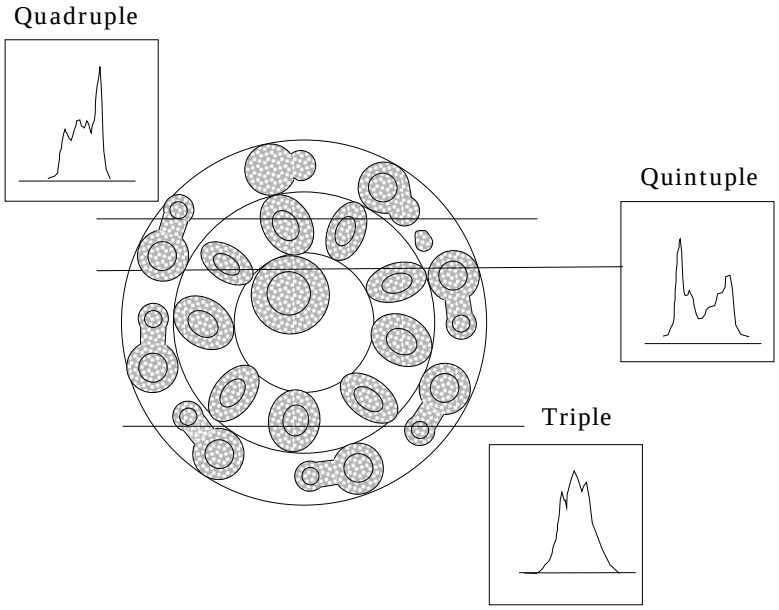

Fig. 1.5.— A schematic diagram showing the possible profiles resulting from various lines of sight across the pulsar beam, which is considered to be a double hollow cone with a central core component. This pulsar beam can result in single, double, triple, quadruple, and quintuple component pulse profiles. Adapted from Rankin (1993a).

the center results in two components, one from each edge of the cone; and a line of sight through the central core results in a triple profile. Rankin introduced a second hollow cone in order to explain pulse profiles with five components (Rankin 1993). The average profiles of some pulsars have two components nearly 180° apart. The weaker *interpulse* is interpreted as emission from the magnetic pole opposite to that of the main pulse, indicating that the *inclination angle* α between the rotation and magnetic axes is nearly orthogonal.

Although the average profile at a particular radio frequency usually remains constant, the shape of the profile changes significantly with frequency. The frequency evolution of the average pulse profiles happens systematically and allows the classification of slow pulsars (Rankin 1983a, 1983b, 1986, 1990, 1993a, 1993b; Lyne & Manchester 1988). Pulse components have been divided into two categories. The central core components already mentioned have steeper spectral indices q than the outer conal components (Rankin 1983a; Lyne & Manchester 1988), frequently have significant circular polarization which changes sign across the pulse profile (see section 1.4; Rankin 1983a), have "white" fluctuation spectra, and do not display drifting sub-pulses (Rankin 1986). Single component pulsars with only core emission exhibit neither moding nor nulling behaviour (Rankin 1986). The *cone* components from the emitting hollow cone have smaller spectral indices, separate with decreasing radio frequency, and occasionally display the drifting sub-pulse phenomenon. Figure 1.3 clearly shows the separation of conal components with decreasing radio frequency.

The quantity $B_{12}/P^2 \propto \left(\dot{P}/P^3\right)^{1/2}$, as will be discussed in section 1.6, measures the acceleration potential available to the particles responsible for the emission. Here the magnetic field is measured in units of 10^{12} Gauss. Pulsars with $B_{12}/P^2 > 2-3$ are dominated by core radiation, while small values of B_{12}/P^2 are associated with pulsars dominated by conal components. Similarly, the parameter $Q = 2P^{1.1}/\dot{P}_{-15}^{-0.4}$ of Beskin, Gurevich, & Istomin (1986, 1988), designed to discriminate between emission modes in their model, separates core and conal pulsars, with $1/Q > 1$ for core emission and $1/Q < 1$ for conal emission, where $\dot{P}$ is measured in units of 10^{-15} s s^{-1}.

The difference in spectral index between the core and cone components means that the core components dominate at low frequencies, while the cone components become more prominent at higher radio frequencies. This difference may be due either to an intrinsic difference in the emission mechanism (Rankin 1990, Rankin 1983a, Weatherall & Eilek 1997) or to purely geometrical effects (Kramer *et al.* 1994, Sieber 1997). It is a function of pulse period, and is greatest for short period pulsars. Most pulsars fit into this classification scheme to explain profile evolution with radio frequency, although there are exceptions (see *e.g.,* Hankins & Rickett 1986).

The observed longitude difference between pulse components can be due to either

angular or vertical separation of the emission region for the various components. Pulse components emitted at lower altitudes arrive later than those emitted at higher altitudes, resulting in a difference in the observed pulse longitude. The observed arrival separation of pulse components emitted at the same altitude is due entirely to their horizontal (angular) separation. If the conal components are in fact emitted at a higher altitude, then the core component should be delayed relative to the symmetry center of the conal components. This is seen in many, but not all, triple component profiles.

In the context of the polar cap models with dipolar magnetic fields, Rankin (1990) found that the core components of pulsars of period P with interpulses (which must all be orthogonal rotators with $\alpha \sim 90°$) follow the relation pulse FWHM (full width at half maximum) $\Delta\Phi \sim 2.45° P^{-1/2}$ for slow pulsars at 1 GHz. The angular size of the last open field line has diameter

$$2\rho \approx 2.49° r_6^{1/2} / P^{1/2}, \tag{1.2}$$

where r is the emission radius in units of the neutron star radius, taken to be 10 km. Thus the observed relation is very nearly the angular size of the last open dipolar magnetic field line at the surface of the neutron star. If the radiation completely fills the open field region, then these components must originate very near the surface of the neutron star to explain the observed widths. They may be emitted at a higher altitude if the components do not fill the open field region. For pulsars which are not orthogonal rotators, we expect the apparent width to be scaled by $1/\sin(\alpha)$. If we assume that they obey the same law as the orthogonal rotators, a measurement of the pulse width allows an estimate of the inclination angle α. Applying this method to the core components of triple and quintuple pulsar profiles allows a determination of α for these pulsars. The observed separations of the symmetric components are then observed to fall along inner and outer cones with radius $4.33° P^{-0.52}$ and $5.75° P^{-1/2}$. If they also originate from the last open field line, then they are emitted at altitudes of 130 and 220 km at a radio frequency of 1 GHz. On the other hand, the dependence on pulse period of the conal component *widths* has not been investigated in detail. For short and long-period pulsars, the similar profile morphologies suggest that this quantity scales with the conal component separation, and therefore also scales with $P^{-1/2}$.

The Monte Carlo simulations of Gil & Han (1996) have also indicated that the pulsar beam size is bimodal with a $P^{-1/2}$ dependence. Lyne & Manchester (1988), however, find a somewhat different relation of pulse width on pulse period, with $\Delta\Phi \sim P^{-1/3}$. Biggs (1990) re-analyzed the same data including the effects of non-circular emission beams, and found the results consistent with $\Delta\Phi \sim P^{-1/2}$. Lyne

& Manchester (1988) also argue for a gradual change in emission properties from the inside to outside of the emission region, rather than two distinct types (core and cone) of emission. In their view, all pulse components are emitted at the same height, along different magnetic field lines within the open field region. The various components arise from the patchy nature of emission within this beam. Investigation of the behaviour of sub-pulses by Gil & Krawczyk (1996) provides one argument that the beam is conal, not patchy. In addition, Gil, Kijak & Seiradakis (1993) confirm the hollow cone component distribution found by Rankin, and argue that a flaw in the analysis of Lyne & Manchester (1988) resulted in the evidence for a patchy beam. They argue, however, for a constant altitude of emission. In further support of this view, Gil (1991) conclude on the basis of dual frequency single pulse observations that the core and conal components of PSR B0329+54 originate at same altitude, indicating that the core emission does not fill the open field region.

Pulse profile studies of slow pulsars have concluded that pulsar radiation is generally emitted at a radius corresponding to a few or a few tens of stellar radii, as was found by Rankin above. Timing measurements at two frequencies place a limit on the departures from the interstellar dispersion delay (cf. section 1.8.1), resulting in a limit on the size of the emission region (Cordes 1978, Phillips 1992, Phillips &Wolszczan 1992). Assuming a dipolar field then places an upper limit on the lower edge of the emission region. Cordes & Stinebring (1984) used multifrequency timing measurements of the millisecond pulsar PSR B1937+21 to restrict the range of emission radii to less than 2 km, for radio frequencies 0.3 to 1.4 GHz. More typically, the emission region is limited to a few hundred km, within a few percent of the light cylinder radius. Scintillation studies have resulted in similar estimates (*e.g.,* Cordes, Weisberg & Boriakoff 1983, Smirnova & Shishov 1989), except during episodes of multiple imaging, when the estimates are near the light cylinder (*e.g.,* Wolszczan & Cordes 1987, Kuzmin 1992). Gwinn *et al.* (1997) used scattering / scintillation to limit the size of the emission region of the Vela pulsar to 500 km, as compared to a light cylinder of 4300 km. Finally, the inclusion of relativistic effects on the polarization profile causes an overall time delay by $4R_e/c$ of the symmetry center of the polarization position angle (PPA) profile relative to that of the intensity profile (cf. section 1.4). This method is independent of assumptions about the magnetic field, and yields emission radii of 100 to 1000 km (Blaskiewicz *et al.* 1991). von Hoensbroech & Xilouris (1997) use both profile widths (and the assumption that the radiation comes from the last open field line) and this relativistic effect to conclude that the emission originates at an altitude of $1-2\%$ of the light cylinder radius.

The integrated profiles typically broaden with decreasing radio frequency; single components broaden, while conal components separate. This is often interpreted as

a radius to frequency mapping. Lower frequencies are emitted higher in the magnetosphere, where the opening angle of the last open field lines is larger. This explains the general evolution of pulse profiles with frequency in Figure 1.3. More specifically, observers find that the observed widths follow the law $\Delta\Phi = A\nu^{-p} + \Delta\Phi_{min}$, for data ranging from 0.1 GHz to 10 GHz (Thorsett 1991, Xilouris *et al.* 1996). At low frequencies, the widths follow a power law, but at high frequencies, there is little change in width with frequency. Observed values of the power law exponent p vary from pulsar to pulsar, but the averages obtained are $\bar{p} \sim 0.1 - 0.3$ (von Hoensbroech & Xilouris 1997a, Thorsett 1991, Kijak & Gil 1997, Kramer *et al.* 1994, Gil & Kijak 1993, Kramer *et al.* 1997, Rankin 1983b). Theoretically, radius to frequency mapping is expected from any model where narrowband emission occurs at a frequency which varies with distance from the surface of the neutron star. Predictions range from $p = 0.14$ to $p = 2/3$ (*e.g.,* Beskin, Gurevich & Istomin 1988, Ruderman & Sutherland 1975).

An alternative interpretation of the data is that the pulse broadening is due to a propagation effect. Broadband emission originates within a narrow range of radius. At high frequencies, the ray paths are straight, so the beam width is independent of frequency, but at low frequencies, refraction causes pulse broadening. Such behaviour is found in models involving propagation of two modes in a birefringent medium (Barnard & Arons 1986, McKinnon 1997). This model can explain those cases where the core component is ahead of the symmetry center of the conal radiation, and the fact that we do not always observe expected altitude delay effects in timing measurements. In particular, only a 2 km range in radius is implied by timing measurements of PSR B1937+21 (Cordes & Stinebring 1984). This model is also attractive for explaining the polarization behaviour of pulsars (cf. section 1.4). The width of the emission beam is determined in this model by pulse widths at high frequencies. Assuming that the emission follows the last open field line, the emission radii are $\lesssim 100$ km (McKinnon 1997). McKinnon (1997) also notes that the model-independent emission heights derived by Blaskiewicz *et al.* (1991) are consistent with emission at a single radius.

The characteristic shape of the emission beam has been a subject of considerable controversy. Jones (1980) and Narayan & Vivekanand (1983) found evidence for beams elongated along the direction of the local longitude, perpendicular to the trajectory of the line of sight. Lyne & Manchester (1988) found no evidence for elongated pulsar beams, and argued for a circular beam. Using the same data set, Biggs (1990) argued that the pulsar beam is compressed along longitude lines, consistent with the expected geometry of the polar cap region for $\alpha \neq 0$. Gil & Han (1996) used Monte Carlo simulations to conclude that the emission beam is circular or slightly elliptical in this same sense.

1.4 Polarization Properties: Pulsar Geometry

The polarization properties of pulsars have enhanced our understanding of these objects. Single pulse studies (*e.g.,* Manchester, Taylor & Huguenin 1975, Backer, Rankin & Campbell 1976) indicate that the degree of polarization varies strongly from one pulse to the next, from very little to almost 100%. Recently, data at 10.55 GHz indicates that the stronger pulses are more weakly polarized (Xilouris *et al.* 1994), while the evidence at lower frequencies suggests the opposite (Rathnasree & Rankin 1996). The polarization position angle (PPA) change of individual sub-pulses is typically less than 30°, with rapid changes usually attributed to the overlap of two sub-pulses with different position angles (Manchester, Taylor & Huguenin 1975). Boriakoff (1996) notes that subpulses generally follow the polarization angle of the average profile (see below). Cordes & Hankins (1977) found that at 430 MHz the PPA remains approximately constant across micropulses, changing only near the edges. Above 1.7 GHz, the PPA of micropulses in PSR B1133+16 may be as found above, or it may sweep up to 60° (Ferguson & Seiradakis 1978). The polarization properties of micropulses can be vastly different from those of the sub-pulse on which they are superimposed (Boriakoff 1996).

The polarization properties of the average profile can be very different from those of the individual pulses, but are usually stable. According to Rathnasree & Rankin (1995), the stabilization rate of polarization profiles correlates with the opening angle of the last open field lines, ρ. Even if the sub-pulses have a large degree of linear polarization, the superposition of many pulses can have a depolarizing effect on the average if the position angle fluctuates from pulse to pulse. Despite this, average pulse profiles are often highly polarized. Some are nearly 100% linearly polarized while others are not. Some pulsars exhibit no significant circular polarization, while pulsar B1702-19 is 60% circularly polarized (Biggs *et al.* 1988). As mentioned in section 1.3, sense-reversing circular polarization is often associated with core components. The polarization position angle (PPA) of the linearly polarized radiation is usually symmetric and independent of frequency, often displaying either a linear gradient or an S-shaped curve across the pulse. The linear polarization of core components may be disorderly (Rankin 1983a). Figure 1.6 displays the polarization properties of the average profile for pulsar B0355+54 at 1.41 GHz. The first component has a high degree of linear polarization, while the second half of the profile is much less polarized. This profile also has significant circular polarization which changes sense part way through the pulse.

The polarized fraction of pulsars is generally constant up to some frequency, and then decreases with increasing radio frequency (Morris *et al.* 1981, Manchester, Taylor

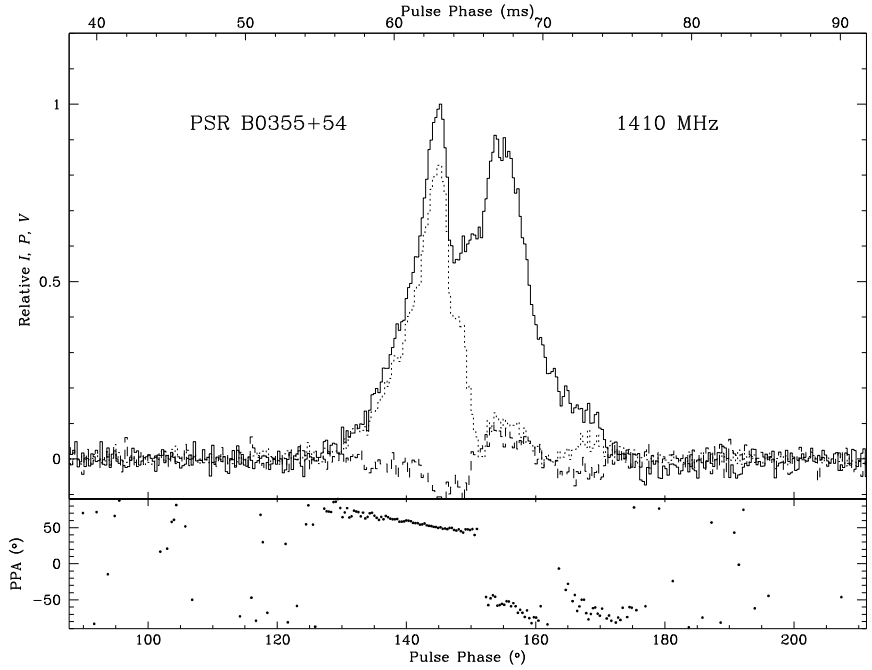

Fig. 1.6.— Polarization profile of pulsar B0355+54 at 1.41 GHz. Solid, dotted, and dot-dashed lines represent the relative intensity, linear, and circular polarizations respectively. The polarization position angle (PPA) is plotted as squares in the lower panel for all points where the linear polarization is greater than the off-pulse rms. The data were taken at the 100-m telescope at Effelsberg with the EBPP (Effelsberg–Berkeley–Pulsar–Processor). The first component is highly linearly polarized, while the remainder of the profile is not. The PPA changes smoothly across the pulse, apart from the abrupt orthogonal mode changes of 90° and associated depolarization. The circular polarization changes sense across the profile, behaviour which is usually associated with a core component.

& Huguenin 1973). In addition, this depolarization appears to correlate with the frequency behaviour of other pulsar parameters, such as pulse width and flux density (Xilouris *et al.* 1996). The depolarization index and the accelerating potential are anti-correlated (Xilouris *et al.* 1995).

Polarization studies led Radhakrishnan and Cooke (1969) to propose a rotating vector model (RVM) which successfully explains the sweep of position angle seen across average pulse profiles of slow pulsars. In this model, the emission which originates near the pole of a dipolar magnetic field is linearly polarized along a direction fixed with respect to the local field. The position angle is then observed to follow the projected direction of the magnetic field. The geometry of the emission region in this model is indicated in Figure 1.7. The inclination of the magnetic axis $\mathbf{B}$ relative to the rotation axis $\mathbf{\Omega}$ is α. The emission beam is centered on $\mathbf{B}$ and has radius ρ. The angle between $\mathbf{B}$ and the observer's line of sight $\mathbf{n}$ attains its minimum value, the

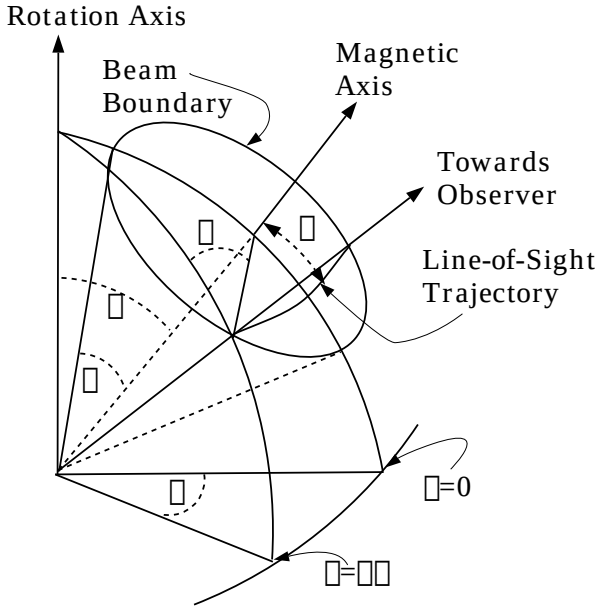

Fig. 1.7.— Geometry of the pulsar emission region as defined by Manchester & Taylor (1977), Rankin (1983a) or Lyne & Manchester(1988). The magnetic axis is inclined relative to the rotation axis by an angle α. The observer's line-of-sight passes through the emission cone with opening angle ρ. The closest approach of the line-of-sight to the magnetic axis occurs at longitude $\phi = 0°$, and defines the impact parameter β. The polarization position angle ψ is measured relative to the projected direction of the magnetic axis. Taken from Kramer (1995).

.

impact parameter β, when the pulse longitude ϕ is zero. The polarization position angle of the linearly polarized radiation, ψ, is measured with respect to the projected direction of the magnetic axis.

In this formulation, the pulse width $\Delta\Phi$ corresponding to the beam radius ρ is given by

$$\sin^2\left(\frac{\Delta\Phi}{4}\right) = \frac{\sin[(\rho/2)+(\beta/2)]\sin[(\rho/2)-(\beta/2)]}{\sin\alpha\sin(\alpha+\beta)}, \tag{1.3}$$

the position angle follows the relation

$$\tan(\psi) = \frac{\sin\alpha\sin\phi}{\sin(\alpha+\beta)\cos\alpha - \cos(\alpha+\beta)\sin\alpha\cos\phi}, \tag{1.4}$$

and the gradient of position angle reaches its maximum when $\phi = 0°$:

$$\left(\frac{d\psi}{d\phi}\right)_{\rm max} = \frac{\sin\alpha}{\sin\beta} \tag{1.5}$$

Figure 1.8 displays the rotating vector model sweep for several different geometries. The steepest slopes at longitude $\phi = 0°$ are attained for small values of the impact

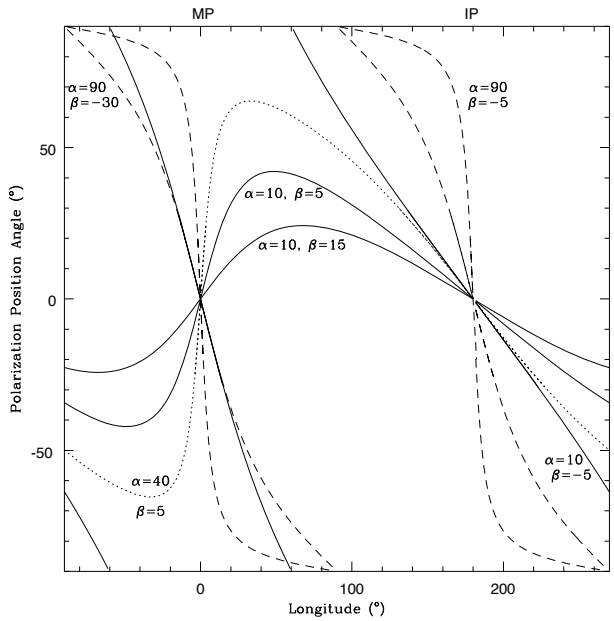

Fig. 1.8.— Rotating vector model of Radhakrishnan & Cooke (1969) for various geometries. Solid lines denote models with magnetic inclination $\alpha = 10°$. Two of the $\alpha = 10°$ models have an impact parameter of $\beta = 5°$, differing only in the sign. This has an enormous impact on the resulting position angle curve. A larger impact angle $\beta = 15$ results in a smaller maximum slope. The effects of different α for different β are seen in the $\alpha = 90°$ (dashed lines) and $\alpha = 40°$ (dotted line) models.

parameter β. The slopes for the main pulse and interpulse are the same for positive β, and opposite for negative β (line of sight between the rotation and magnetic axes). The slopes at the main pulse are nearly the same for $\alpha = 90°, \beta = -30°$ and $\alpha = 10°, \beta = -5°$, but the behaviour at longitudes away from 0° is quite different. The rotating vector model explains the observed sweep of polarization position angle for many pulsars.

Observations of the polarization position angle in principle allow a determination of α and β. The observed pulse width can then be corrected for the effects of the inclination α to provide a value for the beam size ρ. In practice, different values of the inclination angle α mainly affect the wings of the profile, where the data are of poorer quality. The observed central slope provides a relationship between values of α and β via equation 1.5.

Rankin (1990) and Lyne and Manchester (1988) used fits to the polarization angle swing to help determine the geometric angles for many pulsars. Early results indicated that smaller values of the inclination angle α were preferred (Narayan & Vivekanand 1982, Rankin 1990), although Lyne & Manchester (1988) concluded that this was true primarily for older pulsars, with the younger population displaying a more random

distribution. McKinnon (1993) corrected Rankin's data for the meridional beam compression noted by Biggs (1990), and found consistency with a random distribution of inclinations, with no evidence for alignment or counteralignment of the magnetic and rotational axes with time. Using Monte Carlo simulations, Gil & Han (1996) also argue that the distribution of observed inclinations ($\sim \sin\alpha$) is matched by a uniform intrinsic distribution of α.

Not all position angle curves follow the rotating vector model. The PPA in Figure 1.6 displays two abrupt discontinuities in an otherwise smooth progression across the pulse. Such unexpected deviations from simple curves have been successfully interpreted through single pulse polarization observations (Backer, Rankin & Campbell 1976, Backer & Rankin 1980, Stinebring *et al.* 1984a, 1984b). The radiation occurs in two polarization modes, with orthogonal position angles. The two competing modes of emission each trace out a position angle curve consistent with the rotating vector model. A 90° jump in the observed angle occurs when a new mode becomes dominant. The superposition of sub-pulses of different PPAs can result in depolarization of the average, which is frequently observed at such an *orthogonal mode* transition. This effect is visible in the profile shown in Figure 1.6. Gil and collaborators (Gil, Snakowski & Stinebring 1991, Gil *et al.* 1992) have carefully separated the polarization modes in several pulsars, and shown that the polarization modes are not always separated by 90°. The deviations from orthogonality are typically 30°, but may be as much as 60°. The dominant mode follows the rotating vector model, but the weaker one does not always do so. There is also evidence that the two orthogonal polarization modes are associated with the core and cone modes of emission (Gil 1986, Rankin 1988, Radhakrishnan & Rankin 1990).

The observations of these orthogonal modes can be explained in terms of two different modes of propagation through the magnetosphere. The emission mechanism must produce radiation in a mixture of the two modes. In the "adiabatic walking" model of Cheng & Ruderman (1979), the polarization directions of the two propagation modes have a different dependence on $\mathbf{B}$, which bends away from the emission cone, resulting in orthogonal PPAs for the two ray bundles. The more intense mode determines the observed polarization state. More generally, one propagation mode propagates along the magnetic field lines, which separates it from the other mode. This splits the beams for the two polarization states, so orthogonal positional angle changes can occur even if the two beams have equal intensities. At some radius, the conditions in the magnetosphere change so that the second mode no longer follows the magnetic field. This radius is frequency dependent, resulting in the mimicking of the effects of a radius to frequency map. At this *polarization limiting radius*, the polarization properties of the emission are finalized. The pulse width and polariza-

tion reflect conditions at this radius, rather than at the altitude of emission. Barnard (1986) examines this radius, and finds it to be near the light cylinder, which has a significant impact on the predicted shape of the sweep in position angle. If the initial modes of emission are orthogonally polarized, the separation of these beams can result in a change of the dominant mode with pulse longitude. At high frequencies, the two beams of the two modes are not separated, resulting in depolarization of the profiles due to competition between the modes.

The circular polarization properties of the radiation are difficult to explain. It is almost always associated with the core components of radiation, and the direction of anti-symmetry (when present) of the circular polarization is correlated with the direction of the sweep of the linear polarization position angle (Radhakrishnan & Rankin 1990). Symmetric circular polarization is apparent in other profiles. Many models attribute the circular polarization to the effects of propagation through the magnetosphere (*e.g.,* Cheng & Ruderman 1979, Beskin, Gurevich & Istomin 1988, Kazbegi, Machabeli & Melikidze 1991). Radhakrishnan & Rankin (1990) argue that the correlation with the PPA sweep of the linear polarization, which is determined by purely geometric effects, implies that the anti-symmetric circular polarization is also a geometric property of the emission mechanism. The symmetric circular polarization is again attributed to a propagation effect.

1.5 Basic model

The emission in the basic pulsar model introduced in section 1.3, is powered by magnetic dipole radiation, and the energy loss results in the decrease of rotational energy (Ostriker & Gunn 1969).

For radiation produced in a vacuum, the pulsar slows down at a rate given by

$$-\frac{d}{dt}\left(\frac{1}{2}I\Omega^2\right) = \frac{2}{3c^3}|\mathbf{m}|^2\Omega^4\sin^2\alpha \tag{1.6}$$

where $\Omega = 2\pi/P$ is the angular velocity, I is the moment of inertia, and α is the inclination angle between the magnetic moment, $\mathbf{m}$, and the spin axis. For constant moment of inertia (no loss of mass), the change in angular velocity is governed by

$$\dot{\Omega} = -\left(\frac{2m^2\sin^2\alpha}{3c^3I}\right)\Omega^3. \tag{1.7}$$

The braking index, n, is defined by

$$\dot{\Omega} \propto \Omega^n, \qquad n = \frac{\ddot{\Omega}\Omega}{\dot{\Omega}^2},$$

and is 3 for magnetic dipole radiation. This has been measured for a few pulsars and is found to be somewhat lower (see Lyne *et al.* 1996 and references therein), which may be caused by the presence of a particle wind, or variations in the moment of inertia, inclination α, or dipole moment. Nonetheless, integrating this equation gives an estimate of the *characteristic age* τ of the pulsar:

$$\tau = \frac{1}{n-1}\left(\frac{\Omega}{\dot{\Omega}} - \frac{\Omega_i}{\dot{\Omega}_i}\right) = \frac{P}{2\dot{P}} \tag{1.8}$$

for n=3 and the assumption that the initial spin period was much smaller than the current value. The measured value of $\dot{P}$ for a typical slow pulsar is of order $10^{-15}\mathrm{ss}^{-1}$, which leads to characteristic ages of a few million years. Millisecond pulsars have smaller periods, but are observed to have smaller period changes as well, $\dot{P} \lesssim 10^{-19}\mathrm{ss}^{-1}$ (Taylor, Manchester & Lyne 1993, Taylor, *et al.* 1995). The characteristic ages are therefore of the order of a billion years. However, it is unclear that the initial spin period was much less than the current period for these objects (Backer 1998). If that is the case, the age estimates must be revised downwards.

Equation 1.7 also allows us to estimate the strength of the magnetic field $\mathbf{B}$. For $B \approx |\mathbf{m}|/r^3$, the magnetic field at the surface of the star ($r = R_*$) is

$$B_s^2 = \frac{3c^3}{8\pi^2}\frac{I}{R_*^6\sin^2\alpha}P\dot{P}, \tag{1.9}$$

which reduces to

$$B_s = 3.2 \cdot 10^{19} \sqrt{P\dot{P}} \text{ Gauss} \tag{1.10}$$

if we take the moment of inertia to be $I = 10^{45}$g cm^{-3}, the radius of the neutron star to be $R_* = 10$ km, and $\alpha = 90°$. This last assumption of an orthogonal geometry means that equation 1.10 represents a lower limit to the magnetic field. Once again a braking index of $n = 3$ has been assumed, for magnetic dipole radiation. As noted earlier, this leads to typical surface magnetic fields of 10^{12} Gauss for slow pulsars, and 10^9 Gauss for millisecond pulsars (cf. Figure 1.1).

The total energy lost by the pulsar is determined by the rate at which it is slowing down:

$$\dot{E} = -I\Omega\dot{\Omega} = 4\pi^2 I \dot{P} P^{-3}. \tag{1.11}$$

Observed values range from 10^{40} ergs/s to 10^{38} ergs/s. Radio luminosities are typically of order 10^{28} ergs/s, indicating that only a small fraction of the spin-down energy is radiated as radio waves. The *brightness temperature* T_B is defined as the temperature that would be required if the observed radiation were due to blackbody radiation, in the Rayleigh-Jeans approximation:

$$T_B = \frac{c^2}{2k\nu^2}$$

For pulsars, the observed flux F is related to intensity I by $F = \int I \, d\Omega$. An effective solid angle $\Omega_{eff} = (c\Delta t/D)^2$ is used to determine I for the brightness temperature calculation: $I = F/\Omega_{eff}$, where D is the distance to the pulsar, and Δt is the time scale of the observed radiation (the pulse width, for example). Brightness temperatures are typically $\sim 10^{25} - 10^{30}$ K for pulsars.

Pulsars are steep spectrum objects, weakening at high frequencies as noted earlier. At about 100 MHz, the spectrum turns over, while at high frequencies there is a break, and subsequent steepening of the power law(Malofeev *et al.* 1994). At *very* high frequencies there is evidence for a turn-up in the spectrum of some pulsars (Kramer *et al.* 1996).

1.6 Pulsar Magnetospheres

In section 1.5 we restricted our attention to a vacuum magnetic field. Goldreich & Julian (1969) showed, however, that the pulsar must be surrounded by a magnetosphere which substantially exceeds this density. In the case of an aligned rotator, the rotating magnetic field induces in the interior of the star (assumed to be a conductor) an electric field which satisfies

$$\mathbf{E} + \left(\frac{\mathbf{\Omega} \times \mathbf{r}}{c} \right) \times \mathbf{B} = 0.$$

This electric field generates a considerable surface charge density, which then generates an exterior electric field with a non-zero component parallel to the magnetic field at the surface. At the surface of the neutron star, the force due to this electric field will overcome the effects of gravity and atomic binding to strip both electrons and ions from the surface (*e.g.,* Jones 1986, Neuhauser *et al.* 1987, Kossl *et al.* 1988). The pulsar must then be surrounded by a plasma with sufficient charge density to short out the parallel component of this electric field. This Goldreich-Julian density is

$$\rho_{G-J} = \frac{\nabla \cdot \mathbf{E}}{4\pi} = \frac{\mathbf{\Omega} \cdot \mathbf{B}}{2\pi c} \frac{1}{\left(1 - \left(\frac{\Omega r}{c}\right)^2 \sin^2 \theta\right)}$$

In the Goldreich-Julian magnetosphere, particles in the closed field region are trapped and corotate with the neutron star. Charges found along the open magnetic field lines leave the system and are constantly replenished from the surface.

The spin-down torque of this aligned rotator model is similar in magnitude to that of magnetic dipole radiation from an orthogonal rotator. Arons (1992) noted that this is essentially a measure of the Poynting flux crossing the surface at the light cylinder.

Certain perturbations in this charge-density structure magnetosphere are unstable, and allow for the possibility of evacuated regions within the Goldreich-Julian magnetosphere (Holloway 1973). All modern pulsar models rely on the presence of such gaps in the magnetosphere.

Ruderman & Sutherland (1975) expected that positive ions would not flow freely from the surface. Thus in a model with the magnetic axis anti-parallel to the rotation axis, the ions necessary to shield out the parallel electric field are not available, resulting in a gap near the surface above the polar cap. This gap sustains a potential difference given by the voltage difference between the magnetic pole and the surface position of the last open field line:

$$\Delta\Phi = \frac{\Omega^2 m}{2c^2} \propto \frac{B}{P^2}, \tag{1.12}$$

and this accelerates the particles to energies up to

$$E = \frac{\Delta\Phi}{2} = 3 \times 10^{12} \frac{R_6^3 B_{12}}{P^2} \text{ eV}. \tag{1.13}$$

Particles within the gap will therefore be accelerated to ultra-relativistic energies. The positrons are accelerated outward along the curved magnetic field lines, and emit curvature radiation with energy

$$E_{photon} = \frac{3}{2} \frac{\gamma^3 \hbar c}{\rho_c} \tag{1.14}$$

where $\gamma = (1 - v^2/c^2)^{-1/2}$. In the presence of a sufficiently strong component of the magnetic field ($B_{crit} \sim 10^{13}$ G) transverse to its motion, photons with energy exceeding twice the rest mass of an electron can decay into an electron-positron pair. Any such pair produced within the gap is immediately accelerated, leading to more high energy photons and the further generation of pairs. The initial, or primary, particles produce a cascade of secondary particles within the gap (Sturrock 1971), which discharges the gap. These primary particles may arise as a result of the electron-positron decay of a stray background gamma photon. The curvature radiation from these primary and secondary beams of particles provides the observed radiation. The system reaches a quasi-stable state for a certain gap thickness.

This type of polar cap model is believed to produce the observed radio radiation, although as noted above it is now believed that ions will also flow freely from the surface.

This problem is overcome in the slot-gap model of Arons & Scharlemann (Scharlemann, Arons & Fawley 1978, Arons & Scharlemann 1979). Due to curvature of the magnetic field lines, the charge density cannot both maintain the Goldreich-Julian value and flow in such a way as to conserve the current. This inconsistency creates an electric potential to accelerate the particles. An alternative acceleration mechanism due entirely to relativistic effects is proposed (Muslimov & Tsygan 1990, 1992). Such effects will certainly influence the calculations of other models.

Polar cap models generally have the difficulty that the star will become charged, due to the current induced by the flow of charges. This can be resolved by a return current, although it is unclear exactly how this will be achieved.

Polar cap models typically require a radius of curvature much smaller than that for a dipole magnetic field in order to produce the observed radiation. Additional multipoles near the surface are postulated in order to solve this problem. However, higher order multipoles are ruled out on the basis of the location of the spin-up

line of millisecond pulsars, as they are derived from magnetic torques (Arons 1993).[2] Additionally, Kramer *et al.* (1997) find no evidence for non-dipolar effects.

The frame-dragging effects of general relativity (Beskin 1990, Muslimov & Tsygan 1990, Muslimov & Tsygan 1992) significantly alters the electric potential which accelerates the particles, resulting in much higher energy gamma rays. This effect, combined with an offset dipole, provides agreement between theory and the location of the pulsar "death valley" - the voltage ($\propto B/P^2$) below which pulsars are not seen (Arons 1997).

The surface defined by $\mathbf{\Omega}\cdot\mathbf{B} = 0$ separates the space charges of different sign. This surface is problematic in the standard polar cap model, since some open field lines cross this null surface. Outflowing charges must therefore cross regions of opposite sign. Some models (*e.g.,* Michel 1982, Krause-Polstorff & Michel 1985) limit the plasma-filled zones to polar and equatorial regions, leaving this area empty. In other models, these regions are the source of the acceleration potential, due to the formation of *outer gaps* (Cheng, Ho & Ruderman 1986).

The gamma and X-ray radiation may also come from the polar cap region (*e.g.,* Daugherty & Harding 1982). However, the observed properties of the Crab and Vela pulsars are better described by the outer gap model of Cheng, Ho, & Ruderman (1986) mentioned above. Recently, Romani & Yadigaroglu (1995) investigated in detail the geometry of such a system, and find that it explains many facets of the gamma-ray observations, and the relative longitudes of the gamma and radio emission.

1.7 Pulsar Emission

Any proposed mechanism of pulsar radio emission must be coherent in order to explain the high brightness temperatures of the observed radiation. It must also explain the sub-pulse and micropulse fluctuations, and the polarization properties of the individual pulses. The existence of millisecond pulsars implies that the emission mechanism must work over a broad range in both pulse periods and magnetic fields. Any mechanism which depends strongly on either quantity is unlikely to succeed. The voltage B/P^2 is, however, similar for the two classes of objects.

[2]Millisecond pulsars are spun-up to some limiting period during their evolution. The equilibrium period resulting from accretion at the Eddington rate (radiation pressure balances the gravitational force) depends on the magnetic field of the neutron star, resulting in a relation between P and $\dot{P}$. The spin-up line is simply this relation.

There are three main possible types of pulsar emission mechanisms as outlined by Melrose (1992, 1996). These are (i) coherent emission by bunches, (ii) relativistic plasma emission and (iii) maser emission. In the first of these, a bunch of N charged particles within a volume smaller than $\sim \lambda^3$ (so that coherence is maintained within the bunch) flows along the curved magnetic field lines, emitting curvature radiation as though it were a single macroparticle. Then the power emitted by the bunch is equivalent to N^2 times the power emitted by a single particle in the bunch. This was one of the first mechanisms proposed (cf. Sturrock 1971, Ruderman & Sutherland 1975) and was studied in detail by Buchauer & Benford (1976, 1977). The bunching is due to some instability such as the two-stream instability which results when the primary beam of particles interacts with the much less energetic secondary beam. This emission mechanism is still discussed in the literature (*e.g.,* Gil & Snakowski 1990a, Gil & Snakowski 1990b), especially by observers. Melrose points out, however, that the bunch must take the form of a flat pancake that rotates to keep its normal nearly parallel to the magnetic field, which is a rather unlikely configuration. In addition, proposed instabilities grow too slowly to produce or even maintain the required bunches (Melrose 1992), which lose coherence quickly.

Relativistic plasma emission models produce radiation indirectly. A plasma instability such as the streaming instability discussed above generates turbulence. The energy in the turbulence cannot escape directly, but must be converted by some nonlinear process into escaping waves. In the models among this class there are variations in both the type of plasma instability and the conversion process used to convert the energy into radiation (Asséo 1993, Beskin, Gurevich & Istomin 1986, 1988, Kazbegi *et al.* 1991, Weatherall 1997). The frequency of the resulting emission is determined by the local plasma frequency $\omega_p \propto \sqrt{\Omega B}$ and the Lorentz factor, γ, of the particles that drive the instability (Melrose 1996).

Maser emission in atoms or molecules occurs for an inverted energy population, in which the higher energy level is overpopulated with respect to the lower level. Maser emission mechanisms proposed for pulsar emission require some analog to the inverted energy population. This can occur in a variety of models of curvature drift (Luo & Melrose 1992) or the distortion of magnetic field lines (Luo & Melrose 1995), which are sensitive to the value of the magnetic field B, making it difficult to explain both millisecond and normal pulsars. Another possibility is free electron maser emission (Melrose 1978, Rowe 1995), due to a time-varying component of the electric field parallel to B. In both cases, the emission is produced at some characteristic frequency (see Melrose 1996 for details). Like emission from bunches, maser emission can escape the magnetosphere directly, unlike relativistic plasma emission models.

1.8 Propagation Effects

1.8.1 Dispersion delay in cold plasma

Electrons in a plasma are moved by incident electromagnetic waves. This motion in turn influences the propagation of the wave. As a result, pulses emitted simultaneously at two frequencies will reach the observer at different times.

The plasma frequency ω_p is:

$$\omega_p = \sqrt{\frac{4\pi n_e e^2}{m_e}},$$

where e, m_e and n_e are the charge, mass, and number density of electrons. The cyclotron frequency ω_c is the gyration frequency of an electron about a magnetic field B_0

$$\omega_c = \frac{eB_0}{m_e c}.$$

The wave number k of the radiation is then

$$k_{\mathrm{R,L}} = \frac{\omega}{c}\sqrt{1 - \frac{\omega_p^2}{\omega(\omega \pm \omega_c)}},$$

resulting in a group velocity v_g

$$v_g = \frac{d\omega}{dk} = c\sqrt{1 - \frac{\omega_p^2}{\omega^2}}$$

in the absence of a magnetic field. The resulting delay due to the dispersive medium is then (for $\omega \gg \omega_p$)

$$t_p = \int_0^D \frac{ds}{v_g} = t_0 + \frac{2\pi e^2}{m_e c\,\omega^2}\int_0^D n_e(s)\,ds, \tag{1.15}$$

The difference in arrival time between two frequencies ν_1 and ν_2 is

$$\begin{aligned} \Delta t_{DM} &= \frac{e^2}{2\pi m_e c}\left(\frac{1}{\nu_1^2} - \frac{1}{\nu_2^2}\right)\int_0^D n_e(s)\,ds \\ &= \frac{DM}{2.41033 \cdot 10^{-16}}\left(\frac{1}{\nu_1^2} - \frac{1}{\nu_2^2}\right) \end{aligned} \tag{1.16}$$

where we have defined *Dispersion Measure*, DM, to be the column density in units of cm^{-3} pc and the frequency is measured in MHz. Pulsar observers usually round the dispersion coefficient to $2.410 \cdot 10^{-16}$.

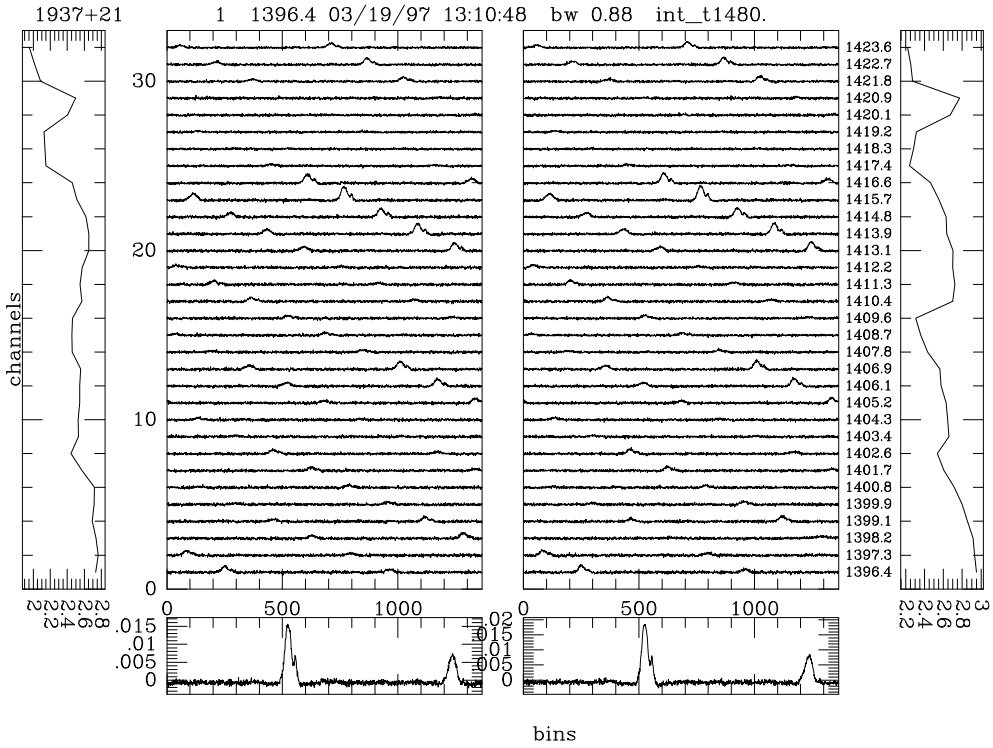

Fig. 1.9.— The differing delay in arrival times due to the dispersion of the interstellar medium for pulsar B1937+21 at 1.41 GHz. The data were taken at the 100-m telescope at Effelsberg with the EBPP (Effelsberg–Berkeley–Pulsar–Processor), which removes the dispersion within each 0.875-MHz channel. The horizontal axis for the central panels is in bins, and covers the full 1.56 ms period of this pulsar. The two large panels display the raw data for left and right circular polarizations, which clearly shows the remaining dispersion delay between channels. In the lower two panels this delay has been removed and the channels have been summed.

The results of dispersion delay are shown for the pulsar B1937+21 at 1.41 GHz in Figure 1.9. The dispersion measure of this pulsar is 71. These data were taken with the EBPP (cf. section 2.2.2), which removes the effects of dispersion within each channel, leaving the delay between channels.

Dispersion Measures vary with time (Backer *et al.* 1993) due to irregularities in the ISM and the relative motions of pulsar and observer.

1.8.2 Faraday rotation

In the presence of magnetic field, the group velocity v_g is different for the two senses of circular polarization. The phase offset between the two circular polarizations increases with distance travelled through the plasma. This introduces a rotation $\Delta\psi$ in the

polarization position angle as the radiation propagates through the ionized medium:

$$\Delta\psi = \frac{1}{2}\int_0^D (k_R - k_L)\, ds = \frac{2\pi e^3}{m_e^2 c^2 \omega^2}\int_0^D n_e B_{||}\, ds \qquad \text{radians}, \tag{1.17}$$

where $B_{||}$ is the component of the magnetic field parallel to the propagation path ds, and we have assumed $\omega \gg \omega_p$, $\omega \gg \omega_c$. The *Rotation Measure RM* is then defined as

$$RM = \frac{\Delta\psi}{\lambda^2} = \frac{e^3}{2\pi m_e^2 c^4}\int_0^D n_e B_{||}\, ds = 8.1 \cdot 10^5 \int_0^D B_{||} n_e\, ds \qquad \text{rad m}^{-2} \tag{1.18}$$

where $B_{||}$ is measured in Gauss, n_e in cm^{-3}, and distance D in parsecs.

The measured polarization position angle will therefore change with radio frequency, resulting in depolarization of the profile if its effects are not removed across the observing band.

1.8.3 Scattering

The interstellar medium also scatters pulsar signals. In the thin screen approximation, an electromagnetic plane wave is incident on a screen made up of electron-density irregularities, which disturb the phase of the incoming wave. The radiation of wavelength λ is scattered into a cone of width $\Theta_s = \lambda/l_\phi$, where l_ϕ is the transverse length scale over which the phase is perturbed by one radian. The delay due to the extra distance travelled along various paths broadens the pulse. The distribution of scattered radiation is assumed to be Gaussian in angle. As a result, the pulse is broadened by convolution with the impulse response of the thin-screen ISM, which is

$$e^{-t/\tau_B}; \qquad \tau_B = x(1-x)\Theta_s^2 D/c, \tag{1.19}$$

for a thin screen at distance xD and pulsar at distance D. This effect is largest for pulsars with large dispersion measures, where the signal has passed through a large column density of electrons, and is strongly dependent on frequency, becoming more important for long wavelengths.

In addition to pulse broadening, interstellar scattering causes temporal variations in the brightness of a pulsar, known as *scintillation*. The phases of the electromagnetic waves are disrupted during their multi-path propagation through the non-uniform interstellar medium. A pattern of constructive and destructive interference is therefore created. Diffraction occurs when the phase in a wavefront is perturbed by large values within the Fresnel-zone radius. Due to the relative motions in the system, the observer

moves relative to this pattern, resulting in time-variations of the pulsar intensity. The intensity variations will occur at different times for different radio frequencies. Such interstellar scintillation variations in the intensity of PSR B1937+21 are visible in the various channels of Figure 1.9.

Large scale gradients and irregularities in the interstellar medium result in refractive scintillation. The irregularities act as weak lenses along the line of sight, distorting the source's intensity by $\sim 25\%$ and possibly its apparent position.

The intensity variations due to interstellar scintillation mean that not all observations of pulsars will result in the same signal-to-noise. The intensity amplification can be extreme in the transition region between strong and weak scattering, if a diffractive maximum occurs within a refractive maximum. Observations taken at times of scintillation maxima are clearly preferred!

1.9 Millisecond Pulsars

Despite their faster spin periods and smaller magnetic fields, the average profiles of millisecond pulsars exhibit many of the same characteristics as those of slow pulsars. Their spectra are the same, although they are slightly less luminous and less efficient (Kramer *et al.* 1998). Their properties do not, however, easily find an interpretation in the well established classification schemes developed by the systematic studies of normal pulsars discussed in section 1.3.

Millisecond pulsars could not be easily studied in detail until recently, due to the increased time resolution required and the difficulty in overcoming the effects of dispersion due to the interstellar medium. The amount of polarization and profile data is increasing, although it is still somewhat limited. Thorsett and Stinebring (Thorsett & Stinebring 1990) obtained polarization measurements at Arecibo for three millisecond pulsars, but only obtained multifrequency polarimetry for one of the objects. Segelstein *et al.* (1986) obtained polarimetry on a single object at a single frequency. Recently, Kramer *et al.* (1997b) and Xilouris *et al.* (1998) reported the results from profile and polarization monitoring of 23 millisecond pulsars at 21cm. There is, however, still a relative paucity of published profiles at other frequencies, and the resolution of the published profiles is sometimes poor.

Such preliminary investigations have shown that decoding the emission geometry of millisecond pulsars will not be simple. The profiles of millisecond pulsars have, on average, one more component than slow pulsars, and are much more likely to have pre- or post-cursors or interpulses (Kramer *et al.* 1998, Ruderman 1991a). Millisecond pulse profiles also have larger duty cycles. The width-Period relation for conal components in slow pulsars scales to a beam width of 180°, and therefore a duty cycle of 1 for a period of 1-4 ms (Kramer *et al.* 1998). This partially explains the large duty cycles, but the widths of millisecond pulsars therefore imply a beam angle narrower than that implied by the scaling law. Similarly, the Rankin core component width-period relation implies a very open magnetic field, and wide pulses for millisecond pulsars. However, Backer (1995) noted that there seem to be unusually narrow components in many millisecond pulsars. As an example, PSR B1937+21 is expected, based on the acceleration potential B/P^2 to be dominated by core emission. Then the predicted pulse width is $\Delta\Phi = 2.45^{\circ}P^{-1/2} = 63^{\circ}$, while the observed width is closer to 10°.

The magnetic field topology in the magnetospheres of millisecond pulsars is a subject of substantial theoretical interest and controversy. A 3 millisecond pulsar has a light cylinder of only 6-10 stellar radii, so the emission (or polarization limiting radius) may occur much closer to the light cylinder. This is supported by emission

altitude estimates of Kramer *et al.* (1998). The relativistic delay of the PPA, relative to the symmetry center of the pulse, is a fraction $2R_e/\pi r_{LC}$ of the pulse period, and is therefore most significant for emission close to the light cylinder. Deviations from a dipole magnetic geometry are also expected to affect the polarization position angle data, since the standard rotating vector model is tied to the magnetic field. The expected openness of the magnetic field configuration at large radii leads to the possibility of observing effects due to magnetic field sweepback. The calculations of Barnard (1986) suggest a flattening of the PPA slope for emission (or cessation of propagation effects) near the light cylinder. In addition, the symmetry center of the PPA profile is moved *earlier* relative to the intensity profile, in opposition to the effects of relativistic delay. On the other hand, Gangadhara (1996) finds that even for emission near the light cylinder, the PPA curve will be similar to that for emission near the magnetic pole. In this context, it has been suggested that many pulse-interpulse pairs are actually produced from a single pole, despite their separation by 180° (Gangadhara 1996, Manchester 1996).

Some magnetospheric models anticipate unusual magnetic field configurations for millisecond pulsars, due to the recycling which occurs during their evolution (Ruderman 1991a, 1991b; Chen & Ruderman 1993a). It is possible that these will affect the polarization observations of these objects. The effects of evolutionary behaviour are already evident, since isolated millisecond pulsars have lower luminosity than those in binary systems (Bailes *et al.* 1997, Kramer *et al.* 1998). The evolution of millisecond profiles with radio frequency is larger for less massive companions, resulting in a dependence on pulse period, which depends on the evolution of the system (Kramer *et al.* 1998). Additionally, the spectral indices of millisecond pulsars are correlated with either age or period (Lorimer *et al.* 1995b; Kramer *et al.* 1998).

Polarization measurements are especially interesting for millisecond pulsars in binaries for which we can measure the Shapiro delay. In these systems, the pulses are delayed by the effects of general relativity as the radiation passes the companion, and the measurement of this effect allows the determination of the orbital inclination. If the pulsar spin axis is aligned with the orbital angular momentum vector (a modest assumption), then we know some of the angles in the radio emission system already. Thus polarization observations which help identify the geometry of the emission region for millisecond pulsars are very important.

Thorsett and Stinebring (1990) stress that although the integrated profiles of the pulsars in their small sample exhibit polarization features similar to those seen in slower pulsars, at least two of them do not fit into classifications designed to accommodate slower pulsars. Navarro and Manchester (1996) have studied the polarization of pulsar J0437−4715, and find a very large number of components, with odd varia-

tions in position angle. In addition, there is mounting evidence for variation in the pulse profiles and polarization properties of millisecond pulsars (Xilouris *et al.* 1998, Sallmen *et al.* 1997). An unusual example of mode changing is the millisecond pulsar PSR B1821−24, whose second component varies relative to the others on the timescale of days (Backer & Sallmen 1997), which is much longer than the typical moding time scale of slow pulsars. The profiles of several millisecond pulsars also show remarkable development with frequency, containing components with relatively flat spectra (*e.g.,* Fruchter *et al.* 1990; Backer 1995). However, on average the millisecond pulsar average profiles seem to evolve less than the slow pulsars (Kramer *et al.* 1998). In the sample of 1400 MHz polarization profiles (Xilouris *et al.* 1998), the development of the pulse profile with frequency is classified as normal for 4 pulsars, abnormal for 8 pulsars, and 15 pulsars show minimal profile evolution with frequency. If the magnetic fields of millisecond pulsars were greatly disturbed from a dipole, then a radius to frequency mapping would imply a *greater* evolution of profile with frequency, due to the increased dependence of the magnetic field on radius. On average, this is not seen.

Results at single frequencies for the slightly longer period pulsars B1534+12 (Arzoumanian *et al.* 1996) and B1913+16 (Cordes, Wasserman & Blaskiewicz 1990) are not entirely consistent with models developed for slower pulsars, but do possess overall similarities to results for slow pulsars. Thus the pulsars in this transition region may provide a link between the fastest millisecond pulsars and the slow pulsars.

It is clear that polarimetric and multifrequency observations of millisecond pulsars are leading to results which are not simply extensions of the theory developed for slow pulsars. Consistent polarization and profile data at several frequencies are essential to obtain an understanding of these objects.

Part I

Polarimetry

Oh all of the questions
All of the stars in the sky
Oh never the answers
Always the wondering why

"I Would I Were" by James Keelaghan

Chapter 2

Observing Particulars

2.1 Telescopes and Receivers

2.1.1 Green Bank 140′

The 800-MHz and 575-MHz polarimetric data presented in this thesis were all obtained at the NRAO 140′ (43m) telescope at Green Bank, WV. This telescope has an equatorial mount, which means the orientation of the feed remains fixed with respect to the source. The feed must be rotated manually in order to deal with polarization calibration issues (cf. section 2.5.2).

The 300-1000 MHz and 1000-1450 MHz prime focus receivers were used for these observations. At 800 and 1400 MHz dual orthogonal linear polarizations were received, amplified, and passed through a quadrature hybrid device for conversion to left and right hand circular polarizations. Independent linearly-polarized diode noise sources were injected prior to the first stage of amplification for secondary calibration purposes. At 575 MHz the hybrid is immediately after the feed, and the independent noise sources are therefore circularly polarized. A correlated noise source was injected prior to the hybrid for these observations. The radio frequency (RF) signals centered at 800 MHz were mixed with a local oscillator (LO) to an intermediate frequency (IF) of 250 MHz, and passed through 80-MHz bandpass filters. The GBPP (cf. section 2.2.1) requires an IF near 400 MHz. The signals were therefore converted to an IF of 420 MHz by mixing with another LO, and passed through another 80-MHz bandpass filter centered at 400 MHz. Our 28-MHz observing band was centered at 400 MHz, corresponding to an RF of 820 MHz. The 575-MHz RF signals were mixed with an LO to an IF of 250 MHz, passed through 80-MHz bandpass filters, converted to an IF of 400 MHz with another LO, and and passed through another set of 80-MHz bandpass filters. Our 28-MHz observing band was centered at a sky radio frequency of 575-MHz.

Typical system temperatures for the 575, 800, and 1400-MHz observations are

60-70K, 40-60K and 20-25K respectively, with antenna gains of 0.25-0.3 K Jy^{-1}.

2.1.2 Green Bank 85-3

The Green Bank 85-3 was one element of an interferometer consisting of three 25-m telescopes. This telescope is now used as a pulsar monitoring telescope, and was used to obtain polarization data for the Crab pulsar. Two linearly polarized 610-MHz signals are mixed to an IF of 400 MHz, and passed to the GBPP.

2.1.3 Effelsberg 100m

The 100-m telescope at Effelsberg, Germany was used for the 1400 MHz observations presented here. The alt-azimuth mount of this telescope results in an automatic rotation of the feed relative to the sky. This *parallactic angle* must be included in the processing of any observations. The 1.41-GHz HEMT receiver located at the prime focus is tunable between 1.3 and 1.7 GHz. The antenna gain at these frequencies is 1.5 K Jy^{-1}, independent of elevation. Dual orthogonal linear polarizations are received, amplified, and passed through a quadrature hybrid device for conversion to left and right hand circular polarizations, following the NRAO design. A single linearly polarized noise source is injected prior to the hybrid for calibration purposes. These incoming radio frequency signals were passed through bandpass filters centered at 1415 MHz which have a 130-MHz bandwidth. The 1410-MHz signals were mixed to an IF of 150 MHz. This IF was passed to the EBPP, which immediately mixed the signals with another LO to an IF of 440 MHz. Our observing bandwidth (28 MHz) was centered at 1410 MHz. The system temperature was 35-50K for these observations.

2.2 Berkeley Pulsar Processors

The effects of interstellar dispersion discussed in section 1.8.1 are most troublesome for short period objects, where the dispersion across even a relatively narrow band can be a significant fraction of a pulse period. Traditionally, the incoming signal has been divided up into many separate narrow frequency channels, within which the dispersion smearing is no larger than the desired temporal resolution. The signal in each channel is later delayed by the expected dispersion delay prior to averaging over the channels. For high resolution profiles at short periods, the channels must become very narrow, limiting the total bandwidth which may be used. An alternative approach has been to record fast-sampled raw voltage data. The effects of interstellar dispersion amount to a frequency-dependent phase rotation of the complex voltages. This complex multiplication in the frequency domain, or convolution in the time domain, may be removed in software prior to detection (Hankins 1971, Hankins & Rickett 1975). This coherent dedispersion technique results in high time resolution, but requires significant computer resources. The Berkeley Pulsar Processors were developed to perform the deconvolution in real-time, to simplify later processing.

2.2.1 GBPP

The Green Bank-Berkeley Pulsar Processor (GBPP) was originally called the Coherent Dispersion Removal Processor, or CDRP. The CDRP was designed for sensitive high resolution timing and polarimetry observations of short period, highly dispersed pulsars. The effects of interstellar dispersion are removed via complex convolution in the time domain. The GBPP currently consists of 32 frequency channels for each polarization. It can remove up to 1024 time samples of dispersion per channel for channel bandwidths up to 1 MHz. The channel widths can be set in steps of 1.414, and full Stokes parameters can be analyzed for channel bandwidths up to 0.875 MHz. Other observing modes allow channel bandwidths up to 4 MHz for intensity observations. The minimum time resolution in the pulse profile for polarization observations is one of (a) period/2048; (b) inverse of the channel bandwidth, whichever is largest.

The CDRP was designed and constructed by the Berkeley Pulsar Group, starting with support from the NSF Science & Technology Center for Particle Astrophysics. In 1994 a half system (16 channel) CDRP-0 was brought to Green Bank. This system was used for some initial polarization observations. In 1995 a full system CDRP-2 was brought to Green Bank. In 1996 the designed CDRP-2 system was completed with the addition of an agile analog stage of electronics. CDRP-2 normally resides at the 85′ telescope, and was used for the small amount of polarimetric data taken with

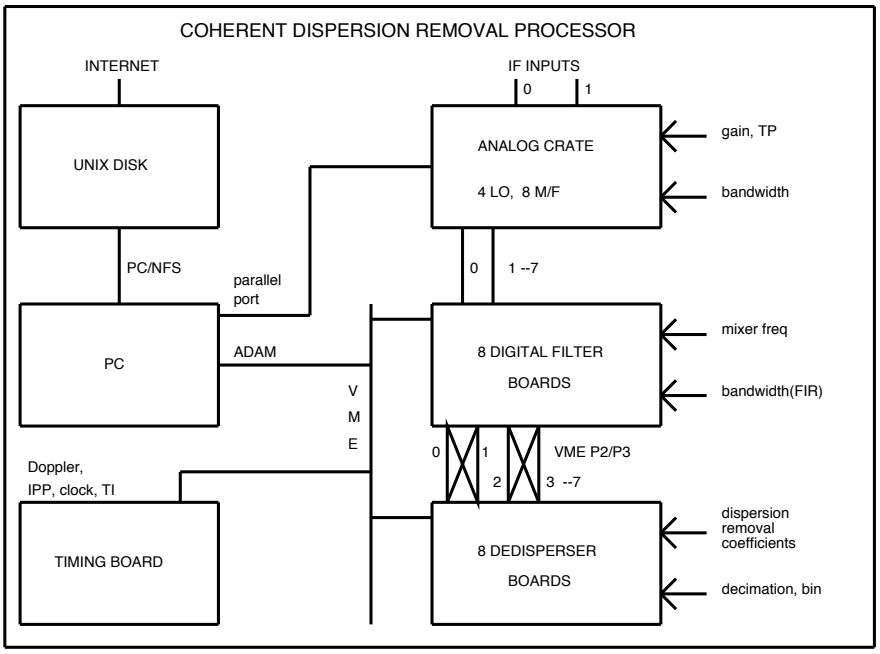

Fig. 2.1.— A block diagram of the Berkeley Pulsar Processor. This coherent dispersion removal processor has an analog crate and 8 digital filter boards to channelize the data, which is dedispersed, detected, and averaged by the dedisperser boards. The timing board synchronizes the system, which is controlled by a PC.

this telescope. CDRP-2 was renamed GBPP to provide uniformity amongst other processors completed or under construction. This processor was used for all of the 575-MHz observations and the majority of the 800-MHz observations. Up to 28 MHz of bandwidth could be used for the polarization observations.

The GBPP consists of Analog and Digital Crates for channelization, dispersion removal, detection and signal averaging. A schematic diagram showing the major components of the GBPP is shown in Figure 2.1. The analog crate divides the incoming signal for each polarization into 4 bands, mixing each to baseband. The Digital Filter Boards (DFBs) divide each of these bands into 8 individual channels, resulting in 32 channels per polarization. Four channels of each polarization (from two DFBs) are passed to a single Dedisperser Board (DB) for processing. On each DB, a VLSI device developed by Amar Kapadia *et al.* (1993) performs a 1024-point complex deconvolution of the dispersion effects of the interstellar plasma. This is followed by detection of the signal (and cross-detection to generate the Stokes parameters), and averaging synchronously with the pulse period. The Timing Board controls the DFBs

and DBs, tracks the apparent pulsar period, and communicates with the PC which controls the system. The A/D (analog to digital) portion of the system has 4-bit output, while the DFB output is 2-bit. This results in a non-linear power correction which must be applied to the data during processing. A partial technical description of the GBPP, focussing on the DFB, may be found in Backer *et al.* (1997).

2.2.2 EBPP

The Effelsberg-Berkeley Pulsar Processor (EBPP) is a clone of the GBPP, and was used for the 1400-MHz observations. The first half of the system (16 channels) was installed at the Effelsberg 100m telescope in 1996 October (denoted EBPP-a in table 2.1), and a limited amount of polarimetry data was obtained at that time. The system was completed before the remainder of the observations in Spring 1997.

2.3 Observing information

Polarimetry observations were obtained at several epochs. The 575-MHz data were all obtained at Green Bank in 1997 July, in a run dedicated to polarization. The 800-MHz data were obtained in 1995 January/February, 1997 February, April, and July. Most of these data were obtained during standard pulsar timing runs (see Foster & Backer 1990 for a description of the Pulsar Timing Array program) which use the Spectral Processor; therefore a limited amount of calibration was possible for these data. Due to concerns about instrumental effects introduced by the hybrid, the hybrid was removed from the system for the 1995 data, resulting in dual linear polarizations. The 1400-MHz data were obtained at Effelsberg in 1996 October, 1997 March/April.In addition, we present polarimetry of the Crab pulsar at 610 MHz, taken at the 85-3 telescope in Green Bank, WV.

The dates of observation are displayed for each pulsar in table 2.1, along with the radio frequency in MHz, channel bandwidth in MHz, number of channels available, the polarization system used, and the processor which obtained the data. In all cases, the raw data consists of scans with 16 or 32 frequency channels, up to 2048 time bins, and 4 polarizations, each having an integration time of 2 to 15 minutes (usually near 5 minutes). The data were inspected for interference, and problem scans and channels were removed from further consideration.

In order to produce a polarization profile for a given pulsar at a given frequency, gain calibration (cf. section 2.4) must be applied, the instrumental polarization effects of the telescope must be removed (cf. section 2.5), any polarization position angle offsets between different sets of data must be removed, and the scans must be temporally aligned (cf. section 2.6).

Summary of Observations

Source	Dates	Freq MHz	CBW MHz	Chans	Poln Sys	Observing System
B0531+21	1996 11/13-4,27,30, 12/2	610	0.5	32	lin	GBPP
J0613-0200	1997 7/28-9	575	0.70	32	circ	GBPP
J0613-0200	1995 1/30-1, 2/06-7	800	0.70	16	lin	CDRP-0
J0613-0200	1997 2/10-1, 4/26,28-9, 7/31-8/01	820	0.875	32	circ	GBPP
J0613-0200	1997 4/09	1410	0.875	32	circ	EBPP
J0751+1807	1997 3/19	1410	0.875	32	circ	EBPP
J1012+5307	1997 7/25-9	575	0.875	32	circ	GBPP
J1012+5307	1997 2/10-2, 4/26-9, 7/31-8/01	820	0.875	32	circ	GBPP
J1012+5307	1996 10/15	1410	0.7	16	circ	EBPP-a
J1012+5307	1997 3/19	1410	0.875	32	circ	EBPP
J1012+5307	1997 4/09	1410	0.875	32	circ	EBPP
J1022+1001	1997 7/25-8	575	0.875	32	circ	GBPP
J1022+1001	1997 2/12, 4/27-30, 7/31	820	0.875	32	circ	GBPP
J1022+1001	1996 10/05	1410	0.7	12	circ	EBPP-a
J1022+1001	1997 3/19, 4/09	1410	0.875	32	circ	EBPP
J1518+4904	1997 3/19	1410	0.875	32	circ	EBPP
B1620-26	1997 7/26-30	575	0.50	32	circ	GBPP
B1620-26	1997 2/10-2, 4/26-30, 7/30-8/01	820	0.875	32	circ	GBPP
B1620-26	1995 1/31, 2/06	800	0.70	16	lin	CDRP-0
B1620-26	1995 2/05	800	0.70	16	circ	CDRP-0
B1620-26	1997 3/20,24,4/10	1410	0.875	32	circ	EBPP
J1640+2224	1997 3/24, 4/10	1410	0.875	32	circ	EBPP
J1643-1224	1997 3/20, 4/10	1410	0.875	32	circ	EBPP
J1713+0747	1997 7/25-30	575	0.875	32	circ	GBPP
J1713+0747	1997 2/10-2, 4/26-30, 7/30-1	820	0.875	32	circ	GBPP
J1713+0747	1995 1/30-1, 2/05-7	800	0.70	16	lin	CDRP-0
J1713+0747	1995 2/05	800	0.70	16	circ	CDRP-0
J1713+0747	1997 3/19-20, 4/09	1410	0.875	32	circ	EBPP
J1730-2304	1997 7/29-30	575	0.875	32	circ	GBPP
J1730-2304	1997 2/10-1, 4/26-7, 7/31-8/01	820	0.875	32	circ	GBPP
J1730-2304	1997 4/10	1410	0.875	32	circ	EBPP
B1821-24	1997 7/25-30	575	0.35	32	circ	GBPP
B1821-24	1997 2/10-1, 4/26-30, 7/31-8/01	820	0.70	32	circ	GBPP
B1821-24	1997 3/20,24, 4/10	1410	0.875	32	circ	EBPP
B1937+21	1997 7/24-30	575	0.50	32	circ	GBPP
B1937+21	1997 2/10-1, 4/26-9, 7/31-8/01	820	0.875	32	circ	GBPP
B1937+21	1995 1/31	800	0.70	16	lin	CDRP-0
B1937+21	1995 2/05-7	800	0.70	16	lin	CDRP-0
B1937+21	1997 3/19-20,24, 4/10	1410	0.875	32	circ	EBPP
J2145-0750	1997 7/25-30	575	0.875	32	circ	GBPP
J2145-0750	1997 2/10-1, 4/26-9, 7/31-8/01	820	0.875	32	circ	GBPP
J2145-0750	1995 1/29-31, 2/05-6	800	0.70	16	lin	CDRP-0
J2145-0750	1995 2/04	800	0.70	16	circ	CDRP-0
J2145-0750	1997 4/10	1410	0.875	32	circ	EBPP

Table 2.1: **Observing Information for Millisecond Pulsars**. For each pulsar, the observing dates, radio frequency in MHz, the channel bandwidth in MHz of the BPP, and the number of channels are listed in columns 2-4. Columns 5 and 6 indicate whether the data were taken in the linear or circular polarization basis, and the observing system which recorded the data.

2.4 Gain Calibration

The data obtained using two orthogonal polarizations A and B must be converted from raw data counts to flux units for each polarization. Observations of a calibrated pulsed noise source allow the determination of the number of counts per CAL deflection. Pulsed noise observations both on and off an unpolarized standard source of known flux F then allow determination of the flux per CAL deflection, and therefore per count. This gain factor g_i is determined for each polarization i in Jy/c, and may then be applied to the data.

If the noise source has a known temperature T_{CAL_i} in polarization i, then we can determine the *system temperature* T_{SYS_i}, the antenna temperature T_{ANT_i}, and the *antenna gain* G_i in K/Jy for the observations. The Kelvins per count for polarization i, $(K/c)_i$, is determined by

$$(K/c)_i = \frac{T_{CAL_i}}{(counts(CAL_{ON}) - counts(CAL_{OFF}))_i}, \tag{2.1}$$

and the system temperature is given by

$$T_{SYS_i} = (K/c)_i \cdot counts(CAL_{OFF_i}). \tag{2.2}$$

Observations of the system temperatures both ON and OFF an unpolarized standard source of known flux F gives the antenna temperature

$$\begin{aligned} T_{ANT_i} &= T_{SYS_i}(ON) - T_{SYS_i}(OFF) \\ &= (K/c)_i \cdot (counts(ON) - counts(OFF))_i, \end{aligned} \tag{2.3}$$

and the gain G_i of the telescope in Kelvins per Jansky:

$$G_i = \frac{T_{ANT_i}}{F}. \tag{2.4}$$

The overall gain factor g_i in Jy/c,

$$g_i = (K/c)_i / G_i \tag{2.5}$$

may then be applied to each polarization i of the data. The calibrated total intensity is then $I = (E_A E_A^* \cdot g_A + E_B E_B^* \cdot g_B)/2$. For polarization data, the cross terms $Re(E_A^* E_B)$ and $Im(E_A^* E_B)$ must be multiplied by a gain factor $g_{AB} = \sqrt{g_A g_B}$.[1]

[1]These quantities are related to the Stokes parameters by equation 2.8

In practice, $(K/c)_i$ may change with parameters such as observing bandwidth, while G_i is expected to be more stable. Observations of a standard source are therefore used to determine this latter quantity. To obtain a gain factor g_i appropriate for each polarization at each observation, G_i (determined as described above), is coupled with $(K/c)_i$ as determined from pulsed noise observations using the current observing parameters. If the calibration observations used to determine $(K/c)_i$ for the current observing parameters are at a different bandwidth than the standard source calibration observations used to determine G_i, then the two quantities are combined by matching channels by frequency.

Note that the value of g_i is independent of the value of T_{CAL_i} which is actually used, and so this method may be used whether or not it is known, as long as the pulsed noise source is stable with time. If the value of T_{CAL} is not accurate, however, the individual values of G and T_{ANT} will not be accurate.

2.4.1 Practicalities

A noise source which is correlated between the two polarizations allows a determination of the instrumental phases in the system, as will be discussed in Section 2.5.3. This was true for most of our observations, allowing the standard calibrator noise signals to be used. For the 575-MHz system at Green Bank, independent noise sources are usually injected after the hybrid, so no measurement of instrumental phase between circular polarizations is possible. A single noise source was therefore coupled into the system at the feed, resulting in a correlated noise source, to allow measurement of the phases for each channel. The temperature of this source was, however, unknown. Values of T_{CAL_i} were chosen such that the antenna temperatures of the two polarizations were nearly equal, as is true when the standard calibration signal with known temperature is used. As noted above, these values do not affect the final gain calibration. For a few observations, this correlated calibration source was not available, so the standard pulsed noise source was used. In these cases, the observations were only included in the calculation if the antenna temperatures were nearly equal for all channels, as is expected. This also gave the most consistent gain calibration between channels.

Table 2.2 displays the standard sources used for each observing run and frequency, along with their fluxes in Janskys, the type of pulsed noise source used (correlated or standard), the observing system, and the rms of the antenna temperature ratio across the channels, which provides some estimate of the error in the resulting gain calibration of the data.

Gain Calibration Sources

Dates	Freq MHz	Source	Flux Jy	CAL Type	Observing System	Estimated Error(%)
1997 7/25-30	575	3C 48	30.9	C/S[a]	GBPP	15/10
		3C 286	22.0	C/S		15/5
1996 11/13-12/02	610	none[b]		C	GBPP	50
1995 1/29-31, 2/5-7	800	3C 48	24.4	S	CDRP-0	6,20
1995 2/3-5	800	none[c]		S	CDRP-0	–
1997 2/10-12, 4/26-30	820	3C 48	24.0	S	GBPP	6,5
1997 7/30-1	820	3C 48	24.0	C	GBPP	10
1997 7/31-8/1	820	3C 48	24.0	S	GBPP	5
1996 10/5,15	1410	none[b]			EBPP-a	–
1997 3/19-20, 3/23-4	1410	1345+12[d]			EBPP	7
1997 4/9-10	1410	1345+12	5.25	C	EBPP	7
		4C12.50				

[a]C-correlated CAL, S-standard independent linearly polarized CALs

[b]Calibration was achieved by assuming that the system temperatures of the two polarizations were equal.

[c]Calibration was achieved using K/c values

[d]used 4/9-10 calibration data

Table 2.2: Gain Calibration Sources are summarized for each observing date and frequency. The standard source and its associated flux in Jy are listed in columns three and four. The CAL type in column 5 is designated C if the injected CAL signal was correlated, and S if it was nominally uncorrelated (although for all but the 575-MHz data a small amount of correlation was introduced in the hybrid). The observing system is listed in column 6. An estimate in the error in the gain calibration is provided by the *rms* variation of the antenna temperature ratio about the mean, and is given in column 7.

2.5 Polarization Calibration

2.5.1 Theory

When taking polarization data, we are measuring radiation from orthogonal polarizations A and B, but the observed radiation will have been affected by passage through the telescope system. Following the formalism of McKinnon (1994), the measured radiation $E_A{}'$ and $E_B{}'$ relates to the intrinsic radiation E_A and E_B via

$$\begin{pmatrix} E_A{}' \\ E_B{}' \end{pmatrix} = \begin{pmatrix} T_{AA} & T_{AB} \\ T_{BA} & T_{BB} \end{pmatrix} \begin{pmatrix} E_A \\ E_B \end{pmatrix} \tag{2.6}$$

where the elements of this transmission matrix are

$$\mathbf{T} = g \begin{pmatrix} 1 & K_{AB}e^{i\theta_{AB}} \\ K_{BA}e^{i\theta_{BA}} & K_{BB}e^{i\theta_{BB}} \end{pmatrix}, \tag{2.7}$$

where g is the overall gain factor, $K_{BB}e^{i\theta_{BB}}$ describes the relative gain and phase between A and B, and the cross terms describe the coupling between the two polarizations. This matrix contains 7 independent parameters.

We now consider the effects of this transmission matrix on the intrinsic Stokes parameters, which are

$$\mathbf{S} = \begin{pmatrix} S_0 \\ S_1 \\ S_2 \\ S_3 \end{pmatrix} = \begin{pmatrix} E_A E_A^* + E_B E_B^* \\ E_A E_A^* - E_B E_B^* \\ 2Re(E_A E_B^*) \\ 2Im(E_A E_B^*) \end{pmatrix}. \tag{2.8}$$

When A and B correspond to linear polarizations X and Y this corresponds to $\mathbf{S}^T = (I, Q, U, V) = (I, P\cos(2\chi), P\sin(2\chi), V)$, whereas for circular polarizations L and R this is $(I, V, Q, U) = (I, V, P\cos(2\chi), P\sin(2\chi))$, where the linear polarization is described by amplitude P and position angle χ with $Pe^{i2\chi} = Q + iU$. Positive V is associated with left-handed circular polarization.

Apart from the overall and relative gain factors g and K_{BB}, which can be removed using gain calibration, the dominant effect is the relative phase between A and B introduced by the telescope. In addition to this phase angle, there are telescope parameters K_{BA}, θ_{BA}, K_{AB}, and θ_{AB} which describe the way in which intrinsic polarization B is detected in measured polarization A and vice versa. For known telescope parameters, the instrumental effect on the intrinsic Stokes parameters $\mathbf{S}$ is given by

$$\mathbf{S}''(\beta) = \mathbf{M} \cdot \mathbf{R}(2\beta) \cdot \mathbf{S}, \tag{2.9}$$

where $\mathbf{M} = \frac{g^2}{2}\mathbf{M_0}$ is the Mueller matrix and $\mathbf{M_0}$ is shown in equation 2.10 on page 47.

The matrix $\mathbf{R}(2\beta)$ is the rotation matrix used to rotate the Q and U components by 2β, which is the orientation angle of the feed relative to the source. In the circular polarization basis, this matrix is

$$\mathbf{R}(2\beta) = \begin{pmatrix} 1 & 0 & 0 & 0 \\ 0 & 1 & 0 & 0 \\ 0 & 0 & \cos(2\beta) & \sin(2\beta) \\ 0 & 0 & -\sin(2\beta) & \cos(2\beta) \end{pmatrix}. \tag{2.11}$$

If A and B are truly orthogonal, then this implies that $K_{BA} = K_{AB} = 0$, and the instrumental effects are described by

$$\mathbf{M} = \frac{g^2}{2}\begin{pmatrix} 1+K_{BB}^2 & 1-K_{BB}^2 & 0 & 0 \\ 1-K_{BB}^2 & 1+K_{BB}^2 & 0 & 0 \\ 0 & 0 & 2K_{BB}\cos(\theta_{BB}) & 2K_{BB}\sin(\theta_{BB}) \\ 0 & 0 & -2K_{BB}\sin(\theta_{BB}) & 2K_{BB}\cos(\theta_{BB}) \end{pmatrix},$$

where $g = K_{BB} = 1$ holds for previously gain-calibrated data.

If A and B are circular polarizations, the relative phase angle θ_{BB} causes a rotation between Stokes parameters Q and U, and is thus simply a rotation of the position angle. If we are using the linear polarization basis, then this angle causes a rotation between Stokes parameters U and V. This completely corrupts observations of the polarization of the source, and must be carefully removed. In the non-orthogonal case, the instrumental terms K_{BA}, θ_{BA}, K_{AB}, and θ_{AB} affect all of the Stokes parameters, and their interdependence is considerably more complicated.

2.5.1.1 Circular Basis

In the basis of circular polarizations L and R, it is physically meaningful to write the transmission matrix $\mathbf{T}$ as

$$\mathbf{T} = \begin{pmatrix} \dfrac{1}{(1+\epsilon_L^2)^{1/2}} & \dfrac{\epsilon_L e^{i\theta_L}}{(1+\epsilon_L^2)^{1/2}} \\ \dfrac{\epsilon_R e^{-i\theta_R}}{(1+\epsilon_R^2)^{1/2}} & \dfrac{1}{(1+\epsilon_R^2)^{1/2}} \end{pmatrix}, \tag{2.12}$$

assuming that the relative gain calibration has been applied, and that the relative instrumental phase between L and R will be dealt with separately. In this case

$$\begin{pmatrix} 1+K_{BB}^2+K_{AB}^2+K_{BA}^2 & 1-K_{BB}^2-K_{AB}^2+K_{BA}^2 & 2(K_{AB}\cos(\theta_{AB})+ & 2(K_{AB}\sin(\theta_{AB})+ \\ & & K_{BA}K_{BB}\cos(\theta_{BB}-\theta_{BA})) & K_{BA}K_{BB}\sin(\theta_{BB}-\theta_{BA})) \\ 1-K_{BB}^2+K_{AB}^2-K_{BA}^2 & 1+K_{BB}^2-K_{AB}^2-K_{BA}^2 & 2(K_{AB}\cos(\theta_{AB})- & K_{AB}\sin(\theta_{AB}))+ \\ & & K_{BA}K_{BB}\cos(\theta_{BA}-\theta_{BB})) & K_{BA}K_{BB}\sin(\theta_{BA}-\theta_{BB})) \\ 2(K_{BA}\cos(\theta_{BA})+ & 2(K_{BA}\cos(\theta_{BA})- & 2(K_{BB}\cos(\theta_{BB})+ & 2(K_{BB}\sin(\theta_{BB})+ \\ K_{AB}K_{BB}\cos(\theta_{AB}-\theta_{BB})) & K_{AB}K_{BB}\cos(\theta_{AB}-\theta_{BB})) & K_{AB}K_{BA}\cos(\theta_{AB}-\theta_{BA})) & K_{AB}K_{BA}\sin(\theta_{AB}-\theta_{BA})) \\ 2(-K_{BA}\sin(\theta_{BA})+ & 2(-K_{BA}\sin(\theta_{BA})- & 2(-K_{BB}\sin(\theta_{BB})+ & 2(K_{BB}\cos(\theta_{BB})- \\ K_{AB}K_{BB}\sin(\theta_{AB}-\theta_{BB})) & K_{AB}K_{BB}\sin(\theta_{AB}-\theta_{BB})) & K_{AB}K_{BA}\sin(\theta_{AB}-\theta_{BA})) & K_{AB}K_{BA}\cos(\theta_{AB}-\theta_{BA})) \end{pmatrix} \tag{2.10}$$

the nominally orthogonal circularly polarized response of the telescope is actually elliptically polarized, with axial ratios $\rho_i = (1-\epsilon_i)/(1+\epsilon_i)$, and position angles of the major axes $\tau_i = \theta_i/2$. See equation A.5 of Stinebring (Stinebring 1982) for the complete Mueller matrix resulting from this definition.

In practice, $\epsilon_i << 1$, so the complex leakage factors $\boldsymbol{\epsilon_L} = \epsilon_L e^{i\theta_L}$ $\boldsymbol{\epsilon_R} = \epsilon_R e^{i\theta_R}$ correspond directly to $K_{LR}e^{i\theta_{LR}}$ and $K_{RL}e^{i(\theta_{RL}-\theta_{RR})}$ in the earlier formulation.

By defining the sum and difference vectors,

$$\begin{aligned} \boldsymbol{\sigma} = \sigma e^{i\psi_\sigma} &= \boldsymbol{\epsilon_L} + \boldsymbol{\epsilon_R} = \epsilon_L e^{i\theta_L} + \epsilon_R e^{-i\theta_R} \\ \boldsymbol{\delta} = \delta e^{i\psi_\delta} &= \boldsymbol{\epsilon_L} - \boldsymbol{\epsilon_R} = \epsilon_L e^{i\theta_L} - \epsilon_R e^{-i\theta_R} \end{aligned} \tag{2.13}$$

and neglecting terms of ϵ_i^2, the Mueller matrix becomes

$$\mathbf{M} = \begin{pmatrix} 1 & 0 & \sigma\cos(\psi_\sigma) & \sigma\sin(\psi_\sigma) \\ 0 & 1 & \delta\cos(\psi_\delta) & \delta\sin(\psi_\delta) \\ \sigma\cos(\psi_\sigma) & -\delta\cos(\psi_\delta) & 1 & 0 \\ \sigma\sin(\psi_\sigma) & -\delta\sin(\psi_\delta) & 0 & 1 \end{pmatrix}.$$

Even if the telescope response is elliptically rather than circularly polarized, they may be orthogonal to one another if $\epsilon_L = \epsilon_R$ and $\theta_L = \theta_R + \pi$, implying $\sigma = 0$.

We have separated out the effects of the relative phase $\psi = \theta_{RR}$ between the polarizations L and R, so we model the measured Stokes by

$$\begin{aligned} \mathbf{S}''(\beta) &= \mathbf{R}(\psi)\cdot\mathbf{M}\cdot\mathbf{R}(2\beta)\cdot\mathbf{S} \\ &= \begin{pmatrix} I + P\sigma\cos(\phi-\psi_\sigma) \\ P\cos(\phi-\psi) + I\sigma\cos(\psi_\sigma+\psi) - V\delta\cos(\psi_\delta+\psi) \\ P\sin(\phi-\psi) + I\sigma\sin(\psi_\sigma+\psi) - V\delta\sin(\psi_\delta+\psi) \\ V + P\delta\cos(\phi-\psi_\delta) \end{pmatrix}, \end{aligned} \tag{2.14}$$

where $\phi = 2(\chi - \beta)$.

Thus the Stokes parameters will vary sinusoidally with the angle β describing the relative orientations of the feed and the source position angle.

2.5.2 Calibration Procedure

In what follows, we assume that the gain calibration has been carried out using the standard method described in section 2.4. We may therefore set the overall and relative gain parameters g and K_{BB} to 1 before proceeding further. To determine the other telescope parameters, we must observe a source for which the Stokes parameters

are known. Equation 2.14 shows that the instrumental polarization parameters will determine the sinusoidal variations of the Stokes parameters with feed angle β. For a source with a single constant position angle, it is necessary to observe the source for many different rotation angles β of the feed, in order to obtain measurements at many effective position angles of the polarized source. For a telescope with an alt-azimuth mount, this is achieved simply by tracking the source across the sky, since the orientation of the feed relative to the source changes during the observation (cf. Stinebring 1982). For a telescope with a polar mount, the relative positions of the feed and the source do not change during tracking, so the feed angle must be intentionally rotated (McKinnon 1994). For N such observations of the measured Stokes $\mathbf{S}'$, we may fit for the n_p parameters of the Mueller matrix $\mathbf{M}$ by comparing these with the model Stokes $\mathbf{S}''$, and minimizing an averaged χ^2 defined by

$$\chi^2 = \frac{1}{4(N - n_p - 1)} \sum_{i=0}^{3} \sum_{j=0}^{N-1} (S_{ij}{}' - S_{ij}{}'')^2. \tag{2.15}$$

In the case of a pulsar, however, we can obtain a measurement of the Stokes parameters at many phases across the pulse. Then the position angle changes automatically across the pulse according to the sweep of the position angle of the pulsar. This approach has been taken by Stinebring (1982) and Xilouris (1991). Even if the position angle changes only modestly across the pulse, a small number of feed rotation angles will adequately sample the total range of effective position angles. Thus, given a pulsar for which the Stokes parameters are known, we can perform the least-squares fit discussed above. In practice, this is complicated by the fact that pulsars scintillate due to the effects of the interstellar medium, and so the total intensity I is not constant in time. Following Stinebring (1982), we note that the quantity $I_{const} = [I^2 - (Q^2 + U^2 + V^2)]^{1/2}$ is a constant under the transformation of the Mueller matrix, so it may be used to correctly normalize all measured Stokes profiles prior to fitting for instrumental parameters.

Once the polarization parameters of the telescope are determined, the Mueller matrix $\mathbf{M}$ is fully known, and the true measured Stokes parameters $\mathbf{S_{cal}}$ of a source of unknown polarization may be determined using simple matrix inversion:

$$\mathbf{S_{cal}}(\beta) = \mathbf{R}(-2\beta) \cdot \mathbf{M^{-1}} \cdot \mathbf{R}(-\theta_{BB}) \cdot \mathbf{S}' \tag{2.16}$$

where the relative phase angle θ_{BB} has been separated from the Mueller matrix as was done explicitly above for the circular basis.

2.5.3 Application to Circular Polarization data

If the relative instrumental phase introduced between the two circular polarizations varies significantly across the bandwidth of the system, then depolarization of the polarization profile will result when the data are averaged, unless this instrumental effect has been first removed.

At Effelsberg, a single linearly polarized pulsed noise source is injected prior to the hybrid. Given knowledge of the intrinsic position angle of this calibrator signal, the instrumental rotation ($\psi = \theta_{RR}$) may be determined by measuring the position angle from the Q and U components of the pulsed noise signal for each channel. In practice, we do not know the intrinsic position angle of the calibrator, but θ_{RR} varies substantially between channels for the BPP systems, and so this measurement allows the relative instrumental phase between channels to be determined. This measurement may then be used to remove the instrumental phase from all the data. This was done for the 1997 March and April data, but was not possible for the 1996 October data. The same is true for the non-standard correlated calibrator signal which was injected into the 575-MHz system at Green Bank (cf. Section 2.4.1).

For the 800-MHz system at Green Bank, independent linearly polarized noise sources are injected prior to the hybrid. If they had equal amplitudes, any pulsed noise signal visible in the polarization cross terms would be introduced by the hybrid. If the amplitudes are not equal, then there is a net linear polarization in the signal. In either case, measurement of the pulsed noise signal in the two cross terms again allows measurement of the instrumental phase. Since most of the 820-MHz data were obtained during standard timing runs, these standard noise sources were used. For a brief period of time in 1997 July, a correlated noise signal was introduced as for the 575-MHz system, to improve the measurement of the relative phase. A comparison of the measurement using the two different CAL signals revealed that for some channels, the results differed systematically by $30 - 40°$. These were exactly the channels for which the instrumental phase resulted in very little signal in one of Q or U. In these cases, the more weakly correlated standard CAL provided insufficient signal for the measurement. As a result, the measurement of the more strongly correlated signal was applied to all the data for that epoch. This procedure was confirmed by inspecting the resulting relative PPA values for PSR B1937+21 after application of the two possibilities. It is possible that similar problems in measurements of the instrumental phase were present for the other 1997 820-MHz data.

For the 1995 January/February data taken in the circular polarization basis, no attempt has been made to remove the relative instrumental phases across the 16 channels of CDRP-0.

2.5.3.1 1410-MHz EBPP data

In order to determine the remaining instrumental parameters, polarization measurements are made of a pulsar with known Stokes parameters at a variety of feed angles. PSR B1929+10 was used for this purpose. To use this object, we needed to know its intrinsic polarization properties. At 1410 MHz we obtained polarization profiles from both Stinebring (1982), who kindly sent us his thesis data, and from Gould & Lyne (1997).[2] These were interpolated to the resolution of our data. The data were gain-calibrated, and the instrumental phase was removed as described above. The model Stokes parameters for this object were compared with the data for all points in the region where the model exceeded a specified threshold (usually 10% of the peak), in a global fit using equations 2.14 and 2.15. The data were normalized as described in Section 2.5.2, after which a simple grid search algorithm determined the following parameters: the offset in polarization position angle between the data and model profiles, the gain factor required to match the data to the model profile, and the Mueller matrix parameters $\delta, \psi_\delta, \sigma$, and ψ_σ. These final parameters were used to invert the Mueller matrix for application to the data for the remaining pulsars. Similar results were obtained in fits using both model profiles. A separate fit was done for data taken on each day of observations. The magnitudes of δ and σ are similar for each day, but the phases ψ_δ and ψ_σ were not constant. The results from the appropriate day were therefore applied to all pulsar data, although the signal to noise of the PSR B1929+10 data for the 1997 April 9/10 was lower, resulting in less certainty about the instrumental calibration.

It is apparent from equation 2.14 that the measured Stokes parameters will vary sinusoidally with the angle β describing the relative orientations of the feed and source PPA, with vertical offsets equal to the true values of the Stokes parameters.

Figure 2.2 displays the B1929+10 Stokes parameters (I', Q', U', V') for a single channel of 1410-MHz EBPP data from a single day, averaged over the center of the gain-calibrated pulse profile, normalized by $I'_{const} = [I'^2 - (Q'^2 + U'^2 + V'^2)]^{1/2}$, and plotted against β, which includes both the feed angle and the parallactic angle correction. The expected sinusoidal variations with β are visible. The top 3 panels of Figure 2.3 display, for all channels, the results of a fit which included only the instrumental parameters δ and ψ_δ, setting $\sigma = 0$. The dotted lines in Figure 2.2 result from applying the Mueller matrix corresponding to these parameters to the average Stokes model. The solid lines result from applying results of a fit which also

[2]Obtained from the data base of published profiles maintained by the European Pulsar Network, available at: http://www.mpifr-bonn.mpg.de/pulsar/data/

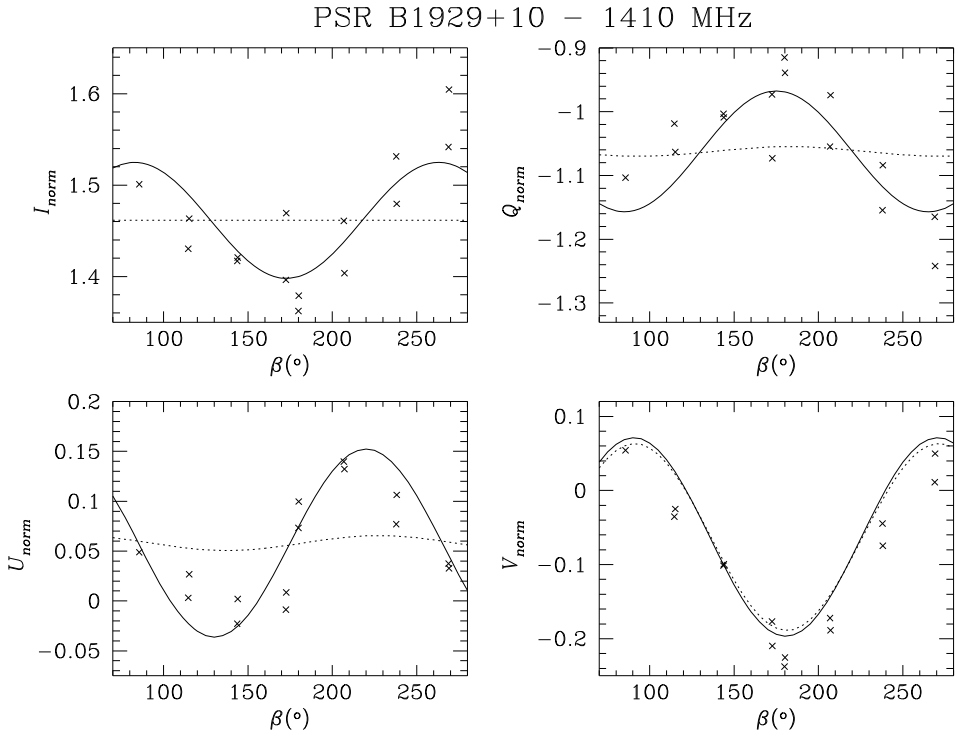

Fig. 2.2.— Stokes vs. β for PSR B1929+10 at 1410 MHz. Gain-calibrated Stokes parameters were produced for the PSR B1929+10 data which were taken with the EBPP on 1997 March 24. The average values for a region centered on the pulse (for which the model Stokes intensity exceeded $I/I_{max} = 0.1$) were determined. These were normalized by $I_{const} = [I^2 - (Q^2 + U^2 + V^2)]^{1/2}$. The results are plotted for a single channel against the feed + parallactic angle β. The dotted and solid lines result from applying an instrumental correction to the average model Stokes. The instrumental parameters determined in a fit for δ and ψ_δ, shown in the top panels of Figure 2.3, were used to produce the dotted lines. The solid lines result from using the results of a fit which also included σ and ψ_σ, which are shown in the bottom panels of Figure 2.3.

included σ and ψ_σ to the model Stokes. The parameters of this fit are displayed in the bottom 5 panels of Figure 2.3. Figure 2.4 displays the same averaged Stokes parameters for data which has been corrected for instrumental effects using the inverse Mueller matrix for the displayed parameters.

In all these figures, the sign of V has been changed in our data to match the published polarization profiles. Although such a sign change in this case could be due to an error in gain calibration, the original sign of the sense-reversing V in our observations of PSR B0355+54 also disagreed with the published literature (Gould & Lyne 1997[2], von Hoensbroech & Xilouris 1997b[3]). Gain calibration errors could not

[3]The sign of V in the 1.7 GHz profile is unclear, but the sense of V in profiles at other frequencies matches that of the other authors at lower frequencies.

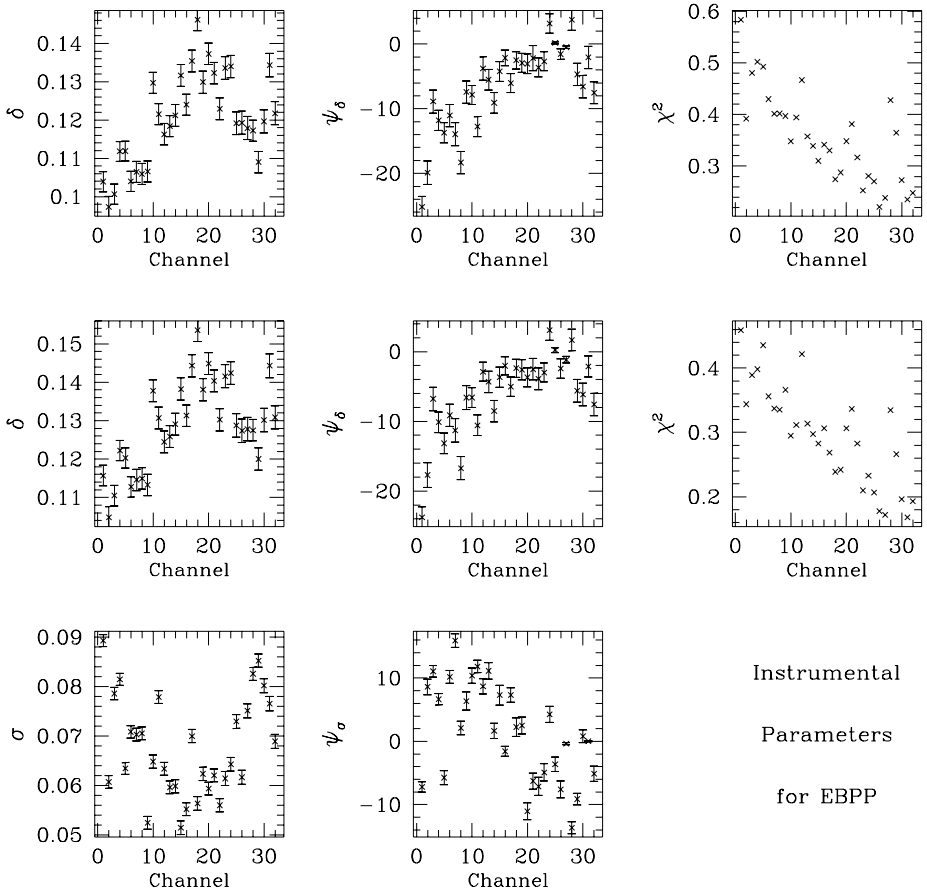

Fig. 2.3.— Instrumental Polarization Parameters for Effelsberg. The top three panels display the values for each channel of the instrumental parameters determined in a fit, along with the χ^2 of the fit. The data used in the fit were the same as that which were used to generate the average quantities displayed in Figure 2.2. The telescope response was assumed to be orthogonal, so only δ and ψ_δ were included in the fit. The bottom five panels display the results for a fit which also included the orthogonality parameters σ and ψ_σ.

have this effect. If the polarizations L and R had been mis-identified at the telescope, then the direction of the PPA curve would also be reversed relative to the published results, which is not the case. This correction has been applied to all 1410-MHz EBPP data. As further confirmation that this is the appropriate action, we note that the signs of V for most of the millisecond pulsars are consistent across all observed frequencies after this correction has been made. The source of this sign reversal of V remains unexplained. No similar sign correction is required for the 820-MHz or 575-MHz data. A similar sign reversal may affect the millisecond pulsar polarization data published in Xilouris *et al.* (1988).

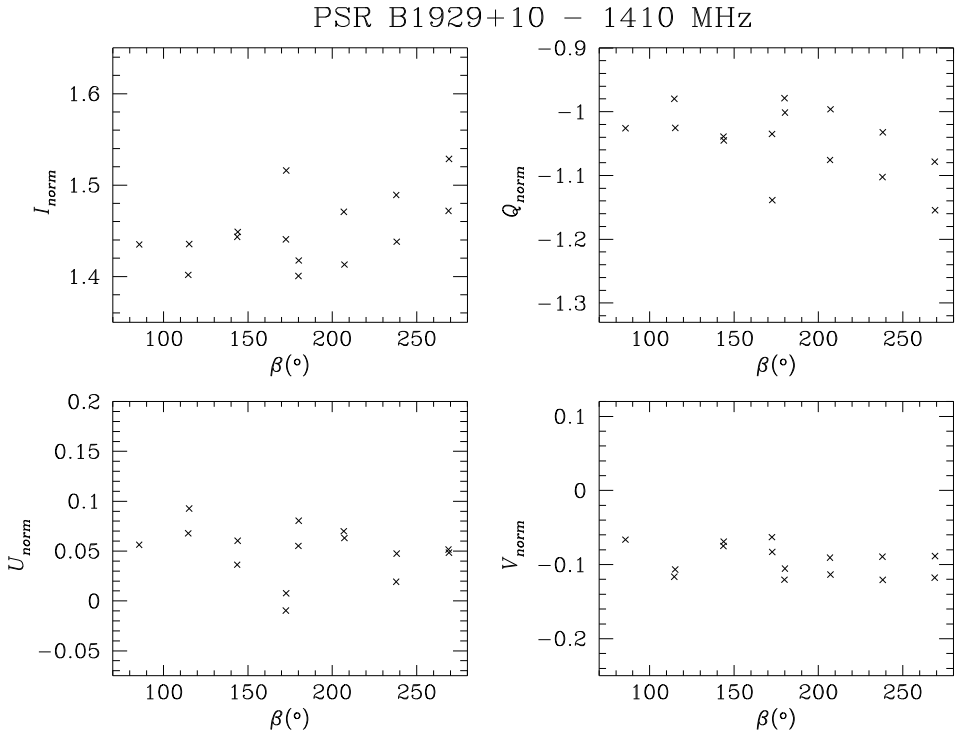

Fig. 2.4.— Corrected Stokes vs. β for PSR B1929+10. The inverse Mueller matrix resulting from the full fit for instrumental parameters shown in Figure 2.3 was applied to the gain calibrated Stokes parameters for the same data as that used to generate Figure 2.2. The average values for the central region were determined, normalized by I_{const}, and plotted against β, as before. The sinusoidal variations have been largely removed.

2.5.3.2 575-MHz GBPP data

It is apparent from equation 2.14 that for $\sigma << 1$,

$$\frac{V'}{P'} = \frac{V}{P} + \delta \cos(2(\chi - \beta) - \psi_\delta). \tag{2.17}$$

The measured value of V'/P' will vary sinusoidally with the angle β, with an offset of the true value of V/P.

The first panel of Figure 2.5 displays V'/P' for the 575-MHz PSR B1929+10 Stokes data for a single day, plotted against β. The data were averaged over the center of the gain-calibrated pulse profile, and over sets of 8 channels. In the GBPP, a separate LO is used for each block of 8 channels, so instrumental parameters are expected to be most similar within a block. Each set of 8 channels is represented by a different symbol. The second panel of Figure 2.5 displays the same quantities for a different day of data. The solid lines result from applying the instrumental parameters $\delta = 0.05$, $\psi_\delta = -60°$ to an estimate of the average model Stokes values derived from the offsets

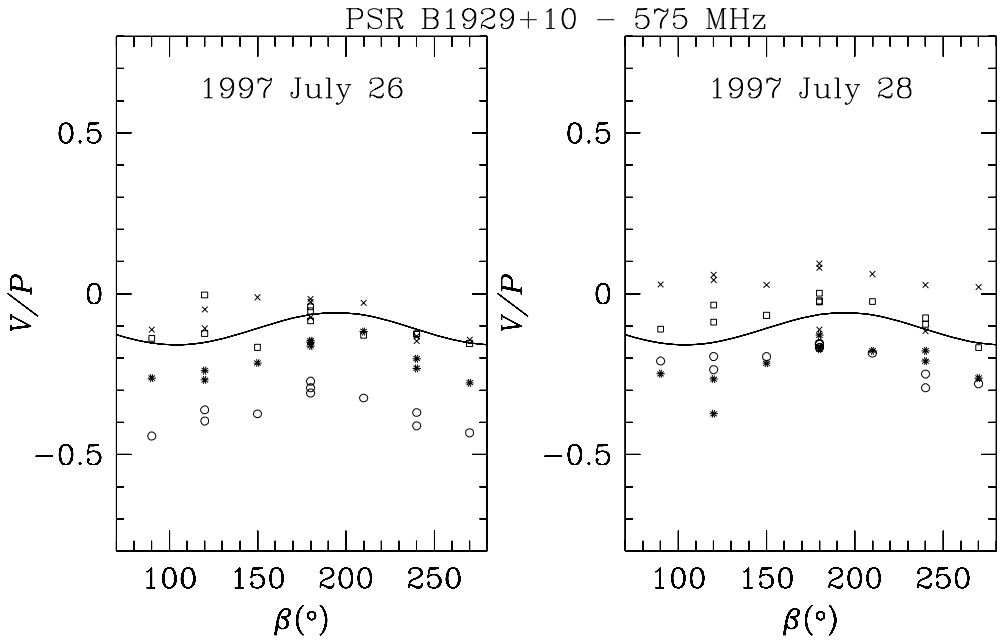

Fig. 2.5.— V/P vs. Feed Angle β for PSR B1929+10 at 575 MHz. The 575-MHz Stokes parameters of PSR B1929+10, averaged in 4 sets of 8 channels, were averaged over the central region of the pulse. The quantity V/P is plotted against feed angle β for each set of channels for 2 separate days (1997 July 26/28). Each set of channels is marked with a different symbol. Note the difference in the results of gain calibration for each set of channels. The solid lines result from applying the instrumental parameters $\delta = 0.05$, $\psi_\delta = -60°$ to the model Stokes.

of the sinusoids in the data for 1997 July 28. Note that there are significant difficulties with the gain calibration of this data, with systematic effects between the channel groups of order $\pm 10\%$. Despite difficulties with the vertical offset, the amplitude and phase of the instrumental effects can be estimated. A correction for these values of δ and ψ_δ has been applied to all 575-MHz data. The corresponding plots produced from the corrected data reveal that the sinusoidal variations are correctly removed. Plots of all four normalized Stokes parameters reveal that $\sigma \lesssim 5\%$. No correction for $\sigma \neq 0$ has been made.

2.5.3.3 820-MHz GBPP data

Most of the 820-MHz GBPP data were obtained during standard pulsar timing runs, with the GBPP obtaining polarimetry using the same schedule as the Spectral Processor. As a result, extensive rotations of the feed were not possible.

Observations of PSR B1929+10 at a single feed angle (1997 February) imply that the instrumental effects could be of order 10-20%, but the fits are poorly constrained in this instance. As a result, no correction for instrumental polarization was applied

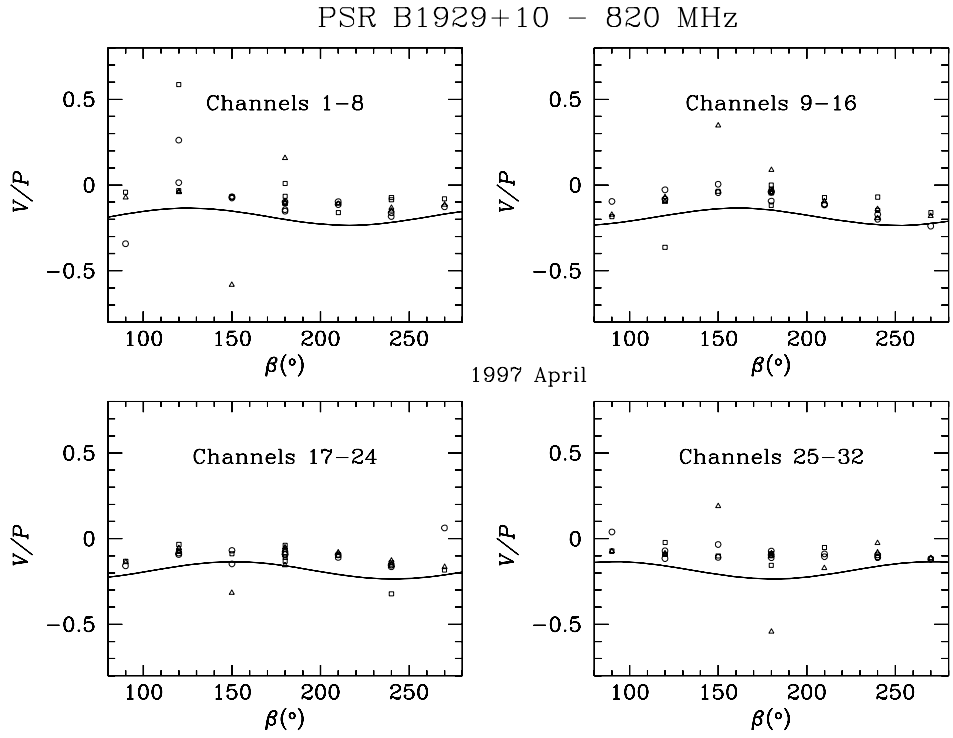

Fig. 2.6.— V/P vs. β at 820 MHz for 1997 April. The 820-MHz Stokes parameters of PSR B1929+10, averaged in 4 sets of 8 channels, were averaged over the central region of the pulse. The quantity V/P is plotted against feed angle β for each set of channels for three separate days (1997 April 28-30). Each symbol represents a different observing date. The solid lines result from applying the instrumental parameters $\delta = 0.05$, $\psi_\delta = 40, -30, -10, 110°$ to the model Stokes. The different values of ψ_δ are required to account for the different sinusoidal phase for each set of 8 channels.

to this data.

During the several days of observing in 1997 April, observations of PSR B1929+21 with feed angle rotation were taken on three days. The four panels of Figure 2.6 display V'/P' for the 820-MHz PSR B1929+10 Stokes data, plotted against feed angle β. The data have been averaged over the center of the gain-calibrated pulse profile, and over the four sets of 8 channels, and plotted against β. Each symbol represents a different day of observations. The solid lines result from applying the instrumental parameters $\delta = 0.05$, $\psi_\delta = 40, -30, -10$ and $110°$ to the average model Stokes, which at this radio frequency were obtained from Stinebring (1982). Plots of all four Stokes parameters limit sigma to $\approx 5\%$. The 1997 April GBPP data were corrected for these instrumental parameters, setting $\sigma = 0$. The corresponding plots of V/P for the corrected data show much less variation with feed angle β.

In 1997 July, a single set of observations of PSR B1929+10 with feed rotation is

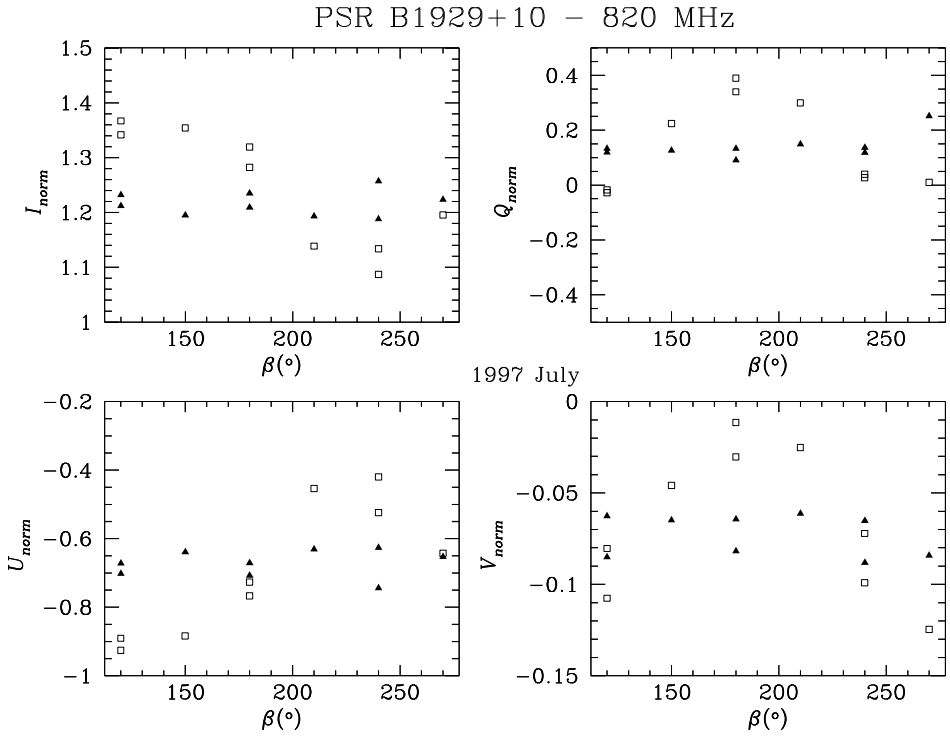

Fig. 2.7.— Stokes vs. β for PSR B1929+10 at 820 MHz for 1997 July. The normalized Stokes parameters, averaged over the center of the pulse, and over all channels, are displayed against feed angle β for the PSR B1929+10 data which were taken with the GBPP on 1997 July 31. No polarization calibration has been applied to the data represented by the open squares. The correction matrix $\mathbf{M^{-1}}$ for the instrumental parameters $\delta = 0.07$, $\psi_\delta = -70°, -80°, -90°, -100°$, $\sigma = 0.2$, $\psi_\sigma = -6°$ has been applied to the data from which the values for the filled triangles were determined. The sinusoidal variation has been largely eliminated.

available. The normalized Stokes parameters, averaged over the central region and all channels, are displayed against β in Figure 2.7. The open squares represent data to which no instrumental corrections have been applied. The sinusoidal amplitude in all Stokes parameters is quite large, indicating $\sigma \sim 0.2$. If σ had been this large in the 1997 April data, it would have been clearly visible. The filled triangles represent data to which an instrumental correction has been applied, using the parameters $\delta = 0.07$, $\psi_\delta = -70, -80, -90, -100°$, $\sigma = 0.2$, and $\psi_\sigma = -6°$. Inspection of blocks of eight channels revealed that similar parameters were appropriate for all. These same parameters were applied to all 1997 July 820-MHz data.

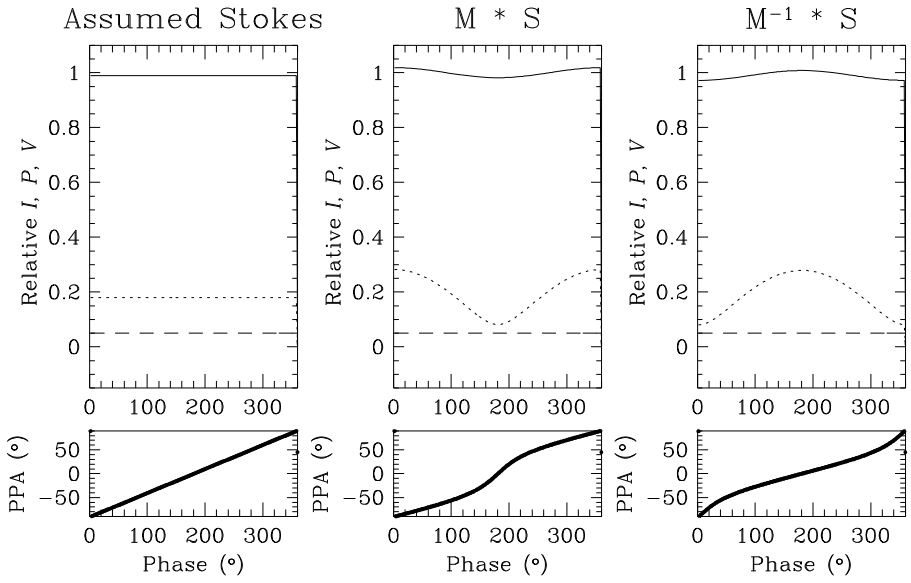

Fig. 2.8.— Effect of $\sigma \neq 0$ on PPA. For Stokes parameters with low linear polarization P, such are displayed in the first panel, even modest values of the instrumental parameter σ have a significant effect on the PPA. In the second and third panels, the forward and inverse Mueller transformations for $\delta = 0$, $\sigma = 0.1$, and $\phi_\sigma = 0$ have been applied to these Stokes. The transformation of the PPA curve is significantly non-linear.

2.5.4 The effects of $\sigma \neq 0$ on PPA

The effects of even modest values of σ on the PPA curve are small, if the linearly polarized fraction is high ($P \sim I$). If the linearly polarized fraction is small, then even $\sigma \sim 0.1$ has a significant effect on the PPA curve. The first panel of Figure 2.8 displays Stokes parameters in which the PPA curve is assumed to vary linearly across the pulse. The linearly polarized fraction is assumed to be $P/I = 0.2$, with $V = 0$. The results of applying a Mueller matrix with $\sigma = 0.1$, $\psi_\sigma = 0$ ($\delta = 0$ has been assumed for clarity) are displayed in the second panel. The expected sinusoidal variations of I and P are visible, and the instrumental effect results in a non-linear transformation of the PPA, with the location of the steepest portion of the new PPA curve depending on ψ_σ. The third panel displays the results of applying the inverse Mueller transformation to the original Stokes. This mimics the effect of an erroneous correction for $\sigma \neq 0$. Again, the PPA curve is distorted in a non-linear fashion. In light of these effects, one must be careful in interpreting the shape of the PPA curve in objects with very low linear polarization P.

2.5.5 Application to Linear Polarization data

2.5.5.1 Application to 140′ 800-MHz Data

Since the circular polarizations at 800 MHz on the 140′ telescope are produced by sampling of linear polarizations with subsequent mixing in a hybrid, the cross terms K_{LR} and K_{RL} are likely to be more important than the cross terms K_{xy} and K_{yx} for the linear polarizations. Thus linear polarizations were used for the first experiment. This has the disadvantage that the relative phase angle θ_{yy} causes a rotation between U and V, instead of the rotation between Q and U which is the principal effect of θ_{RR}, and is simply a rotation of position angle.

Gain calibration of all data discussed below was done using observations of the source 3C 48. The telescope polarization parameters were determined in two ways. First, by measuring at many feed angles the Stokes parameters of the standard source 3C 286, and second, by measuring the Stokes parameters of the well-studied pulsar B1929+10.

We determined the measured Stokes at several positions of the feed for 3C 286, which has a linear polarization of 9%. This was done through on and off source pulsed CAL measurements. Following McKinnon (1994), when $K_{yy} \sim 1.0$ and $S_1/S_0 << 1.0$, the quantity $f = S_1'/S_0' = Q/I$ reduces to

$$f(\beta) \sim b + m cos[2(\beta - \chi)], \tag{2.18}$$

where the percent linear polarization is given by the amplitude m of the sinusoid, and the intrinsic position angle is given by the phase χ. The offset $b \sim (1-K_{yy}^2)/(1+K_{yy}^2)$ should be zero for correctly gain calibrated data, since then $K_{yy} = 1.0$. Our data correctly displays the results of the 9% linear polarization of this object.

Using the fitted values for the intrinsic polarization of 3C 286, which has virtually no circular polarization, the intrinsic Stokes parameters are given by

$$\mathbf{S} = I \begin{pmatrix} 1 \\ m\cos(2\chi) \\ m\sin(2\chi) \\ 0 \end{pmatrix}. \tag{2.19}$$

These can be used to fit for the parameters defining the elements of the Mueller matrix, using the same methods discussed earlier. The values of K_{xy} and K_{yx} determined in this fit represent cross-coupling of at most a few percent.

We also observed the pulsar B1929+10 at a few feed angles, and fit for the PPA offset and the instrumental parameter θ_{yy} using data at a single feed angle. The

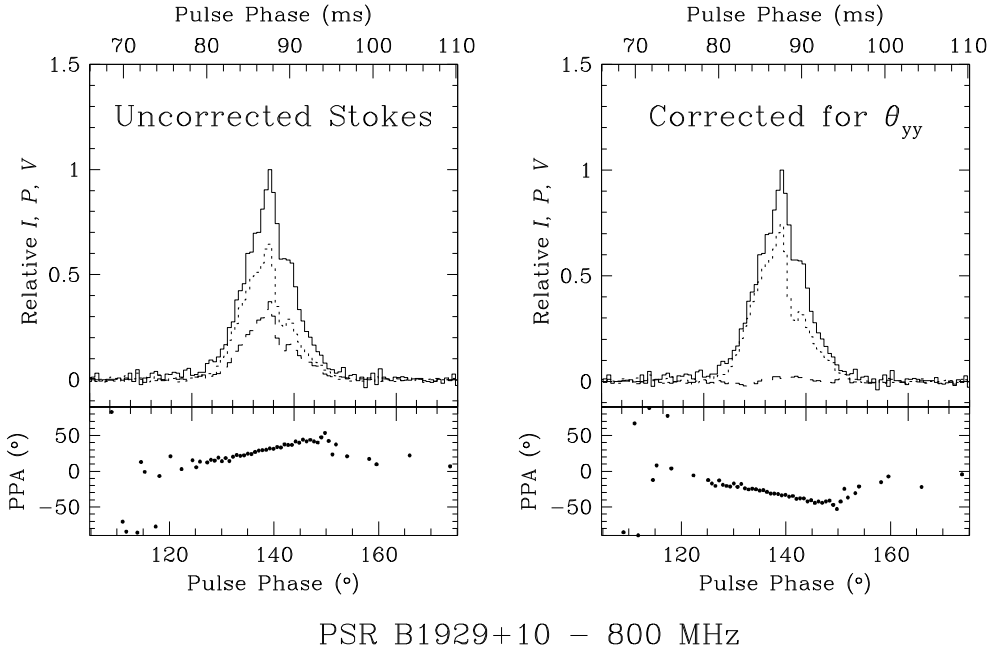

Fig. 2.9.— The effects of θ_{yy} on PSR B1929+10. The first panel displays gain-calibrated polarization data for a single channel to which no instrumental correction has been applied. The second panel displays the data after a correction for $\theta_{yy} \sim 145°$ has been applied.

results were largely consistent for data taken with each feed angle. The θ_{yy} values determined in these fits also agreed with the results for 3C 286, to within the errors.

The first panel of Figure 2.9 displays the gain-calibrated polarization data for PSR B1929+10. No instrumental correction has been applied. The second panel displays the results correcting for θ_{yy} as determined in a fit to another PSR B1929+10 data scan. This now compares favourably with the model Stokes obtained from Stinebring (1982).

An instrumental correction was applied to all of the data, using the results of the fits for θ_{yy} from PSR B1929+10, as this was available for both the 1997 January and 1997 February observations, whereas the 3C 286 calibration was available for only one of these.

2.5.5.2 Application to 85-3 data

The instrumental phase θ_{yy} introduced between the X and Y polarizations is also the dominant instrumental effect for the 610-MHz data presented here.

As in the case of circular polarizations, one measure of this angle θ^c_{yy} is given by the correlated pulsed CAL signal which can be injected into the signal path. The amount of pulsed signal which appears in the polarization cross terms is governed by

Polarization Calibration Summary

Dates	Freq MHz	δ	ψ_δ °	σ	ψ_σ °
1997 7/25-30	575	0.05	-60	0.	–
1995 2/3-5[a]	800	0.	–	0.	–
1997 2/10-12[a]	820	0.	–	0.	–
1997 4/26-30	820	0.05	$40, -30, 10, 110$	0.	–
1997 7/30-8/1	820	0.07	$-70, -80, -90, -100$	0.2	-6
1996 10/5,15[b]	1410	0.	–	0.	–
1997 3/19-20, 3/23-4	1410	~ 0.12	various	~ 0.07	various
1997 4/9-10	1410	~ 0.12	various	~ 0.07	various

Dates	Freq MHz	θ_{yy} °
1995 1/29-31	800	135 to 145
1995 2/5-7	800	-90 to -60

[a] none available - standard timing run

[b] none available

Table 2.3: Polarization Calibration Summary. For each observing session, the observing frequency is listed, followed by the polarization parameters used to correct the data for instrumental effects. See text for details.

the value of this phase angle for the signal path *following* the CAL. This is sufficient in the case of circular polarizations, where only the relative value between channels is important. In this case, however, we need to know the true value. To measure this phase angle for the entire signal path, observations of the Vela pulsar were used to fit for both θ^d_{yy} and the rotation in position angle due to the atmosphere, as was done for PSR B1929+21 in the previous section. The phase angle due to the signal path *before* the CAL signal is injected was found to be relatively constant, over a large range of dates. This

$$\Delta\theta_{yy} = \theta^d_{yy} - \theta^c_{yy}$$

was then added to the value of θ^c_{yy} determined for observations of the Crab pulsar.

Table 2.3 contains a summary of instrumental parameters used to apply corrections to the GBPP and EBPP data. For each date and frequency, the values of δ, ψ_δ, σ, and ψ_σ are tabulated for the observations taken using the circular basis, while θ_{yy} is tabulated for the linear polarization basis.

2.6 Data Reduction

The calibration procedures described in sections 2.4 and 2.5 may be applied to each channel of the BPP, for each scan. In principle the resulting polarization profiles may be averaged to improve signal to noise once any parallactic angle differences have been removed. In practice this is complicated by the rotation measure RM as defined in equation 1.18, as well as any remaining systematic PPA variations due to instrumental effects. Addition of two polarization profiles with improperly aligned position angles results in depolarization of the summed profile. Specifically, if two profiles with linear polarization P_0 are combined, then the linear polarization of the average P is

$$\frac{P}{P_0} = \frac{1 + \cos(\Delta\chi)}{2} \tag{2.20}$$

where $\Delta\chi$ is the rotation in position angle between the two profiles. For smooth variations of PPA resulting in a total change $\Delta\chi$ across our observing bandwidth, the effect will be smaller than that indicated by equation 2.20.

The rotation measure of the ionosphere is typically $1 - 10$ rad m^{-1}. The variation is dominated by a diurnal effect, but solar flux and magnetic field variations also play a role. For a rotation measure of 10, and a bandwidth of 30 MHz, the change in polarization position angle across the band is then $\Delta\psi = 1°$ at 1410 MHz, 6° at 820 MHz, and 16° at 575 MHz. If the rotation measure changes by $\Delta RM = 9$, then the change in position angle at the center of our band is 23° at 1410 MHz, 69° at 820 MHz, and 140° at 575 MHz. This affects not only the summing over the frequency channels, but also the averaging of data taken at different times.

In addition to the RM of the ionosphere, the pulsar has a rotation measure due to propagation through the interstellar medium. Although the magnetic field is weak, the long propagation path results in measurable effects. For these objects, the true interstellar rotation measure is unknown, and so we must determine if a large RM is present.

In order to assess these effects, average polarization profiles (1-3 per pulsar observation) were originally produced with $RM = 0$ and the effects of θ_{RR} removed. These were added together to create profiles with a reasonable S/N. The PPA offset between these profiles was determined, by fitting using one of the profiles as a template. These angle offsets were then removed from polarization profiles for all frequency channels, which were added, and a PPA offset was determined for each channel. Finally, a least-squares fit was performed to determine the RM, assuming that the instrumental phases have been correctly removed. The observing bandwidth is relatively narrow, so this will not be a good determination unless the intrinsic

RM of the object is large, especially at high frequencies. In almost all cases, the systematic variation in PPA across the band was less than 15°, and for these cases, the depolarization is at most a few percent. In fact, if $RM \neq 0$ introduces a total change across our 28-MHz band of $\Delta\chi = 30°$, the resulting depolarization is only 5%, not the 25% suggested by equation 2.20. This corresponds to an RM of 300 at 1410 MHz, 60 at 820 MHz, and 20 at 575 MHz. Frequently, random variations and systematic trends which did not follow λ^2 were comparable or larger than any linear trend. For PSR B1821−24, the RM at 820 MHz was found to be somewhere between 60 and 100. This causes only slight depolarization at this frequency, due to the narrow bandwidth, but has a significant effect at 575 MHz, where we had been previously unable to measure the RM. A rotation measure of 80 was applied to the 575-MHz data. This resulted in less depolarization of the profile, and any remaining trend of PPA across the band was less than 10°.

The angle offsets determined above were applied to each scan prior to temporal alignment and adding of the profiles. In some cases, the PPA offset between data sets was insufficiently determined, due to low S/N or small linear polarization, and no offset was applied before averaging.

In order to properly align the data temporally, TOAs (pulse arrival times) were generated for each scan by cross-correlation with a template. At each frequency, these were then compared with the pulsar timing model used to take the observations, using the TEMPO timing package developed at Princeton (Taylor & Weisberg 1989). If the timing residuals were small, then the data were averaged with no further alignment. If significant timing residuals remained, then TEMPO was used to fit for a new timing model for those observations. This new model was then used to align and average the polarization data. In some cases, insufficient information was available to obtain a new timing model. In these cases, sub-averages of several scans were created where no drift in pulse phase was expected. These were then aligned and averaged by cross-correlation. In some cases, a small portion of the data was very much stronger, due to interstellar scintillation. In these cases, only the data with the highest S/N were included. In a few cases, the resolution of the data was not the same for all observations. These data were interpolated to the same number of bins prior to their addition.

Gaussian Component Decomposition of Pulse Profiles

Source	Freq	Comp 1		Comp 2/5			Comp 3/6			Comp 4/7		
		Amp	σ	Pos	Amp	σ	Pos	Amp	σ	Pos	Amp	σ
	MHz	%	°	°	%	°	°	%	°	°	%	°
J0613−0200	575	100	13	-34	40	54	-87	19	20			
	820	100	13	-34	77	56	-87	33	20			
	1410	72	11	-35	100	38	-76	48	16			
J1012+5309	575	60	11	-23	100	46	-44	-21	7	169	48	27
				109	26	4	122	17	7	-163	13	10
	820	49	11	-18	100	45	-38	14	8	167	36	26
				108	27	4	120	32	14			
	1410	86	12	-19	100	40	-40	13	8	166	24	21
				110	41	4	118	39	7	113	18	31
J1022+1001	575	100	5	-12	46	12	-18	36	32	-4	18	4
	820	100	5	-11	59	13	-22	31	26	-3	27	6
	1410	100	5	-12	59	9	-19	41	24	-5	29	4
B1620−26	575	100	14	-19	33	21	20	25	14			
	820	100	14	-22	29	24	25	26	20			
	1410	100	10	-21	22	27	22	21	16			
J1713+0747	575	96	8	-5	71	14	-22	21	11	45	18	7
				8	100	10	19	63	20			
	820	100	8	-6	55	18	-27	16	9			
				9	76	14	22	18	15	33	10	8
	1410	100	8	-12	14	11	-28	7	9	45	3	8
				8	36	10	20	7	15			
J1730−2304	575	30	10	20	100	19	35	32	10	-6	23	29
	820	31	11	16	100	15	32	60	11	-9	34	22
	1410	94	10	15	100	14	31	76	10	-9	50	9
B1821−24	575	100	17	108	33	20	177	28	44			
	820	100	13	106	67	10	177	17	61			
	1410	60	9	107	100	6	-176	12	18	107	16	45
B1937+21	575	100	13	-174	55	13	10	5	8	-163	10	8
	820	100	9	-172	56	11	7	39	4	-161	5	3
	1410	100	9	-172	45	11	9	38	4	-159	6	3
J2145−0750	575	100	10	69	67	24	79	19	4	-60	14	10
				7	15	20	32	14	51			
	820	100	10	70	45	24	78	21	4	-59	8	12
				10	11	21	33	15	47			
	1410	100	9	72	28	26	80	17	4			
				11	14	21	34	16	35			

Table 3.1: Gaussian Component Decomposition of Intensity Profiles. A multicomponent Gaussian was fit to the total intensity profile of each source at each frequency. A single component was arbitrarily chosen as the reference (usually the strongest component at some frequency). Column 3 gives the amplitude of this reference component relative to the component with maximum height (%). Column 4 gives the FWHM of the reference component in degrees. The first column of each remaining component gives the phase location in degrees relative to the reference component. The remaining two columns are again amplitudes relative to the maximum component, and FWHM in degrees. For objects which required more than four components, components 5-7 are displayed on a second line. In two cases, one of the components was not required at one of the frequencies, and it has been left blank so as to keep the remainder of the components aligned across frequency.

Chapter 3

Polarization Observations of Millisecond Pulsars

3.1 Data Presentation

The data discussed in the previous chapter are presented for each pulsar and radio frequency in Figures 3.1-3.34. For each object for which multi-frequency data are available, three figures are presented. For these objects, the total intensity profiles were decomposed into Gaussian components, using fitting software developed elsewhere (Kramer 1994, Kramer *et al.* 1994). The resulting Gaussian components are displayed at a single frequency in the first figure for each pulsar. The results of these fits at all frequencies are presented in Table 3.1. For each pulsar and radio frequency, the relative positions, relative amplitudes, and widths of the Gaussian components are given.

The polarization profiles across the full pulse period for all three observing frequencies are shown in the second figure for each object. This allows examination of the profile and polarization evolution with frequency, and object-to-object comparison of the duty cycles. In each case, the intensity, normalized to a peak value of 1, is plotted as a solid line against pulse phase in degrees. The fractional linear polarization is plotted as a dotted line, while the fractional circular polarization is shown by a dashed line. The polarization position angle (PPA) is displayed in the bottom panel of each plot for values of the linear polarization which exceed the rms away from the pulse by a set threshold T. The pulse phase in milliseconds is shown along the top of each plot. The phase and PPA alignment between frequencies is arbitrary. Finally, the polarization properties for a region surrounding the pulsed emission is shown for each pulsar at a single frequency, to clarify the detailed features.

Table 3.2 summarizes the data reduction of the polarization profiles presented in Figures 3.1-3.34. For each source and radio frequency, column 2 indicates the

Polarization Profile Summary

Source	Freq MHz	Epoch yymon	Integration Time (s)	Resolution (μs)	PPA Thresh	Alignment Technique
B0531+21	610	96nov/dec	125100	34.1	1	sa-cc[a]
J0613−0200	575	97jul	16560	17.1	2	sa-cc
	820	97feb/apr/jul	51230	18.4	2	sa-cc
	1410	97apr	1500	18.4	2	add
J0751+1807	1410	97mar	2609	18.2	2	align
J1012+5309	575	97jul	7920	18.3	1	ephem
	820	97feb/apr/jul	47221	20.5	1	ae-cc[b]
	1410	97mar/97apr	6200	10.3	1	sa-cc
J1022+1001	575	97jul	7560	18.3	1	ephem
	820	97feb/apr/jul	56895	27.4	1	ae-cc
	1410	97mar/97apr	5864	18.3	1	sa-cc
J1518+4904	1410	97mar	1818	123.	2	sa-cc
B1620−26	575	97jul	27900	47.9	1	ephem
	820	97feb/apr/jul	56164	34.3	1	sa-cc
	1410	97mar/97apr	6352	34.3	1	sa-cc
J1640+2224	1410	97mar/97apr	1265	18.3	2	add
J1643+1224	1410	97mar/97apr	5104	18.3	2	ephem
J1713+0747	575	97jul	39060	13.7	1	ephem
	800	95feb	6000	22.9	1	sa-cc
	820	97feb/apr/jul	71168	11.4	1	ae-cc
	1410	97mar/97apr	5487	2.3	3	ephem
J1730−2304	575	97jul	12960	27.4	2	add
	820	97feb/apr/jul	20398	27.4	2	ae-cc
	1410	97apr	1500	27.4	2	add
B1821−24	575	97jul	25380	17.1	1	add
	820	97feb/apr/jul	58501	12.0	1	sa-cc
	820	97feb	13800	24.0	1	add
	820	97apr	31201	24.0	1	add
	820	97jul	13501	24.0	1	add
	1410	97mar/97apr	3022	9.1	1	add
B1937+21	575	97jul	17161	2.0	1	add
	820	97feb/apr/jul	31740	1.1	3	ae-cc
	1410	97mar/97apr	3900	1.1	2	sa-cc
J2145−0750	575	97jul	38879	54.9	3	ephem
	800	95feb	2400	78.6	1	add
	820	97apr	3000	32.0	3	add
	1410	97apr	840	64.0	3	add

[a] Sub-average over short times, then align via cross-correlation

[b] Add within an epoch, and align via cross-correlation between them

Table 3.2: Polarization Profile Summary. For each polarization profile displayed in Chapter 3, the observing frequency and epoch are listed in columns two and three. Column 4 displays the accumulated integration time of the displayed profile, with the resolution of the plot in μs in column 5. The technique used to align the data is in column 6.

epoch(s) at which the displayed observations were taken. The total integration time of the profile is given by column 3, and the plot resolution and PPA threshold T are in columns 4 and 5. Column 6 indicates the alignment technique used to produce the polarization profile.

Polarization of Millisecond Pulsars

Source	Frequency	$\frac{P}{I}$	$\frac{V}{I}$
	MHz	%	%
J0613-0200	575	4.7±2.3	-4.6±3.2
	820	9.1±2.02	-2.2±2.1
	1410	6.8±3.7	4.6±5.6
J1012+5307	575	36.7±2.4	1.5±2.0
	820	41.6±4.0	5.6±3.5
	1410	37.1±1.1	-3.6±1.7
J1022+1001	575	56.9±0.4	-13.3±0.4
	820	41.0±1.2	-12.2±1.4
	1410	44.3±0.4	-14.2±0.5
B1620-26	575	16.2±2.3	-13.5±3.7
	820	24.3±1.2	-9.5±1.5
	1410	28.2±1.2	-15.2±1.9
J1713+0747	575	21.1±0.9	-5.7±1.1
	820	14.5±1.1	-2.3±1.5
	1410	18.1±0.3	-0.68±0.5
J1730-2304	575	4.7±1.5	-3.8±2.0
	820	9.3±1.5	-23.1±2.6
	1410	19.1±1.3	-25.4±2.0
B1821-24	575	40.4±4.5	-5.1±5.1
	820	36.9±4.0	10.0±4.6
	1410	36.2±8.5	-6.9±8.5
B1937+21 MP	575	57.9±0.3	-2.1±0.4
	820	47.5±0.2	3.1±0.2
	1410	30.0±0.2	0.5±0.3
B1937+21 IP	575	10.1±0.4	-1.7±0.7
	820	8.8±0.3	3.8±0.4
	1410	13.1±0.5	1.6±0.7
J2145-0750	575	9.8±0.7	3.2±1.1
	820	8.8±0.6	7.8±0.8
	1410	-1.0±1.2	-0.53±2.2

Table 3.3: Polarization of Millisecond Pulsars. For each pulsar and observing frequency (columns 1 and 2), the fractions of the radiation in linear and circular polarizations, averaged across the pulse, are displayed in columns 3 and 4. The quoted errors are based on the *rms* of the profile, and do not include systematic calibration errors.

The total fraction of polarization across the pulse profile was calculated for the multi-frequency data. Table 3.3 contains the total linear and circular polarizations in columns 3 and 4.

3.2 PSR J0613−0200

This 3.06-millisecond pulsar has three distinct components in its profile. As seen in Figure 3.1, the sharp trailing component (1) dominates at 575 MHz, but has a steeper spectrum than the other two, whose amplitude ratio remains approximately constant at all three frequencies. The two broader components precede the sharp component by $\sim 35°$and $80°$. Profiles presented in Bell *et al.* (1997) indicate that the trailing component continues to weaken at higher frequencies. For a classical triple profile with core and cone components, we would expect both conal outriders to strengthen relative to the central core at high frequencies. The widths of all three components are similar at the two lower frequencies, and sharper at 1410 MHz. The leading component is also closer to the others by $10°$ at this frequency. In the 820-MHz and 575-MHz profiles there is evidence for a small amount of emission following the strong sharp component. This also appears in shorter averages.

The 1410-MHz profile in Figure 3.2 shows no detectable polarization, although Xilouris *et al.* (1998) detected $\sim 25\%$ linear polarization. At both 820 and 575 MHz the strong trailing component is partially linearly polarized with $P \sim 25\%$. This same component displays a small amount of right-handed circular polarization at these frequencies, with $V \sim -10\%$. The PPA curve is only defined under this component, and appears similar for the two frequencies.

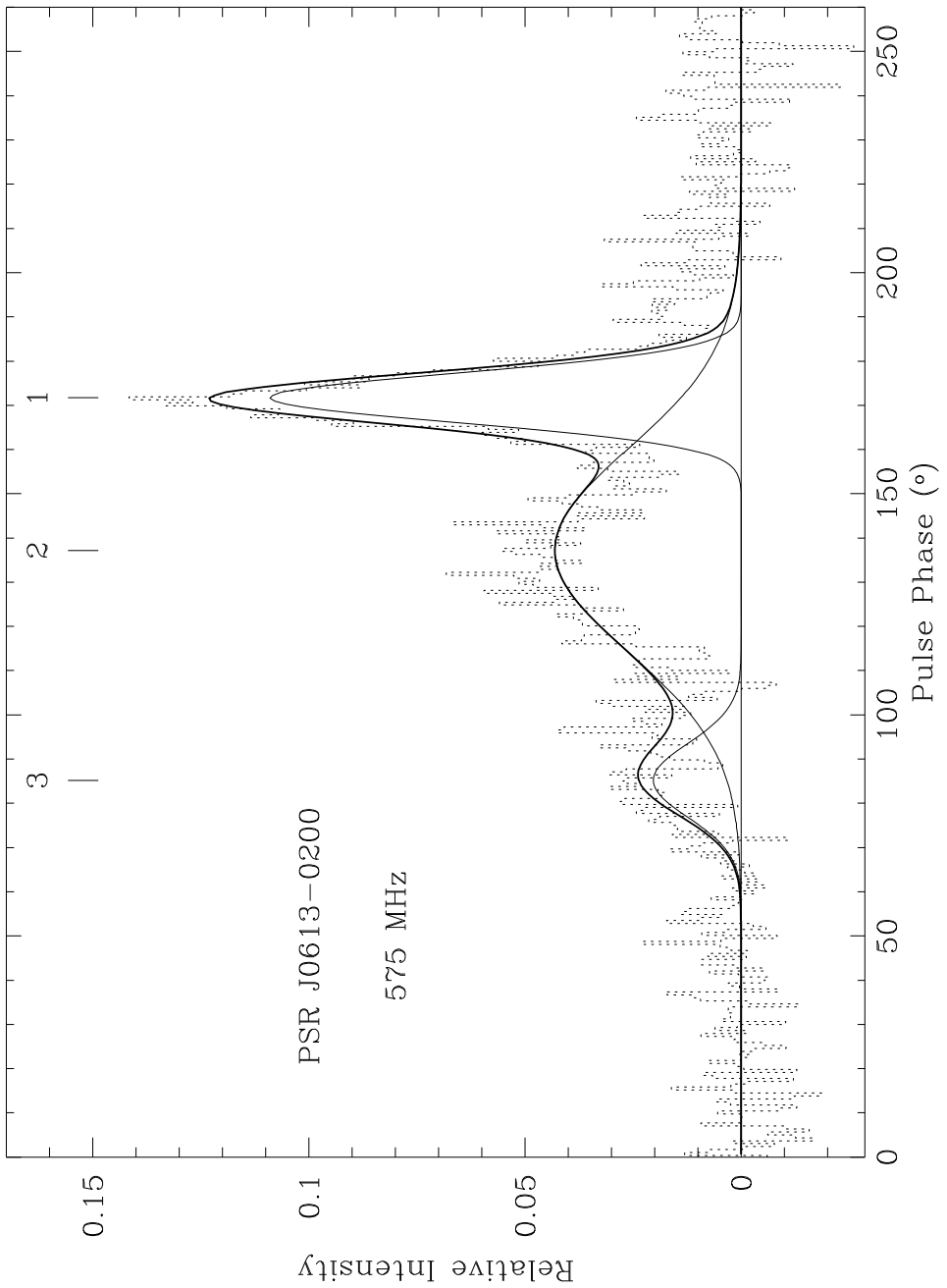

Fig. 3.1.— The Gaussian component decomposition for PSR J0613−0200 at 575 MHz is shown. The dotted histogram represents the data. The light solid lines are individual Gaussian components, whose sum is given by the dark solid line. Each component is identified with a number associated with the component number in Table 3.1.

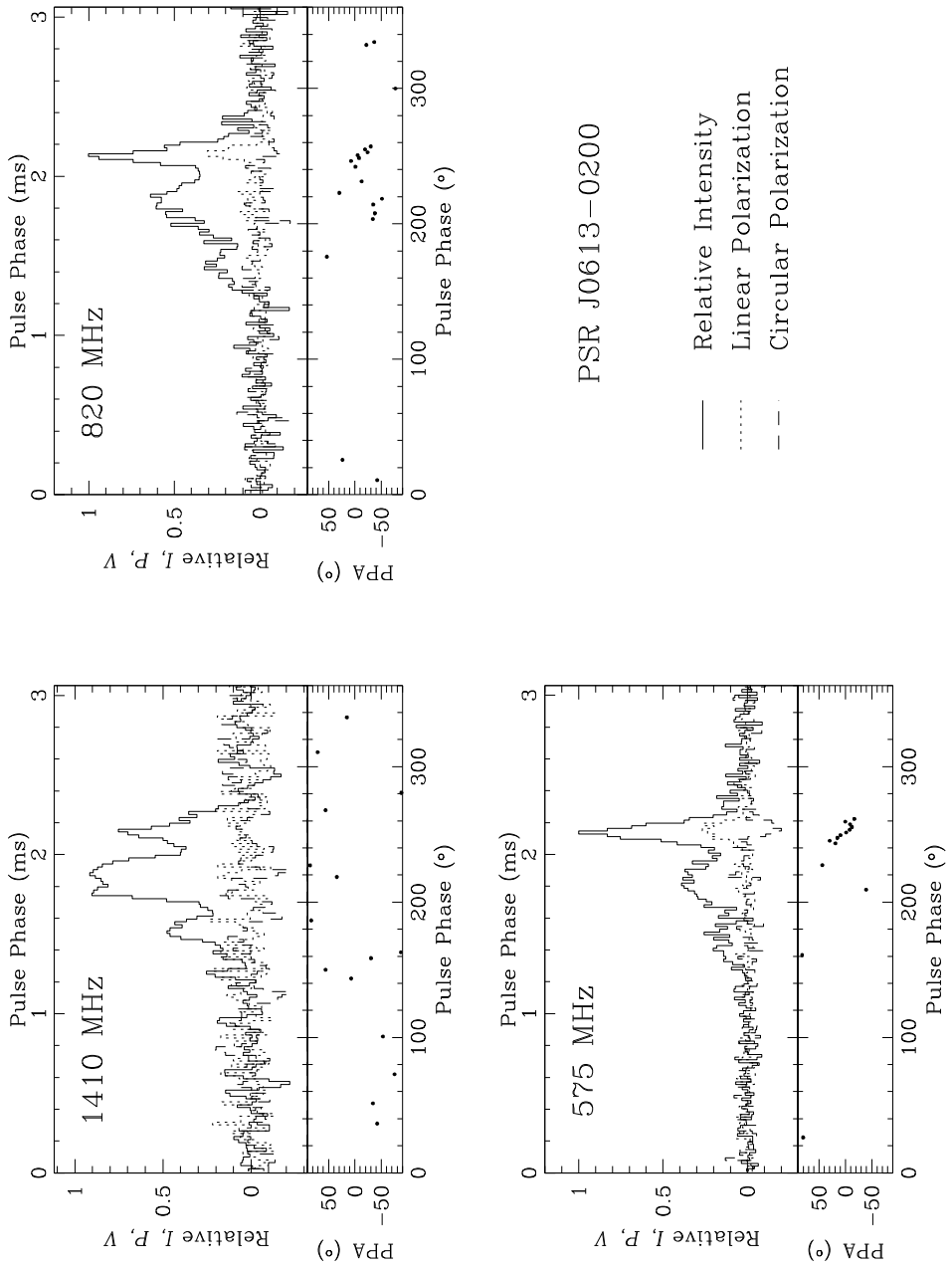

Fig. 3.2.— Polarization profiles of PSR J0613−0200 are displayed for three radio frequencies. For each one, the relative intensity, linear, and circular polarizations are plotted against pulse phase using solid, dotted, and dashed lines, respectively. The bottom axis indicates the pulse phase in degrees, while the top axis displays the same quantity in milliseconds. The polarization position angle (PPA) is plotted for phases where the linear polarization exceeds a certain threshold times the off-pulse *rms*. The resolution of the plots is given in Table 3.2, along with the integration time of the data presented, and the PPA threshold used. In this particular case, the 1410-MHz profile has been smoothed by an additional 3 time bins.

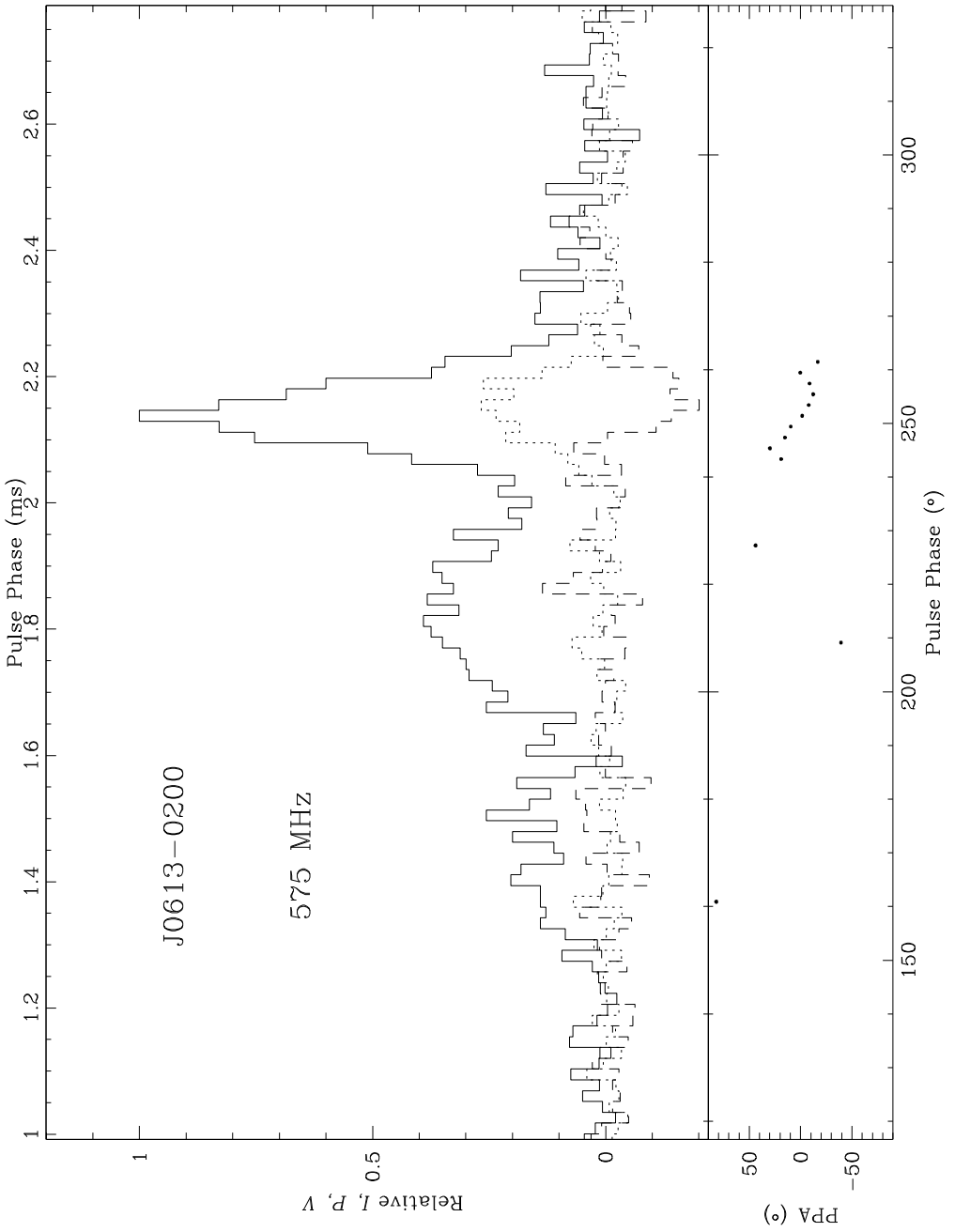

Fig. 3.3.— A region around the pulsed emission has been expanded in the 575-MHz polarization profile of PSR J0613−0200.

3.3 PSR J1012+5307

The profile of this pulsar is fairly complex, with many components in 3 distinct structures. The main pulse at 1410 MHz has at least 3 components, and is followed by a double-peaked interpulse (IPa), and then another weak component (IPb). Up to 7 Gaussians were required to achieve a reasonable fit to the intensity profile (cf. Figure 3.4), while Kramer *et al.* (1998) fits the profile at 1410 MHz with 9 Gaussian components (the two extra components accounted for low-level emission which is not obvious in our data, which have lower SNR). Emission is present over a wide range of longitudes, which may indicate that the emission is all from a single pole. The $\sim 180^\circ$ separation between the MP complex and IPb supports a classic two-pole pulse/interpulse morphology, however. The trailing component of the main pulse, and the double-peaked IPa strengthen relative to the other components with increasing radio frequency. IPb strengthens relative to the other components with decreasing radio frequency. The separations between the various components are not a strong function of observing frequency.

The last component of the main pulse (1) is highly linearly polarized. Significant linear polarization is also seen in the two interpulse structures. The leading edge of the MP is weakly polarized, becoming less polarized with increasing radio frequency. Sense-reversing circular polarization is associated with the main pulse at all frequencies. Both interpulse structures also show evidence for weak sense-reversing circular polarization (cf. Figure 3.6). The PPA curve is very flat.

A separate profile at 1410 MHz taken in 1996 October with the EBPP displays a similar intensity profile, circular polarization, and PPA curve, but the trailing component of the main pulse structure is even more linearly polarized ($\sim 70\%$) than that displayed here ($\sim 60\%$, cf. Figure 3.5). The linear polarization of IPb is also stronger in this profile. The data at the lower frequencies are too weak to place useful limits on polarization variations between observations.

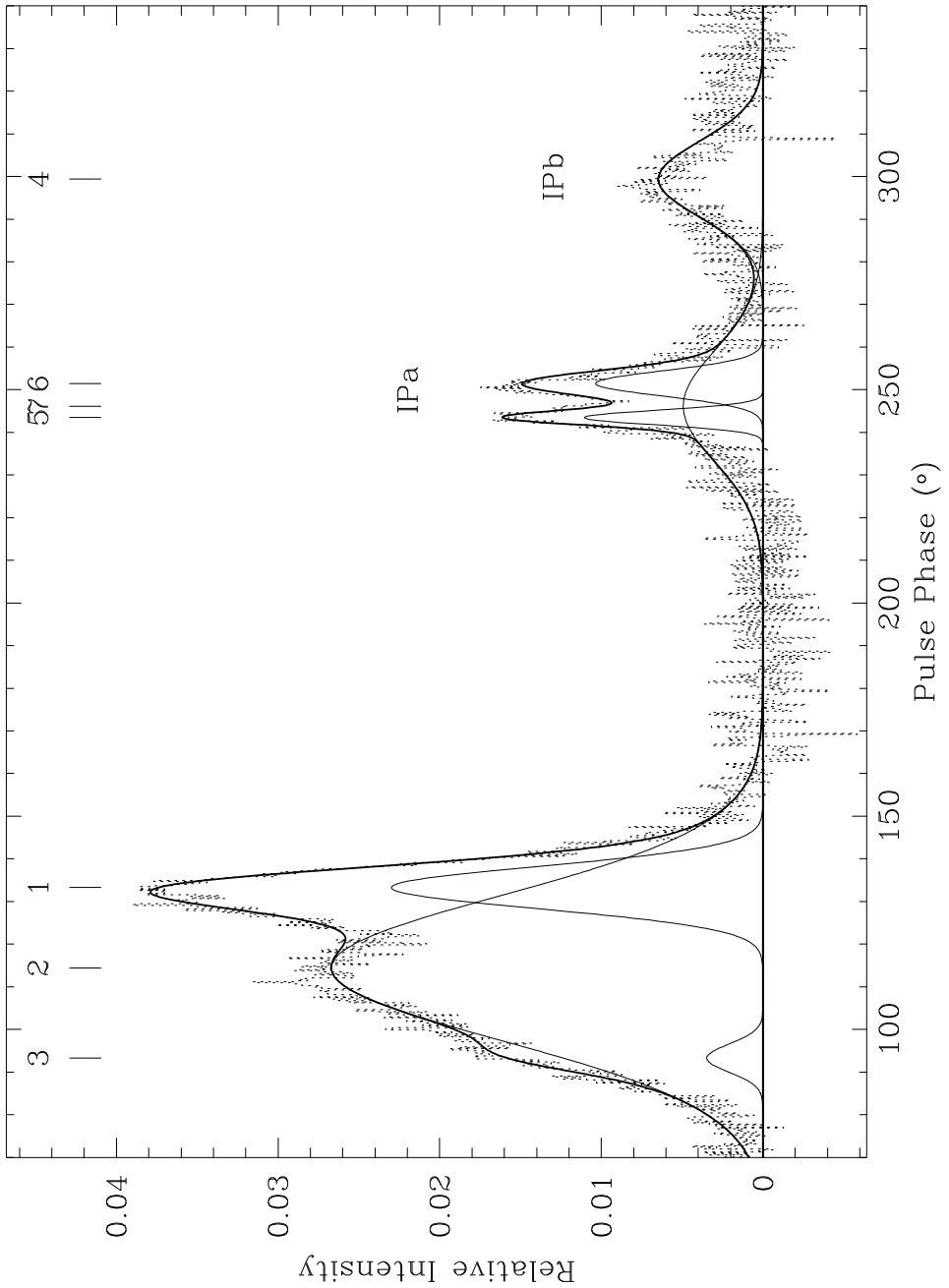

Fig. 3.4.— The Gaussian component decomposition for PSR J1012+5307 at 1410 MHz is shown. See the caption of Figure 3.1 for details.

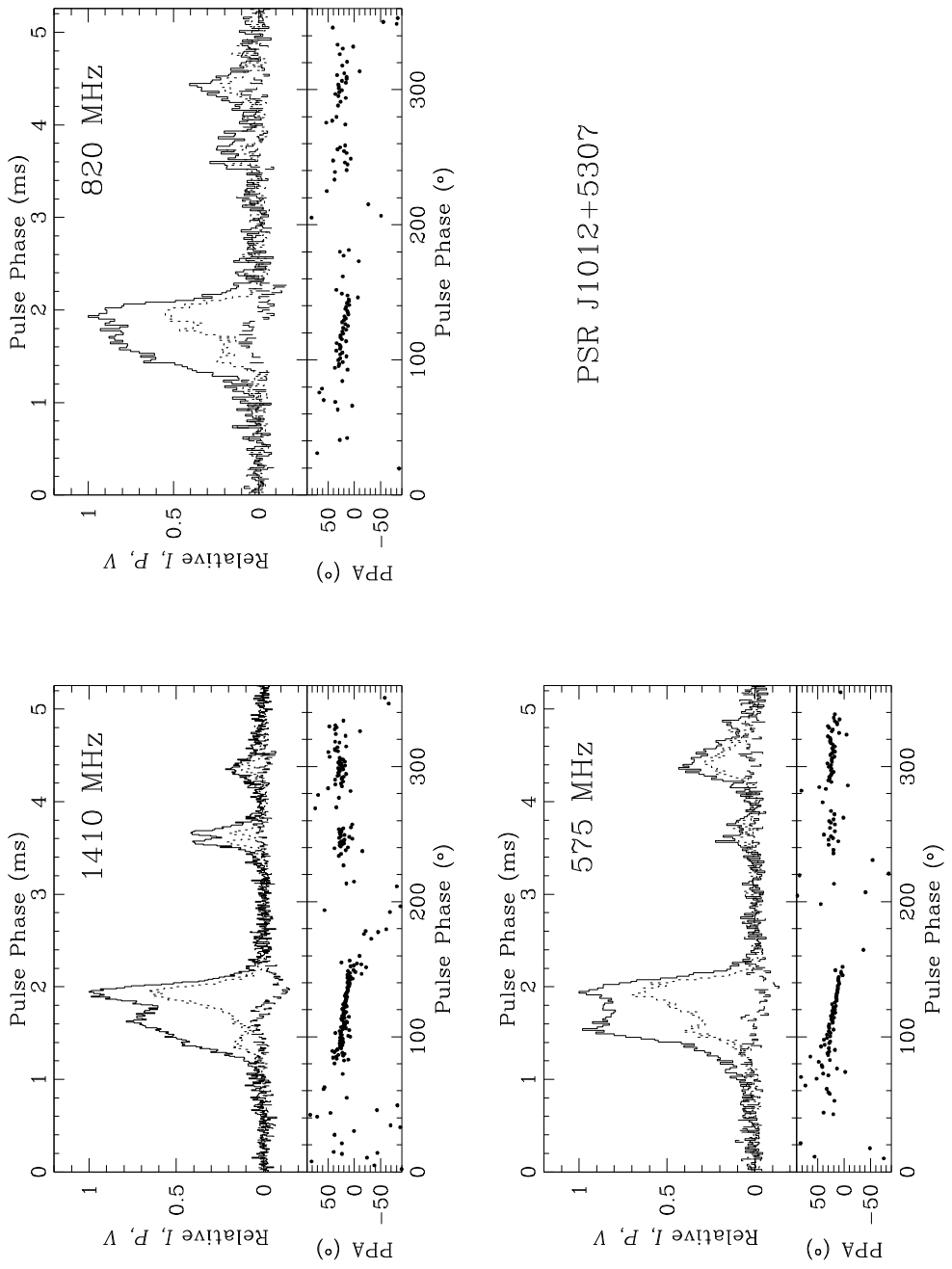

Fig. 3.5.— Polarization profiles of PSR J1012+5307 are displayed for three radio frequencies. See the caption of Figure 3.2 for details.

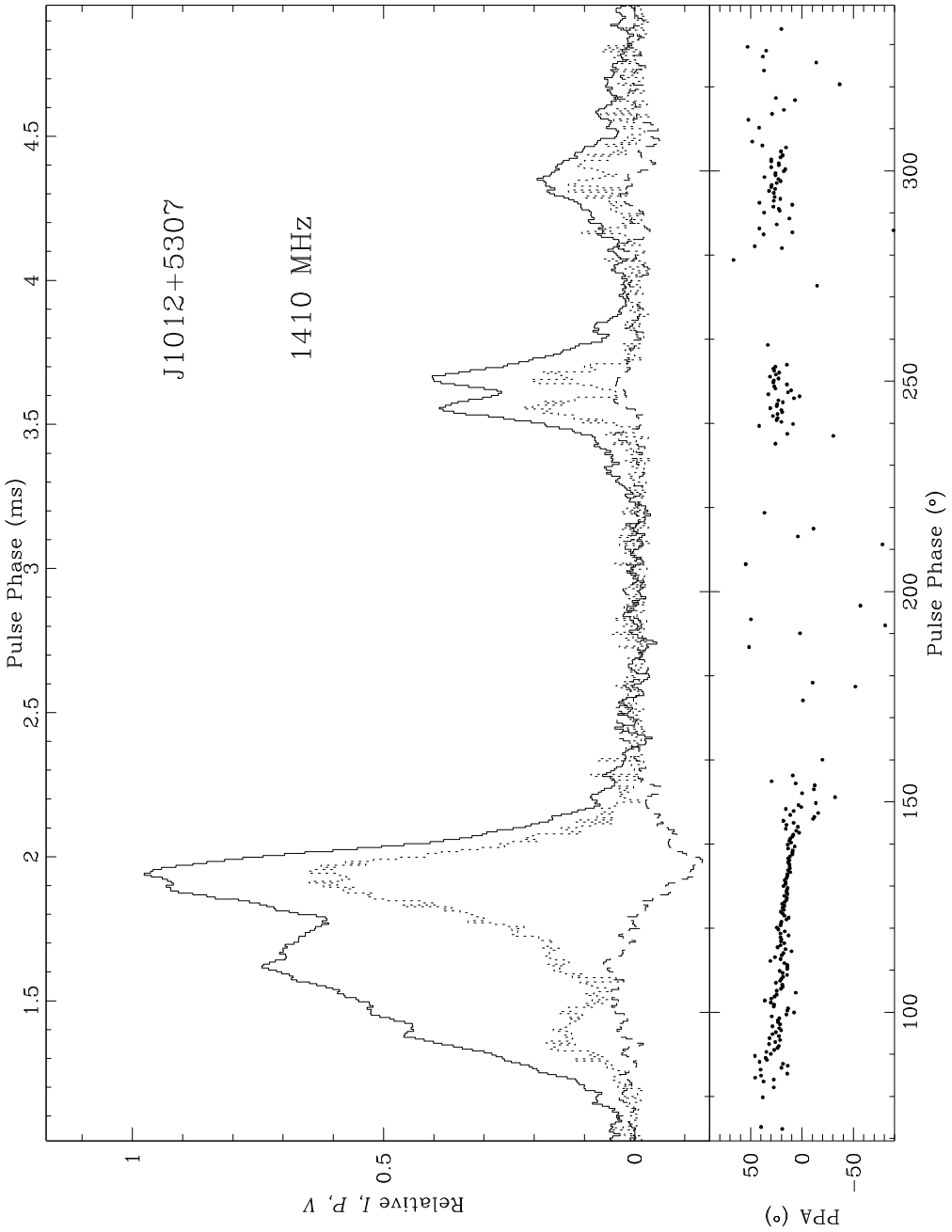

Fig. 3.6.— A region around the pulsed emission has been expanded in the 1410-MHz polarization profile of PSR J1012+5307. The resolution of this profile is 6.9μs. The data have also been smoothed by 5 time bins.

3.4 PSR J1022+1001

The intensity profile of this pulsar can be fit at all three frequencies by a sharp trailing component (1), a relatively sharp component (2) which precedes this by $\sim 11°$, a small sharp component (4) between the two, and a broad leading component (3) which precedes the others by $\sim 20°$. In general, the trailing component is more dominant at low frequencies (cf. Figure 3.8), but the intensity ratio of the two main components is not constant in time. This ratio varies on a time scale of hours at 430 MHz (Camilo 1995), and also changes at 1410 MHz (Kramer *et al.* 1998). At 1.7 GHz, however, the leading component is usually brighter, (Camilo *et al.* in prep), and at 4.85 GHz (Kijak *et al.* 1997), the trailing component has faded with respect to the leading one. The averages for this object look much the same from epoch to epoch, with the 1410-MHz data from 1996 October being indistinguishable from the results displayed here. Inspection of daily averages of our data reveal, however, that at 1410 MHz, the component ratio of the two main peaks varies slightly from day to day, while at 820 MHz, it reverses for a single day, with the trailing component stronger the remainder of the time. The trailing component is also stronger for each daily average of 575-MHz data. The overall average profile development is not consistent with normal triple or multiple profile frequency development.

The sharp trailing component (1) is highly linearly polarized at all RFs (75%). The early portion of the profile is also linearly polarized, although more weakly. The pulsar seems to be most weakly polarized at 820 MHz, but as noted by Xilouris *et al.* (1998) and Sallmen *et al.* (1997) the polarization of this pulsar is not constant, changing with the profile variations. The PPA curve is well defined, but with an orthogonal mode transition associated with the leading main component, and accompanied by depolarization. The circular polarization is small or non-existent for the leading portion of the pulse, but is about -20% on the trailing edge of the leading main component, and -15% under the trailing sharp component.

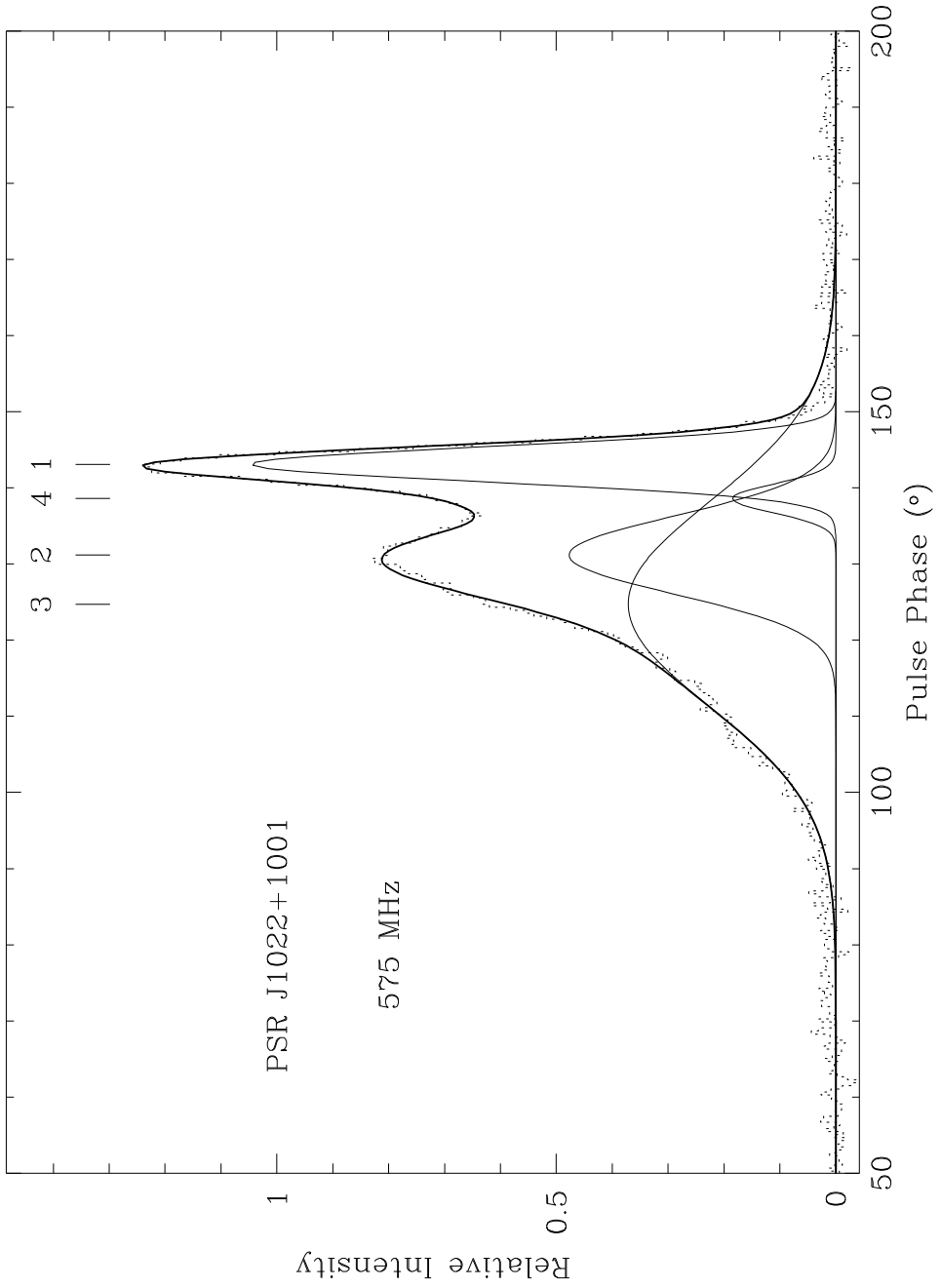

Fig. 3.7.— The Gaussian component decomposition for PSR J1022+1001 at 575 MHz is shown. See the caption of Figure 3.1 for details.

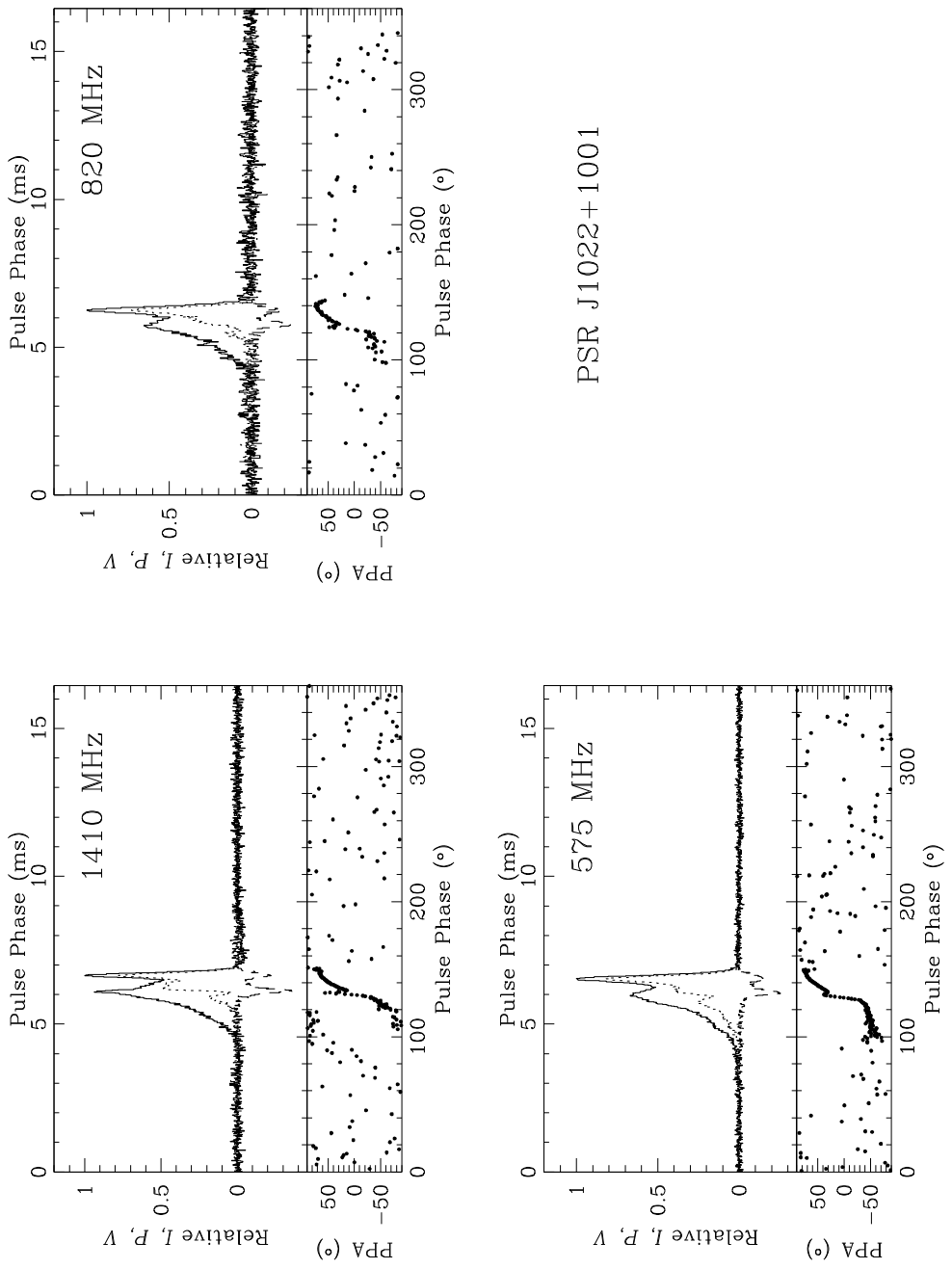

Fig. 3.8.— Polarization profiles of PSR J1022+1001 for three radio frequencies. See the caption of Figure 3.2 for details.

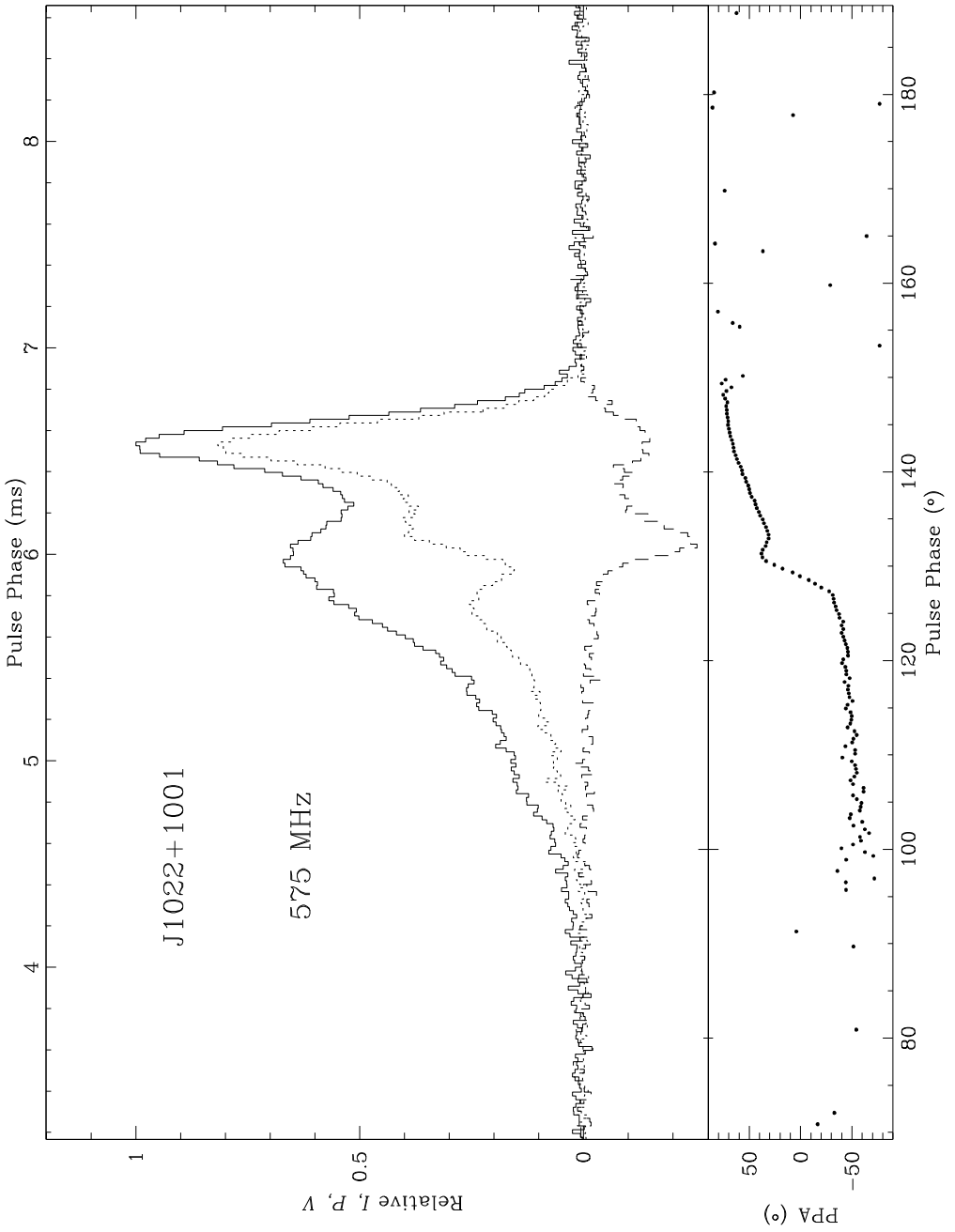

Fig. 3.9.— A region around the pulsed emission has been expanded in the 575-MHz polarization profile of PSR J1022+1001.

3.5 PSR B1620−26

The profile of this 11.1-millisecond pulsar shows 3 components, apparently a core component (1) with conal outriders. The strongest central component shows significant linear polarization, increasing with increasing radio frequency to about 40% at 1410 MHz (cf. Figure 3.11. This is larger than that seen by Xilouris *et al.* (1998), indicating possible variations in the polarization of this pulsar. The signal to noise of short term averages of our data is insufficient to place interesting limits on possible polarization variations.

The trailing component shows no polarization, while the leading component is somewhat linearly polarized. The circular polarization of the central component is $\sim -20\%$, but is negligible for the surrounding components. The PPA curve is well defined, with an orthogonal mode change occurring between the first and second components, accompanied by a decrease in linear polarization. All of these properties are consistent with a classical triple profile. The central component becomes *stronger* at high frequencies, in contrast to the expected behaviour. In addition, there is no significant frequency development of component separations or widths. The two outriders are always $\sim 20^\circ$ on either side of the central component, and the trailing component is always slightly weaker than the preceding one.

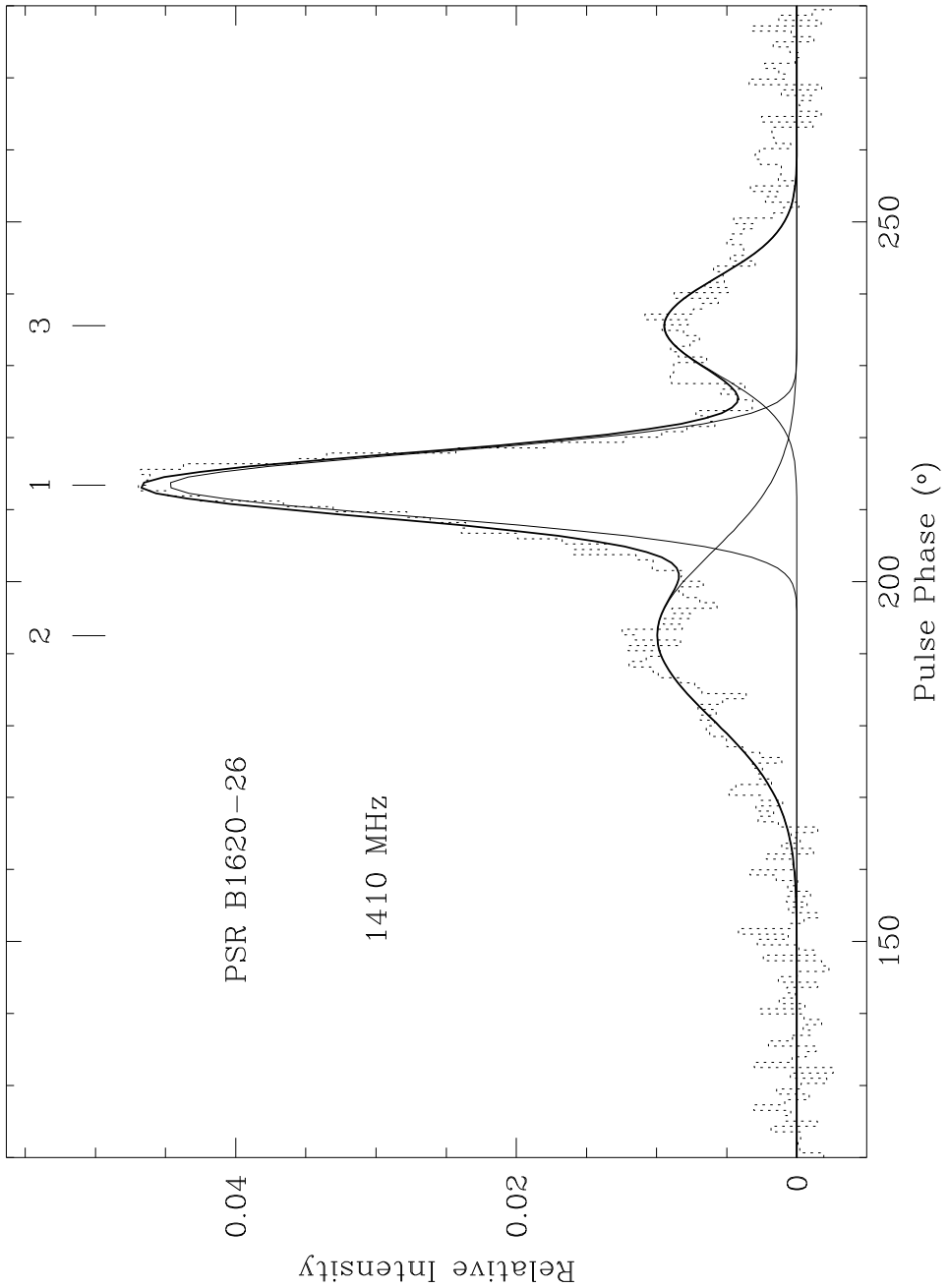

Fig. 3.10.— The Gaussian component decomposition for PSR B1620−26 at 1410 MHz is shown. See the caption of Figure 3.1 for details.

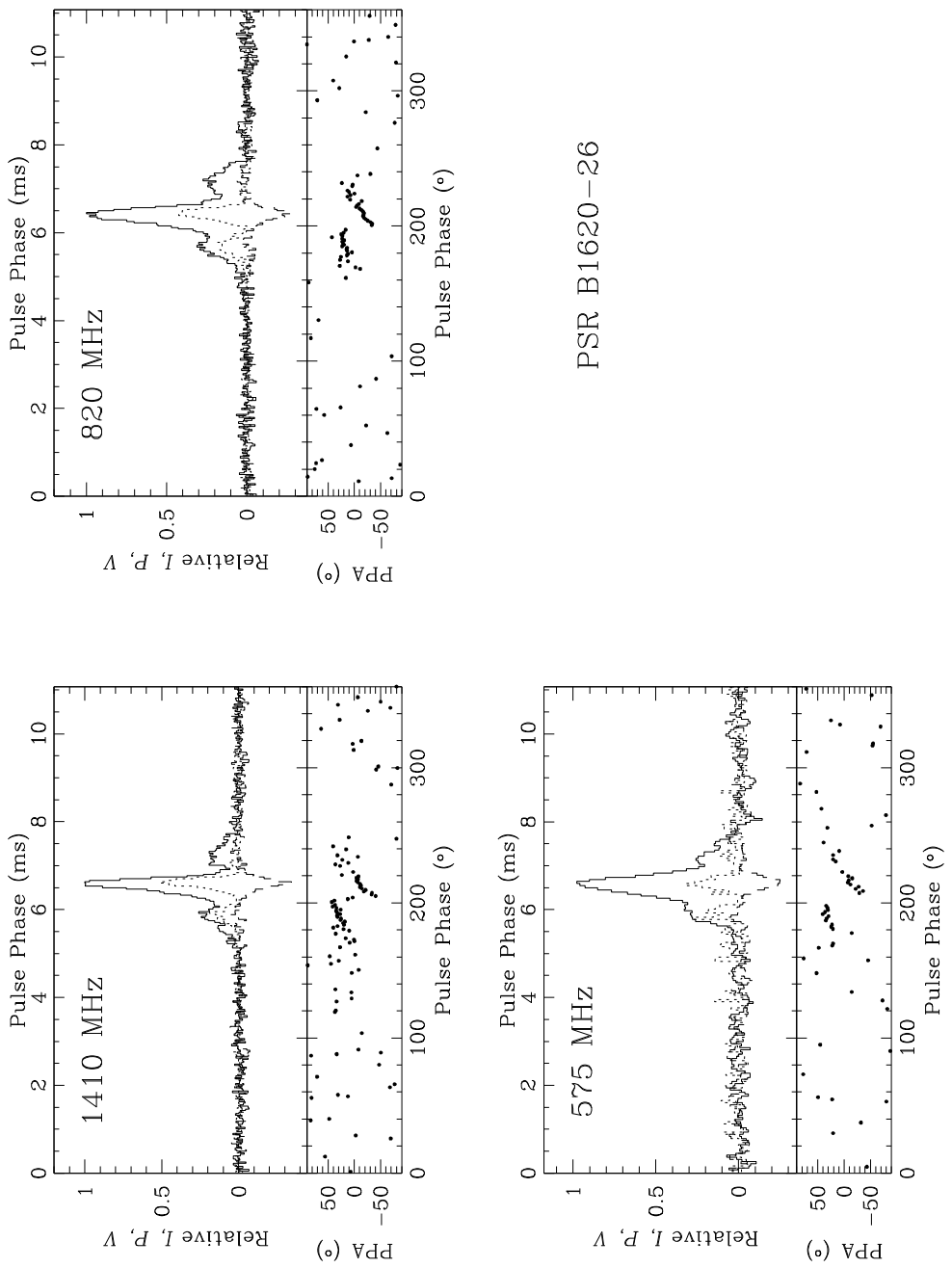

Fig. 3.11.— Polarization profiles of PSR B1620−26 for three radio frequencies. See the caption of Figure 3.2 for details. In this particular case, the 575-MHz profile has been smoothed by an additional 3 time bins.

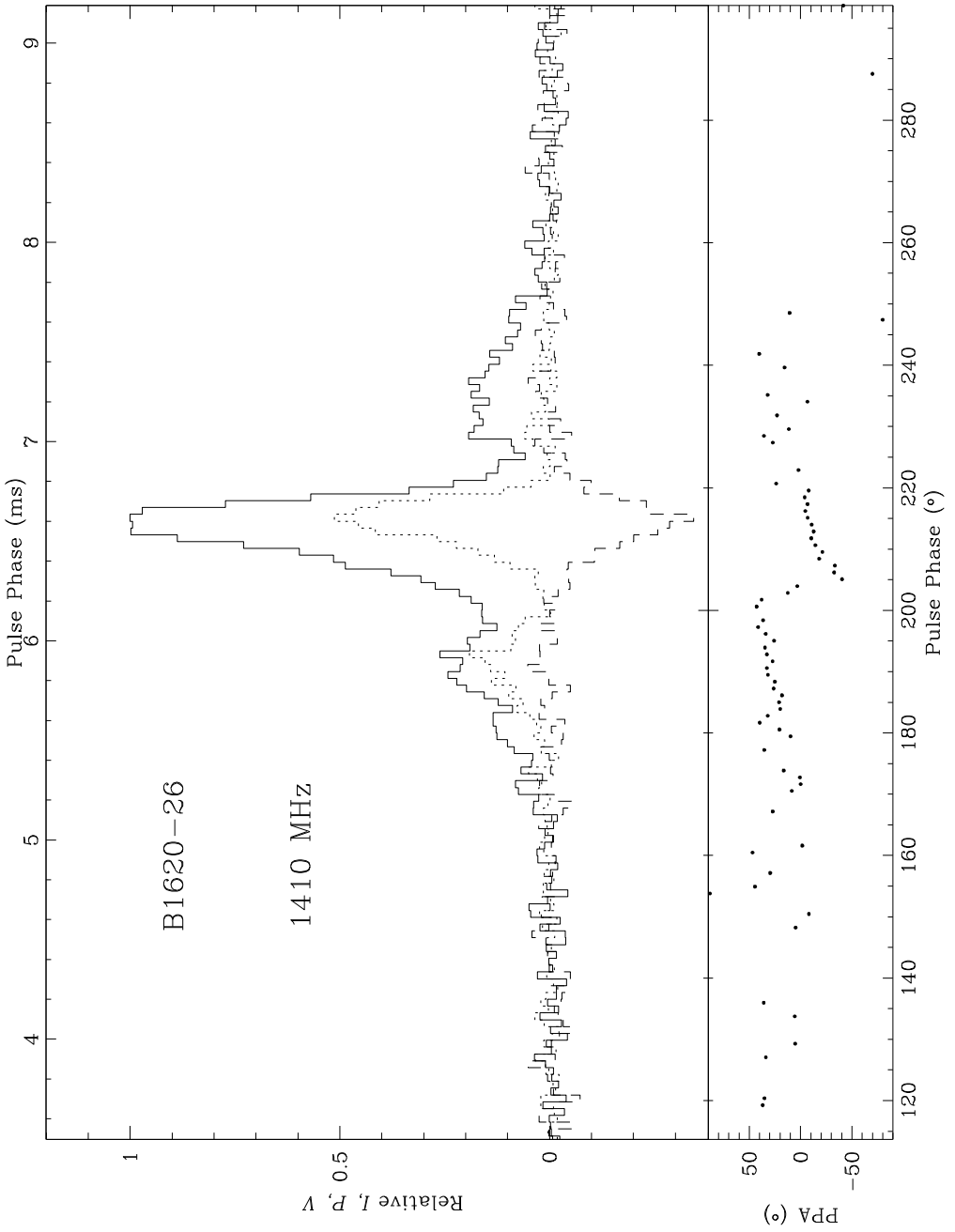

Fig. 3.12.— A region around the pulsed emission has been expanded in the 1410-MHz polarization profile of PSR B1620−26.

3.6 PSR J1713+0747

At 1410 MHz, the profile of this 4.5-millisecond pulsar has many components within a single structure, as can be seen in Figure 3.13. Six Gaussian components were required to fit the 1410-MHz data of Kramer *et al.* (1998). The same is true here. The shape of the overall profile is fairly similar at all frequencies, although the small preceding and trailing components are more important at 2.38 and 4.85 GHz (Camilo 1995, Kijak *et al.* 1997). The apparent broadening of the profile at the lower frequency is not due to interstellar broadening, but the increased importance of the trailing components.

The leading components are significantly linearly polarized at 1410 MHz, while the trailing component shows only weak polarization. At 575 MHz and 820 MHz, the small preceding component is weakly polarized. Modest linear polarization occurs under the main peak at all frequencies, as seen in Figure 3.14. The peak linear polarization is $\sim 20 - 40\%$, with the lowest values occurring at 820 MHz. This does not agree with the expected depolarization with increasing radio frequency. The low linear polarization at 820 MHz is present in data from each of the three separate 1997 observing runs. However, Figure 3.16 displays a profile from February 1995, taken in the circular polarization basis. Significant linear polarization is present under the main peak. Only two of our observations of this pulsar near 800 MHz display a significantly larger degree of linear polarization than that of the average in Figure 3.14. No similar variations were observed at the other frequencies.

Weak sense-reversing circular polarization is centered near the main peak, identifying it as a core component. The PPA curve is relatively flat, but is disturbed by orthogonal mode changes which occur on either side of the main pulse, and are associated with drops in the linear polarization. The second orthogonal mode change is also associated with the sense-reversal of the circular polarization.

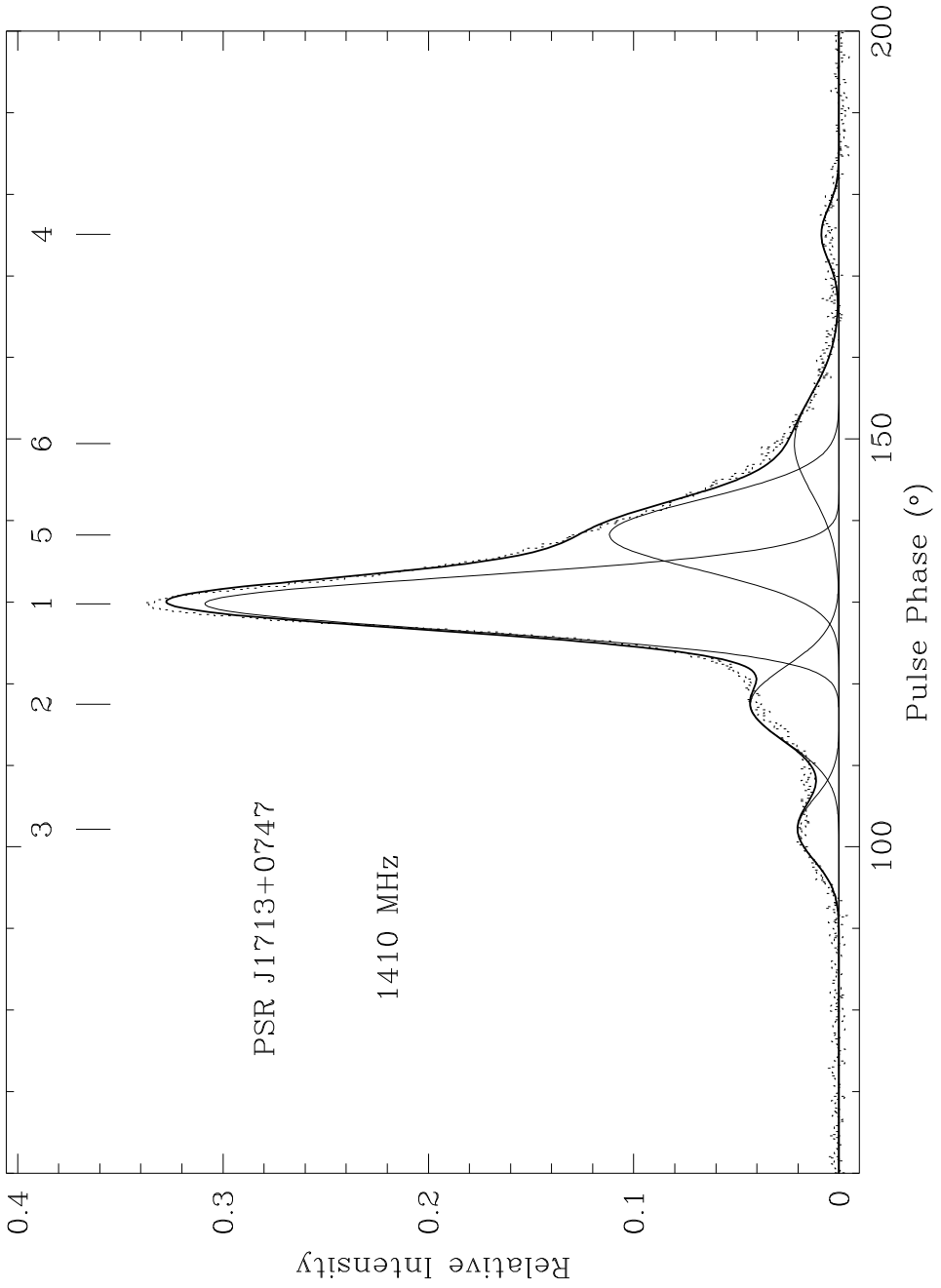

Fig. 3.13.— The Gaussian component decomposition for PSR J1713+0747 at 1410 MHz is shown. See the caption of Figure 3.1 for details.

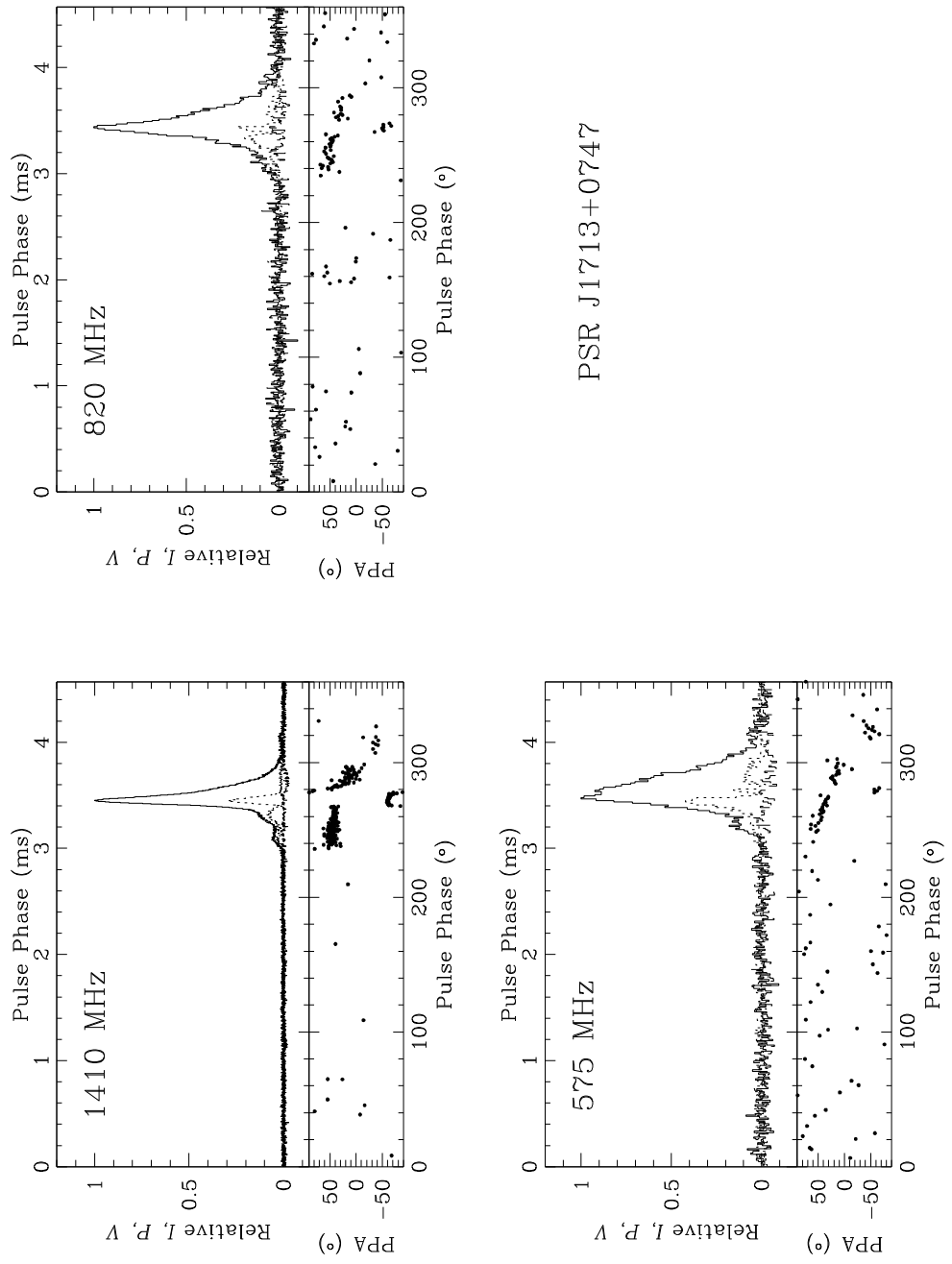

Fig. 3.14.— Polarization profiles of PSR J1713+0747 for three radio frequencies. The apparent sweep in the 1410-MHz PPA at 280° is due to a slightly incorrect instrumental correction for σ, combined with the extremely low linearly polarized fraction at that longitude. The PPA undergoes a second orthogonal mode transition at this longitude. See the caption of Figure 3.2 for details.

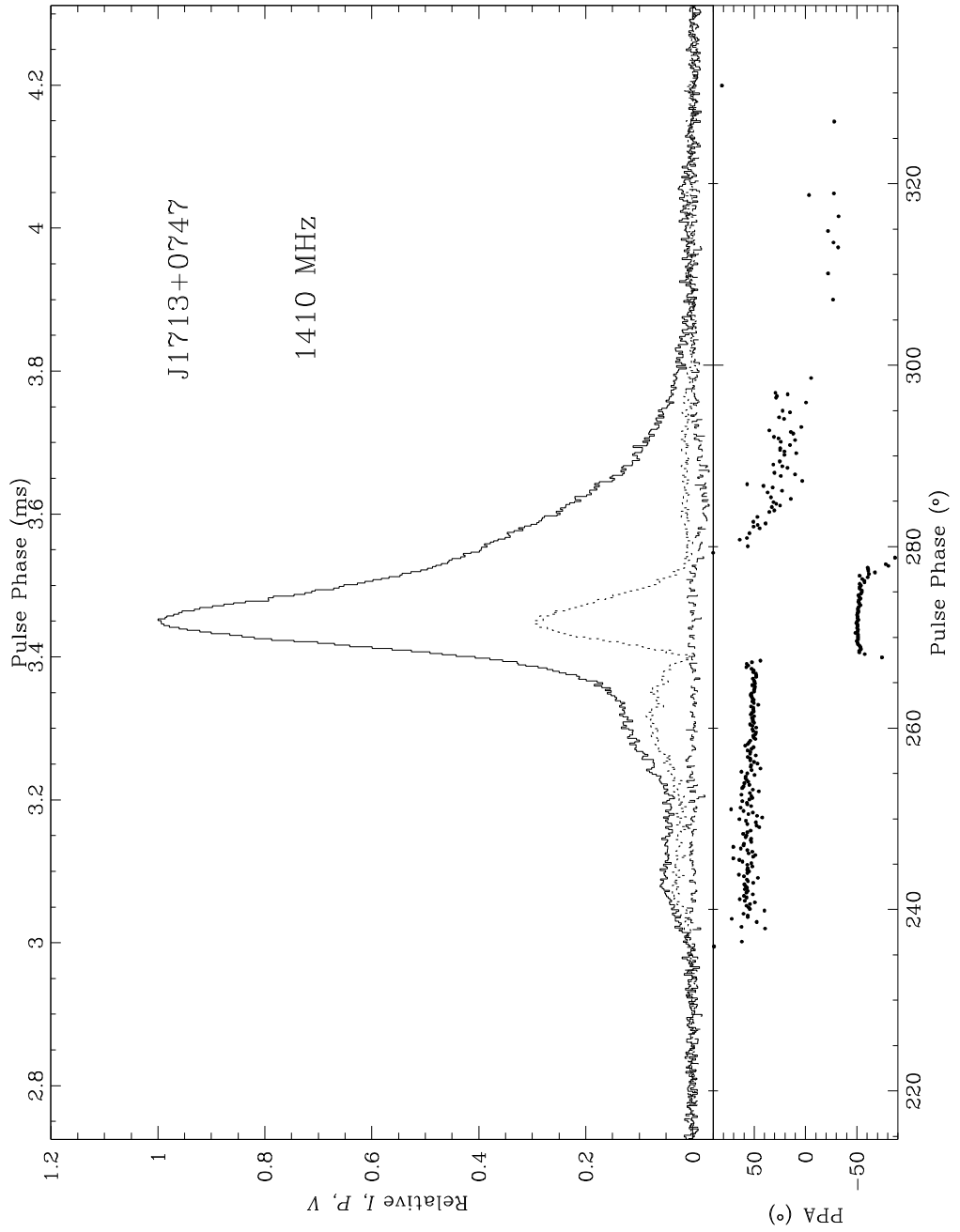

Fig. 3.15.— A region around the pulsed emission has been expanded in the 1410-MHz polarization profile of PSR J1713+0747.

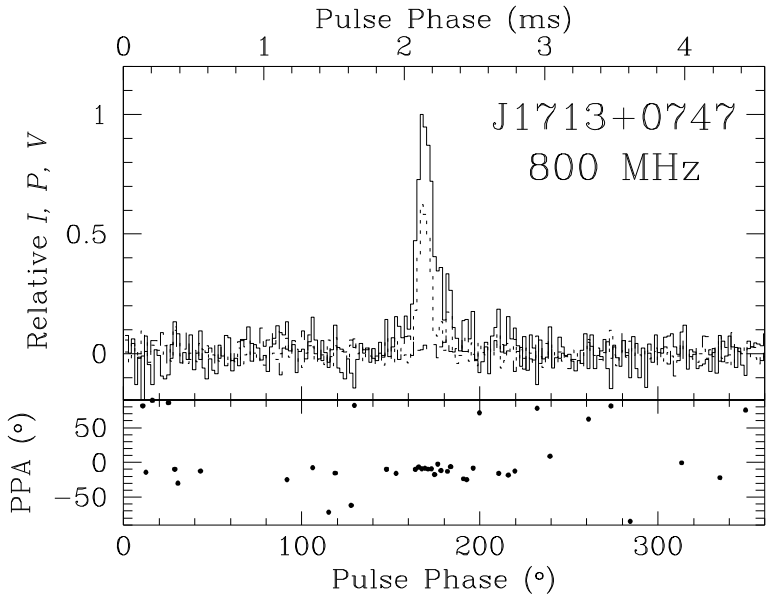

Fig. 3.16.— Polarization profile of PSR J1713+0747 at 800 MHz. This observation has a higher linearly polarized fraction than that typically seen at 820 MHz. See the caption of Figure 3.2 for details.

3.7 PSR J1730−2304

The profile presented in Figure 3.17 shows a clear triple structure at 1410 MHz, plus small outer components. Kramer *et al.* (1994) fit five Gaussians to the intensity profile; here only four were required, as the trailing component is quite weak. The central component (2) is less prominent at higher frequencies, behaviour which is consistent with a core/cone interpretation of this profile. As is expected for a symmetric triple or multiple profile, the separation of the three main components decreases with increasing radio frequency, The width of the central component decreases slightly with frequency, as does that of the small preceding component (4). No significant width change is seen in the other two main components (2,3). The central feature seems delayed relative to the symmetry center of the profile at lower frequencies.

The pulsar is only modestly linearly polarized in all the data displayed here, and increases with increasing radio frequency, contrary to expectation. Little or no polarization is associated with the central component. The relatively small polarized fraction is in sharp contrast to the 1410-MHz profile presented by Xilouris *et al.* (1998), which is almost 100% polarized for the outer components of the triple. This is undoubtedly a reflection of the profile mode changes discussed therein, in which variations of the linear polarization from 0-100% are associated with profile shape variations. The circular polarization was found to remain relatively stable.

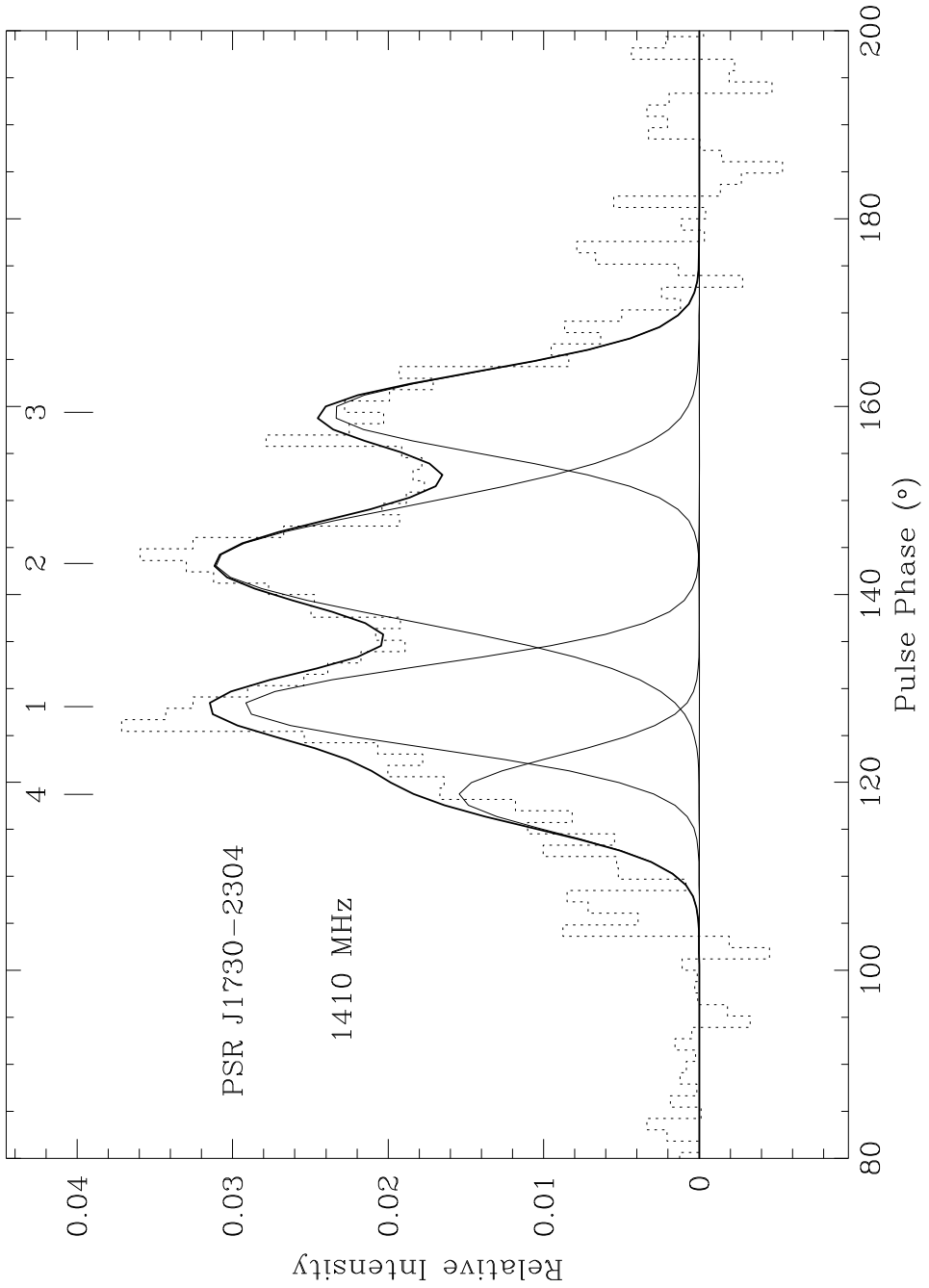

Fig. 3.17.— The Gaussian component decomposition for PSR J1730−2304 at 1410 MHz is shown. See the caption of Figure 3.1 for details.

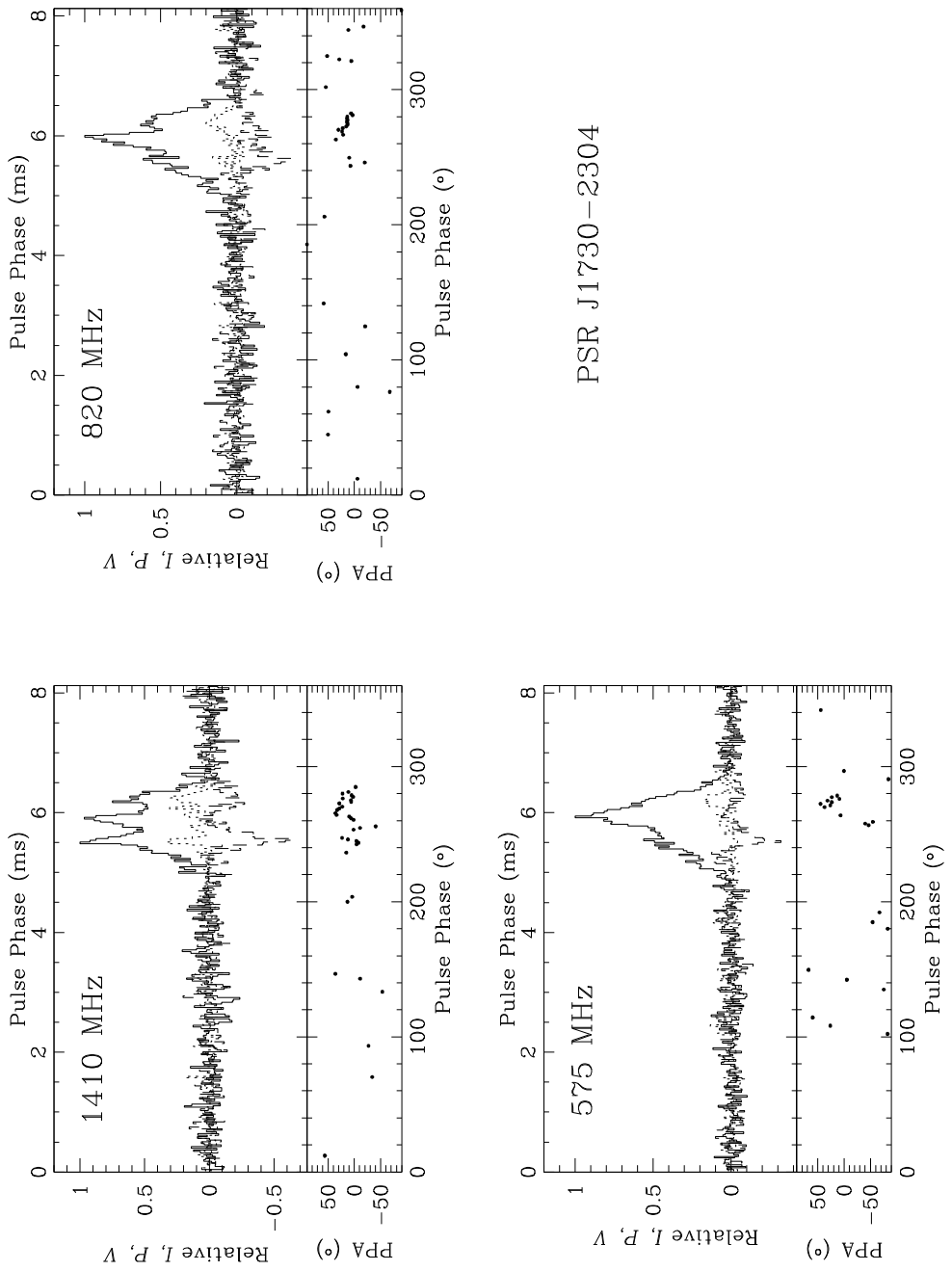

Fig. 3.18.— Polarization profiles of PSR J1730−2304 for three radio frequencies. See the caption of Figure 3.2 for details.

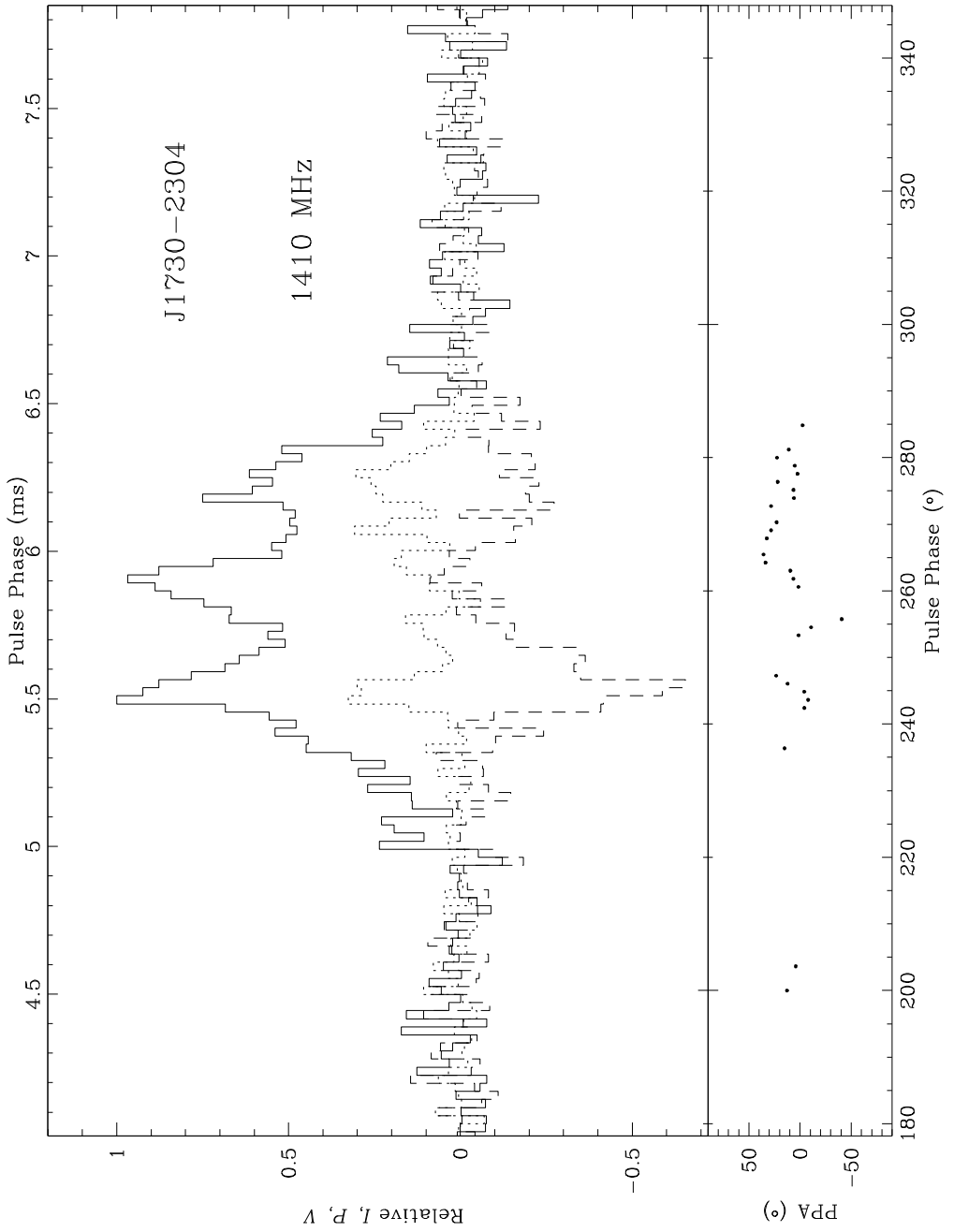

Fig. 3.19.— A region around the pulsed emission has been expanded in the 1410-MHz polarization profile of PSR J1730−2304.

Despite the expectation from this that the circular polarization displayed here should match the $\approx 10\%$ shown in the 1410-MHz profile of Xilouris *et al.* (1998), the leading component of this profile has a circular polarization of -50%. Due to the low level of linear polarization in this profile, the PPA curve is poorly defined, although it is consistent with the published data. At 575 MHz, the only linear polarization is on the trailing edge of the profile, while moderate circular polarization is seen.

3.8 PSR B1821−24

This 3-millisecond pulsar has a three component profile (cf. Figure 3.20). Two sharp components (1,2) are separated by approximately 108 degrees, and are followed by a weaker broad component, about 180° from the first component. At 1410 MHz, an extra broad component under the second peak was required to explain the pulse shape. The component separations are frequency-independent, suggesting a possible two-pole model for the pulsar.

The profile is significantly broadened due to interstellar scattering at lower frequencies. This is reflected in the component widths listed in Table 3.1. The 1410-MHz widths for components 1 and 2 are consistent with the 1330-MHz component widths measured by Foster, Fairhead & Backer (1991). The component separations also agree. The second component becomes increasingly dominant at higher frequencies, so that by 1410 MHz it has become the largest component. Backer & Sallmen (1997) have reported that this pulsar undergoes mode changes at 1400 MHz. About one-third of the time, this component is much weaker relative to the other two, whose intensity ratio remains roughly constant. No such variations were seen in their data at 800 MHz. Figure 3.23 displays results that indicate that the component ratios do vary at this frequency. In 1997 July, an apparent increase in the relative strength of the broad component was seen which can be explained if the two sharp components are broadened due to increased interstellar scattering at this epoch. The second component is, however, stronger relative to the first at this epoch.

The two sharp components are both strongly linearly polarized (40-60%), while the third broad component is unpolarized. No significant circular polarization is present. Under each component, the PPA curve is relatively flat, with an offset of about 40 degrees between the two.

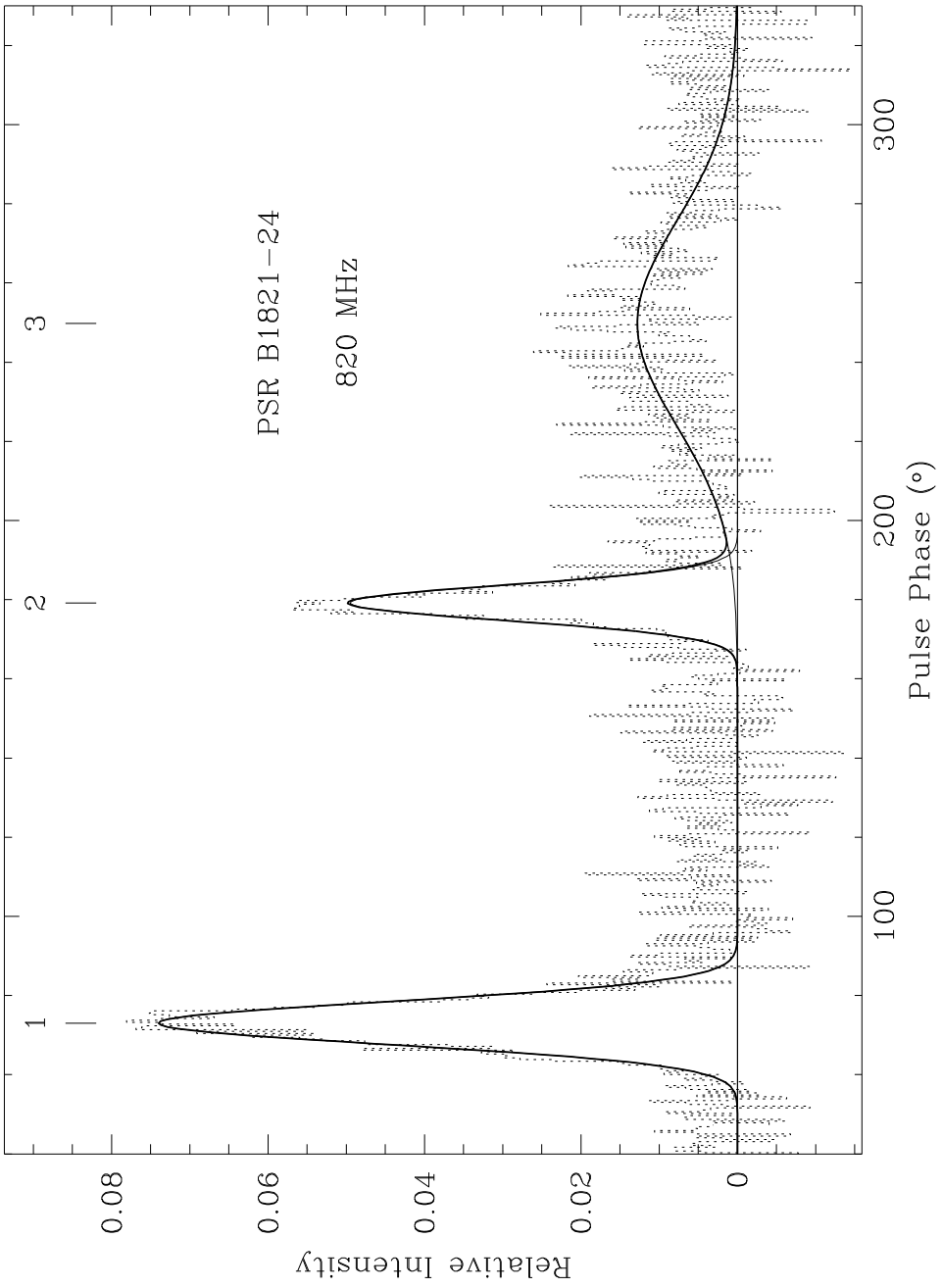

Fig. 3.20.— The Gaussian component decomposition for PSR B1821−24 at 820 MHz is shown. See the caption of Figure 3.1 for details.

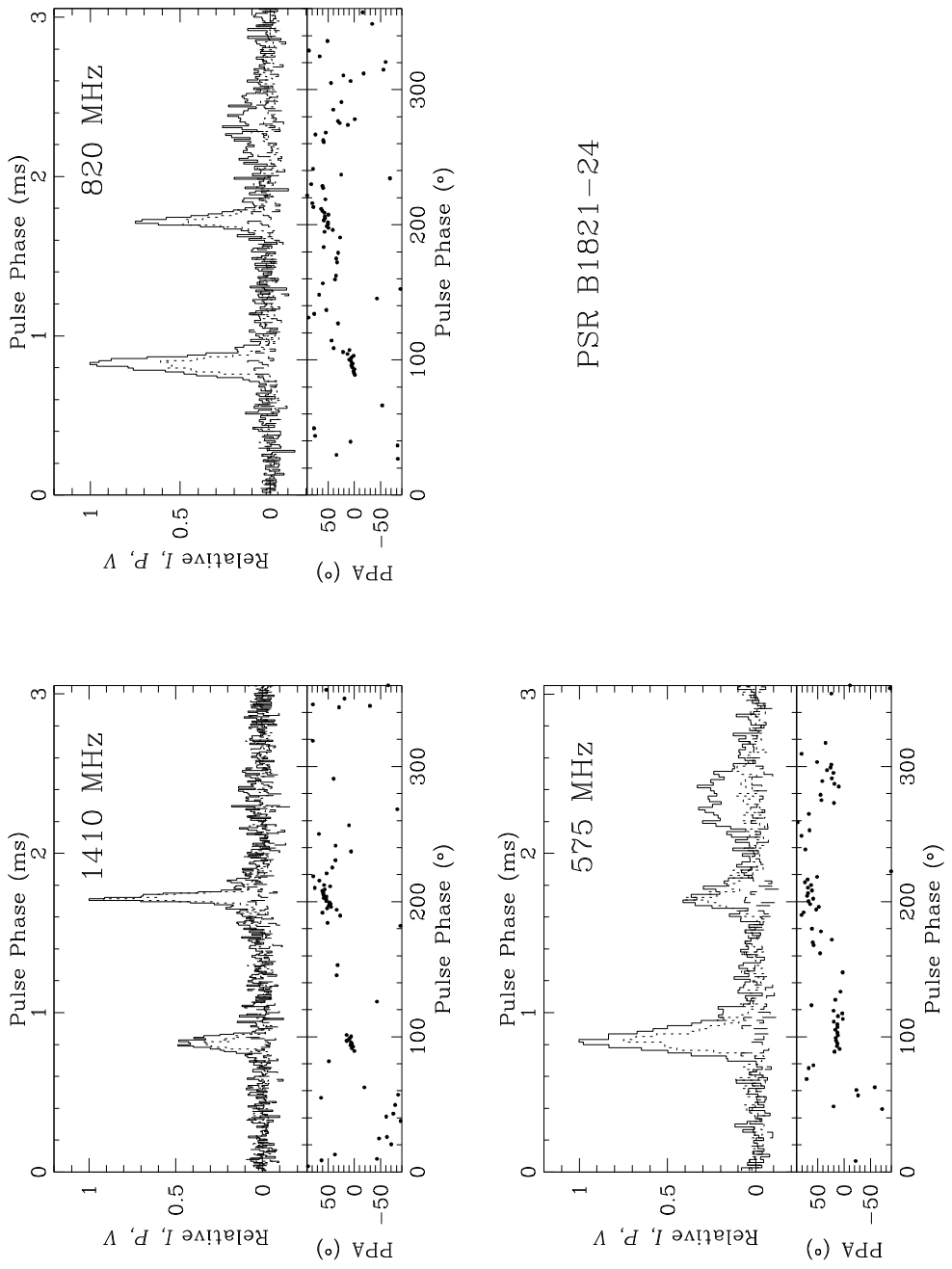

Fig. 3.21.— Polarization profiles of PSR B1821−24 for three radio frequencies. See the caption of Figure 3.2 for details.

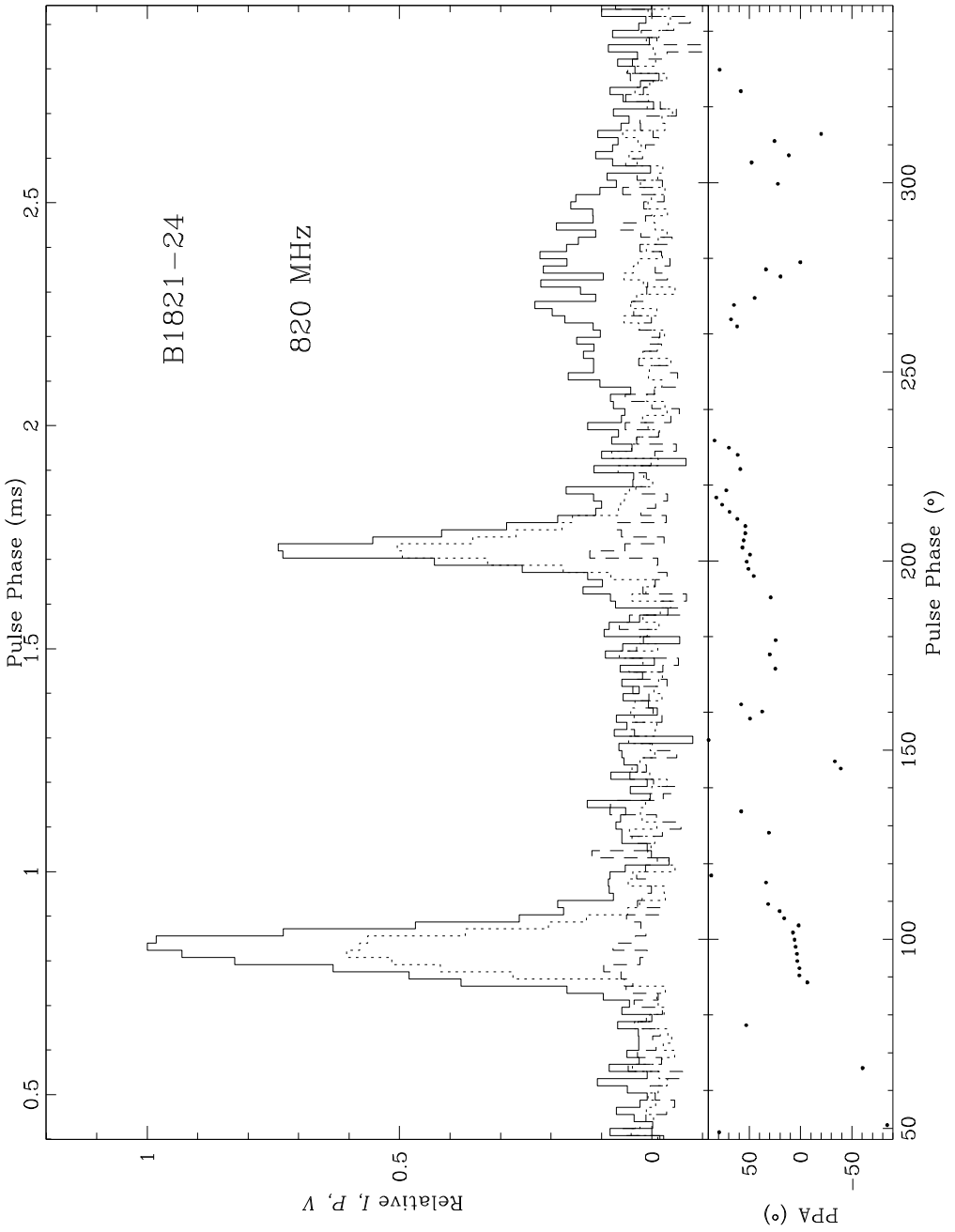

Fig. 3.22.— A region around the pulsed emission has been expanded in the 820-MHz polarization profile of PSR B1821−24. The resolution of this profile is 16.0μs.

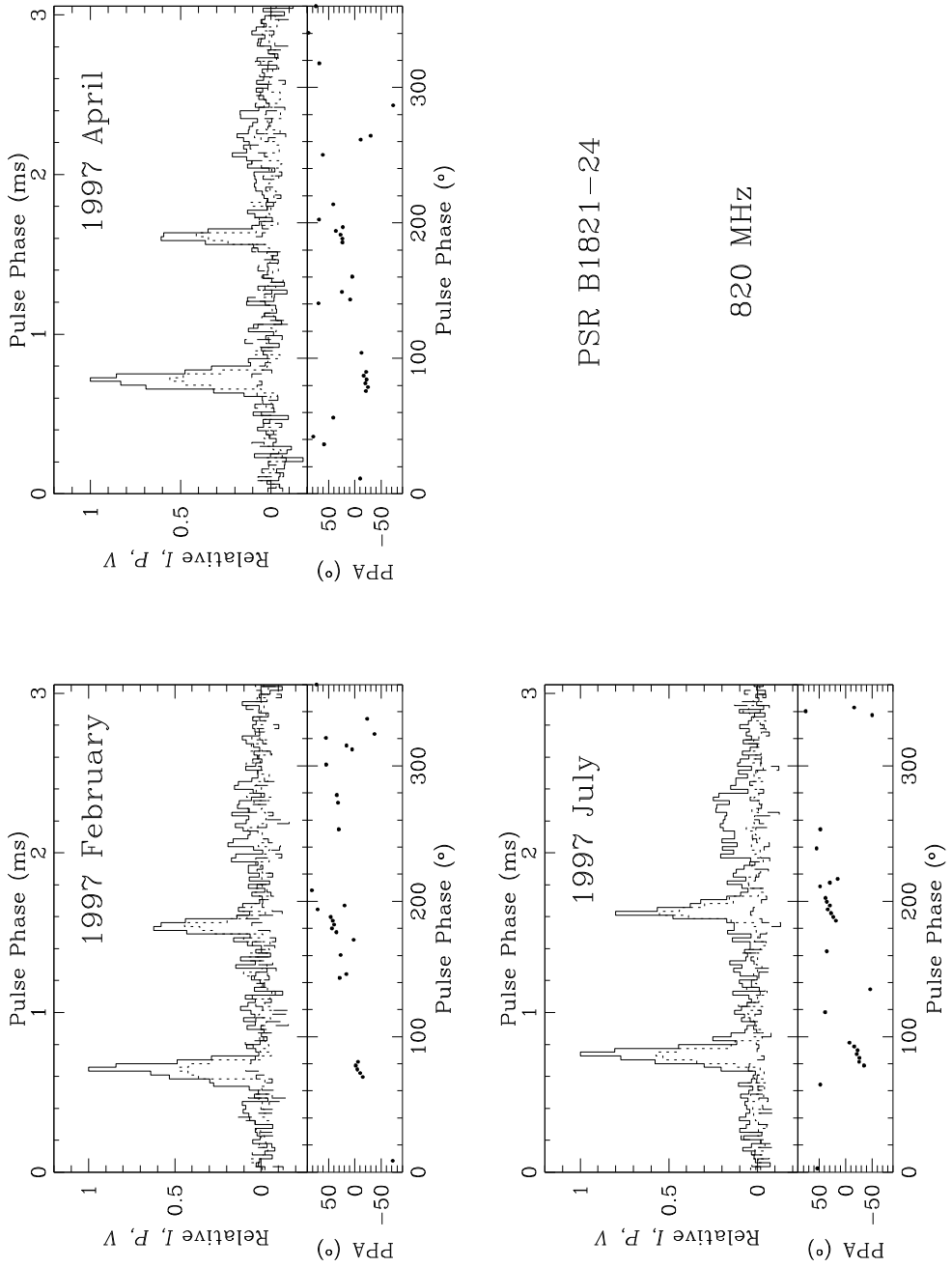

Fig. 3.23.— Polarization profiles of PSR B1821−24 for three epochs at 820 MHz. the caption of Figure 3.2 for details. The second component is stronger relative to the first in 1997 July. Investigation reveals that this amplitude ratio change cannot be explained as a binning effect. The apparent strengthening of the broad component can be explained if the two sharp components are broadened due to increased interstellar scattering.

3.9 PSR B1937+21

The fastest millisecond pulsar has a pulse/interpulse morphology at all radio frequencies. The main pulse and interpulse are always separated by $\sim 172°$, in agreement with the observations of Foster, Fairhead & Backer (1991). The effects of interstellar scattering broaden the pulse at low frequencies, hiding these features. These scattering effects are reflected in the 575-MHz component widths for this object listed in Table 3.1. The remaining component widths are comparable to previous measurements (Foster, Fairhead & Backer 1991). Their amplitude ratio remains relatively stable with frequency (cf. Figure 3.25. Both the main pulse and interpulse have trailing secondary features, following a local minimum, at 1410 MHz. These are also visible as shoulders in the 820-MHz profile. These secondary components occur at the pulse phase of the giant pulses which are seen in this pulsar at 430 MHz, and which are discussed in Chapter 6.

The main pulse is relatively strongly polarized, with polarization decreasing from $\sim 60\%$ at 575 MHz to $\sim 30\%$ at 1410 MHz. The interpulse is more weakly polarized. Our results are similar to those reported by Thorsett & Stinebring (1990) at 1420 MHz. Only a small amount of circular polarization is present at any frequency. The polarization position angle remains relatively flat across each pulse, with an orthogonal mode transition on the leading edge of the main pulse at 1410 MHz, the trailing edge of the 820-MHz interpulse, and the leading edge of the 575-MHz interpulse, accompanied by a decrease in the linear polarization.

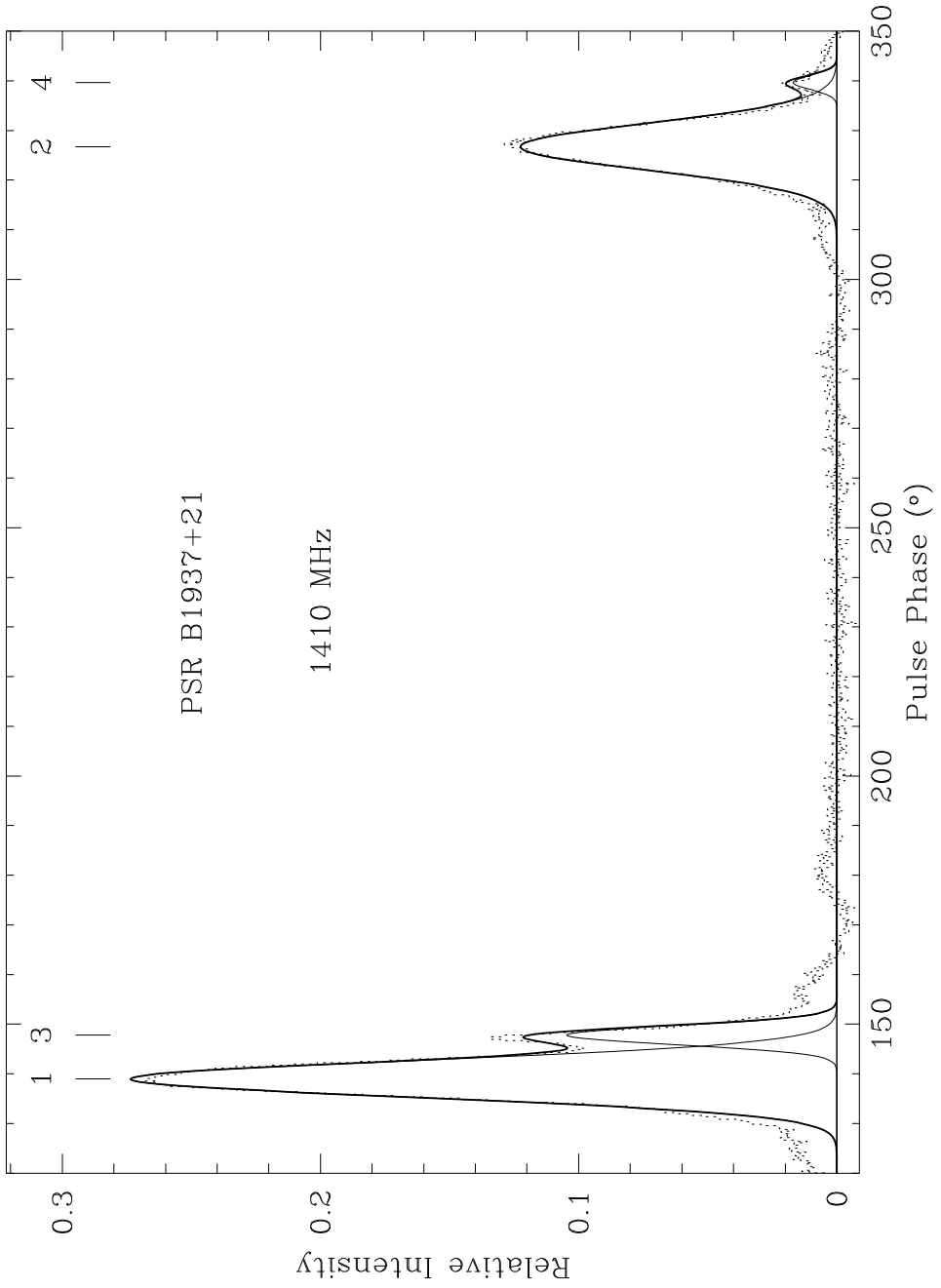

Fig. 3.24.— The Gaussian component decomposition for PSR B1937+21 at 1410 MHz is shown. See the caption of Figure 3.1 for details.

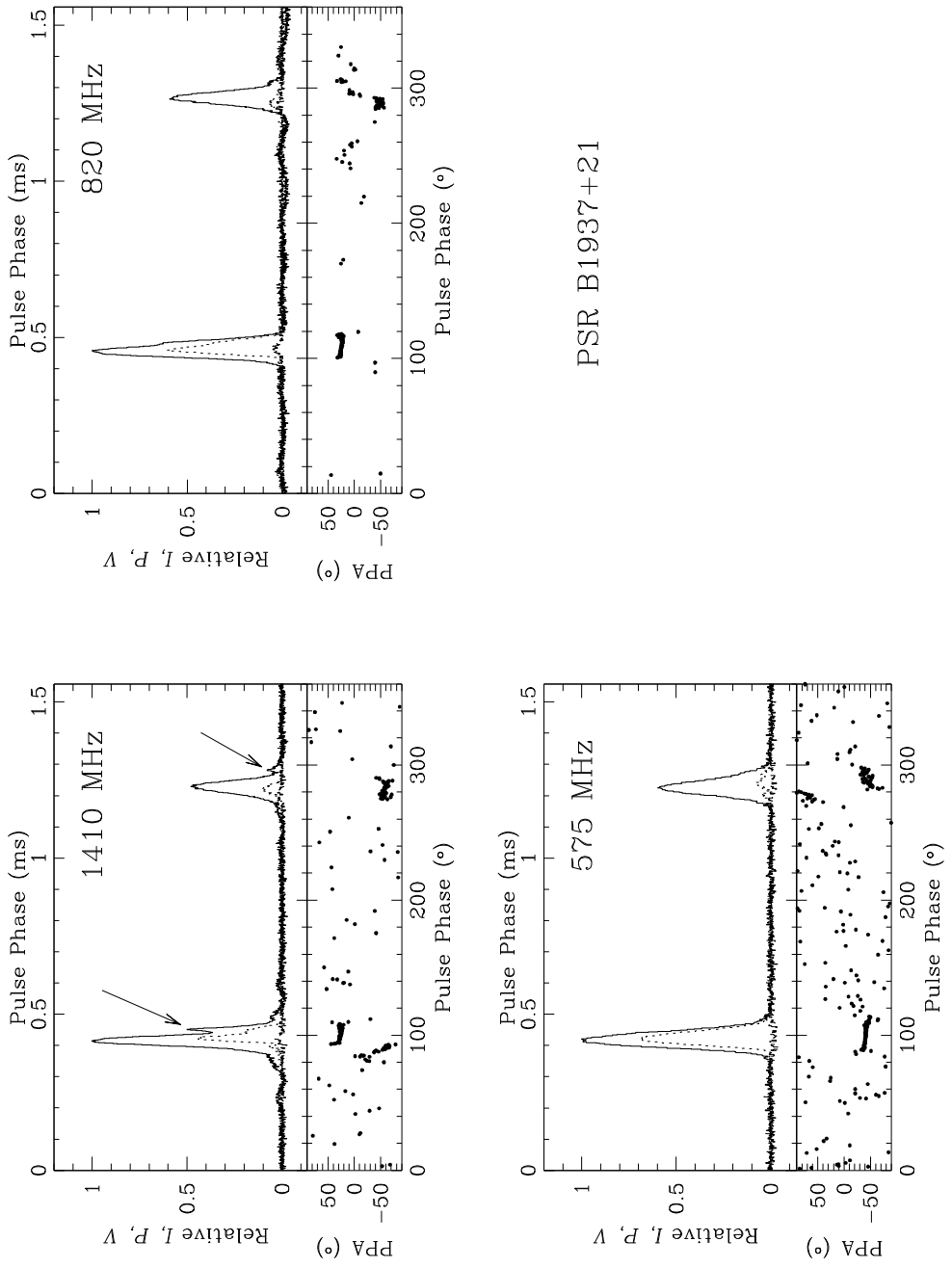

Fig. 3.25.— Polarization profiles of PSR B1937+21 for three radio frequencies. See the caption of Figure 3.2 for details. Systematic variations in the off-pulse baseline at 820 MHz, and at the edges of the pulse at 1410 MHz, are instrumental effects. The arrows point to the secondary maxima, which are at the pulse phase of the 430-MHz giant pulses discussed in Chapter 6.

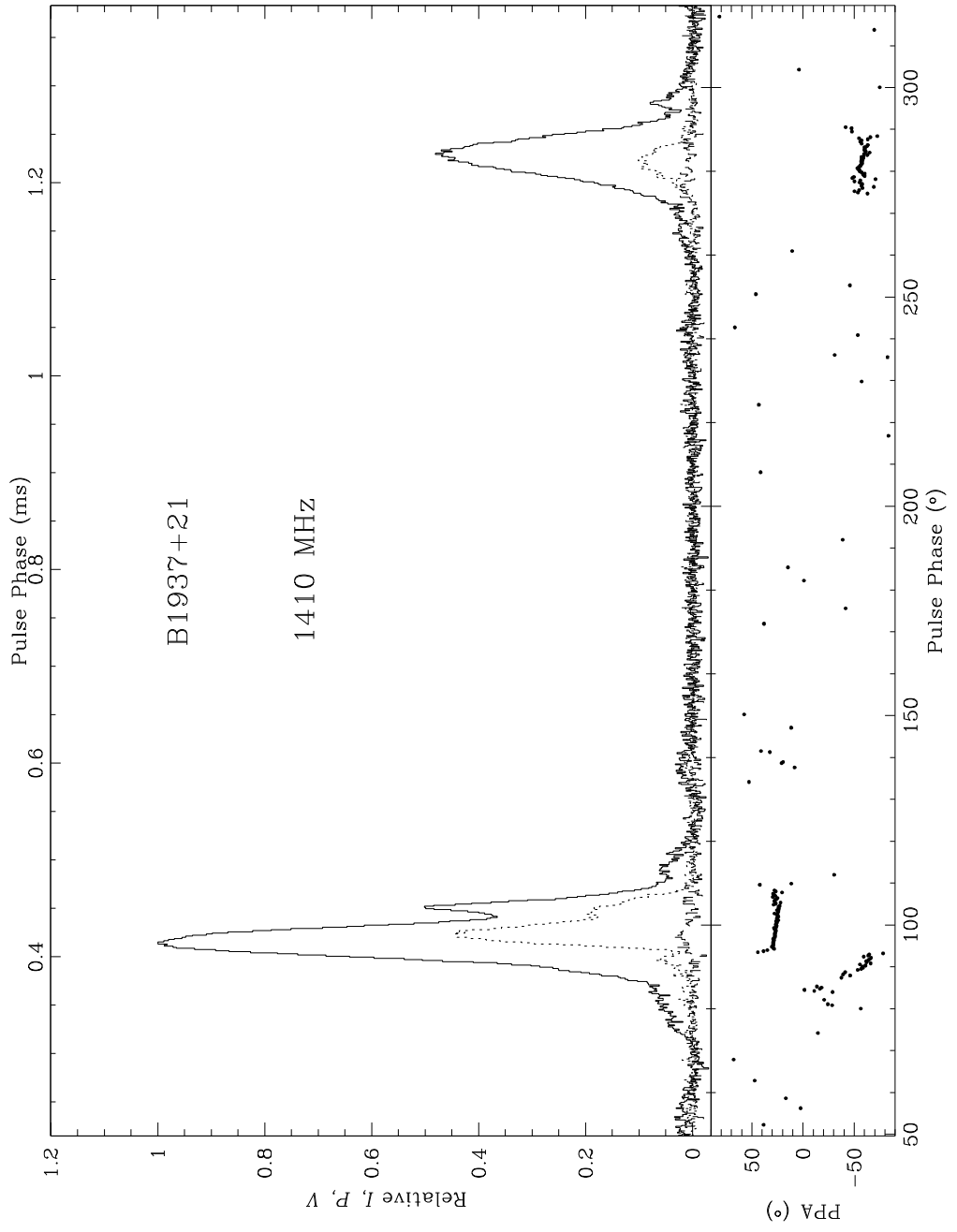

Fig. 3.26.— A region around the pulsed emission has been expanded in the 1410-MHz polarization profile of PSR B1937+21.

3.10 PSR J2145−0750

The profile of this 16-millisecond pulsar has been fit with up to 6 components at 1410 MHz (Kramer *et al.* 1998). The main pulse has two main components (1,2), separated by about 70 degrees at all frequencies. A precursor (4) precedes the main peak by 60 degrees, although it is not visible in the 1410-MHz profile shown here. This is consistent with its occasional disappearance in the observations of Xilouris *et al.* (1998). The trailing half of the pulse profile is less important at high frequencies, and is much reduced at 4.85 GHz (Kijak *et al.* 1997). The leading component of the main structure is much less dominant at 100 MHz (Kuzmin & Losovsky 1994). On the basis of published data, Xilouris (1998) concludes that the separation between the precursor and the leading edge of the MP is unchanged between 430, 800, and 1400/1700 MHz, consistent with the results presented here. The data suggest a slight increase in separation of the remaining components with increasing frequency, consistent with that seen by Kuzmin & Losovsky (1994), and contrary to the usual results for normal pulsars. At 1410 MHz, the intensity ratio of the trailing and leading profile components varies in shorter integrations, suggesting moding activity in this pulsar (Xilouris *et al.* 1998). The intensity ratio in our 1410-MHz profile matches that published there. At 820 MHz, the stronger daily averages all have a consistent component ratio, except for a single observation obtained in 1995 February. This profile is displayed in Figure 3.30. The intensity ratio of the two components may vary slightly at 575 MHz, with no significant variation in the accompanying polarization.

The profiles here are only weakly polarized. At 1410 MHz, the first main component is slightly polarized, with linear and circular polarization of order 5-10%, while the rest of the pulse is unpolarized. This same component is again about 10% polarized at 820 MHz and 575 MHz. The strong trailing component is slightly linearly polarized, with depolarization occurring at the orthogonal mode change in the PPA curve. The PPA curve itself is quite complex, but is consistent with frequency. It is most clearly defined in the 820-MHz data, where the displayed profile was accumulated in less than an hour, in a period of extreme amplification due to interstellar scintillation. The orthogonal mode change associated with the trailing portion of the profile is accompanied by reduced linear polarization. A decrease in linear polarization associated with the sharp sweep in PPA under the main pulse suggests that this may be another orthogonal mode transition. The precursor shows significant polarization at these frequencies, and its PPA curve extrapolates to match that of the leading edge of the main pulse. At 820 MHz, the signal is sufficiently strong to determine that the precursor exhibits sense-reversing circular polarization. The

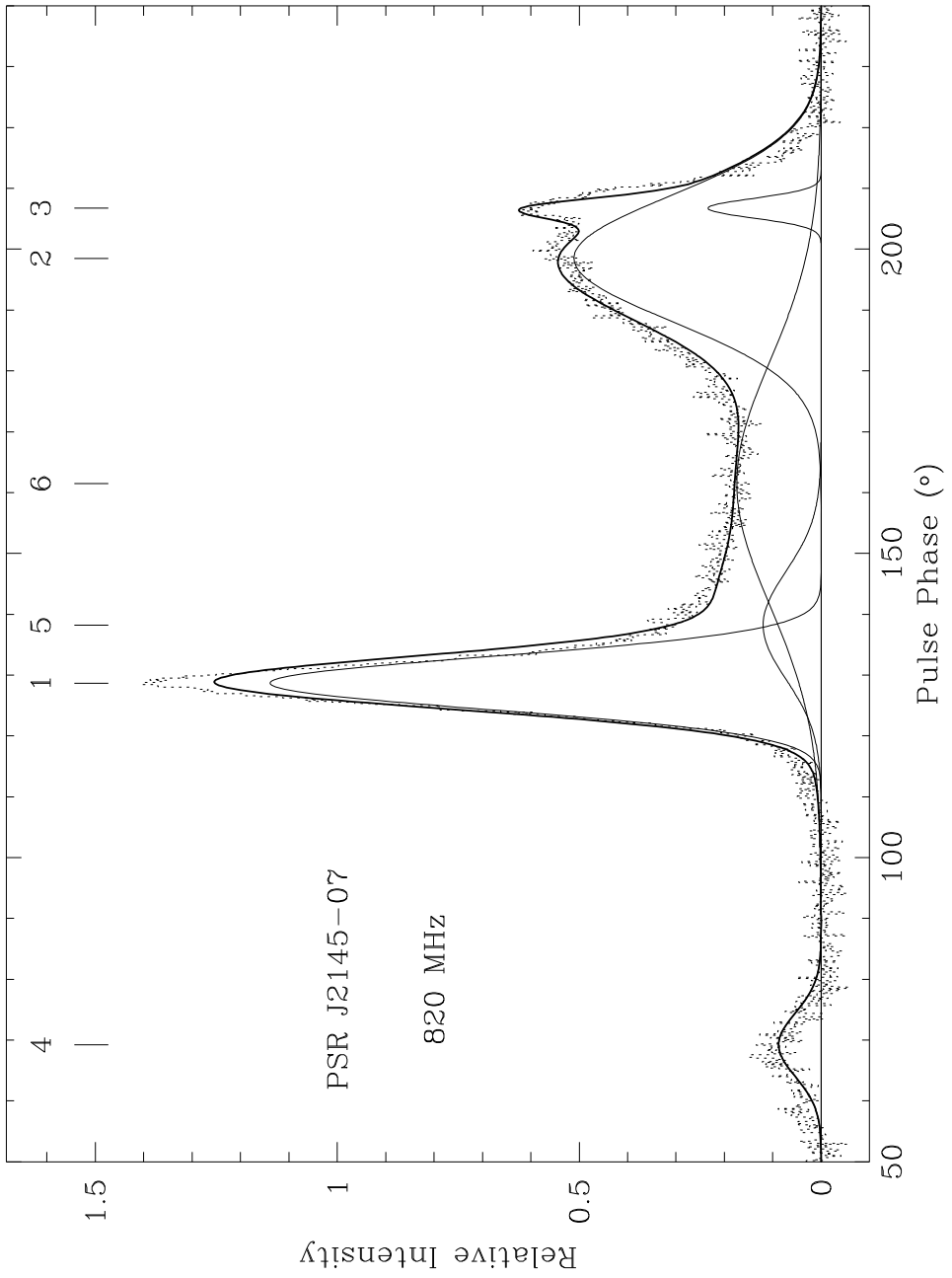

Fig. 3.27.— The Gaussian component decomposition for PSR J2145−0750 at 820 MHz is shown. See the caption of Figure 3.1 for details.

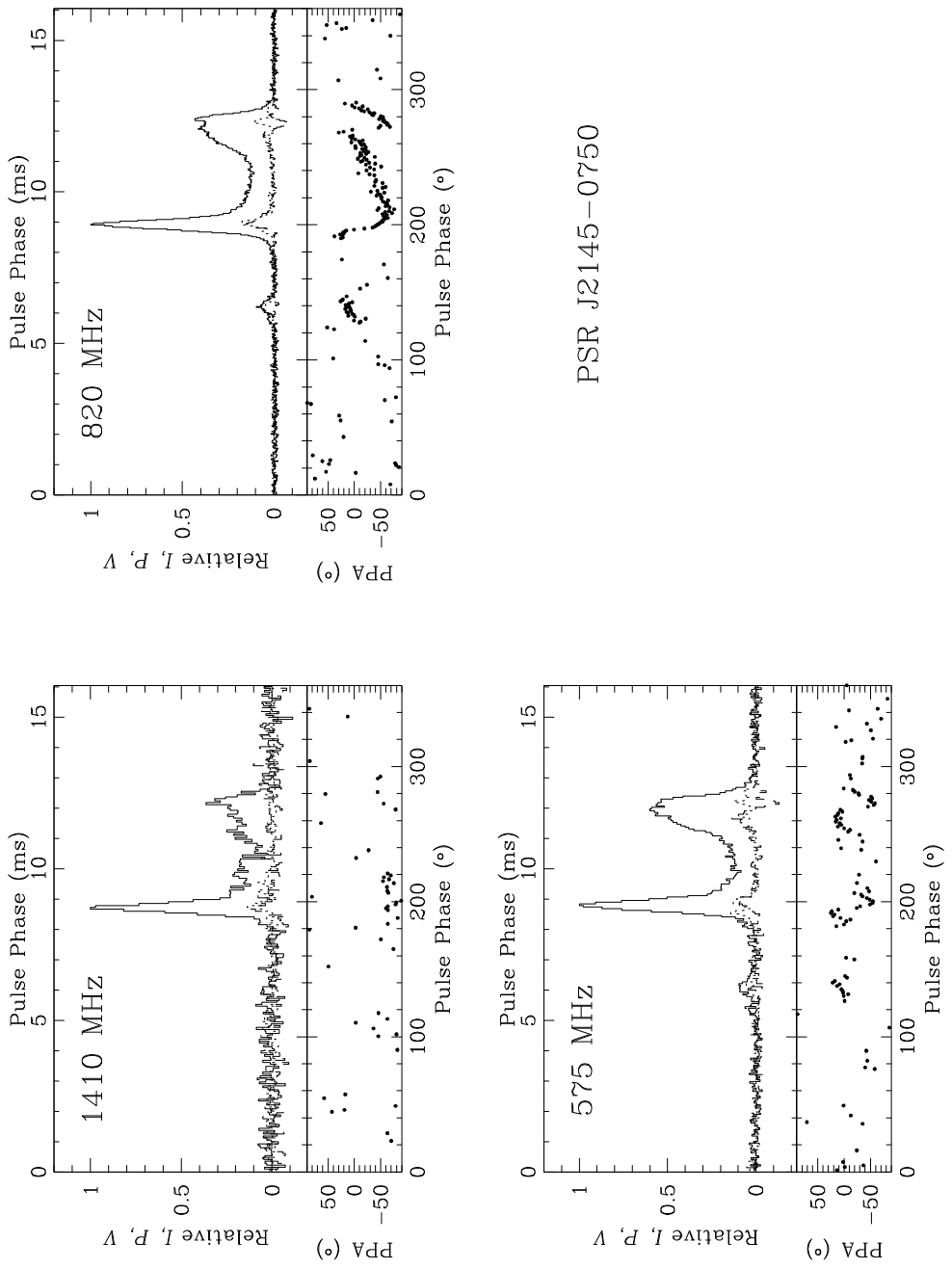

Fig. 3.28.— Polarization profiles of PSR J2145−0750 for three radio frequencies. See the caption of Figure 3.2 for details.

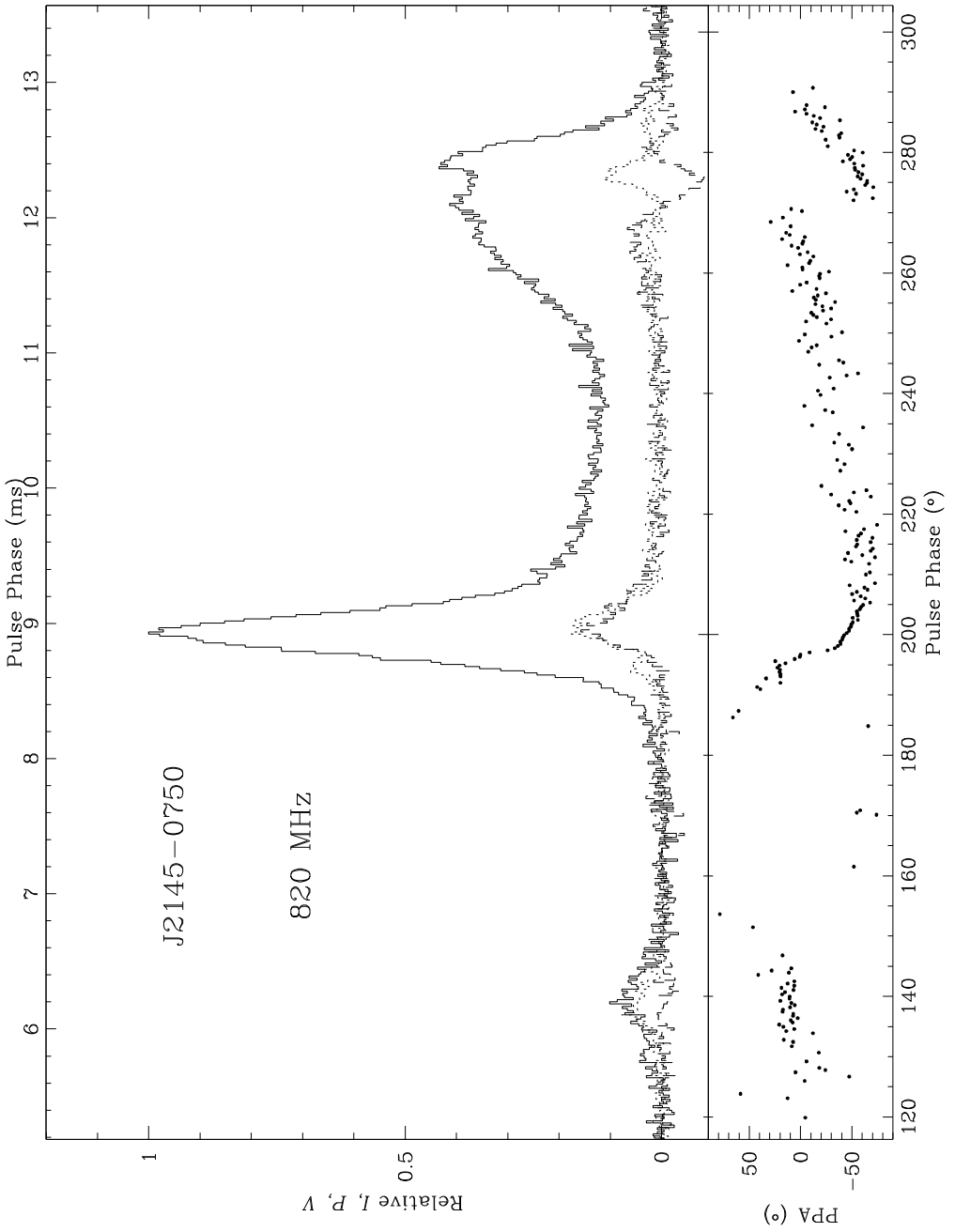

Fig. 3.29.— A region around the pulsed emission has been expanded in the 820-MHz polarization profile of PSR J2145−0750. The resolution of this profile is 16.0 μs.

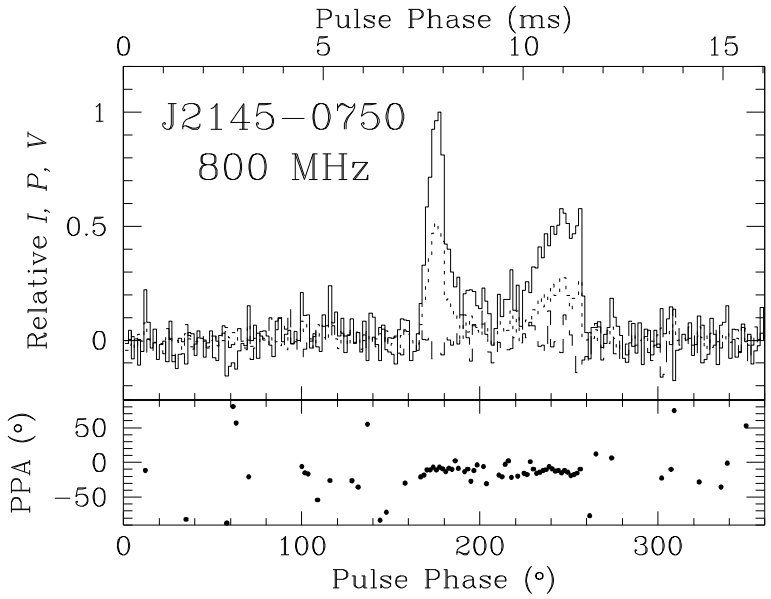

Fig. 3.30.— Polarization profile of PSR J2145−0750 at 800 MHz. This polarization profile resembles that published at 1410 MHz by Xilouris *et al.* (1998). The rest of our data is similar to that in Figure 3.28. The amplitude ratio of the trailing and leading halves of this profile is also different from that seen in the remainder of our data. See the caption of Figure 3.2 for details.

trailing component shows sense-reversing circular polarization of a few percent, while the leading main component is about 10% circularly polarized.

This PPA curve is not like that of Xilouris *et al.* (1998). The published 1410-MHz profile is significantly linearly polarized ($\sim$ 45%), with circular polarization (-18%) mirroring the linear polarization. In two days of observations at widely spaced epochs at 1410 MHz, five days of observations at 575 MHz, and 13 days of observations over four epochs near 800 MHz, only one profile exhibits polarization results similar to the published 1410-MHz data. That 800-MHz profile, obtained in 1995 February, is precisely the one for which a different intensity ratio between the two main components was found (cf. Figure 3.30). This suggests that the intensity and polarization moding are related. Although the circular polarization is still weak, the linear polarization is about 50% and the PPA curve is extremely flat. Other profiles obtained in the same observing epoch are similar to that displayed in Figure 3.28. For this pulsar, not only does the polarized fraction vary, but the PPA curve undergoes a radical transformation at the same time.

3.11 1410-MHz Polarization Profiles

Polarization profiles were obtained for several pulsars at 1410 MHz, for which no usable information was obtained at other radio frequencies. These are presented in Figures 3.31-3.32 for completeness.

3.11.1 PSR J0751+1807

The profile of this pulsar is relatively symmetric at 1410 MHz. The polarization results are similar to those presented by Xilouris *et al.* (1998), who found that the linearly polarized fraction of the leading component fluctuated, along with its associated PPA. The profile shape, and polarization properties of the trailing component remained stable.

3.11.2 PSR 1518+4904

This double-peaked profile has a post-cursor which follows the main pulse by about 25° (Kramer *et al.* 1998). Although the linear and circular polarized fractions are similar, the polarization properties displayed here do not match those of Xilouris *et al.* (1998). The linear polarization is significant here only in the leading portion of the pulse, as opposed to the trailing edge of the profile in that work. The SNR of this profile is too weak to meaningfully compare the PPA results.

3.11.3 PSR 1640+2224

Only a small amount of polarization is present here, whereas Xilouris *et al.* (1998) present a highly polarized profile, with no mention of variations.

3.11.4 PSR 1643−1224

This profile is once again much less polarized than the profile presented by Xilouris *et al.* (1998), although the PPAs are similar. An orthogonal mode is apparently present near the center of the pulse, accompanied by linear depolarization, and a reversal in the sense of the weak circular polarization. This, along with the pulse morphology, suggests that this is a core component with conal outriders.

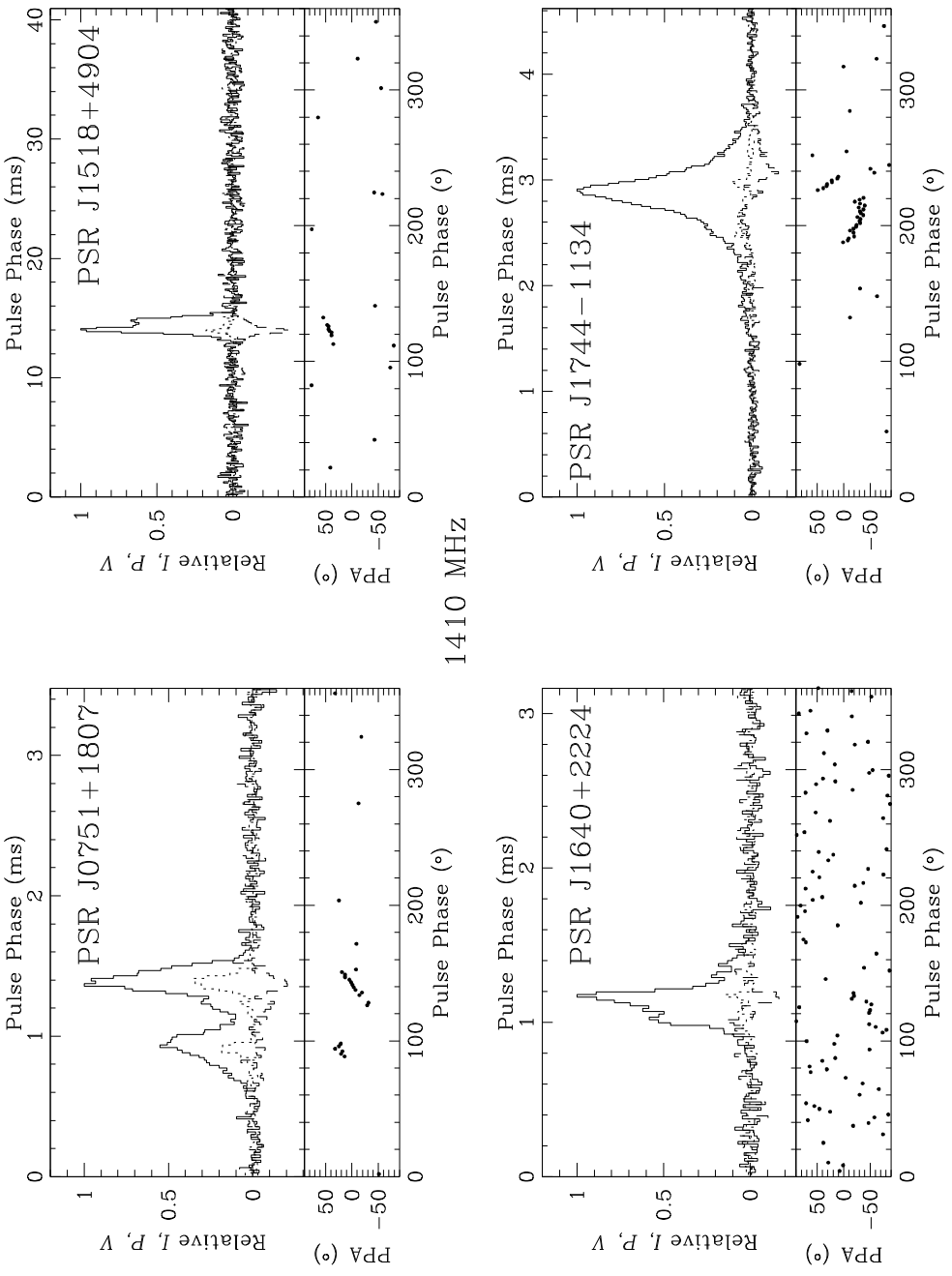

Fig. 3.31.— Polarization profiles of PSRs J0751+1807, J1518+4904, J1640+2224 , and J1643−1224at 1410 MHz. See caption of Figure 3.2 for details.

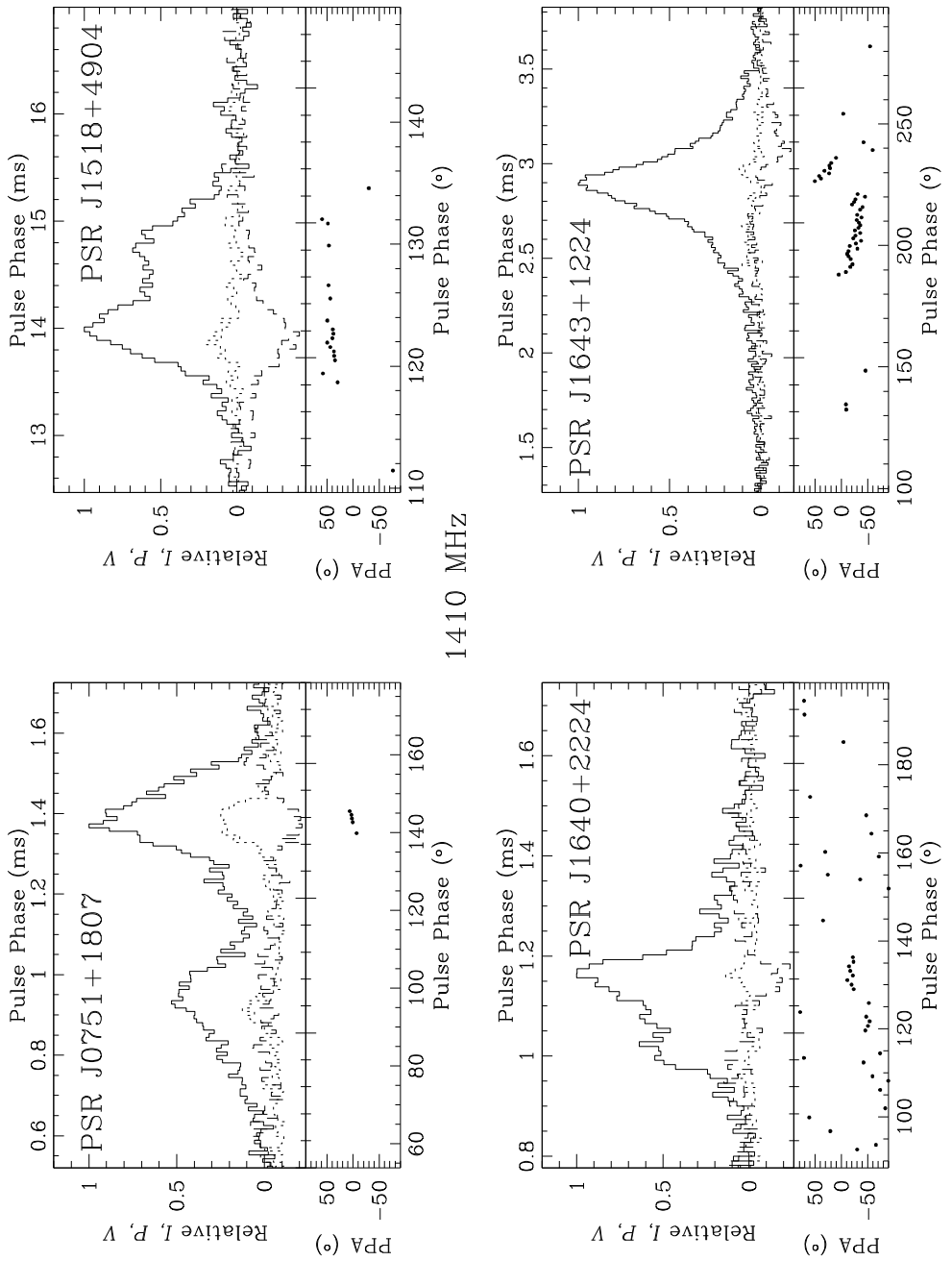

Fig. 3.32.— A region surrounding the pulsed emission has been expanded for the polarization profiles of PSRs J0751+1807, J1518+4904, J1640+2224 , and J1643−1224at 1410 MHz. See caption of Figure 3.2 for details. The resolutions of the four profiles are 9.1 μs, 41.1μs, 13.7 μs and 9.1 μs.

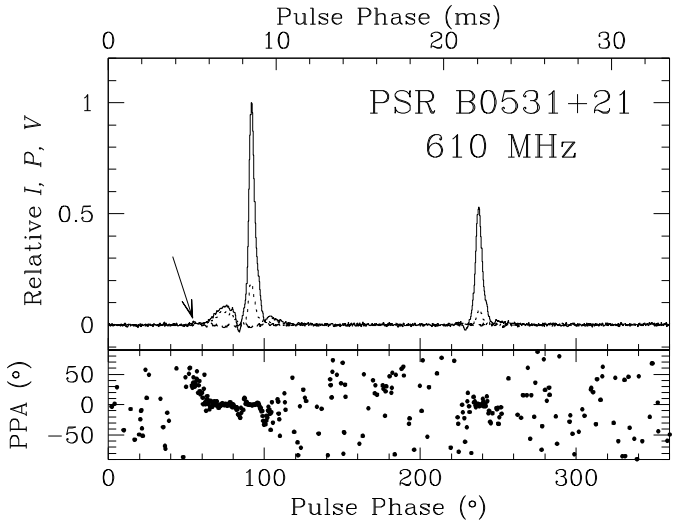

Fig. 3.33.— A polarization profile of PSR B0531+21 at 610 MHz is displayed for 34.75 hours of data. The the relative intensity, linear, and circular polarizations are plotted against pulse phase using solid, dotted, and dashed lines, respectively. The bottom axis indicates the pulse phase in degrees, while the top axis displays the same quantity in milliseconds. The polarization position angle (PPA) is plotted for phases where the linear polarization exceeds the off-pulse *rms*. The resolution of the plot is 34.1 μs. The arrow points to the position of the low frequency component (LFC) detected by Moffett & Hankins (1996).

3.12 PSR B0531+21 at 610 MHz

The 610-MHz high resolution profile of the Crab pulsar shown in Figure 3.33 is consistent with multifrequency profiles from Moffett & Hankins (1996). These data show the presence of the low frequency component (LFC) which they see above 600 MHz, just before the precursor. The polarization profile indicates that the precursor is highly polarized, while the main pulse (MP) and interpulse (IP) are $\sim$ 20% polarized. No significant circular polarization is seen. The position angle curve has a series of relatively flat (slightly downward) trends across each of the three largest components. The excursions from a slow linear trend in the MP and IP are due to artifacts in the profile are caused by the GBPP's use of a dedispersion filter with a slightly incorrect length. Note that the LFC has a much sharper trend in position angle. The MP, IP, and precursor properties are similar at lower frequencies (Campbell, Heiles & Rankin 1970, Manchester 1971, Manchester, Huguenin & Taylor 1972). At frequencies above 1400 MHz, the precursor is no longer visible, but the main pulse and interpulse polarization properties remain similar to those shown here (Manchester 1971, Moffett 1997). Moffett (1997) finds that at 1400 MHz, the LFC is about 40% polarized, and the main pulse shows weak sense-reversing circular polarization. The PPA is similar

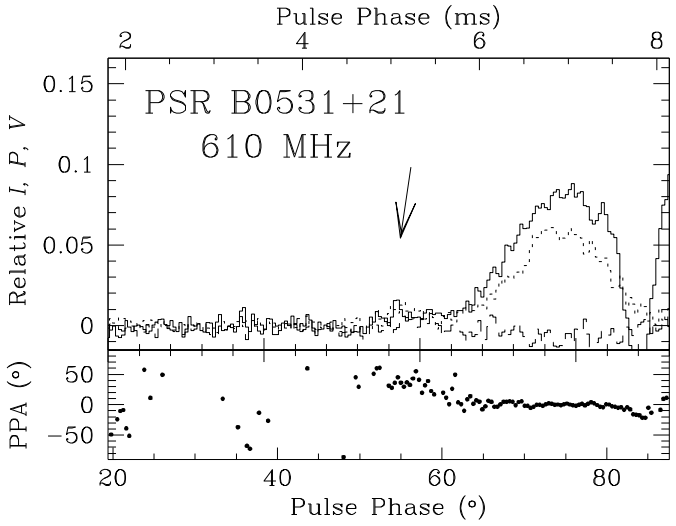

Fig. 3.34.— The region near the LFC and precursor are expanded in this plot of the 610-MHz polarization profile of PSR B0531+21.

to that displayed here. At still higher frequencies, the pulse morphology changes dramatically (Moffett 1997).

Chapter 4

Polarization Analysis of Millisecond Pulsars

4.1 Pulsar Geometry

The polarization data presented in Chapter 3 indicate that the polarization position angle (PPA) curve remains approximately the same for all radio frequencies. The rotating vector model discussed in Section 1.4 can therefore, in principle, be used in conjunction with the PPA results to determine the geometry for these millisecond pulsars. This is not straightforward, due to the presence of orthogonal modes, the limited longitude range of the PPA data, and the fact that the effect of magnetic inclination α on the PPA curve can be quite subtle. Investigation of the evolution of the intensity profile with frequency sometimes allows the pulse components to be classified as core or cone, which can help to constrain the emission geometry.

The intrinsic distribution of magnetic inclinations α is uniform for slow pulsars, as noted in Section 1.4. This may not necessarily be true for millisecond pulsars. Observations of binary pulsars offer other clues to the geometry. The spin and orbit angular momentum axes are expected to be aligned, due to the evolutionary spin-up of these objects via mass accretion. The mass function

$$f(M_c) = \frac{(M_c \sin i)^3}{(M_{NS} + M_c)^2} = \frac{4\pi^2 (a \sin i)^3}{G P_{orb}^2} \tag{4.1}$$

relates the companion mass M_c to the orbital period P_{orb} and projected semi-major axis $a \sin i$, where the inclination i of the orbit is unknown. A calculation of the minimum companion mass compatible with the observations is therefore possible. Backer (1998) discussed the population of rapidly rotating pulsars with Helium white dwarf companions, and concluded that the observed distribution of minimum companion masses required non-random inclinations. One possible explanation is that the magnetic and spin axes are preferentially orthogonal, so we see only binary systems with

$i = \alpha \sim 90°$. Chen & Ruderman (1993a) predict an unusual magnetic field topology for these objects that results in a preference for inclinations of 90°. If the pulsars in this class are all nearly orthogonal, then it is possible that this geometry extends to other millisecond pulsars as well. This hypothesis would predict that almost all millisecond pulsars would exhibit a pulse-interpulse morphology, if radio emission occurs within the broad beam at *both* magnetic poles. Several objects do not have interpulse components in their pulse profiles.

A theoretical relation between white dwarf mass and orbital period can also be used to constrain values of α. Rappaport *et al.* (1995) discuss the theoretical evolution of binary stars leading to pulsar systems with low-mass white dwarf companions in nearly circular orbits, and orbital periods in excess of one day. These evolutionary calculations lead to the expectation that the orbital period and white dwarf mass are related. If their model is correct, then this relation can be combined with the mass function to give the inclination $i = \alpha$ of the system, again with the assumption that the orbital and spin angular momentum axes are aligned. This value of α can then be used to constrain the rotating vector model fits to the PPA data. In general, the relation yields $i = \alpha \neq 90°$.

4.2 PPA Fits

The multifrequency polarization position angle data presented in Chapter 3 were fit to a rotating vector model (equation 1.4) at each individual radio frequency. The fit included the geometric parameters α and β, as well as pulse longitude and PPA offsets. Any apparent orthogonal mode transitions were removed prior to the fit. In order to reduce the sensitivity of the fit to the region in pulse phase immediately surrounding an orthogonal mode transition, the PPAs were weighted by the SNR of the linear polarization, which decreases during an orthogonal mode transition. This also prevented the fit from becoming biased by the random PPAs between pulse components. For fixed α, the other parameters were varied until a satisfactory fit was obtained. Various values of α were used, and the results compared. In some cases, the location of the center of symmetry for the rotating vector model was poorly constrained, and was held fixed at a particular pulse longitude. Values of magnetic inclination $90° < \alpha < 180°$ and impact parameter β relative to the rotation axis are equivalent to a measurement of $\alpha' = 180° - \alpha$, $\beta' = -\beta$ relative to the opposite rotation axis. For comparison to the predictions based on orbital inclinations, α' should be used. The PPA data are measured counter-clockwise from north on the plane of the sky, contrary to the suggestion of Arzoumanian *et al.* (1996). This failure to flip the sign of the PPA data so that they are measured clockwise changes none of

the geometrical conclusions, but simply moves the magnetic axis from the proximity of one rotational pole to the other.

The intensity data for each pulsar are presented once again, this time in the form of a log-polar diagram, for the purpose of investigating the structure of the emission beam. In these diagrams, first used by Hankins & Fowler (1986), the relative intensity is plotted (on a logarithmic scale) in polar coordinates, using the pulse phase as the angle. The geometrical radiation pattern of the pulsar is immediately apparent. An example is Figure 4.1. Dotted circles represent the level of maximum emission, 10% emission, and (when shown) 1% emission. The radiation pattern rotates clockwise with respect to a fixed observer to reproduce the polarization profile vs. pulse longitude plots displayed in Chapter 3 (cf. Figure 3.2). The PPA data and accompanying fits are plotted on an enlarged scale for each pulsar, as is shown for PSR J0613−0200 in Figure 4.2. The smoothed polarization profile is located at the top of each plot for reference purposes. The polarization position angle is duplicated and plotted over the range −180 to 180° for clarity. Rotating vector model fits are represented by smooth lines through the data. A legend accompanies each plot.

Table 4.1 lists the derived fit parameters α, β and the maximum slope $(d\psi/d\phi)_{max}$ for each pulsar. Any temporal variations in the intensity or polarization profile are also noted here.

Pulsar Geometries and Moding Behaviour

Source	α (°)	β (°)	$\frac{(d\psi)}{(d\phi)_{max}}$ (°/°)	$\frac{(d\psi)}{(d\phi)_{xil}}$ (°/°)	Profile Variation	Polarization Variation	Comments
			Multifrequency Data				
J0613−0200	–	~ -10	-2.4	–		p	
J1012+5307	40	11	3.5	-2.7		y	
J1022+1001	60	6	9	6	y	y	well-defined PPA
B1620−26	–	–	2.6	-1.5		p	
J1713+0747	105	-18	-3.	-1.7		y	
J1730−2304	–	–	-1.	2.2	x	x	
B1821−24	50	40	1.2	–	y	y	outer-gap emission?
B1937+21	–	–	-.8	–			Crab-like
J2145−0750	90	16	3.6	-.65	y	y	complex PPA
			1410-MHz Data				
J0751+1807	–	–	–	–		x	
J1518+4904	–	–	–	–		p	
J1640+2224	–	–	–	–		p	
J1643−1224	–	–	–	–		p	
			Xilouris *et al.* (1998)				
B1855+09	–	–	–	–		x	
B1953+29	–	–	–	–	?	x	

Table 4.1: Information on the pulsar's geometry and moding behaviour are summarized for our multifrequency observations. The magnetic inclination α and impact parameter β given in columns 2 and 3 are given whenever our fitting procedure yielded a preferred result. They are not necessarily well-determined. The maximum slopes $(d\psi/d\phi)_{max}$ tabulated in column 4 are derived from these and other fits, or estimated from the data when a fit was unavailable. The values quoted by Xilouris *et al.* (1998) are quoted in column 5 for comparison. The main thing to note is the fact that the slopes are relatively flat for all objects, even when the detailed models are different. Columns 6 and 7 describe the presence of profile and polarization variations, respectively: y-seen in our data, p-possibly seen in comparison with data of Xilouris *et al.* (1998), x-Xilouris *et al.* (1998) report variations. These are also reported for the objects for which we have only 1410-MHz observations. Two other objects exhibiting temporal variations in the dataset of Xilouris *et al.* (1998) are also included.

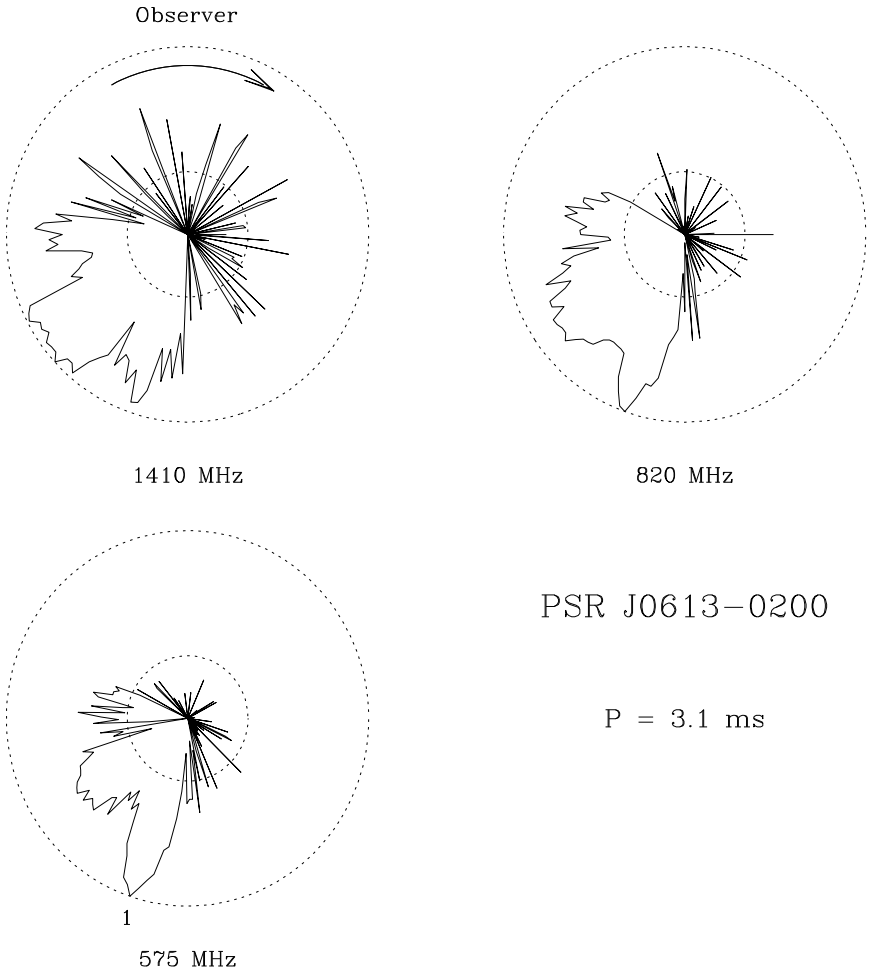

Fig. 4.1.— The relative intensity of PSR J0613−0200 is presented at each radio frequency in a log-polar plot. The intensity, on a logarithmic scale, is presented (solid lines) in polar coordinates, using pulse phase as the angle. The dotted circles represent the levels of maximum emission and 10% of this value. Component 1 in the fits of Chapter 3 is identified in the 575-MHz data.

4.2.1 PSR J0613−0200

This 3.06 millisecond pulsar has a binary companion with mass $0.13 M_{\odot} / \sin i$ (Lorimer *et al.* 1995a) in a 28.8 hour orbit. This object is one of the pulsars which Backer (1998) considered in concluding that the inclinations were not random. Equation 4.1 predicts an inclination of 66°, although the orbital period is at the lower end of the range for which their model is valid, and the relationship is more uncertain there (Rappaport *et al.* 1995).

Based on the spectral and polarization behaviour of the components, we would expect the trailing sharp feature (component 1 in Figure 4.1) to be identified as a core component. The substantial offset of this component from the symmetry center of the pulse is not at all in line with this interpretation.

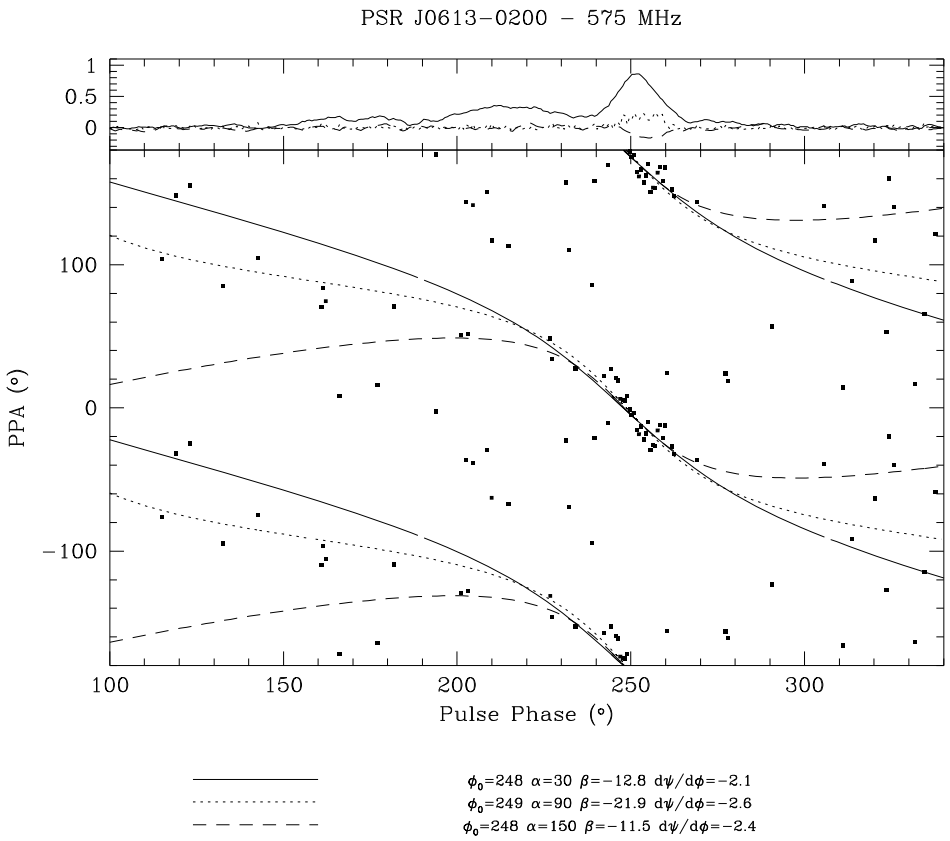

Fig. 4.2.— Rotating vector models are fit to the PPA data of PSR J0613−0200 at 575 MHz. The data (filled squares) are plotted against pulse longitude (°) for pulse phases where the linear polarization exceeds the off-pulse *rms*. Three different rotating vector models are shown, corresponding to $\alpha = 30, 60, 90°$. The legend below the figure identifies each curve with the parameters of the associated model. The phase offset ϕ_0, magnetic inclination α, impact parameter β, and maximum slope $d\psi/d\phi$ are quoted in degrees, or °/deg. The data do not significantly constrain the geometry of the system. The smoothed polarization profile is displayed at the top of the figure for reference purposes (I, P, V=solid, dotted, and dashed lines, respectively).

The fits to the polarization position angle data do not significantly constrain the geometry, due to the very narrow range of longitudes exhibiting significant linear polarization. Figure 4.2 displays the PPA data at 575 MHz, in conjunction with a variety of rotating vector model fits. The inclination α is not significantly constrained by the data, although formal χ^2 considerations favour an aligned geometry. In the fits presented in Figure 4.2, the center of symmetry of the PPA curve is located near the center of the available PPA data (at the leading edge of the sharp trailing component). This provides a lower limit on the absolute value of the maximum slope $(d\psi/d\phi)_{max} \sim -2.4 \pm 0.2$. If the symmetry center of the PPA data is not at the

center of the data, then the data do not lie along the portion of the curve with maximum slope. The relativistic correction to the rotating vector model (Blaskiewicz *et al.* 1991) predicts that the symmetry center of the PPA curve will be delayed relative to the symmetry center of the pulse intensity profile, while for emission near the light cylinder, the magnetic field configuration predicts that it will precede the center of the total intensity (Barnard 1986). The narrow range in longitude of the PPA data, combined with the unusual pulse profile, makes confirmation or exclusion of either effect impossible. The 820-MHz and 1410-MHz PPA data provide no further useful information.

For slow pulsars, the width of core components is proportional to $P^{-1/2}/\sin\alpha$ (Rankin 1990). The width of the broad central component in this pulsar is more or less consistent with the expected value at this spin period, for $\alpha \sim 90°$. The other components are all narrower than the predicted core width. A similar relationship is true for the separations of conal components in slow pulsars. Extrapolation to 3 milliseconds yields the expectation that the inner and outer cones should have diameters of $\sim 160°/\sin\alpha$ and $\sim 210°/\sin\alpha$, respectively. If the outer components in this profile are a conal pair, then the observed separation requires (to be consistent with this relationship), $\alpha \sim 35°$ for the inner cone, or 25° for the outer cone. These values are consistent with the aligned geometry which is slightly preferred in the fits to the PPA data. Caution should, however, be exercised when extending the relationship for conal separations to periods where the conal diameter is $> 180°$

4.2.2 PSR J1012+5309

This millisecond pulsar has a binary companion with an orbital period of 14.5 hours. The mass function gives an estimate of $M_c = 0.11 M_\odot/\sin i$ for a neutron star mass of $1.4 M_\odot$ (Nicastro *et al.* 1995). Based on optical observations, the white dwarf mass is $0.16 \pm 0.02 M_\odot$ (van Kerkwijk *et al.* 1996), which gives an inclination of $i = \alpha \sim 45°$. The ratio of masses M_{NS}/M_c is also constrained by these observations, however, and this provides a somewhat different estimate of $\alpha \sim 65°$, since the resulting formal value for the neutron star mass is above $2M_\odot$. The uncertainties in M_c and the mass ratio are such that at the 95% confidence limit the inclination is $50 \lesssim \alpha \lesssim 90°$. This is consistent with the suggestion of Backer (1998) that objects in this class are orthogonal rotators. The white dwarf mass-orbital period relationship of Rappaport *et al.* (1995) is invalid for orbital periods less than a day, such as this one.

Few clues to the geometry are available based on the frequency evolution of the pulse profile. Figure 4.3 highlights the relevant features. The MP and IPb are separated by close to 180°, indicating a possible pulse-interpulse morphology, but the

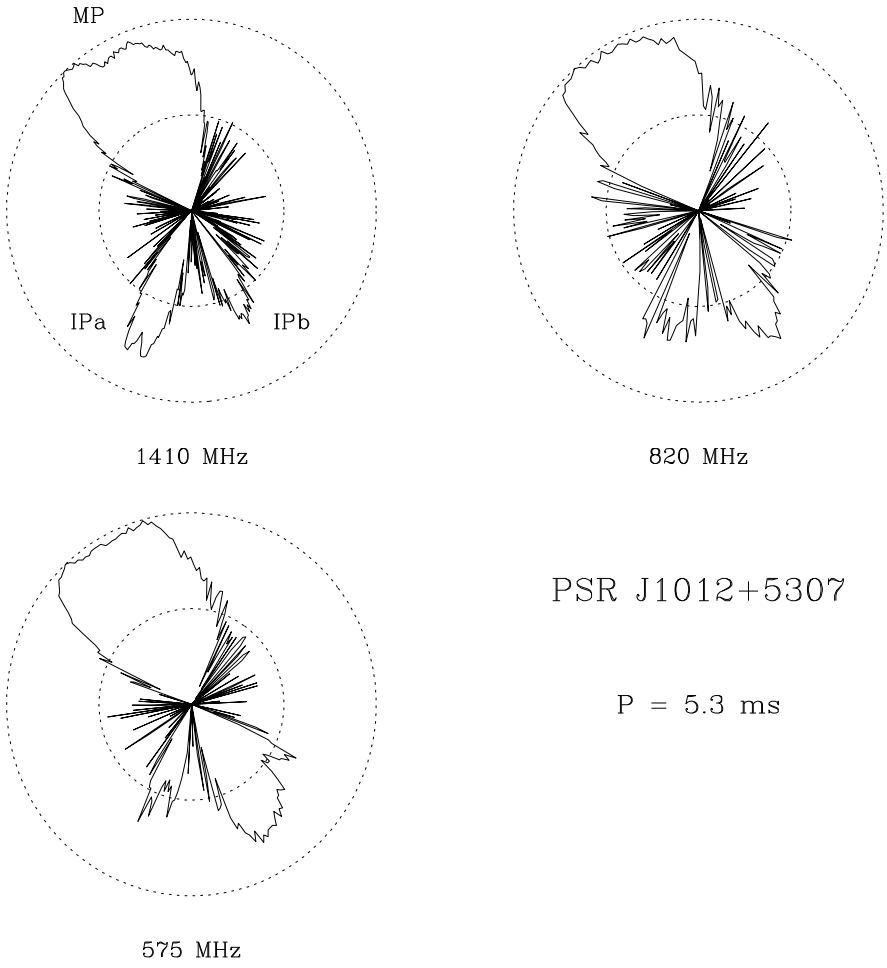

Fig. 4.3.— The relative intensity of PSR J1012+5307 is presented at each radio frequency in a log-polar plot. The main pulse (MP) and IPb are separated by nearly 180°. Emission is present throughout a significant fraction of the pulse period. See the caption of Figure 4.1 for details.

large number of components indicates a possible aligned geometry. Sense-reversing circular is to some degree present under all three structures and cannot therefore be taken as an indication of a central core component. The frequency evolution of the profile does not fall into any standard classification.

Xilouris *et al.* (1998) fit a model of $\alpha \sim 88°$, $\beta \sim 5°$ to this pulsar at 1410 MHz, with the center of symmetry located between the main pulse and IPa. One of the fits displayed in Figure 4.4 (dotted line) represents a similar model. The 1410-MHz data provides the most severe constraints on the model, due to the low linear polarization of IPa at lower frequencies. A significantly better model can be obtained at all radio frequencies by rotating the PPA data for the interpulse structures by 90°, under the assumption that an unseen orthogonal mode transition is present. These data are represented by the open squares in Figure 4.4. A fit for $\alpha = 40°$, $\beta \sim 11°$ provides

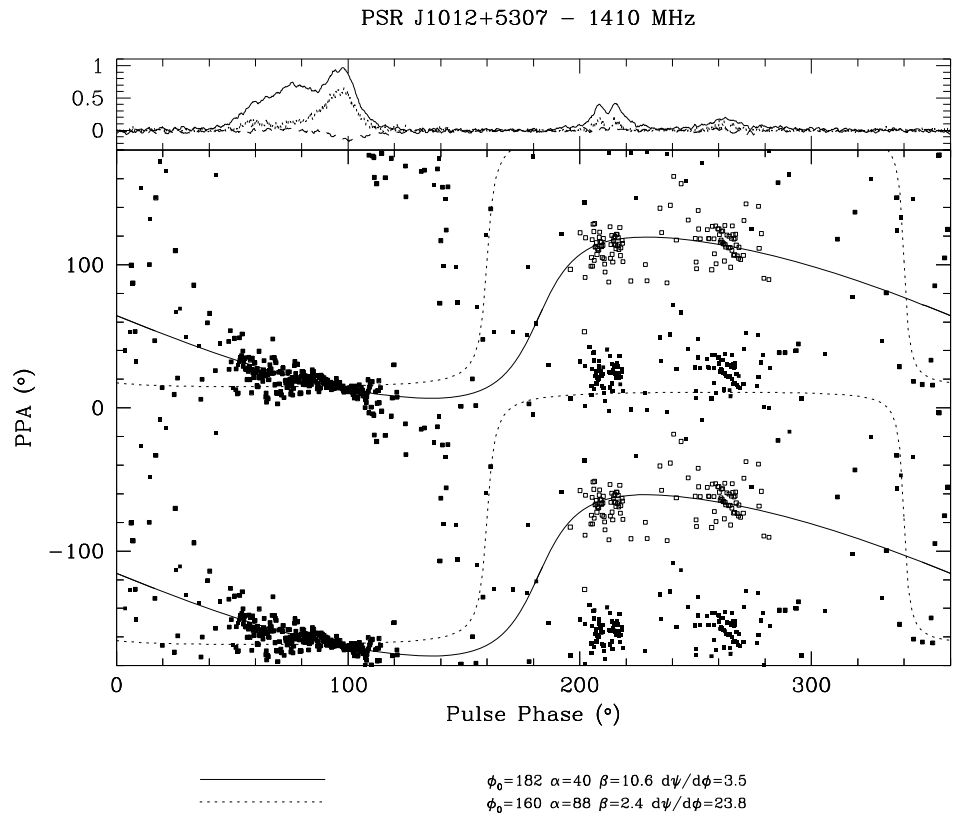

Fig. 4.4.— Rotating vector models are fit to the PPA data of PSR J1012+5307 at 1410 MHz. The data (filled squares) are plotted against pulse longitude (°) for pulse phases where the linear polarization exceeds the off-pulse *rms*. Two different models are shown. One model (dotted line) corresponds to an orthogonal rotator. For the second model (solid line), the data for the interpulse structures have1 been offset by 90° (open squares), under the assumption that an unidentified orthogonal mode is present. This model has $\alpha = 40°$, $\beta \sim 11°$. The smoothed polarization profile is displayed at the top of the figure for reference purposes (I, P, V=solid, dotted, and dashed lines, respectively).

a good fit to the data. The center of symmetry of the PPA curve lies approximately midway between the main pulse and IPb, indicating that this is perhaps a hollow cone system. The slope of the PPA curve at this point is $\sim 3.4°$/deg.

In either of these models, the maximum slope of the PPA curve $(d\psi/d\phi)_{max}$ occurs between the main pulse and IPa, and is significantly greater than the slope of the observed PPA data ($\sim -0.5°$/deg under the MP). The PPA data are difficult to explain using a model with the symmetry center under one of the components.

Based on Rankin's (1993) relation for slow pulsars, the inner and outer conal diameters are expected to be $W_i \sim 8.6° P^{-1/2}/\sin\alpha \sim 120°/\sin\alpha$ and $W_o \sim$

$11.5^\circ P^{-1/2}/\sin\alpha \sim 160^\circ/\sin\alpha$, if the emission occurs at a similar altitude. If both magnetic poles produce radio emission, then the large angular extent of the open-field line region in millisecond pulsars makes it difficult to determine which components originate at a given pole. This complicates the analysis of component separations in complex pulse profiles. Nonetheless, for $\alpha = 90^\circ$, the MP-IPa separation (components 1 to 5/6 in Figure 3.4) of $\sim 120^\circ$ is comparable to the full size of the inner cone. Similarly, the $\sim 165^\circ$ MP-IPb (components 1-4) separation is comparable to the full extent of the outer cone for an orthogonal rotator. The component separations are therefore consistent in the case of an orthogonal rotator. For $\alpha \sim 40^\circ$, as is true for the fit represented by a solid line in Figure 4.4, the IPa-MP separation of $\sim 360 - 120 = 240^\circ$ corresponds to a beam width of $\sim 160^\circ$, comparable to the full size of the outer cone, where we now consider that the components are actually coming from the pole 180° away. The IPb-MP separation is in this case $\sim 195^\circ$, corresponding to a beam size of $\sim 125^\circ$, comparable to the size of the inner cone. The IPb-component 2 separation is $\sim 175^\circ$, corresponding to a beam size of $\sim 110^\circ$, again consistent with the size of the inner cone. The conal beam size and rotating vector model geometry are therefore also consistent for $\alpha \sim 40^\circ$. Apart from the broad component 2, all components in this profile are narrower than the core-width relation for slow pulsars would predict.

A magnetic inclination $\alpha = 40^\circ$ lies outside the 95% confidence limits placed on the orbital inclination i by observations of the masses in the system. This discrepancy can be resolved if the orbital and angular momentum axes are not completely aligned. A fit for $\alpha = 50^\circ$ is somewhat compatible with our data, although the PPA offset between the MP and IPa cannot be matched perfectly. This could be explained if the presumed orthogonal mode change were not exactly 90°, as is seen in some slow pulsars.

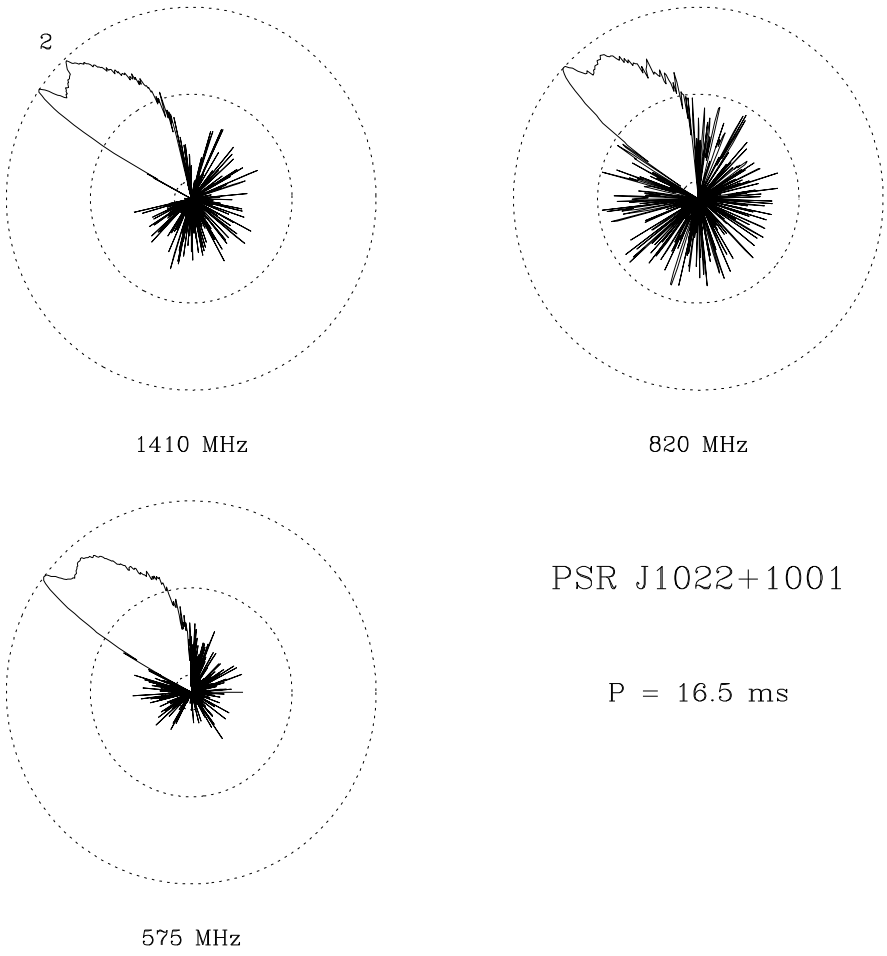

Fig. 4.5.— The relative intensity of PSR J1022+1001 is presented at each radio frequency in a log-polar plot. The intensity, on a logarithmic scale, is presented (solid lines) in polar coordinates, using pulse phase as the angle. Component 2 in the fits of Chapter 3 is identified in the 1410-MHz data. The dotted circles represent the levels of maximum emission, 10%, and 1% of this value.

4.2.3 PSR J1022+1001

This 16 millisecond pulsar has a companion with $M_c \sim 0.73 M_\odot / \sin i$ in a 7.8 day orbit (Camilo *et al.* 1996). This object was not included in the analysis of Backer (1998), due to the large companion mass. If the orthogonal rotator hypothesis applies to some millisecond pulsars, however, it may very well apply to all. The profile evolves very little with frequency (Figure 4.5), so few clues to the geometry are provided. Fortuitously, the PPA data for this pulsar are perhaps the most unambiguous in our data set. A clear sweep in polarization position angle is present across the pulse, although it is disturbed at all frequencies by an orthogonal mode change which occurs over a very narrow range in longitude.

Xilouris *et al.* (1998) found $\alpha \sim 53.2°$, $\beta \sim 7.3°$ at 1410 MHz. In the fits presented

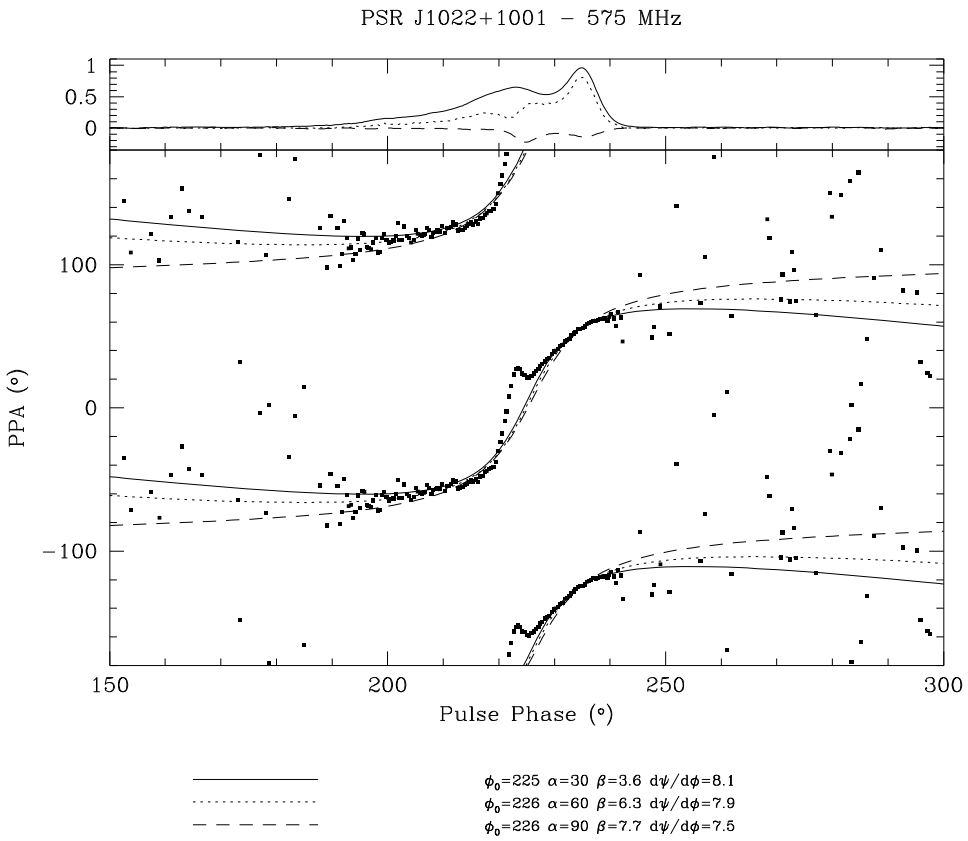

Fig. 4.6.— Rotating vector models are fit to the PPA data of PSR J1022+1001 at 575 MHz. The data (filled squares) are plotted against pulse longitude (°) for pulse phases where the linear polarization exceeds the off-pulse *rms*. A rapid orthogonal mode transition disturbs the data near the center. Models for three values of α are shown. Among those shown, the model with $\alpha = 60°$, $\beta \sim 6.3°$ is preferred. The smoothed polarization profile is displayed at the top of the figure for reference purposes (I, P, V=solid, dotted, and dashed lines, respectively).

here, no correction has been made for the presence of the orthogonal mode in the PPA data, under the assumption that the accompanying depolarization will sufficiently suppress the weight of these data. At 575 MHz, the depolarization accompanying the mode transition was not sufficient to suppress these PPA data relative to that in the leading portion of the profile, so more parameters were held fixed in the fit than was usual. The results of the 575-MHz fits are shown in Figure 4.6, for $\alpha = 30°, 60°$,and $90°$. In all cases, the maximum slope is $(d\psi/d\phi)_{max} \sim 8°$/deg, and the center of symmetry lies below component 2, which is near the symmetry center of the profile (cf. Figures 3.7 and 4.5). The model with $\alpha = 60°$, $\beta \sim 6°$ is preferred on the basis of the PPA data at the edges of the profile. At 1410 MHz, the leading edge of the profile suggests that larger α may be preferable (cf. Figure 4.7), while $\alpha = 60°$ is

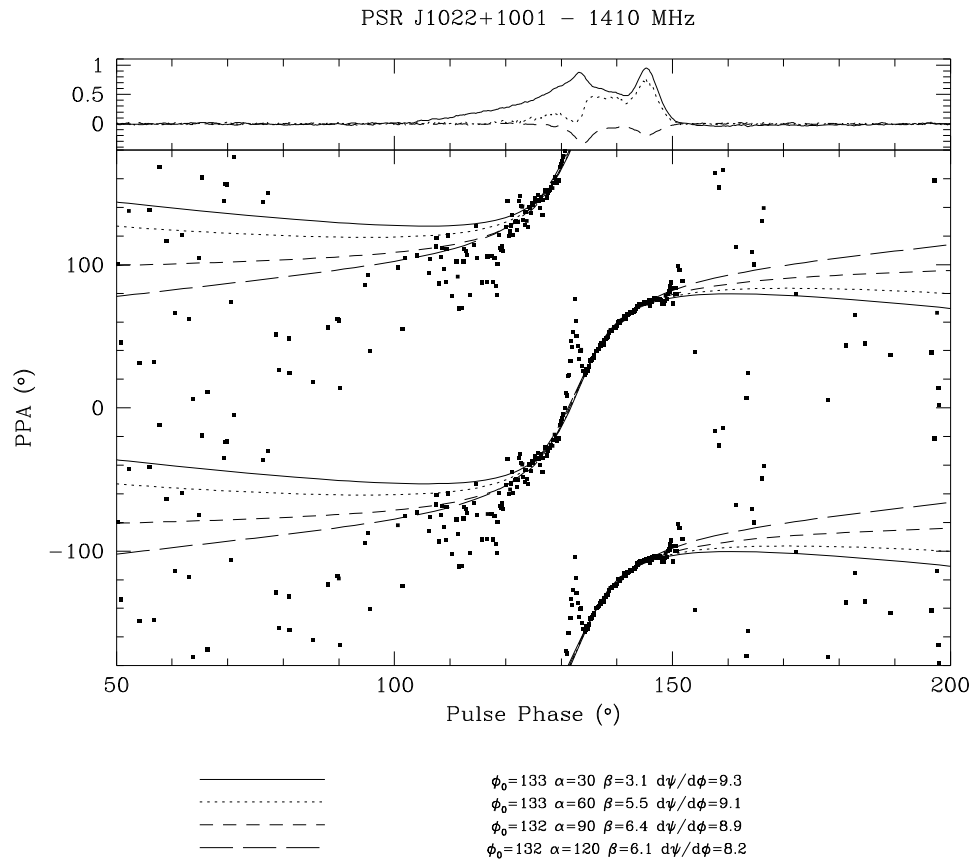

Fig. 4.7.— Rotating vector models are fit to the PPA data of PSR J1022+1001 at 1410 MHz. The data (filled squares) are plotted against pulse longitude (°) for pulse phases where the linear polarization exceeds the off-pulse *rms*. The orthogonal mode is once again clearly visible in the data. Models for four values of α are shown. The smoothed polarization profile is displayed at the top of the figure for reference purposes (I, P, V=solid, dotted, and dashed lines, respectively).

satisfactory on the trailing edge. However, this is less true for the PPA data if no correction for instrumental cross-coupling ($\sigma \neq 0$) has been done. The contradictory result is likely due to the non-linear effects of an error in our correction for σ, as the linear polarization is extremely small in this section of the pulse profile (cf. Section 2.5). The maximum slope in this case is $\sim 9°$. The 820-MHz data do not significantly constrain our results.

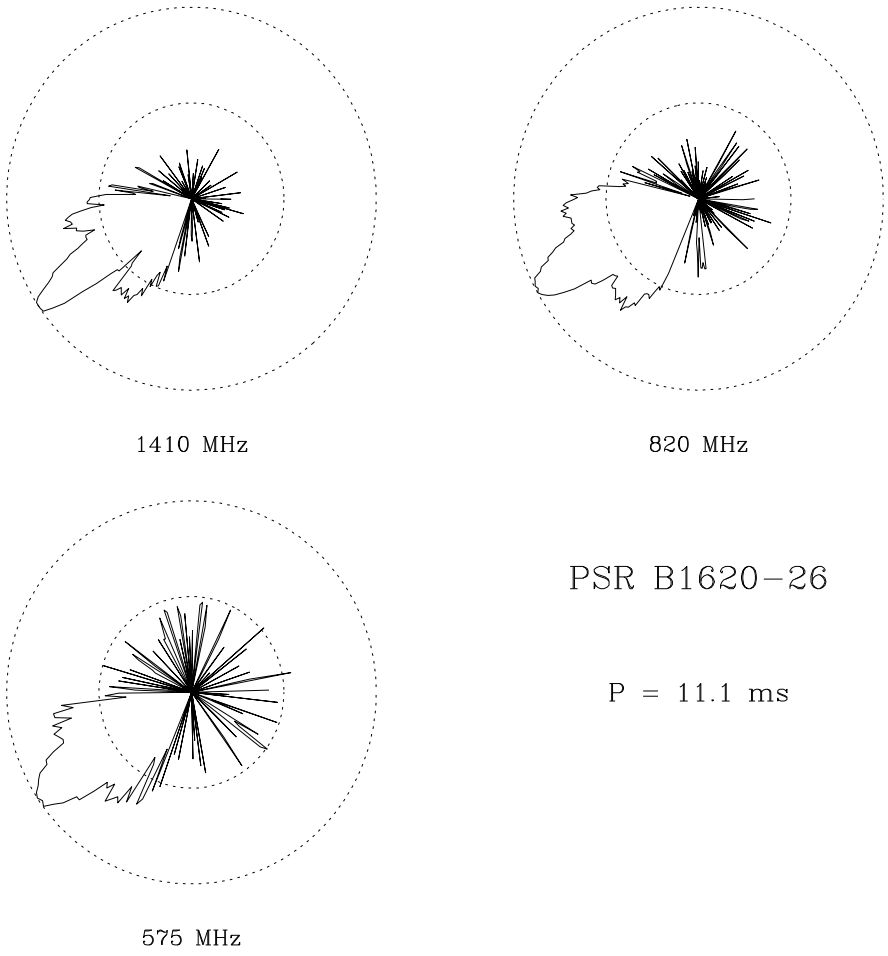

Fig. 4.8.— The relative intensity of PSR B1620−26 is presented at each radio frequency in a log-polar plot. See caption of Figure 4.1 for details.

4.2.4 PSR B1620−26

This pulsar, located in the globular cluster M4 (Lyne *et al.* 1988) has a 0.3 $M_\odot/\sin i$ companion in a 191 day orbit, plus a second companion in a wide outer orbit (Backer, Foster & Sallmen 1993). The orbital period-companion mass relation predicts an inclination $i = \alpha \sim 45°$ for alignment of the orbital and spin angular momentum axes. This relation may not apply in this case, however, since the history of the binary system may be significantly influenced by encounters with other stars in the globular cluster.

The profile resembles a triple profile consisting of a core component with conal outriders, but the core component is stronger at higher frequencies, contrary to expectations (see Figure 4.8). This component is also somewhat narrower than that expected on the basis of the width-period relationship from slow pulsars. On the

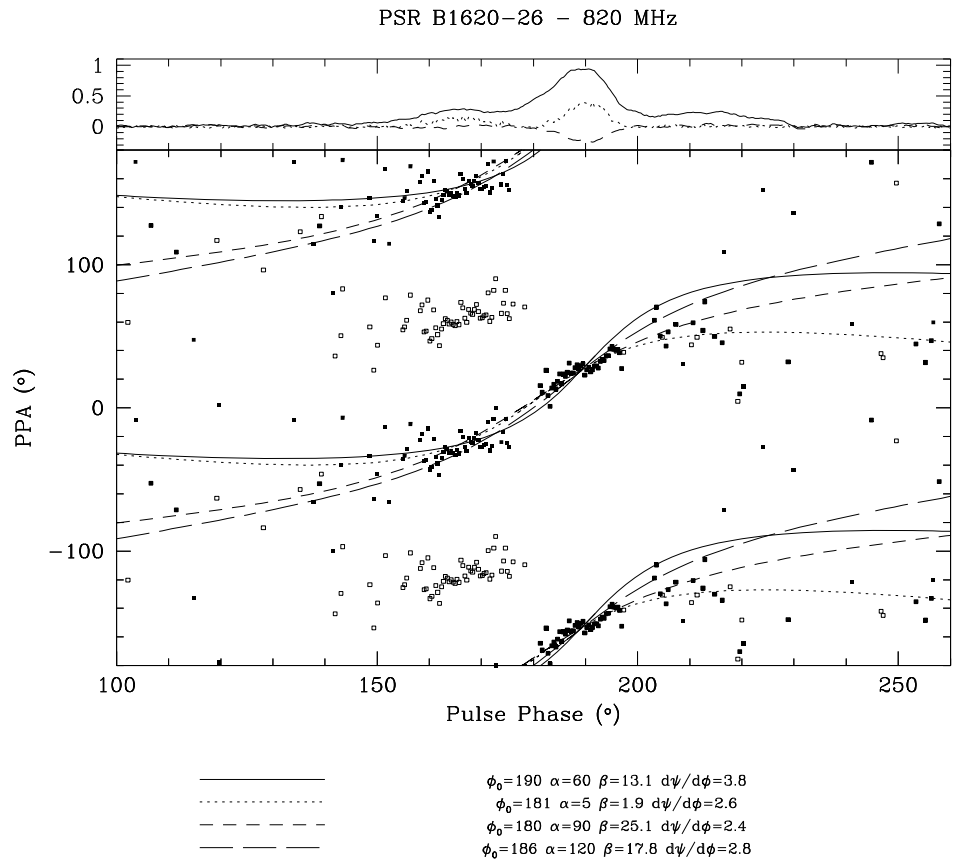

Fig. 4.9.— Rotating vector models are fit to the PPA data of PSR B1620−26 at 820 MHz. The data (filled squares) are plotted against pulse longitude (°) for pulse phases where the linear polarization exceeds the off-pulse *rms*. An orthogonal mode transition has been removed. The original data are shown by open squares. Four different models are shown. The solid line represents a model in which the symmetry center was forced to lie under the (presumed) central core component. In the remaining three models, the symmetry center lies near the center of the available PPA data. The smoothed polarization profile is displayed at the top of the figure for reference purposes (I, P, V=solid, dotted, and dashed lines, respectively).

other hand, the predicted diameter of an inner cone, which is 80° at this spin period, is consistent with the observed separations for $\alpha \sim 30°$.

For the fits presented for this object, the PPA data preceding the observed orthogonal mode transition were shifted by 90°. The 820-MHz data provides the best constraint on the pulsar geometry. Figure 4.9 shows the results of fits for $\alpha = 5°$, 90°, and 120°. Their center of symmetry is located in the middle of the PPA data, near the location of the orthogonal mode transition, and preceding the symmetry center of the intensity profile by $\sim 15°$. Many values of α are acceptable, due to the small range in pulse longitude covered by the PPA data. In fact, the 1410-MHz data are

consistent with values for the inclination ranging from 5 to 150°. A χ^2 analysis at 820-MHz indicates that an aligned geometry is somewhat preferred. The maximum slope is 2.5 ± 0.2, based on the 820-MHz and 1410-MHz data. The 575-MHz data is of poorer quality. A fourth fit is presented (solid line), where the symmetry center of the profile lies under the central component, and $\alpha = 60°$. In this case, the maximum slope is $\sim 3.8°$/deg. This model does not fit the data as well. If the symmetry center of the PPA curve truly precedes that of the intensity profile, it suggests that the emission occurs near the light cylinder, where the azimuthal component of the magnetic field has a significant effect. The values for the maximum slopes may be biased if the mode transition were not truly orthogonal. A slight offset between the two portions of the PPA data suggests that this might be the case. If true, the maximum slopes are smaller than those quoted here. The transition may also be truly orthogonal, with the apparent offset due entirely to the missing data accompanying the mode transition. The depolarization accompanying this "orthogonal" mode makes it difficult to determine the behaviour of the PPA in this region. If this were possible, the ambiguity might be resolved.

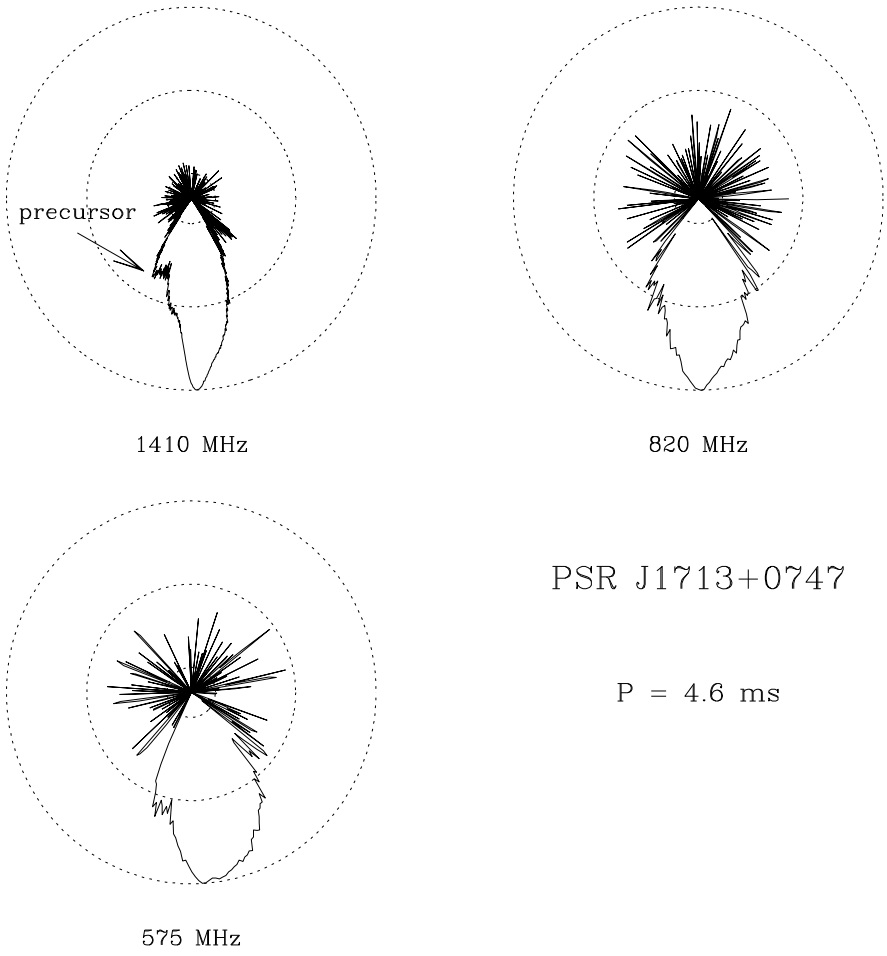

Fig. 4.10.— The relative intensity of PSR J1713+0747 is presented at each radio frequency in a log-polar plot. See caption of Figure 4.5 for details.

4.2.5 PSR J1713+0747

The overall extent of the emission beam in this pulsar appears to decrease significantly with increasing frequency (cf. Figure 4.10), although the results of component fitting in Chapter 3 suggest that this is probably due to the increased dominance of the central component relative to the others, rather than a change in the size of the emission region. The many components of the profile are difficult to classify, although sense-reversing circular polarization under the main pulse indicates that this is a core component. The components of this profile are, however, all narrower than the predicted core component width at this spin period. The separation of the main pulse and the trailing component (components 1-4 in Figure 3.13) is $\sim 45°$, which is narrower than the predicted radius of the inner hollow cone. The classification of components within this profile is uncertain.

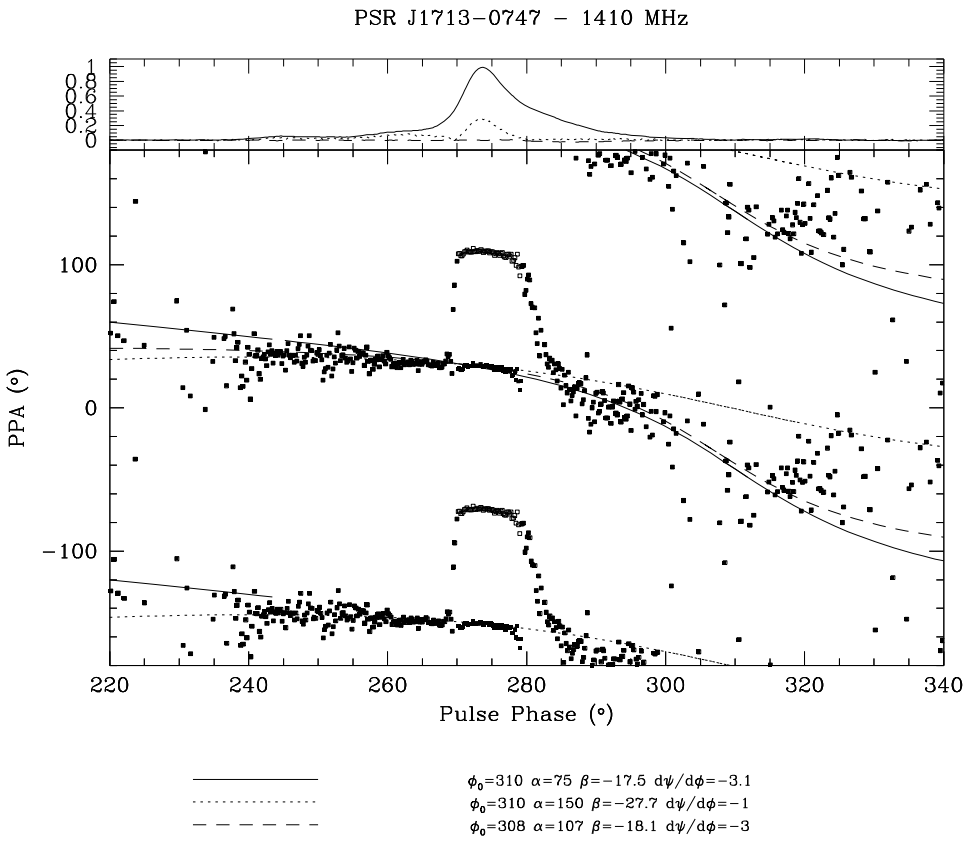

Fig. 4.11.— Rotating vector models are fit to the PPA data of PSR J1713+0747 at 1410 MHz. The data (filled squares) are plotted against pulse longitude (°) for pulse phases where the linear polarization exceeds the off-pulse *rms*. An orthogonal mode transition has been removed. The original data are represented by open squares. Three different rotating vector models are shown. The smoothed polarization profile is displayed at the top of the figure for reference purposes (I, P, V=solid, dotted, and dashed lines, respectively).

This 4.5-millisecond pulsar has a companion in a wide, circular, 67.8-day orbit (Foster *et al.* 1993). The pulses are delayed by the effects of general relativity as they pass the companion, and measurement of this Shapiro delay allows an estimate of the orbital inclination. These measurements suggest a companion mass of $0.33 M_\odot$, and the inclination angle is restricted to the range 57° to 81° by requiring that the neutron star mass be $\lesssim 3 M_\odot$ (Camilo *et al.* 1994). Non-aligned geometries are preferred. The relation of Rappaport *et al.* suggests $i = 56.5°$, which is just barely consistent with this measurement.

An orthogonal mode transition has been removed from the data presented in Figure 4.11. The apparent sharp sweep which remains is an artifact due to the low linear polarization accompanying the mode transition, and the non-linear effects of

the instrumental parameter σ for $P/I << 1$ (cf. Section 2.5). The remaining PPA data are relatively flat under the main portion of the pulse, with a slope that increases on the trailing edge of the pulse. Data which have had no correction for $\sigma \neq 0$ also show this trend on the trailing edge of the pulse. The 1410-MHz data provides the strongest constraints on the PPA curve, although all frequencies are consistent with the results presented here. Figure 4.11 displays the results of three fits, for $\alpha = 75°$, $105°$, and $150°$. The best results are obtained for α near $105°$, or $75°$ measured relative to the other rotation axis. This is consistent with the Shapiro delay measurement. The center of symmetry of the PPA model trails the main pulse by $\sim 30°$, which would indicate an emission radius of $R_e = c\Delta t/4 = 0.13 r_{LC} = 28$ km if it is due to relativistic effects. The maximum slope is $\sim -3°/\mathrm{deg}$.

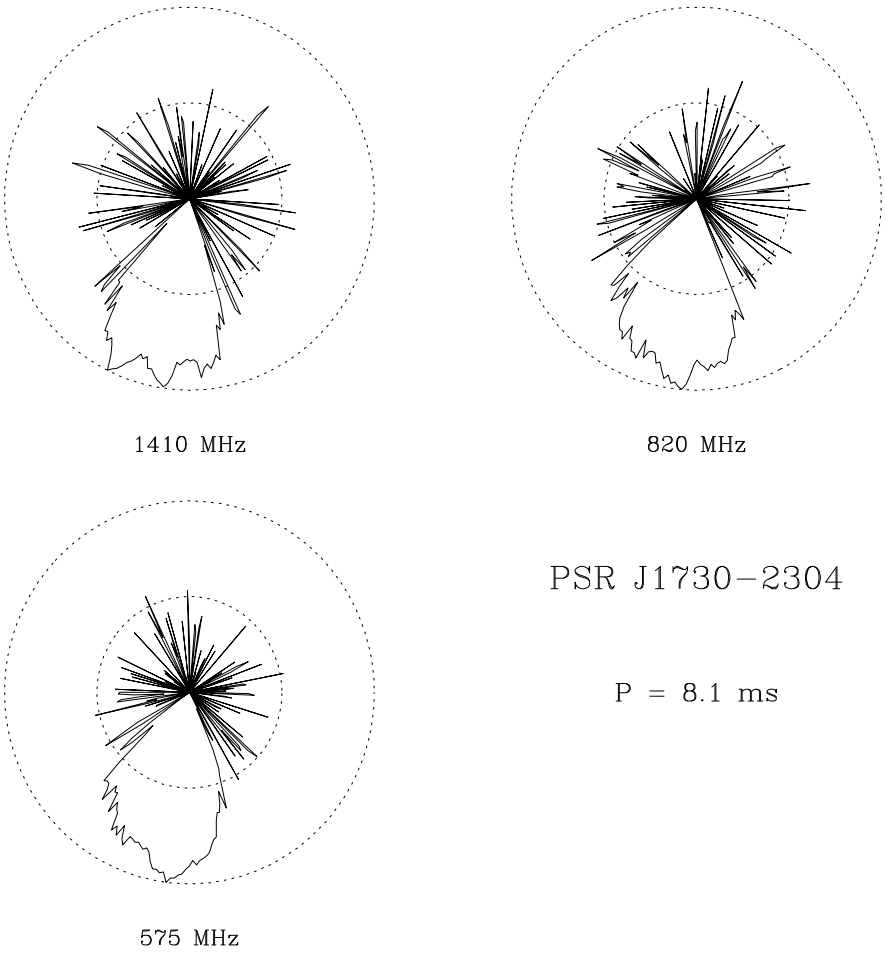

Fig. 4.12.— The relative intensity of PSR J1730−2304 is presented at each radio frequency in a log-polar plot. See caption of Figure 4.1 for details.

4.2.6 PSR J1730−2304

This 8-millisecond pulsar has no companion. The PPA data are confined to a very narrow range of pulse longitudes. Therefore the geometry cannot be easily determined from a rotating vector model. The frequency evolution of the intensity profile is as expected for a symmetric multiple component profile, indicating that the central component may be identified as a core component (cf. Figure 4.12). However, all components are narrower than is expected on the basis of the core width-period relation. The center of symmetry is expected to lie at the pulse phase of the core component, apart from relativistic effects and magnetic field distortion near the light cylinder. The PPA data, which lie under the trailing component, have a slope of $\sim -1.0°$/deg at 820 MHz. Figure 4.13 displays the rotating vector model for a variety of values of α. The fits are poorly constrained by the data.

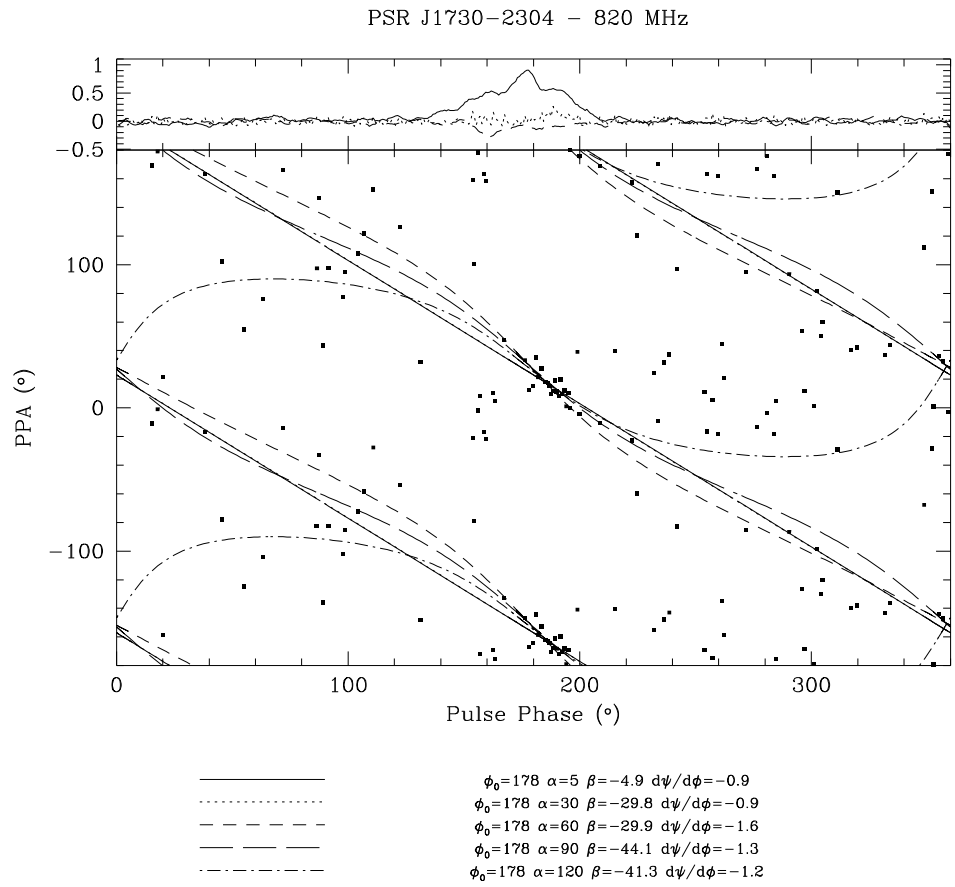

Fig. 4.13.— Rotating vector models are fit to the PPA data of PSR J1730−2304 at 820 MHz. The data (filled squares) are plotted against pulse longitude (°) for pulse phases where the linear polarization exceeds the off-pulse *rms*. Five different models are shown, indicating that the magnetic inclination α is poorly constrained. The smoothed polarization profile is displayed at the top of the figure for reference purposes (I, P, V=solid, dotted, and dashed lines, respectively).

4.2.7 PSR B1821−24

The profile of this isolated 3-millisecond pulsar does not fall easily into the usual classification schemes. The sharp components are significantly narrower than that expected on the basis of the core-width relation for slow pulsars. The intrinsic width of the trailing broad component is difficult to determine accurately, since the components are broadened by interstellar scattering at the lower radio frequencies, and it has faded significantly at 1410 MHz. With this caveat, the 1410-MHz width determined through component fitting is still narrower than the expected core width at this spin period (cf. Chapter 3).

Due to the approximately 180° separation between components 1 and 3 (cf. Figures 3.20 and 4.14), Backer & Sallmen (1997) suggested a two-pole model for this

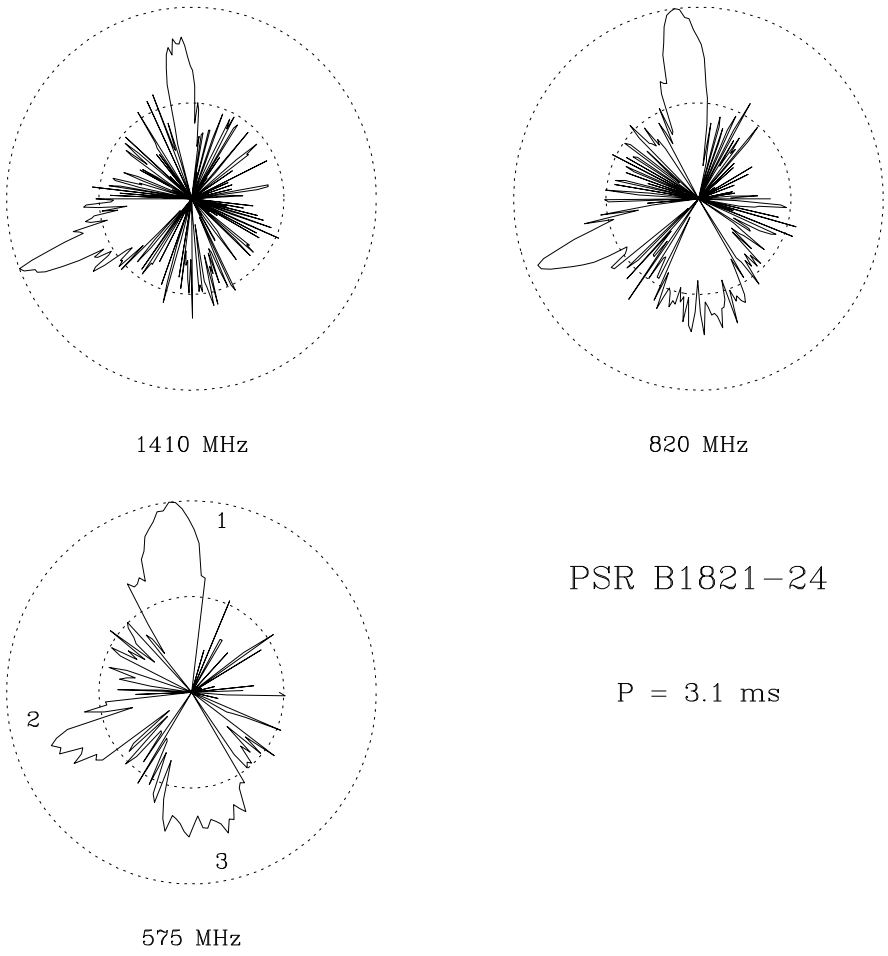

Fig. 4.14.— The relative intensity of PSR B1821−24 is presented at each radio frequency in a log-polar plot. The component numbers from the fits discussed in Chapter 3 are used to identify the components in the 575-MHz plot. See caption of Figure 4.1 for details.

pulsar. Assuming that component 1 is associated with one pole of the pulsar, a rotating vector model with $\alpha = 50°$, $\beta \sim 40°$ was fit to the 820-MHz data to match the slope of the main pulse PPA data ($\sim 1°$/deg) and the relative offset of the PPA data for component two. A similar model is shown in Figure 4.15 for the 1410-MHz data (solid line). The 820-MHz data presented in their paper were a subset of those presented here, and the results do not differ significantly. At 575-MHz, the slope of the main pulse PPA decreases slightly, probably due to the effects of interstellar scattering. In this model, component 2 is a conal outrider to component 1. The separation between the two is $\sim 108°$. This is consistent with the outer conal half-width separation predicted for this inclination α by extrapolating the slow-pulsar relation to this spin period. In this case, however, the full conal diameter is $> 180°$, and extending the relation to this extreme may be invalid.

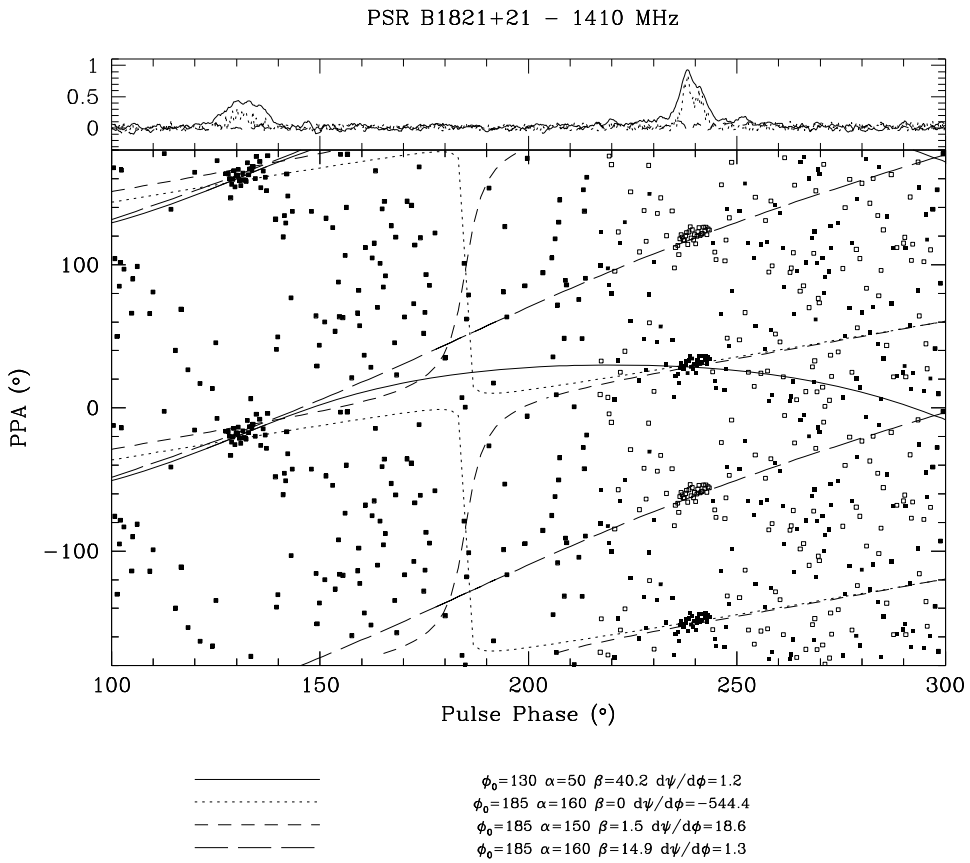

Fig. 4.15.— Rotating vector models are fit to the PPA data of PSR B1821−24 at 1410 MHz. The PPA data (filled squares) are plotted against pulse longitude (°) for pulse phases where the linear polarization exceeds the off-pulse *rms*. The open squares represent data to which a 90° rotation has been applied. The model associated with the solid line has its symmetry center under the first component, and is relatively well constrained by the PPA slope for this component, and the PPA offset of the other component. The other models have their center of symmetry between the two components, and α is poorly constrained for these cases. The long-dashed line represents a model for the rotated data. The smoothed polarization profile is displayed at the top of the figure for reference purposes (I, P, V=solid, dotted, and dashed lines, respectively).

By placing the center of symmetry between components 1 and 2, it is possible to fit the PPA data for a wide variety of inclinations α. This is also true if the PPA data of component two are shifted by 90° relative to that of component 1, under the assumption that an unobserved orthogonal mode transition occurs. The open squares in Figure 4.15 represent the rotated data. Three models with the symmetry center between components 1 and 2 are shown in Figure 4.15, displaying the insensitivity of the fits to magnetic inclination α. The separation between the two components can be made consistent with the expected inner cone diameter if α is chosen judiciously.

The cusp-like components in this pulsar have led to the suggestion that these are

due to emission in the outer magnetosphere (Chen & Ruderman 1993b, Backer & Sallmen 1997). Chen & Ruderman (1993b) note that the magnitude of the surface magnetic field for this pulsar places it in or near region I in their Figure 2, which is associated with Crab-like outer-magnetospheric emission. Romani & Yadigaroglu (1995) show that widely spaced pairs of components are produced by the outer-gap emission associated with a single pole, and that the "normal" polar cap radio beam (which is from the opposite pole) precedes the outer-gap emission by 0.35-0.50 period. The Crab pulsar has radio emission associated with the high-energy, outer gap radiation, while the Vela pulsar does not. The tentative identification of the observed X-ray components (Saito *et al.* 1997) with components 1 and 3 (Backer & Sallmen 1997) has now been confirmed (Rots *et al.* 1998). The observations would therefore imply that this pulsar also displays outer-magnetospheric emission. Component two is associated with the typical polar cap beam in this model. Intriguingly, the extra broad component required under component 2 in the 1410-MHz fit does have the expected core component width for an inclination of $\alpha \sim 90°$, although the sharp feature superimposed upon it is much narrower. An inconsistency in this picture is that there is non-zero radio emission between components 1 and 3 relative to that between components 3 and 1 (Backer & Sallmen 1997). The reverse is expected to be true in the Romani & Yadigaroglu model. Furthermore, this model predicts cusp-like component profiles for the outer-gap radiation, while we associate the sharp component 2 with the polar cap emission, and the broader component 3 with the outer-gap emission. The PPA data for components 1 and 2 are in many ways similar to that of the MP and IP of the Crab pulsar, exhibiting shallow slopes under two sharp components (cf. Figure 3.33). It is unfortunate that component 3 shows no significant polarization, since PPA data in that longitude region could help to distinguish between various models.

4.2.8 PSR B1937+21

The original millisecond pulsar, PSR B1937+21 is still the most rapidly rotating pulsar known. The MP-IP separation is 173° at all radio frequencies, suggesting a two-pole model for this pulsar (see Figure 4.16). The components are significantly narrower than the predicted core width for an object with this spin period. Once it has been corrected for orthogonal modes, the PPA is very flat, with a slope of $\sim -.5$ to $-1°$/deg under the main pulse. At 1410 MHz, the PPA data for the pulse and interpulse each have a shallow downward trend across the pulse. At 820 MHz and 575 MHz, the IP trend is reduced or even reversed (cf. Figure 4.17). If this effect is real, a single geometric rotating vector model cannot fit the data at all frequencies. The

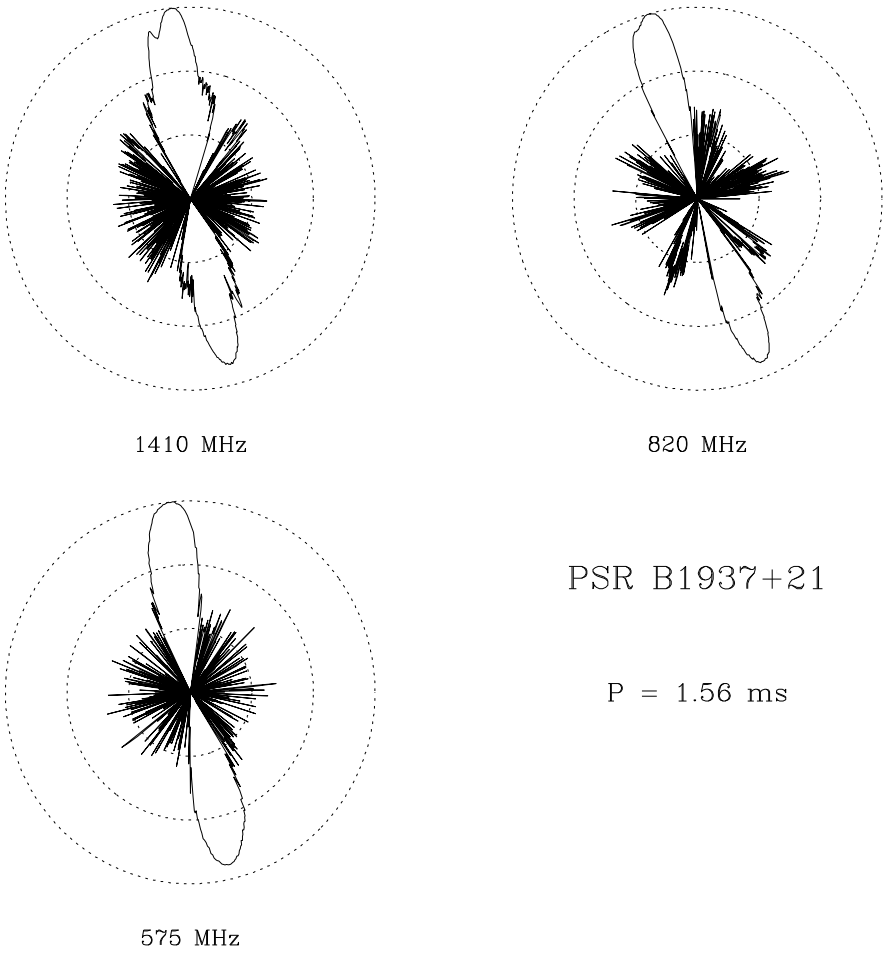

Fig. 4.16.— The relative intensity of PSR B1937+21 is presented at each radio frequency in a log-polar plot. The low-level systematics at 820 MHz and 575 MHz are instrumental effects. See caption of Figure 4.5 for details.

1410-MHz data can be fit by models with a large range in α, centered either under the main pulse, or between the two components. Due to the slope reversal of the IP at lower frequencies, the models required there are significantly different.

In the absence of a rotating vector model, the flat PPAs seen here can be explained in the model of Barnard (1986) by the presence of an azimuthal B field outside the light cylinder. Alternatively, Rankin (1990) suggests that the PPA behaviour of core components is disorderly, and should not be used as an indicator of pulsar geometry.

The MP-IP morphology of this pulsar is similar to that of the Crab pulsar (cf. Figure 3.33). In addition, the PPA data at 1410 MHz strongly resemble that for the MP and IP of the Crab pulsar, which also exhibit a shallow downward trend under each component. This, combined with the fact that these are the only two pulsars known to exhibit giant pulses (cf. Chapter 6), suggests a common source for their

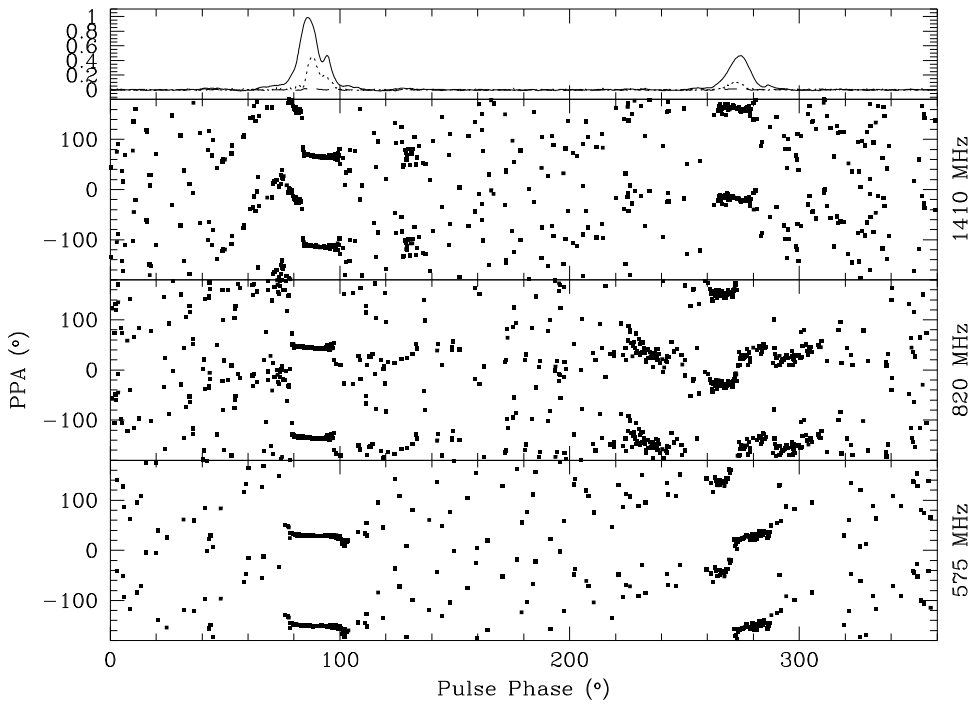

Fig. 4.17.— The PPA data are displayed for PSR B1937+21 at three radio frequencies. The PPA data (filled squares) are plotted against pulse longitude (°) for pulse phases where the linear polarization exceeds the off-pulse *rms*. The data are disturbed by orthogonal mode transitions. Once these have been taken into account, the PPA slope under the main pulse is roughly consistent at all frequencies, but the slope of the IP data changes sign. If this is real, and not due to imperfect calibration, no single simple geometric model can fit all of the data. The off-pulse systematics in the 820-MHz PPA curve are instrumental in origin. The smoothed 1410-MHz polarization profile is displayed at the top of the figure for reference purposes (I, P, V=solid, dotted, and dashed lines, respectively).

emission. The MP and IP in the Crab pulsar are widely believed to originate in an emission region in the outer magnetosphere (*e.g.,* Romani & Yadigaroglu 1995). In the model of Chen & Ruderman (1993b), pulsars which lie in region I of their Figure 2 are expected to produce outer magnetospheric emission. PSR B1937+21 falls in this "Crab-like" region of that figure, indicating outer magnetospheric emission is expected. On the other hand, they note that the component separation is extremely close to 180°, which is not expected for outer magnetospheric emission in their model. They attribute the profile morphology to an unusual magnetic field configuration (Chen & Ruderman 1993a). During prolonged spin-up, the moving crust compresses the surface magnetic field, resulting in a magnetic field centered on the rotation axis

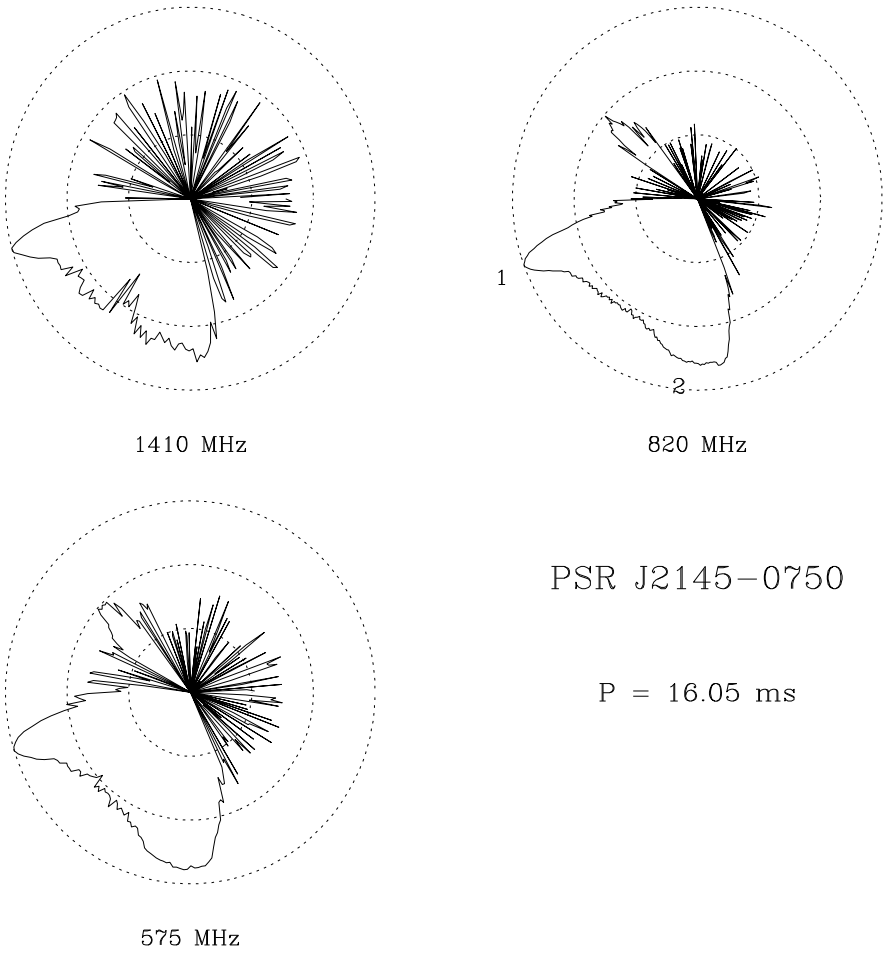

Fig. 4.18.— The relative intensity of PSR J2145−0747 is presented at each radio frequency in a log-polar plot. Components 1 and 2 in the fits described in Chapter 3 are identified in the 820-MHz data. See caption of Figure 4.1 for details.

at the surface, and orthogonal to the rotation axis.

4.2.9 PSR J2145−0750

This 16-millisecond pulsar is in a 6.8-day binary orbit with a $0.51 M_{\odot}$ white dwarf (optically identified by Bell *et al.* 1995). The mass function for this particular system indicates that the white dwarf has a minimum companion mass incompatible with the theoretical mass-orbital period relation.

The profile here is complex, with many components, and pulsed-emission over a wide fraction of a pulse period (see Figure 4.18). The separation of the two main components is consistent with the extrapolation of the expected inner-cone diameter to this spin period, for $\alpha = 90°$. The precursor and component 2 each exhibit sense-

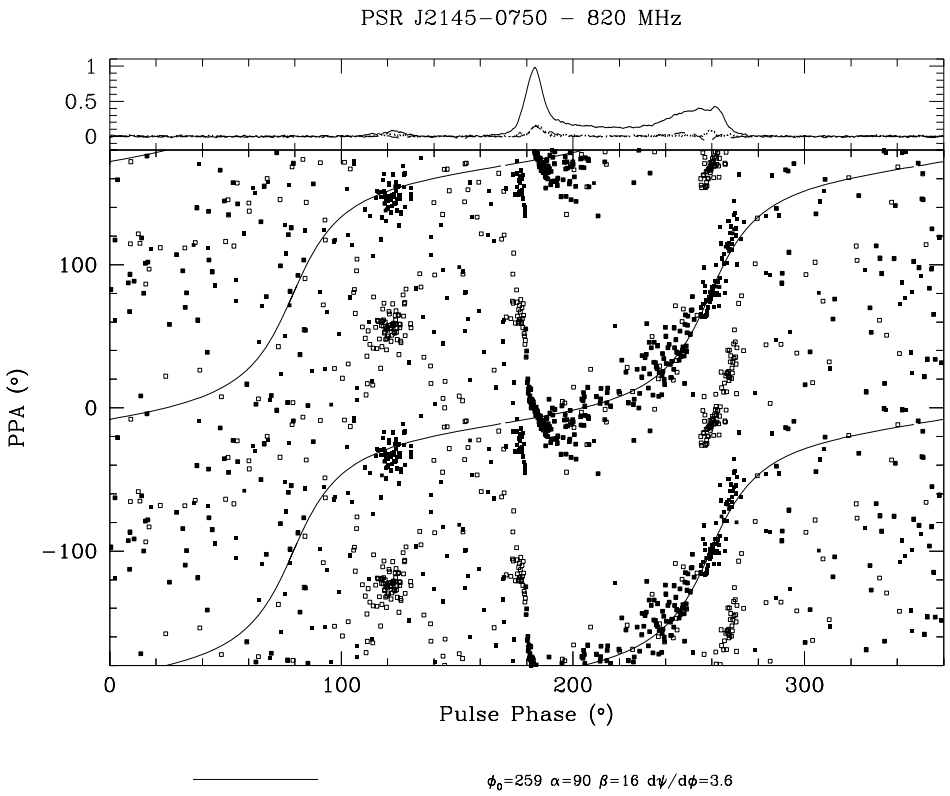

Fig. 4.19.— Rotating vector models are fit to the PPA data of PSR J2145−0750 at 1410 MHz. The data (filled squares) are plotted against pulse longitude (°) for pulse phases where the linear polarization exceeds the off-pulse *rms*. Two orthogonal mode changes have been removed from the data. The original data are represented by open squares. The solid line represents a particular rotating vector model. The smoothed polarization profile is displayed at the top of the figure for reference purposes (I, P, V=solid, dotted, and dashed lines, respectively).

reversing circular polarization, which is often a sign of core component emission. Their separation is only $\sim 130°$, making it difficult to associate these with opposite magnetic poles in a dipolar field geometry. The FWHM of component 2 is, however, similar to the expected width of a core component for $\alpha = 90°$. Kuzmin & Losovsky (1994) note that the separation of the pulse components *increases* at higher radio frequencies, contrary to expectations. They propose a significant quadrupolar component to the magnetic field, which would be somewhat surprising in light of the results of Arons (1993), which limit the non-dipolar nature of the magnetic field in millisecond pulsars.

The polarization position angle data presented here, although consistent across all frequencies, are complicated. The 820-MHz data were used for the fitting process,

although the 575-MHz PPA data are consistent with the results. The 1410-MHz data were too weakly polarized to be of assistance. For the fit presented in Figure 4.19, correction has been made for two orthogonal mode transitions. The original data are shown by the open squares. The apparent sweep in PPA accompanying the linear depolarization preceding component 1 has been assumed to be an orthogonal mode transition. The remaining PPA sweep under component 1 does not match the trends in the remainder of the PPA data, but must be real. The solid line gives the rotating vector model for $\alpha = 90°$, $\beta = 16°$ and is centered near the sense-reversing circular polarization of component two, strengthening its possible identification as a core component in this picture. The resulting maximum PPA slope is $\sim 3.5°$/deg.

Another possibility is that the steep sweep in PPA preceding component 1 is real, and no orthogonal mode transition is present at these longitudes. In this case, the sweep under the main peak can be fit by a rotating vector model, but the PPA data accompanying the remainder of the profile cannot be successfully modelled.

The PPA data presented here are significantly different from the results when the pulsar is in a mode of emission with much greater polarization. In that case the PPA data are *extremely* flat. This suggests that the PPA data presented here are not necessarily geometrical in origin, but are due to competition between modes of emission which are non-orthogonal. For non-orthogonal emission modes, the PPA at a given phase depends on the relative frequencies of occurrence of the two modes. If the relative frequencies of occurrence vary across the pulse, then the observed average PPA will vary accordingly. The significant depolarization of the pulsar emission in this emission mode supports this model. The fact that the (presumed) "orthogonal" mode transition preceding the main component does not appear to be completely orthogonal also suggests this interpretation. Similar frequencies of occurrence are, however, required at all radio frequencies to explain the similarity of the 820-MHz and 575-MHz PPA data.

4.3 Shallow PPA Slopes

Xilouris *et al.* (1998) noted that the maximum slopes of the rotating vector models for millisecond pulsars were, on average, significantly flatter than those seen in slow pulsars. The two distributions differ significantly. The observations presented here also indicate that millisecond pulsars have shallow slopes, as can be seen in Table 4.1. The slopes derived here, along with those quoted by Xilouris *et al.* (1998) are listed in columns 4 and 5. The details differ, but the essential flatness of the PPA data remains the same. The distributions of slopes for the populations of normal pulsars and millisecond pulsars are shown in Figure 4.20. These are reproduced from Xilouris

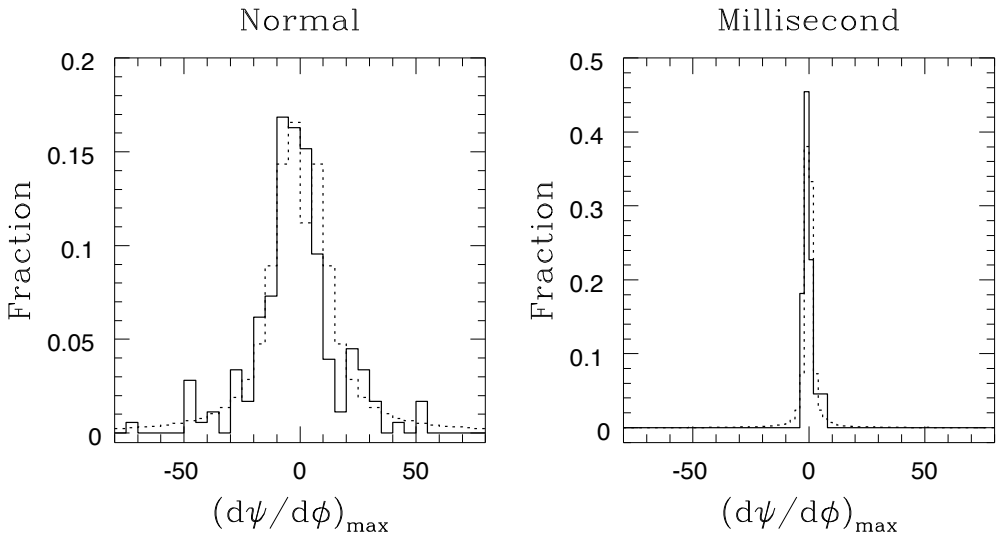

Fig. 4.20.— The distributions of maximum PPA slopes, $(d\psi/d\phi)_{max}$ are displayed. The fraction of pulsars is plotted against slope for both the normal and the millisecond pulsars. The solid-line histograms represent the data, taken from Xilouris *et al.* (1998). The dotted lines result from the simple simulation discussed in the text.

et al. (1998).[1]

Several possible explanations for the flatness of the millisecond pulsar PPA slopes have been discussed. All rely on deviations of the magnetic field from a dipolar structure. In one, special magnetic field geometries created during mass accretion and spin-up are invoked (Chen & Ruderman 1993a). The distorted field can influence the polarization and flatten the PPA curve. Higher order magnetic multipoles near the surface could have a similar effect. For emission near the light cylinder (or at least a polarization limiting radius near the light cylinder), Barnard (1986) has shown that the sweep-back of magnetic fields becomes important, resulting in a flattening of the PPA curve, and its shift to earlier phase. If the absolute emission radius is similar for slow and millisecond pulsars, then this is a tempting interpretation.

These relatively complex explanations are, however, essentially unnecessary. The maximum slope of a simple rotating vector model curve depends on the geometry of

[1]It should be noted that the observed PPA slope is a lower limit to the value of the maximum slope. For cases in which the symmetry center is placed in a region of little or no emission, the data constrain the rotating vector model only in the wings, where the curves are flatter. This can result in significantly larger slopes than the data immediately suggest.

the system, as is evident in equation 1.5. For a given inclination angle α, the flattest slopes $(d\psi/d\phi)_{max}$ occur for large impact parameters β. The size of the polar cap ρ is expected to scale with the pulsar rotational period P as $\rho \propto P^{-1/2}$. Since the maximum possible value of impact parameter β for which the pulsar will be visible is ρ, β_{max} must also scale as $P^{-1/2}$. Thus for millisecond pulsars, we expect that the population of visible pulsars will include objects with larger impact parameter β than is true for the population of slow pulsars. This simple fact can, to a large degree, explain the flat slopes of the PPA curves of millisecond pulsars.

With this in mind, we explored the expected observed distribution of slopes for a population of pulsars with random inclinations and impact parameters. For a given period, the maximum impact parameter was set to $\beta_{max} = 6^{\circ}P^{-1/2}$, comparable to the size of the outer cone of emission in Rankin's model (Rankin 1993). For each of 21 values for the inclination angle α between 0 and 90°, the slope $(d\psi/d\phi)_{max}$ was calculated for 401 values of β from $-\beta_{max}$ to $+\beta_{max}$ (with a slight offset to avoid $\beta = 0$). The resulting distribution of PPA slopes was then normalized to have a cumulative value of one (1).

The above distribution was calculated for 16 different pulsar periods, uniformly distributed in $\log(period)$ between 3 seconds and 0.1 seconds. In order to determine the distribution of PPA slopes for normal (slow) pulsars, these were then combined according to the relative frequency of occurrence of each pulsar period, as determined by inspection of the distribution of pulsar periods from the Princeton Pulsar Catalog (Taylor, *et al.* 1995). Similarly, the millisecond pulsar distribution was determined by an appropriate combination of the distributions for periods of 30, 10, 3, and 1 millisecond.

Figure 4.20 displays the resulting PPA slope distributions. The solid histogram is for the data at 1410 MHz, taken from Xilouris *et al.* (1998). The dashed histogram is a result of the simulation discussed above. Clearly, even this crude simulation recovers many features of the observed distribution. A simple geometric model can explain the data. No unusual magnetic field configurations are required.

The simulation does, however, ignore the difficulties of the fact that the width relationships following $P^{-1/2}$ fail to explain the component widths of millisecond pulsars (cf. Section 4.4).

4.4 Characteristics of Pulse Profiles

The millisecond pulsar polarization profiles discussed here all have several components. Most of the objects cannot be classified using the standard methods applicable to slow pulsars. Exceptions to this classification scheme exist even among long-period objects, but convincing identifications of core and cone pulse components are rare among the short-period pulsars. Conal components originating from two active magnetic poles cannot be easily distinguished, due to the large angular extent of the open-field region above each pole. In addition, components which might otherwise be considered core components frequently have relatively flat spectra, and flat-spectrum components are not necessarily located near the center of the pulse profile.

Among slow pulsars, pulsars with dominant core radiation can be distinguished on the basis of their values of the accelerating potential B/P^2, or on Beskin's Q parameter, which discriminates between modes of emission in their model (Rankin 1990, Beskin, Gurevich & Istomin 1988) Based on these criteria, virtually all millisecond pulsars should be dominated by core emission. Most pulse components are, however, narrower than is predicted for core components using the $P^{-1/2}$ scaling law. This strongly suggests the possibility that the emission does not fill the open field line region for short-period pulsars. Intriguingly, the component separations can be reconciled with the expected conal component separations (appropriately scaled) for several objects. Little is known about the relationship between the widths of conal components and pulse period, but the similarity in pulse profile morphology for all periods suggests that this quantity scales with the conal component separation.

The component separations of millisecond pulsars change very little with radio frequency (cf. Table 3.1). The same is often true of the pulse widths. This indicates that the emission region is very compact. The radiation for all frequencies originates within a narrow range of altitude so that the opening angle of the magnetic field is the same for all. Very little variation in emission altitude is possible if the radiation fills the open field lines. This is consistent with the $\pm$ 2 km emission radius for PSR B1937+21 (Cordes & Stinebring 1984).

The components seen in radio pulse profiles correspond to elementary beams of emission within the pulsar magnetosphere. Charged particles moving along the open magnetic field lines determine the current distribution within the magnetosphere (cf. Section 1.6). The motion of these particles may be perturbed by a plasma instability or population inversion leading to radio emission (cf. Section 1.7). Elementary beams of angular size $1/\gamma$ are anticipated, where γ is the relativistic Lorentz factor for the charges responsible for the emission. The divergence of open field lines in millisecond pulsars implies that the overlapping of these elementary beams may be reduced for

these objects, particularly if the characteristic beam size is independent of spin period. Structure that is seen in their pulse profiles may therefore be hidden in observations of slow pulsars, as several components may be buried within a single observable structure.

Kramer *et al.* (1998) found that the frequency evolution of the pulse profiles was correlated with the mass of any companion star. This indicates that the evolutionary history has a significant impact on the magnetospheric configuration for these objects. Chen & Ruderman (1993a) propose a concrete example of such evolutionary effects, and suggest that the profile of PSR B1937+21 may have formed in this way. A comparison of this object with the Crab pulsar, however, suggests that its profile, along with that of PSR B1821−24, may be the result of radio emission from the outer-gap region of the magnetosphere. In at least some models (Chen & Ruderman 1993b), the strength of the magnetic field at a given pulse period controls outer-gap emission, and the emission processes in these objects are expected to be similar to those of the Crab pulsar.

4.5 Frequency Dependence of Polarization

The results of Chapter 3 lead to the immediate conclusion that the polarization properties of millisecond pulsars are not strongly dependent on frequency. Figure 4.21 displays the average linear polarization across the pulse, using the data presented in Table 3.3. No strong depolarization with frequency occurs, in contrast to the results for normal pulsars, many of which show significant depolarization at 1.4 GHz (Manchester, Taylor & Huguenin 1973, Morris *et al.* 1981, Morris, Graham & Sieber 1981), relative to observations at lower frequencies.

The lack of depolarization with increasing radio frequency is consistent with the fact that Xilouris *et al.* (1998) found that millisecond pulsars were more highly polarized than normal pulsars at 1410 MHz. The depolarization index is correlated with the accelerating potential $\Delta\Phi \propto B/P^2$ (Xilouris *et al.* 1995). Xilouris *et al.* (1998) note that millisecond pulsars with "abnormal" frequency development tend to have a slightly higher accelerating potential, $\Delta\Phi \propto B/P^2$, as do young core-single pulsars. These latter objects have moderate linear and circular polarization, similar to that seen here. If the voltage $\Delta\Phi$ controls the emission properties, these objects may be related in some way. The two sets of objects also both have $Q > 1$, where Q is a parameter which distinguishes between propagation modes in pulsar magnetospheres (Beskin, Gurevich & Istomin 1988)

McKinnon suggests that the increasing depolarization of pulsars with radio frequency is due to the superposition of orthogonal modes of emission in a birefringent

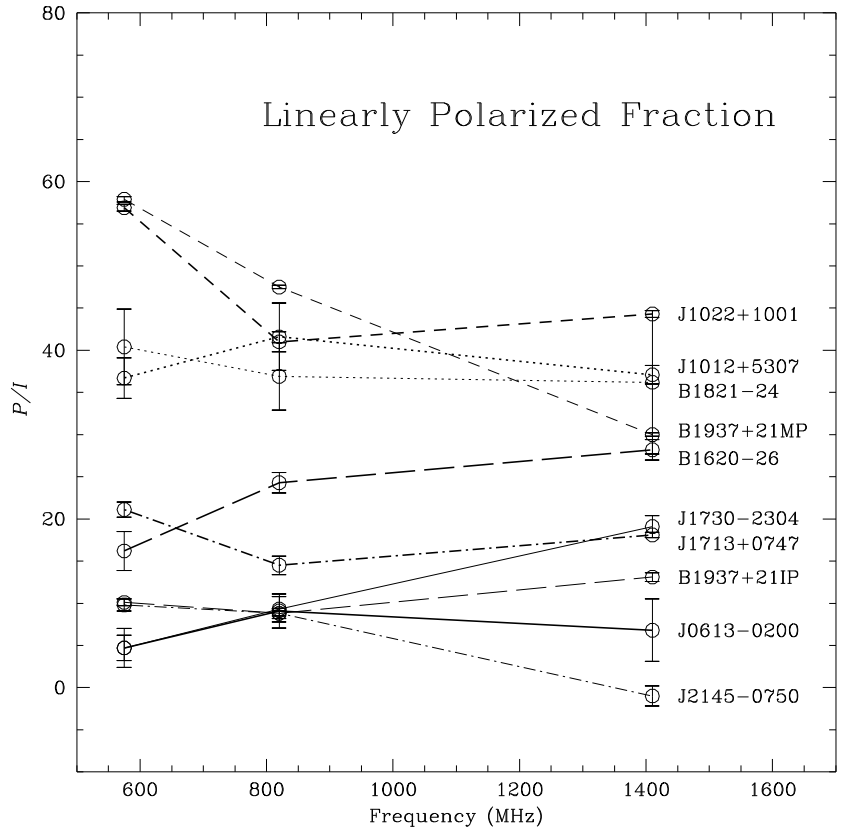

Fig. 4.21.— The fraction of linearly polarized radiation (%), averaged across the pulse, is displayed as a function of frequency for 10 millisecond pulsars. The 1-σ error bars are based on the off-pulse *rms*, and do not include systematic errors, such as those due to incorrect calibration.

medium. The depolarization depends on the relative frequencies of occurrence of the competing modes. Large depolarization rates result when the two modes have similar frequencies of occurrence. This would then suggest that one mode dominates for millisecond pulsars.

Geometric arguments (Morris, Graham & Sieber 1981, Xilouris *et al.* 1995) relate the polarization state of the radio emission to the size of the magnetosphere. Beams of curvature radiation are assumed in this model. Dipolar field lines diverge more for short-period objects, and it is these field lines which control the motion of the charged particles. The increased divergence at short spin periods could result in less overlapping of elementary beams of emission, as noted in Section 4.4, and can result in a larger fraction of linear polarization than is seen in long-period objects. Xilouris *et al.* (1998) reject this argument because it cannot explain the shallow PPA slopes of millisecond pulsars, but we have seen in Section 4.3 that these are also explained by the divergence of the dipolar field lines.

Relative to the pulse peak, the location of orthogonal mode transitions is relatively constant with radio frequency for pulsars B1620−26, J1713+0747 and J2145−0750 (cf. Figures 3.11, 3.14, 3.28). The longitude extent of the orthogonal mode may, however, increase slightly with increasing frequency for PSR J1713+0747. The approximate frequency-independence of these transitions means that the relative frequencies of occurrence of the two orthogonal modes must remain more or less constant with radio frequency. Attributing the complex PPA curve of PSR J2145−0750 to competition between non-orthogonal modes leads to the same conclusion (cf. Section 4.2.9). This can be difficult in models where the orthogonal modes are attributed to propagation effects.

4.6 Moding Behaviour

A number of the pulsars studied here exhibit long-term variations in either the intensity or polarization profiles. This is somewhat surprising in light of the relative constancy of the polarization properties with frequency. This 'moding' behaviour differs from that observed in slow pulsars, in that it occurs on longer time scales, and the transition between modes may be less abrupt.

Of the nine pulsars for which we present multi-frequency data, 3 display long-term variations in the intensity profile (PSRs J1022+1001, B1821−24 and J2145−0750), while at least 5 (PSRs J1012+5307, J1022+1001, J1713+0747, B1821−24 and J2145−0750) exhibit temporal polarization variations at one frequency or another. In addition, comparison of our polarization results at 1410 MHz (including the four pulsars for which we have only 1410-MHz data) with those of Xilouris *et al.* (1998) reveals possible polarization variations for 5 more pulsars (PSRs J0613−0200, J1518+4904, B1620−26, J1640+2224 and J1643−1224). Those authors further note polarization variations for PSRs J0751+1807, J1730−2304, B1855+09 and B1953+29, and profile variations for PSR J1730−2304, and possibly PSR B1953+29. We exclude the variations of the eclipsing pulsar PSR J1744−24A from further consideration, since its polarization properties are a function of orbital phase. These properties are summarized in Table 4.1. Of the thirteen objects in our data set, 3 exhibit temporal total intensity profile variations, while 7-12 vary in their polarization properties. Of the 27 objects in the combined data set, the intensity profiles vary on long time scales for 4-5 pulsars, and the polarization properties change for 9-14 objects.

The average pulse profiles of slow pulsars typically stabilize after a few thousand pulse periods (Helfand, Manchester & Taylor 1975). These stabilization time scales are themselves stable on 20-year time scales (Rathnasree & Rankin 1995). For most slow pulsars, the average profile remains stable. Blaskiewicz (1991) found shape vari-

ations in only 2 of 14 pulsars, while secular changes in the profile of the binary pulsar PSR B1913+16 are attributed to the effects of precession (Weisberg *et al.* 1989). Dramatic intensity mode changes were first reported in the slow pulsar B1237+25 (Backer 1970), and have been identified in several other slow pulsars. These can be accompanied by changes in the polarization properties of the pulsar as well (Bartel *et al.* 1982). Rankin (1986) discussed profile changes in 9 slow pulsars, and sub-pulse drift-mode changes in two others, concluding that mode changing is associated with complex emission profiles, at least in part because the phenomenon is easiest to identify in these cases. At that time, it was unclear whether only a few pulsars exhibited the phenomenon, or if it was simply more readily identifiable in certain objects. Recent polarization observations of 98 pulsars at 1400 MHz were carefully compared by the authors to previous observations when possible (Weisberg *et al.* 1998). This was possible for approximately 60 objects, of which 7 are known to exhibit mode changing at some frequency. Possible profile differences, not obviously attributable to SNR or resolution considerations, were discovered in two pulsars. In one of these, PSR B2020+28, temporal variations in both the intensity and polarization profiles are seen on time scales of days or months, although it is possible that their short daily integration times (2-4 min)[2] do not allow the profile sufficient time to stabilize. Cordes *et al.* (1978) found that on a given day, stable profiles resulted in about 300 pulse periods, but variations between daily averages were present. In addition, the polarization properties of this object exhibited slow variations on a timescale of weeks (Cordes *et al.* 1978). Possible polarization variations were seen in another 12 objects. The polarization differences between the published profiles (which do not have uniform resolution or SNR) are fairly significant in 6 objects, although proper calibration is an issue. Thus, 7-9 of the 60 pulsars exhibit profile variations. Polarization variations may be seen in 5-10 objects, although they are generally subtle.

Intensity variations may occur with similar frequency in the two sets of objects. Temporal changes in the polarization properties are apparently more prevalent in the millisecond pulsar population, however. Profile variations are most easily identifiable in profiles with multiple components. The profiles of millisecond pulsars typically satisfy this criterion.

The intensity profile mode changes in slow pulsars are typically abrupt, and last tens to thousands of pulse periods. PSR B2020+28 is an exception, showing long-term variations in its profile and polarization, as noted above. Another possible example of similar behaviour in the population of slow pulsars is PSR B0355+54.

[2]This corresponds to fewer than 1000 pulse periods.

Morris *et al.* (1980) report observations of a single occurrence of a mode change in this object in which the profile apparently changed gradually over $\sim$ 1000 pulse periods, and remained in the new state for at least 3600 periods. The temporal profile changes observed in the millisecond pulsars occur on much longer time scales. The intensity profile changes of PSR J1022+1001 may be relatively continuous (Camilo 1995), indicating that they are not necessarily as abrupt and distinct as those observed in classic moding behaviour. This may indicate a long-term instability in the emission beam, rather than a switch between a few stable configurations of current in the magnetosphere. The profiles of millisecond pulsars have not been observed on short time scales. The presence of abrupt profile changes lasting 10-1000 periods, analogous to those in slow pulsars, can be neither confirmed nor excluded.

Rathnasree and Rankin (1995) find that the stabilization rate of pulse profiles correlates with beam size ρ. Pulse profiles converge to a stable average faster for objects with larger beam size ρ. This correlation would indicate that we might have expected minimal profile variations in the class of millisecond pulsars, whose open field line region is significantly larger.

The changes in shape of the intensity profiles have particularly disturbing implications for the use of these objects in millisecond pulsar timing programs. These rely on the presence of a stable average profile in order to determine the precise arrival time of each pulse. The effects of the intensity moding of PSR B1821$-$24 at 1400 MHz are clearly visible in timing data from Green Bank.

4.7 Polarization Summary

Multi-frequency polarimetry observations with high time resolution have been presented for several millisecond pulsars. The polarization position angle (PPA) data, along with information about the total intensity profiles and binary companions, were used to place constraints on the magnetic inclination and observer's location relative to the emission beam.

The polarization properties of the millisecond pulsars are remarkably constant with radio frequency. Little depolarization is observed, in contrast to the observations of slower pulsars. The PPA curves are consistent across a modest range of radio frequency, indicating a probable geometric origin. Orthogonal modes are present in these data, similar to those seen in normal pulsars.

The maximum slopes of the PPA data are much smaller than those for normal, slower pulsars. Unusual configurations of the magnetic field have been suggested as a possible explanation. Here we demonstrated that by scaling the open field line region with the inverse square-root of the period, we can reproduce the characteristics of the observed distributions. Simple geometric considerations can explain this effect.

The components of millisecond pulsars are unusually narrow, and millisecond pulsar intensity profiles are not easily classified according to the slow-pulsar categories. The emission may not fill the open field line region. Outer-gap emission may play a role in a few objects.

Long-term variations are seen in the intensity profiles and polarization properties of millisecond pulsars. The mode changes of slow pulsars typically occur on much shorter time scales. The intensity mode changes observed here have a significant impact on pulsar timing programs for at least one object.

Part II

Single Pulses

Oh Bonny Pulsar, you shine where you spin
And the more I think on you, the more I think long

adapted from "Bonny Portmore" Irish trad.

Chapter 5

Simultaneous Dual Frequency Observations of Giant Pulses from the Crab Pulsar

5.1 Summary

An analysis of $\simeq$1 ms of signals, approximately 1 hour of 1 pulsar day, from the Crab pulsar.

Simultaneous measurements of giant pulses from the Crab pulsar were taken at two widely spaced frequencies using the detection of a giant pulse at 1.4 GHz at the Very Large Array to trigger the observation of that same pulse at 0.61 GHz at a 25-m telescope in Green Bank, WV.[1] Interstellar dispersion of the signals provided the necessary time to communicate the trigger across the country *via* the Internet. About 70% of the pulses are seen at both 1.4 and 0.61 GHz, implying an emission mechanism bandwidth of *at least* 0.8 GHz at 1 GHz. The arrival times at both frequencies display a jitter of 100 μs within the window defined by the average main pulse profile and are tightly correlated. This tight correlation places limits on both the emission mechanism and on frequency dependent propagation within the magnetosphere. At both frequencies the pulses are characterized by a fast rise time and an exponential decay time. At 0.61 GHz the rise time is not resolved, and the decay is a result of multipath propagation in the ionized gas surrounding the Crab nebula. At 1.4 GHz the giant pulses are resolved into several individual components. The rise and fall times of these components are correlated and vary from component to component and pulse to pulse. This indicates that the broadening does not result from propagation

[1]This is the 85-3 discussed in Chapter 2.

through the interstellar medium. It may be intrinsic to the emission mechanism, or due to propagation within the pulsar magnetosphere, or the product of multiple imaging caused by material in the surrounding nebula. The giant pulse spectral indices fall between -2.2 and -4.9, which may be compared to the average main pulse value for this pulsar of -3.0. The giant pulse contribution to the average increases with frequency, and so the giant pulses must, on average, have flatter spectra than the average main pulse, yet several of the giant pulses have steeper spectra. Several models of giant pulse emission are considered. The giant pulses can be either a temporal or an angular effect, and implications of both models are considered. The broadband nature of the radiation constrains the emission process, which must be coherent.

5.2 Introduction

The Crab pulsar was discovered in 1968 by the detection of its extremely strong individual pulses (Staelin & Reifenstein 1968). Such pulses, which are 100's of times stronger than the average, are not seen in most pulsars. The properties of these giant pulses have been explored for many years (*e.g.*, Heiles, Campbell & Rankin 1970, Staelin & Sutton 1970, Friedman & Boriakoff 1990, Lundgren *et al.* 1995). Giant pulses in the Crab pulsar occur at all radio frequencies, but only at the rotational phase of the main pulse and interpulse components. These two components have counterpart nonthermal emission at high frequencies – from the infrared to gamma ray energies – and may be associated with the outer voltage gaps in the pulsar magnetosphere (Romani & Yadigaroglu 1995). Giant pulses are not seen in the radio precursor or at the phases of the high frequency components recently described by Moffett and Hankins (1996). The radio precursor is identified as being more typical of a radio pulsar and is believed to originate at, and be aligned with, the magnetic pole.

Lundgren *et al.* (1995) found that two separate distributions were required to describe the fluctuations of single pulse energies [2] for the Crab pulsar main pulse and interpulse components at 0.8 GHz. About 2.5% of the pulses lie in the giant pulse distribution with a power law slope extending to high values and a low energy cutoff of 20 times the average of all pulse energies. The distinct distributions suggest different emission mechanisms for the giant and weak pulses and possibly different emission locations within the magnetosphere. However, the lack of an offset in the timing residuals between giant pulses and the average pulse profile (Lundgren 1994; for opposing evidence see Friedman & Boriakoff 1990) suggests that the emission region is the same.

The contribution of the giant pulses to the average energy of all pulses decreases with radio frequency. The probability distribution of the giant pulse energies can be written as

$$P(E_{\rm GP} > E_\circ) = f_\circ \left(\frac{E_\circ}{E_{\rm min}}\right)^{-\alpha},$$

where $f_\circ$ is the frequency of occurrence of the giant pulses, and $E_{\rm min}$ is the minimum

[2] Pulsar emission profiles are generally given in units of *flux* (Jy) even though in the context of rotating neutron stars one actually samples a one dimensional cut of the *specific intensity* pattern (Jy sr^{-1}). The integral of emission over a pulse component in the latter case would be its flux, while in the former and conventional case one quantifies the integrated component emission in units of energy (Jy-s).

energy. Correspondingly the probability density function is

$$p(E_{\rm GP}) = \frac{f_\circ \alpha}{E_{\rm min}} \left(\frac{E_{\rm GP}}{E_{\rm min}} \right)^{-\alpha-1},$$

and the corresponding mean giant pulse energy averaged over all pulses is $\frac{f_\circ \alpha}{(1-\alpha)} E_{\rm min}$. The probability distribution P has a slope $\alpha = 2.3 \pm .15$ at 0.8 GHz (Lundgren *et al.* 1995), and $\alpha = 2.5$ with significant errors at 0.146 GHz (Argyle & Gower 1972). At 1.4 GHz and 0.43 GHz the overall slope is roughly consistent with these, but is not the same for all energies (Friedman & Boriakoff 1990, Moffett 1997). Using the scaling law $\alpha \approx 2.5$ at all radio frequencies below 0.8 GHz, we find that the contribution of giant pulses with energy more than 20 times the average of all pulses, $E_{\rm GP} > 20\, E_{avg}$, is 89% of the average at 0.8 GHz (Lundgren *et al.* 1995), 9% at 0.43 GHz (Friedman & Boriakoff 1990), and only about 1% at 0.146 GHz (Argyle & Gower 1972). The frequency of occurrence of pulses ($f_\circ$) with energy greater than 20 times the average also increases with frequency, from 10^{-4} at 0.146 GHz, to 0.025 at 0.8 GHz. At 1.4 GHz, 80% of the energy comes from the 2% of pulses with greater than 20 times the average energy, using a power law slope of $\alpha = -2$.

There is no evidence of increased flux density in pulses near the giant pulses (Sutton, Staelin, & Price 1971, Lundgren 1994), nor is there any correlation between giant pulses. We note that many pulsars do show strong pulse to pulse correlation in amplitude (the "nulling" phenomenon) and in shape (the "drifting subpulse" phenomenon), indicating a memory process with a duration of many rotational periods. The timescale of giant pulses is, in contrast, less than a single period. In addition, the time separation distribution of giant pulses is consistent with Poisson process (Lundgren 1994).

Despite all these studies, the emission bandwidth of the giant pulses has been poorly determined. Comella *et al.* (1969) found that 50% of giant pulses were seen simultaneously at 0.074 GHz and 0.111 GHz. Goldstein & Meisel (1969) also found that some but not all pulses were correlated between 0.112 GHz and 0.170 GHz. Sutton, Staelin & Price (1971) noted that there was no evidence that the largest pulses at 0.16 GHz and 0.43 GHz were correlated. Heiles & Rankin (1971) observed giant pulses simultaneously at 0.318 GHz and 0.111 GHz, for a bandwidth spread of about 3:1. They found that pulses classified as giant at one frequency were stronger than the average at the other, but not usually classified as giant. Much more recently, Moffett (1997) reported that fully 90% of the giant pulses detected at 4.9 GHz were also detected at 1.4 GHz, implying an emission bandwidth of 3.5 GHz at high radio frequencies. In this paper, we report on giant pulses observed simultaneously at 1.4 GHz and 0.61 GHz to explore the correlation in this intermediate range of frequencies.

Section 5.3 describes the observations, while analysis of the simultaneous pulses lies in Section 5.4.

5.3 Observations

The data shown here were all taken on 1996 May 21 at UT $17^{\rm h}45^{\rm m} - 19^{\rm h}15^{\rm m}$. The 1.435-GHz data were taken at the NRAO Very Large Array (VLA) with all 27 antennas phased to create the equivalent sensitivity of a 130-m antenna, while the 0.61-GHz data were taken using a 25-m telescope at the NRAO Green Bank, WV, site.

The peculiar phases of each antenna at the VLA were determined by observing a standard point-source calibrator. These phases were then applied to the antennas to synthesize a pencil beam pointed at the Crab pulsar, which essentially resolves out the bright Crab Nebula and vastly improves the signal to noise ratio compared to a single-dish antenna. The received voltages from each antenna are summed to form orthogonally circularly polarized 50-MHz bandwidth signals centered at 1.4351 GHz. These are passed through a 1-MHz filter (centered at 1.4356 GHz), then detected and summed with a 100-μs time constant. The detector rms noise power was determined using an rms to DC converter. A detector threshold was set at either 5 or 6 times the running average of this rms noise level. Pulses that exceeded this threshold generated a trigger pulse that was sent to the data recorder, and were then saved to disk and archived to tape using the full 50-MHz bandwidth. In an off-line computer the data were coherently dedispersed using the method developed by Hankins (1971) and described by Hankins and Rickett (1975). Although the ultimate time resolution of the dedispersed data is 10 ns, for the analyses described here the data were smoothed to 0.5 μs after software detection.

The two linearly polarized signals at 0.61 GHz were converted to 90 MHz and 110 MHz, summed, and then sent *via* a single fiber optic link from the 25-m telescope to the Green Bank–Berkeley Pulsar Processor (GBPP) described in Chapter 2, which was at that time located at the 140ft telescope. The GBPP converted the signals to baseband, split these into 32 0.5-MHz channels, and dedispersed the pulsar signal in each channel *via* (de-)convolution in the time domain. The dispersion delay across the 16-MHz bandwidth of the GBPP at 0.61 GHz is about 33 ms, or one pulse period for the dispersion measure of the Crab pulsar ($DM \approx 56.8$ pc cm^{-3}). Full Stokes information was recorded with 982 samples across the pulsar period and an accurate UTC start time for each pulse.

This experiment utilized the difference in pulse arrival time between the two frequencies due to interstellar dispersion to provide the time interval needed to com-

municate the trigger information between the sites. At the VLA, the same trigger pulse that was sent to the data recorder was also sent, as an interrupt, to the SUN workstation used for experiment control and recording. The program that received the interrupt had a socket link open over the Internet to a slave program running on another SUN workstation in Green Bank, and communicated the 1.4356-GHz arrival time of the pulse to Green Bank.

We arranged for the GBPP to begin taking data just before the giant pulse reached the top of the band, in order to obtain data for the same main pulse across the entire band. The dispersion delay between 1.4351 GHz and 0.618 GHz (the top of our 0.61-GHz band) allowed a half second (0.503 s) to arrange this. The SUN workstations at the two sites were synchronized to the local versions of UTC which were derived from accurate atomic clocks using the `xntp` protocol. Both remote sites had 56-kB links to the Internet, with the typical Internet transfer time of 200 ms during our observation. The program running in Green Bank received the trigger message with its VLA time stamp, calculated the transit time of the trigger, and compared that to the dispersion delay difference of 0.503 s. In addition to this delay, the program included other factors such as the difference in pulse arrival due to the separation between observing sites on the Earth and the latency in the GBPP hardware, both of which were of order 1–3 ms. If sufficient time remained, it waited until the appropriate time and issued a trigger to the GBPP via the SUN parallel port to take data for the next pulse period. Due to the slow rate of data transfer from the GBPP, it could only accept such a command approximately every 12 seconds. Some VLA-initiated triggers were therefore missed by the GBPP.

The Stokes parameters for the high-time resolution data from the VLA were formed from the dedispersed voltages. To obtain the necessary 90° phase shift a FIR approximation to the Hilbert Transform was applied to the right circular polarization signal before forming the Stokes parameters. No instrumental polarization corrections were made other than bandpass leveling and gain matching; concurrent calibration (Moffett 1997) has shown that the polarization cross-coupling is less than 10% for the VLA phase array. The polarization error then is comparable with the radiometer uncertainty imposed by the limited number of degrees of freedom in the data ($(\Delta\nu\,\Delta\tau)^{-1/2} = 0.14$) in Figure 5.1).

The single pulse polarization profiles at 0.61 GHz were calibrated using factors derived from pulsed noise observations. The telescope introduces a relative phase between the two linear polarizations which couples the Stokes parameters U and V. This phase was determined and removed using nearby observations of the Vela pulsar, and comparison to a template polarization profile, as described in Section 2.5.5.2. No attempt has been made to remove coupling between the two polarizations. The error

in polarization due to improper calibration is estimated at 10%. For each pulse, the relative dispersion between the 32 channels was removed, and the resultant data were summed over channels, after first removing the effects of the pulsar's rotation measure ($RM = -42.3$ rad m^{-2}) across the band. The ionosphere could cause an additional rotation of 1 to 10 degrees across the total band, and has not been removed. Incomplete removal of rotation measure causes depolarization of the resulting pulse profiles.

5.4 Analysis

5.4.1 Wide Bandwidth Correlation

Of the 85 triggers initiated at the VLA a total of 77 trigger events reached Green Bank within the required time, and were accepted by the GBPP. The `xntp` protocol requires 24 hours to stabilize to the accuracy required by our experiment. The minimum time stabilization period was not available for the SUN at the VLA. Consequently the VLA clock used to identify the time at which the trigger was sent drifted by a small amount. For this reason, and others, we are currently only certain that we observed the correct period with the GBPP for 42 pulses.

The arrival times and pulse energy amplitudes were determined at both frequencies for each of these pulses. The 0.61-GHz arrival times were determined by cross-correlation with a model template, which consisted of a single-sided exponential with a decay time scale of 3 time bins, about 100 μs. The pulse amplitude was defined as the integral of the on-pulse energy in units of Jy-s. At 0.61 GHz, this was determined by removing an off-pulse average, then summing the flux in the time bins from 1 before the peak to 6 after the peak (accounting for fractional bins as determined in the cross-correlation). The 1.4-GHz pulse arrival times were obtained by computing the location of the centroid of the pulses; the amplitude was computed as the total energy received for each pulse by integrating its flux, after first removing the off-pulse baseline level.

We definitely detected 29 of the 42 correctly timed pulses at both radio frequencies. This corresponds to a 0.61-GHz pulse energy threshold of about 4.5 times the typical measurement uncertainty, or 0.075 Jy-s using 0.14 K Jy^{-1} for the 25-m telescope. This gain factor was determined using on and off measurements of the Crab nebula, and has an estimated uncertainty of 50%. We conclude that about 70% of the pulses are detected at both frequencies. The remaining pulses may be giant pulses that are too weak to be seen with the 25-m telescope at Green Bank, or may be normal pulses too weak to be classified as giant.

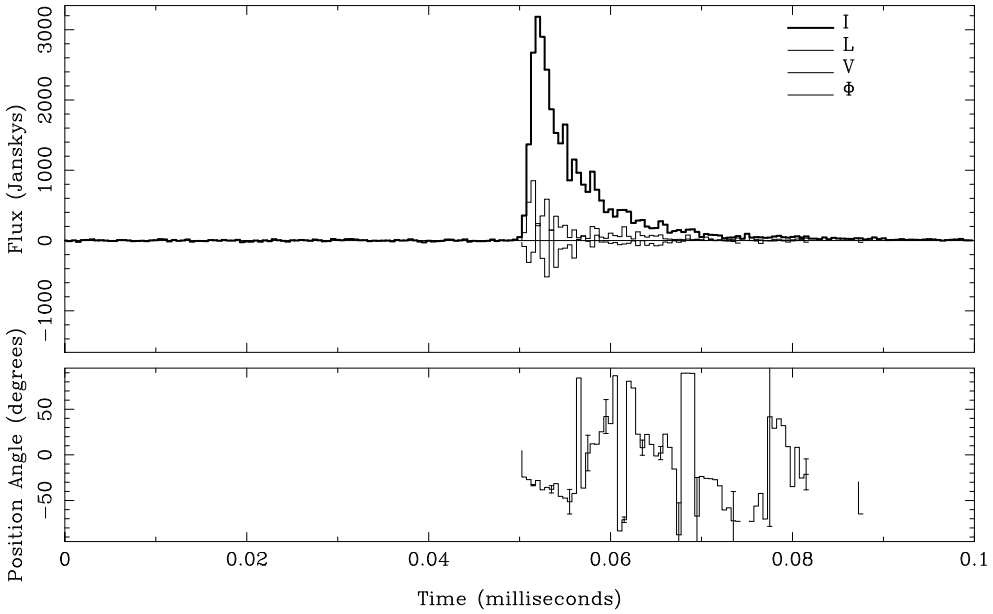

Fig. 5.1.— This figure displays the data for a single giant pulse at 1.4 GHz, taken at the VLA on 1996 May 21, with a temporal resolution of 0.5 μs. The top panel displays the total intensity I, along with linear and circular polarizations L and V. The vertical scale indicates that this pulse reached a peak flux of 3000 Janskys. The lower panel indicates the position angle of the linear polarization across the pulse.

The data for a single giant pulse at 1.4 GHz and 0.61 GHz are displayed in Figures 5.1 and 5.2, respectively. This pulse is strongly polarized at both frequencies, although fully two thirds of the giant pulses at the lower frequency are consistent with zero polarization. The 0.61-GHz data has a low number of degrees of freedom, and so the polarization estimation uncertainty is about 5%. At 1.4 GHz, the typical polarization is about 8% although at least one pulse is 50% polarized. The position angle of the linear polarization generally varies significantly across the pulse, as is seen in Figure 5.1.

The arrival times for the 29 giant pulses detected at the two frequencies were separately compared to a single model for this pulsar using the TEMPO program developed for pulsar timing (Taylor & Weisberg 1989). For each radio frequency, the arrival times are well-represented by the model, leaving timing residuals of order $\pm 100\mu$s. The residuals are comparable to the pulse width of the average profile during periods of low scattering, which is 275 $\pm 50\mu$s (FWHM) at 0.61 GHz, and 257 $\pm 50\mu$s at 1.395 GHz (*cf.* section 5.4.4).

The residuals for 1.4 and 0.61 GHz are plotted against one another in the top panel of Figure 5.3, which shows that they are highly correlated. The solid line has a slope of 1 and goes through the origin. In order for the points to fall along this

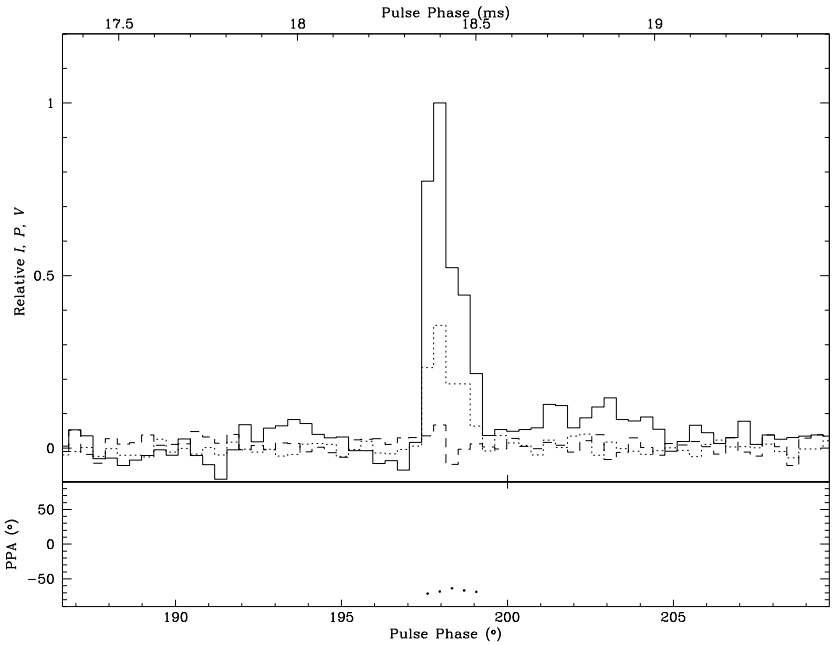

Fig. 5.2.— Figure 5.2 displays data for the same single pulse at 0.61 GHz, taken with the GBPP. The temporal resolution is approximately $34\mu s$. The top panel displays the total intensity I, along with linear and circular polarizations L and V. The peak flux for this pulse was $\approx$ 7000 Jy. The negative and positive features on either side of the main peak are artifacts due to the non-linear response of the GBPP. The lower panel indicates the position angle of the linear polarization across the pulse. Here only points with $L > 3$ times the off pulse rms noise are shown.

line, the 1.049 ms digital latency of the GBPP and the 235.42 μs latency of the VLA samplers and delay lines were removed, and a further fit for dispersion measure was done in TEMPO. The derived DM is 56.830 pc cm^{-3} although systematic errors may remain in the arrival times from the two sites. The bottom panel displays the same 1.4-GHz residuals with the solid line removed.

Eilek (1996) has shown that the dispersion law in the polar cap is different from that in the interstellar medium, proportional to ν^{-1}, as opposed to ν^{-2} for the cold interstellar medium (ISM). No systematic trends remain in the data in the lower panel of Figure 5.3, indicating that systematic variations with pulse phase from the differential effects of propagation through the magnetosphere are less than $\pm 15\mu$s between our two bands, corresponding to an angle of 0.164 degrees of pulsar rotation phase, or a range of 4.5 km in altitude. It would have been possible to have correlated emission from subpulses at different pulse longitudes at each frequency. In this case, the radiation at the two frequencies need not have come from the same radiating unit of charges. The observed rms jitter in arrival time at either frequency is $\approx$ 100 μs, so the fact that the difference between the residuals has such a small dispersion indicates that the emission must be from the same radiating unit at both frequencies.

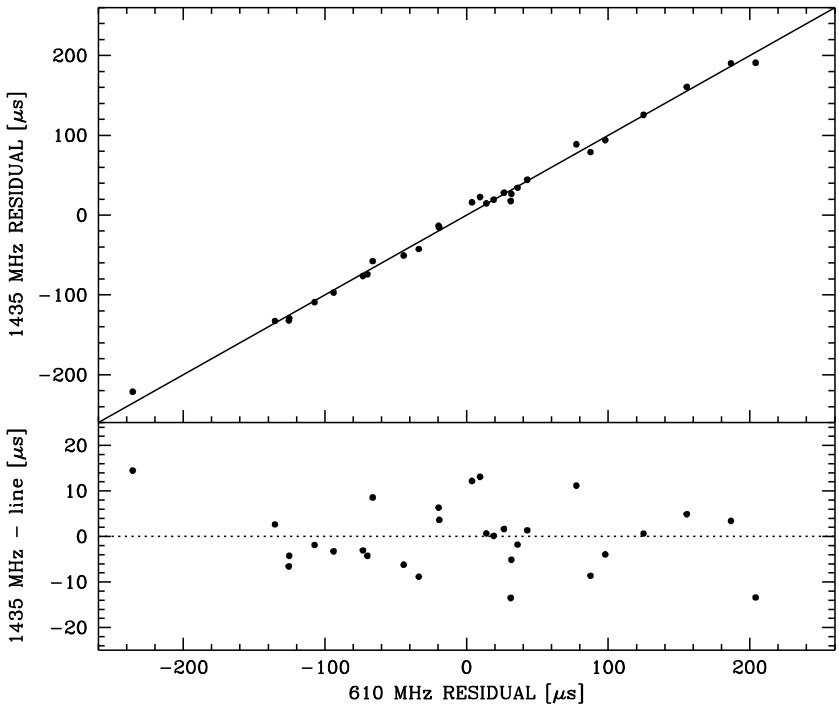

Fig. 5.3.— The top panel of Figure 5.3 displays the 1.4-GHz timing residuals against the 0.61-GHz timing residuals. The solid line passes through the origin with slope 1. The bottom panel displays the same data with this line removed.

This means that 70% of the giant pulses must have a bandwidth of *at least* 0.8 GHz at 1 GHz. The emission is clearly wide band for these cases, as expected for models wherein the fundamental radiating unit has a scale of about 30 cm and emits a pulse of nanosecond width.

5.4.2 Profile Shape

The giant pulses at 0.61 GHz all have profiles displaying a fast rise, followed by an exponential decay, similar to the profile shown in Figure 5.2. The fast rise indicates that the intrinsic time scale of the pulse is unresolved, $\lesssim 10\mu$s. The exponential decay time scale is $90-100\mu s$. At the time of these observations, the Crab was undergoing a period of unusually large scattering, as evidenced by monitoring of pulse broadening at 0.327 GHz using the 25-m telescope (Backer & Wong 1996). The scattering time scale at 0.327 GHz from these monitoring observations was $\tau_{\rm ISS}(0.327\ {\rm GHz}) = 1.3\pm0.2$ ms, which can be compared to 0.28 ms at an earlier epoch. The enhanced value at the time of our observations is presumably the result of a turbulent ionized filament in the periphery of the Crab nebula passing through the line of sight owing to motions of both the filament and the pulsar. The 0.61-GHz exponential decay time scale for these observations is therefore consistent with multipath propagation in the intervening perturbed plasma.

The giant pulses at 1.4 GHz have a wide variety of shapes. Figures 5.4 and 5.5 display two further single pulse profiles. The first pulse is extremely narrow, and is dominated by a single component, while the second has several components contributing to the emission. The darker solid line is a model fit to the data, where the model $S(t)$ consists of up to six components, and is of the form $S(t) = \sum_{i=1}^{n} a_{1_i}(t - a_{2_i})e^{-(t-a_{2_i})/a_{3_i}}, \quad n \leq 6$. These components rise to their peak in a time a_3, fall by e^{-1} in a further $2.15a_3$, and have a pulse energy amplitude of $a_1 a_3^2$. The majority of giant pulse components are well represented by this model, with widths a_3 ranging from 1.2 μs to 10 μs. At 1.4 GHz, the narrow component of the giant pulse shown in Figure 5.4 has a rise time of 1.2 μs, and a decay time scale of 2.5 μs. The second fitted component is clearly necessary to account for the emission on the trailing edge of the pulse, which does not follow an exponential tail. Thus the interstellar scattering time scale must be $\tau_{\rm ISS}(1.4\ {\rm GHz}) \lesssim 2.5\mu$s.

If the scattering along the line of sight obeys a Kolmogorov spectrum, then $\tau_{\rm ISS}(\nu) \propto \nu^{-4.4}$ and, based on the 0.327-GHz data, we expect $\tau_{\rm ISS}(1.4\ {\rm GHz}) = 1.9 \pm 0.3\mu$s, which is comparable to the observed minimum decay value of 2.5 μs. If the spectrum of the nebular material is not Kolmogorov, but follows a law more like $\tau_{\rm ISS}(\nu) \propto \nu^{-4}$, then the expected $\tau_{\rm ISS}(1.4\ {\rm GHz}) \approx 3.5\mu$s, which is somewhat larger than the observed minimum decay time. We conclude that the *minimum* component width at 1.4 GHz *is* a result of ISS. A future experiment during an interval of reduced scattering is planned to determine the intrinsic pulse width.

Many giant pulse components possess much longer time scales than 2 μs, although they are still well characterized by the functional form of the xe^{-x} fit. For example,

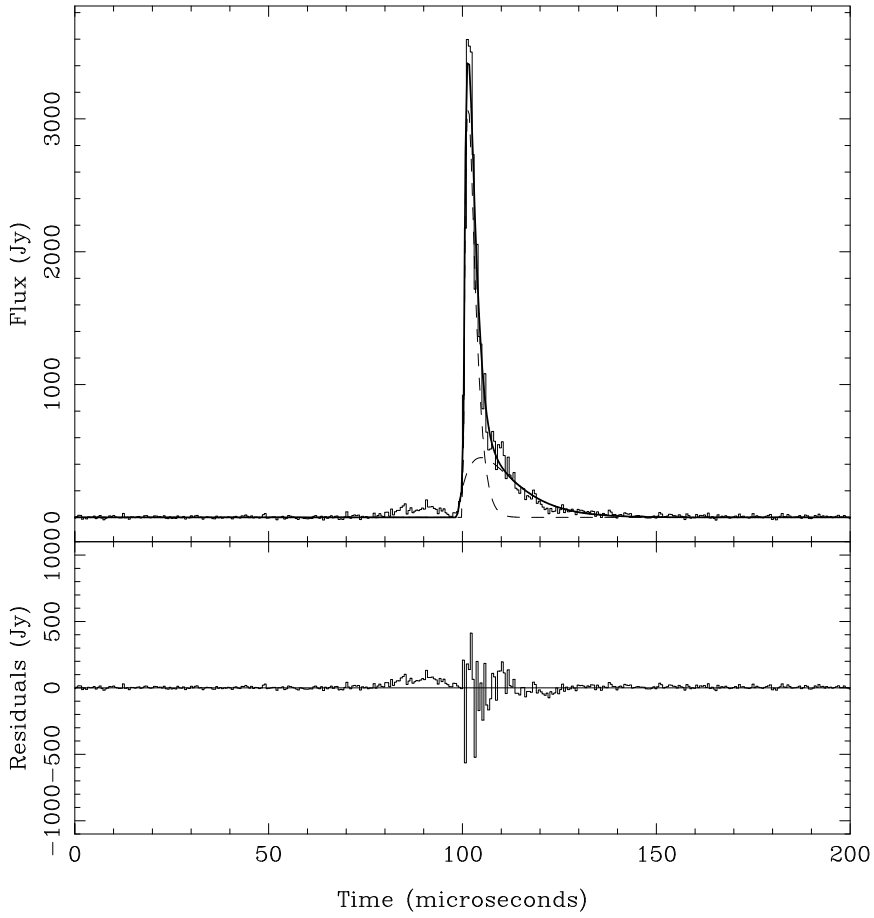

Fig. 5.4.— Figure 5.4 displays an example of a 1.4-GHz single pulse profile. The intensity data are modelled by the dark solid line, which is created using the fitted components represented by the dashed lines. These components are characterized by a fast, nearly linear rise, followed by an exponential decay. The narrow component of the giant pulse shown here has a characteristic time scale of 1.2 μs.

the final component of the pulse displayed in Figure 5.5 has a decay time scale of 12.3 μs. Furthermore, pulses such as this one clearly display several xe^{-x} components superposed with different decay times. Both pulse to pulse variations and component to component variations are not consistent with scattering in a distant screen. We conclude that these variations are intrinsic to the immediate vicinity of the pulsar.

These fitted components of the form te^{-t/a_3} are bunched within the window defined by the average main pulse. The distribution of their separations is not consistent with a random scattering of components within the average pulse window. The energies $a_1 a_3^2$ are independent of pulse width a_3, have an average of 6.3×10^{-3} Jy-s, and are scattered over two orders of magnitude. This means that the peak flux scales with

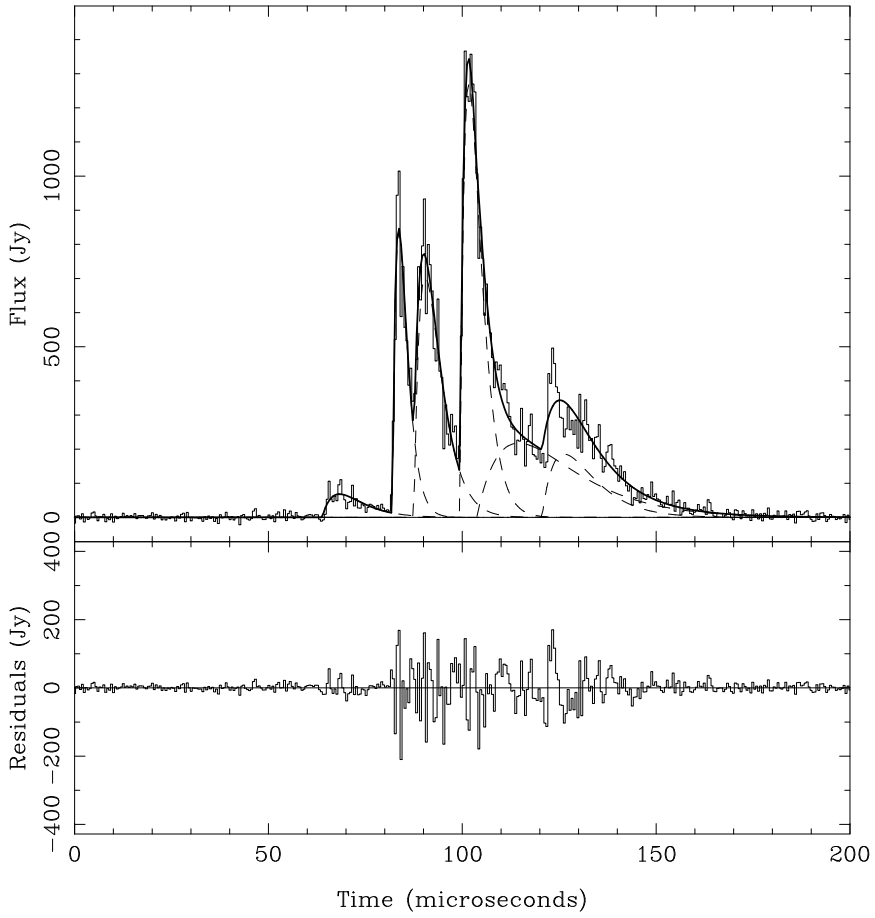

Fig. 5.5.— Figure 5.5 displays an example of a complex 1.4-GHz single pulse profile. The intensity data are modelled by the dark solid line, which is created using the fitted components represented by the dashed lines. These components are characterized by a fast, nearly linear rise, followed by an exponential decay. The final component of the giant pulse shown here has a characteristic time scale of 5.7 μs.

a_3^{-1}, and the energy scales with a_3^{-2}. It is possible that the bunching of components is due to multiple imaging of the pulse by refraction in the nebula surrounding the pulsar (Cordes, Hankins & Moffett 1998, in prep.). These may be associated with bright, dense optical filaments. If this cannot explain the observed shapes, then either the emission of a component is intrinsically asymmetric with linear growth, saturation and decay phases in time, or intrinsically narrow pulses of emission are variably spread as they exit the pulsar magnetosphere. These possibilities are further discussed in Section 5.4.5.

5.4.3 Energies and Spectral Indices

Lundgren *et al.* (1995) concluded (*cf.* section 5.2) that if the emission is narrow band, the rate of giant pulses must increase with frequency, while if the emission is broad band, then the giant pulses must have flatter spectra than the weak pulses. At least 70% of the pulses are broadband, so we expect their spectral indices to be, on average, flatter than the average main pulse spectral index.

Figure 5.6 displays 1.4-GHz and 0.61-GHz pulse energy amplitudes against one another, for the 29 pulses detected at 0.61 GHz. The 1.4-GHz amplitudes of the 13 pulses which were certainly not detected at 0.61 GHz are also shown. The vertical dashed line indicates our estimate of the threshold used at the VLA, and the horizontal dashed line represents the amplitude cutoff corresponding to the 0.61-GHz detection of pulses at Green Bank. Solid lines corresponding to spectral indices -2.2 and -4.9 are also shown, where spectral index q is defined by $A_{\rm GB}/A_{\rm VLA} = (0.61/1.4)^q$. The pulse amplitude of the average main pulse, shown as a horizontal dotted line in Figure 5.6, is 5.4×10^{-3} Jy-s at 0.61 GHz. The largest 0.61-GHz giant pulse therefore has a pulse amplitude of about 150 times the amplitude of the average pulse. The giant pulses are narrower than the average pulse, and so are even stronger relative to the average pulse within this window.

The spectral indices of the giant pulses detected at both frequencies fall between -2.2 and -4.9, with an average of -3.4. Moffett (1997) found that between 1.4 and 4.9 GHz, giant pulse spectral indices ranged from 0 to -4, with an average of about -2. At least 2 of the pulses in our sample which were undetected at 0.61 GHz *must* have flatter spectral indices if they are giant but too weak to be seen. The overall spectral index for the Crab pulsar is -3.1, while the spectral index for the average main pulse is -3.0, and is shown as a dotted line in Figure 5.6 (Moffett 1997). Despite the expectation that the average giant pulse should have a flatter spectrum than the average, we see many giant pulses steeper than the main pulse index of -3.0. The average spectral index of the giant pulses is -3.4, but this estimate is biased by the fact that the undetected giant pulses could contribute flatter spectral indices, and by possible systematic errors in flux calibration, which could change the average spectral index by up to 0.4. Alternatively, these pulses may simply not be giant at the lower frequency, which would indicate that the giant pulse emission process is not always broadband. The 30% which are missing are insufficient to explain the strong variation with frequency in the energy contribution of the giant pulses, if the typical giant pulse spectral index matches that of the average main pulse. The measured scatter in spectral indices of the giant pulses indicates that this is not the case, and the distributions will transform in a more complicated fashion.

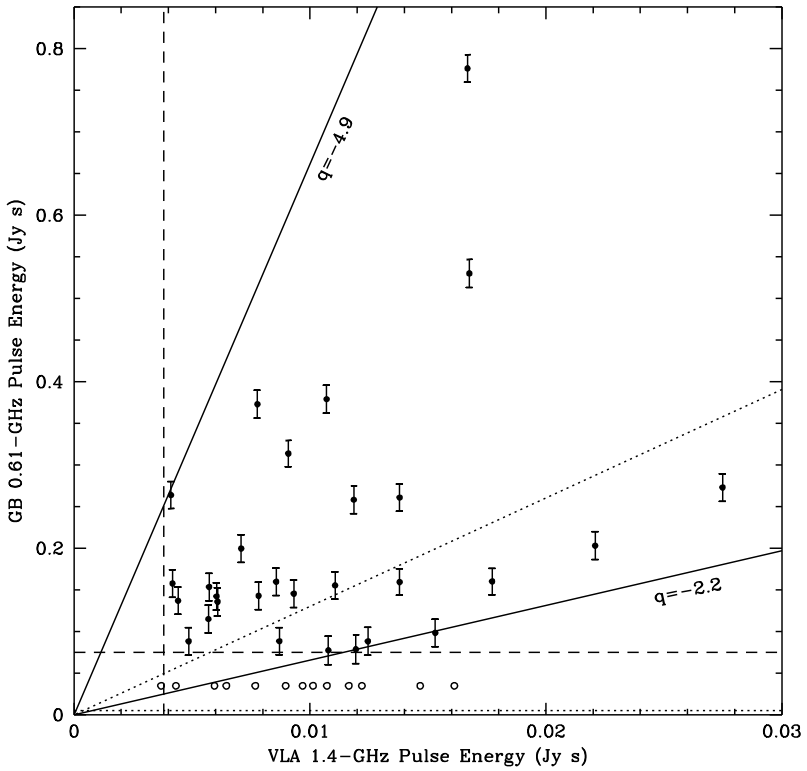

Fig. 5.6.— This figure displays the pulse energy amplitudes in Jy-s at 0.61 GHz and 1.4 GHz. The solid circles denote the 29 pulses which were detected at both frequencies. Error bars reflect the measurement uncertainty, which is negligible for the 1.4-GHz data. Uncertainty in the K Jy^{-1} calibration used at 0.61 GHz introduces an additional systematic uncertainty of 50%. The open circles represent those pulses seen at 1.4 GHz which were certainly not detected at 0.61 GHz. The horizontal dashed line represents the cutoff of 0.075 Jy-s, below which we could not detect pulses at 0.61 GHz. The vertical dashed line indicates our estimate of the VLA threshold corresponding to 6 times the rms noise. The one pulse with a 1.4-GHz energy less than this occurred while our threshold was 5 times the rms noise. The solid lines represent spectral indices $q = -2.2$ and $q = -4.9$. The dotted lines indicate the average main pulse energy and spectral index.

The individual giant pulse spectral indices display a relatively large scatter. Similarly, Heiles & Rankin (1971) found that their measured spectral indices at low radio frequencies ranged from nearly 0 to less than -3.0. There are several possible explanations. The spectral index variations could be due to the stochastic uncertainty in the determination of the amplitudes, introduced by the low number of degrees of freedom. We estimate this uncertainty to be of order 10% at 1.4 GHz, for an intrinsic pulse width of 1 μs. At 0.61 GHz, this is estimated to be less than the measurement uncertainty for the pulse energy. These are not large enough to explain the scatter in the spectral indices. The scatter could also be intrinsic to the radiation emission process. The signal could consist of a randomly occurring series of nanosecond im-

pulses whose Fourier transform in power is irregular. This would cause scatter in the observed spectral indices. But with the radiation extending over a few to 10 μs, there are many nanosecond pulses which might be expected to smooth out this distribution. Alternatively, one might expect the spectral index to vary due to properties of the emission beam.

5.4.4 Models of the Emission Beam

There are several possible models for giant pulse emission. In the temporal model, the enhanced emission is turned on only when we see a giant pulse, but covers the same beam as the average pulse, and has the same amplitude shape. Following Lundgren (1994), we also consider a model in which the enhanced emission is due entirely to a steady pencil beam with a random angular wobble. We see a giant pulse when the beam enters the line of sight. In both models, the average beam may be circular, as in polar cap models, or fan-shaped, as is likely if the emission comes from the outer gaps.

In the temporal model, if the width of the average beam varies with frequency, then the spectral index of the average pulse varies with pulse longitude. Using the data of Moffett & Hankins (1996) at 4.8 GHz, along with GBPP data from the 25-m telescope at 0.61 GHz, and from the 140ft telescope at 1.4 GHz, we performed Gaussian fits to determine the average component widths. We find that the main pulse width (FWHM) is $3.0 \pm .5$ degrees at 0.61 GHz, $2.8 \pm .5$ degrees at 1.4 GHz, and $3.5 \pm .5$ degrees at 4.8 GHz, implying that it does not vary significantly with frequency. Then the spectral index of the average pulse is not expected to vary across the pulse. A plot of our measured spectral indices *vs.* arrival time residuals at 0.61 GHz in fact shows no systematic variations. If the average beam varied with frequency, this would detract from the temporal model. This lack of variation cannot rule out the temporal model in this case because the width of the average beam is independent of frequency.

In the model with steady emission from a wobbling pencil beam, the width of the giant pulses $w_{\rm gp}$ corresponds to the size of the beam. If the intrinsic width of the giant pulses varies with frequency, then the observed spectral index will depend on how directly we are viewing the pencil beam. This model could explain the scatter in our spectral indices. Current measurements of giant pulse widths do show a small variation in width with frequency, which does not follow the Kolmogorov law, but the lower frequency data are contaminated by the effects of interstellar dispersion (Moffett 1997). The wobbling beam may also provide an explanation for the scatter in the energies of our fitted components. If the beam has a Gaussian intensity distribution,

then the observed energy again depends on the line of sight, with the most central ones producing the largest energy.

In this angular model, the pencil beam of emission may wobble in either the l direction (along the trajectory of the line of sight, a line of constant latitude), or the ϕ direction (perpendicular to the trajectory of the line of sight, a change in latitude). The width of the giant pulses corresponds to the size of the beam in this model, while the jitter in arrival times $\sigma_{\rm toa}$ corresponds to the wobbling of the beam along l. For giant pulses which occur a fraction f of the time, the wobble in ϕ is then $w_{\rm gp}/(Pf)$ where P is the pulse period (following Lundgren *et al.* 1995). Lundgren was able to separate the giant pulse and normal pulse distributions at 0.8 GHz, and found that 1 of 40 pulses is giant. At 1.4 GHz we see that the intrinsic width of the giant pulses is $w_{\rm gp} \approx \pm 1 - 10\mu$s. Since the giant pulses form a separate distribution, then if they are all broadband, they will all appear at both radio frequencies. Then at 1.4 GHz, 1 of 40 pulses should be giant. In fact, Moffett (1997) finds that one of 50 pulses has an energy greater than 20 times the average. We find $\sigma_{\rm toa} \approx 100\mu$s, so the 0.01 to 0.1-degree beam then wobbles 1.1 degrees in l and 0.5 to 5 degrees in ϕ. This is consistent with a pencil beam wobbling within a roughly circular average beam. If the average beam is a fan beam, it will be elongated in the ϕ direction. Given that the giant pulses dominate the emission at 1.4 GHz, they must stochastically fill the fan beam. This is impossible in this model unless the giant pulse beam is also elongated parallel to the fan beam, or multiple round pencil beams fill the average fan beam.

5.4.5 The Emission Mechanism

Radio emission from pulsars must come from a coherent emission process (Cordes 1981). The exact process is very uncertain, as is the location of the emission. It is not necessary for the giant pulse emission to originate at the same place or in the same way as the weak pulse emission. The broadband nature of the giant pulse emission provides the main constraint on its origin. According to Melrose (1996), broadband emission is traditionally associated with models in which the emission occurs at a pair production front in the polar cap, or *via* Schott radiation from a corotating charge and current distribution outside the light cylinder (*e.g.*, da Costa & Kahn 1985; Ardavan 1992, 1994). The emission process itself could rely on plasma instabilities (Cheng & Ruderman 1977, Asséo 1993, Machabeli & Usov 1979, Kazbegi *et al.* 1991). Alternatively, other maser processes such as linear acceleration emission (Melrose 1978, Rowe 1995) or maser curvature emission (Luo & Melrose 1992, 1995) could produce the radiation. In any case, if the giant pulses are a temporal effect, this variability in radio emission could be due to variations in the number of coherently

emitting regions (incoherently summed), or an increase in the coherence within a single emission region.

Given the characteristic shape of the giant pulse components at 1.4 GHz, any model producing giant pulse radiation must be characterized by an approximately linear rise, followed by an exponential decay. This intrinsically asymmetric shape is not expected for a simple pencil beam with an angular wobble. In either model, this shape can be explained by propagation in the magnetosphere (Eilek, Hankins & Moffett 1998), or in the medium immediately surrounding the pulsar. The effects of aberration are too small to produce the broadening and asymmetry seen in these pulses, if one confines the range of emission altitudes to 4.5 km, according to the difference between the residuals at the two frequencies. In the temporal model, this shape is consistent with any emission process which turns on with a rapid nearly linear rise, then saturates and decays. In this case one would expect the peak energy to be independent of width, whereas we have seen that it is the total pulse energy which is independent of width.

We assume that the shape is intrinsic to the emission mechanism and consider a temporal model in which a bunch of charges radiates so as to produce a single pulse component. For coherent curvature radiation, the power lost by the N excess charged particles in the bunch will be

$$P_{curv} = N^2 \left(\frac{2e^2\gamma^4 c}{3\rho_c^2} \right),$$

where e is the charge on an electron, γ is the relativistic factor $(1 - v^2/c^2)^{-1/2}$, and ρ_c is the radius of curvature of the magnetic field. We observe 6.3×10^{-3} Jy s in a 50-MHz band, so P_{curv} must equal the measured luminosity, which is therefore greater than 4.3×10^{22} erg s^{-1}, assuming a distance of 2 kpc, and a circular beam 100 μs $= 1^\circ$ wide. Then the number of particles in the bunch must be at least

$$N = 3.07 \times 10^{19} \left(\frac{\gamma}{100} \right)^{-2} \left(\frac{\rho_c}{10^8 \mathrm{cm}} \right).$$

These particles must fit within a cube with volume $\leq \lambda_{em}^3$, so the number density of excess charges must be $\delta n_e = N/\lambda_{em}^3 = N/(\gamma\lambda_{obs})^3 = 3.3 \times 10^9$ cm^{-3} for the parameters used above, and a wavelength of 21 cm. This density can be further reduced if several bunches are radiating in a periodic structure.

If the model is truly temporal, then the angular size of the beam does not affect the pulse width. The radiation will be beamed into a beam width $\theta \sim \gamma^{-1}$. Requiring that the beam be wider than 50μs, so it is wider than any given pulse component, then implies that $\gamma \lesssim 100$. Since complex pulses such as the one shown in Figure

5.5 have many overlapping pulse components, we must have several bunches whose radiation adds incoherently to produce the observed profiles. The radiation from one bunch must not affect the charges in another bunch. For a temporal separation Δt between components, this restriction is satisfied for bunches with an angular separation of $\Delta\theta = 2\pi\Delta t/P$, which corresponds to a horizontal separation of $\Delta s = r\Delta\theta$. Given a component separation of 10 μs, we find $\Delta s = 1.9$ km for an emission height of 10^8 cm, a substantial fraction of the distance to the light cylinder. The same temporal separation could be achieved with two bunches at altitudes differing by $c\Delta t/(1+\sin i) \sim 3$ km, but the radiation from the lower bunch would affect the upper one. If the two bunches are separated both horizontally and vertically, the observed time separation must include the angular, time-of-flight, and aberration effects, and the bunch at the higher altitude must be sufficiently separated horizontally to be out of the γ^{-1} beam of the lower bunch. For the parameters above, and $\gamma = 100$, this means that $\Delta s \geq 7.5$ m, and $\Delta r \leq (c\Delta t + \Delta s)/(1 + \sin i) \sim 1.5$ km for $\Delta s = 7.5$ m.

As suggested in Section 5.4.2, the multiple components can be explained by a single emitted pulse that is multiply imaged by finite-width plasma structures near the pulsar (Cordes, Hankins & Moffett 1998). This model can also explain the high frequency deviation of observed giant pulse widths from the $\nu^{-4.4}$ dependence that is otherwise expected (Moffett 1997). One prediction of this model is that late-arriving pulses should be broader. This test has not yet been performed, but should be possible with 1.4-GHz data taken at the VLA. Of additional interest is whether the range of 1.4-GHz broadening times remains constant, or is larger during this epoch of unusually large scattering. If it is the same even when the scattering at low frequencies is smaller, then the finite-width structures causing the multiple images are not the same as the material causing the variations in pulse broadening at low frequencies.

5.5 Conclusion

Simultaneous dual frequency observations of giant pulses from the Crab pulsar reveal that the emission is broadband, since 70% of the pulses are observed at both frequencies. The tight correlation in arrival times implies that the same radiating unit is operating at both frequencies. The pulses are characterized by a fast rise and exponential decay, which cannot be entirely due to interstellar scattering at the higher frequency. The giant pulses display a scatter in spectral index, which is not due to measurement uncertainty. Pulsar emission models are restricted to those which can explain the broadband nature of the giant pulse radiation.

Chapter 6

Individual Pulses in Millisecond Pulsars

6.1 Summary

Studies of single pulses from two millisecond pulsars ares presented. The energy distribution of PSR B1534+12 is similar to that of slow pulsars, but extends to somewhat higher energies. There is correlation in the pulse energy on time scales of a few pulse periods. The individual pulses are narrower than the average, but there is no evidence for microstructure which scales with pulse period. The energy distribution of PSR B1937+21 indicates that this pulsar possesses a small number of very strong pulses which are reminiscent of the giant pulses seen in the Crab Pulsar. These large pulses occur in both the pulse and interpulse, and are always delayed relative to the average pulse profile, suggesting that they come from a different emission region, and perhaps are due to a somewhat different emission mechanism. The pulses are delayed about 50μs while the interpulses are delayed about 65μs. No pulse to pulse or pulse-interpulse energy correlations were found, indicating that the phenomenon occurs on extremely short time scales. The delay of these pulses to a location relative to the average profile where the emission is significantly less than the peak average emission implies that they have energies hundreds of times that of the average emission in that region. Pulses or interpulses with total energies > 15 times the mean pulse energy occur about 10 times each in this sample of $757,876$ pulses. Thus these pulses are significantly weaker and occur less frequently than the giant pulses seen in the Crab pulsar. They are energetically unimportant, relative to the average. The average pulse profile of these strong pulses is consistent with the exponential impulse response of the interstellar medium, coupled with some phase jitter between strong pulses. The $\sim 50\mu$s delay between strong pulses and the average suggests a difference in the emission location, corresponding to 7.5 km in altitude, or 11° in phase.

6.2 Introduction

PSR B1937+21, with a spin period of 1.56 ms, was the first millisecond pulsar to be discovered (Backer *et al.* 1982). This relatively new class of pulsars consists of objects with short (millisecond) spin periods, extremely small period derivatives, and therefore weak magnetic fields ($\sim 10^8 - 10^9$ Gauss). The radio emission mechanism of these pulsars, as for normal (slow) pulsars, is not well understood. Due to their weaker magnetic fields, and much shorter spin periods, they may provide new clues to the physics of pulsar emission. In any case, the emission mechanism itself cannot be sensitive to either spin period or magnetic field strength.

The unusually sharp pulse components of PSR B1937+21 have already been noted in Chapter 1. These highlight the difficulty of extending our understanding of slow pulsar geometries to these short spin periods.

Studies of the individual pulses from slow pulsars revealed that the emission is quite erratic, especially when compared to the stable average pulse profiles exploited for precise pulsar timing. The pulse to pulse emission is highly modulated, with fluctuating energies, and varying shapes. Subpulses, micropulses, and their behaviour have been discussed in Chapter 1. There are two possibilities for the origin of the micropulses which are seen in slow pulsars. They could be due either to time variation of the emission beam or to an angular effect. If the emission mechanism does not depend on period, then in the first case structure would be seen on the same time scale in pulsars of all periods. An angular effect would scale with period and be seen on much smaller time scales in millisecond pulsars. The rotation periods of millisecond pulsars are three orders of magnitude smaller than those typical of the slow pulsars. A study of the statistics of the individual pulses of millisecond pulsars allows comparison of the time and angle scales of the emission in the two classes of objects. In addition, a single pulse study of millisecond pulsars may give information about the emission region or mechanism, and how it relates to that in slow pulsars.

The distributions of individual pulse energies for most normal pulsars have maxima somewhat below the mean pulse energy, and are skewed, extending to 4 to 10 times the mean (Hesse & Wielebinski 1974, Backer 1971). The giant pulses of the Crab pulsar discussed in Chapter 5 are exceptional, and have been observed for many years (Heiles, Campbell & Rankin 1970, Staelin & Sutton 1970). Phinney & Taylor (1977) placed strong limits on the existence of giant pulses from other pulsars, using data from Hulse & Taylor (1975). In this chapter, single pulse observations are presented for two millisecond pulsars: PSRs B1534+12 and B1937+21. The pulse-to-pulse energy distribution is analyzed for PSR B1534+12. Observations of giant pulses in PSR B1937+21, are discussed in detail. These were first displayed at 430 MHz and

1400 MHz by Wolszczan *et al.* (1984), while Sallmen & Backer (1995) and Backer (1995) have highlighted their peculiar properties. A separate analysis of the giant pulses from this pulsar has been carried out by Cognard *et al.* (1996).

6.3 Observations & Data Reduction

The data discussed in this chapter were taken at Arecibo on 1992 November 19-22. Signals from the two circular polarizations at 430 MHz were passed through 500 kHz (B1534+12) or 250 kHz (B1937+21) filters and split into real and imaginary parts. This dual polarization complex voltage data was recorded with 2-bit sampling at 1 or 2 μs respectively, or twice the Nyquist frequency. Observing using the ADAGIO package allowed us to record the data with a constant number of samples per apparent period throughout. For PSR B1534+12, which has a period of 37.9 milliseconds, we recorded $\sim$4.1 milliseconds of data for each pulse period, in a window centered on the pulsed portion of the profile. Limited by the speed with which we could write to tape, we were able to record data for 10 out of every 12 pulse periods of PSR B1937+21. These data were coherently dedispersed offline in the frequency domain, using the method described by Hankins & Rickett (1975). The length of the Fourier Transform which is involved was set by the need to include a full dispersed pulse in each transform, resulting in a loss of 3 of the 10 pulse periods for PSR B1937+21. Detection then resulted in dedispersed profiles for 7 out of every 12 pulse periods for this pulsar, and every pulse for PSR B1534+12.

For each of these pulse profiles, the cumulative intensity in windows ON and OFF the pulse were calculated and saved. A $COMPARISON$ window of the same size was located off the pulse, and a larger OFF window was also located away from the pulse. The comparison window was used to estimate the noise distribution for each pulsar, and hence the error in our determination of the energy distribution.

For PSR B1937+21, two windows were designated for both the pulse and interpulse, during the early and late halves of the emission. Two $COMPARISON$ windows of the same size were also used. Initially, only one window was used for each of the pulse, interpulse, and comparison regions, whose widths of 60 (2μs) bins were chosen to contain a large fraction of the emission in the pulse and interpulse. The presence of very strong pulses late in the pulse, where the average emission is low, caused us to increase the size of the windows to 120 bins, to include essentially all of the emission. These larger windows were each split into two 60 bin windows to investigate the possibility that we were selecting against a significant number of narrow late pulses by using only one wide window. At the same time as the energy

calculation, the pulse profile was saved for any pulse in which the average energy per bin in any ON window exceeded that in the OFF window by a given threshold.

$$\frac{E_{window}}{N_{window}} - \frac{E_{Off}}{N_{Off}} > \sqrt{2}T$$

The threshold T used was 5-6 times the estimated error in the mean for 1 pulse, $\overline{E}$. The windows and thresholds used above were determined using an average profile created using a limited amount of data.

6.4 Analysis of PSR B1534+12

The above procedure resulted in an energy *vs.* time series for each of the ON, OFF, and $COMPARISON$ windows, for a given observation. The analysis presented for this pulsar was performed for areas of data for which the effects of interstellar scintillation were judged to be approximately constant.

Figure 6.1 displays the energy histogram obtained for PSR B1534+12 using 12000 pulses. The dotted line shows the distribution of energies in the comparison region (which is centered on zero energy, as expected), while the solid line displays that for the pulse energies. The vertical line indicates the location of the average pulse energy. This distribution has a shape similar to that for some slow pulsars, such as PSR B0950+08 (Backer 1971). However it extends out to about 15 times the average pulse energy, which is not typically found in slow pulsars.

The correlation function for the pulse energies drops to zero for a separation of three pulses, and indicates that there is about 25% correlation between adjacent pulses. The time scale of fluctuations is therefore longer than a pulse period, in contrast to the observations of giant pulses presented here and in Chapter 5. There are no periodicities in the power spectrum of these energies.

The average of the autocorrelation functions for a subset of strong individual pulses was calculated and compared to the autocorrelation function of the average pulse. The results are shown in the first panel of Figure 6.2. The effects of the off-pulse distribution have been removed from the two ACFs, and they have been normalized to the same value at lag 1. These indicate that the individual pulses (dotted line) are somewhat narrower than the average, with a characteristic width of 160 μs *vs* 250 μs. There is no evidence for a break in the ACF on very short time scales and so no evidence for microstructure scaled by the pulse period. There may be evidence for a break at $\sim$ 300 μs, which is not that different from the time scales of microstructure in slow pulsars. Even if there is no break, the characteristic width of 160 μs is also of about this scale. The second panel displays the ACF of the individual pulses, at

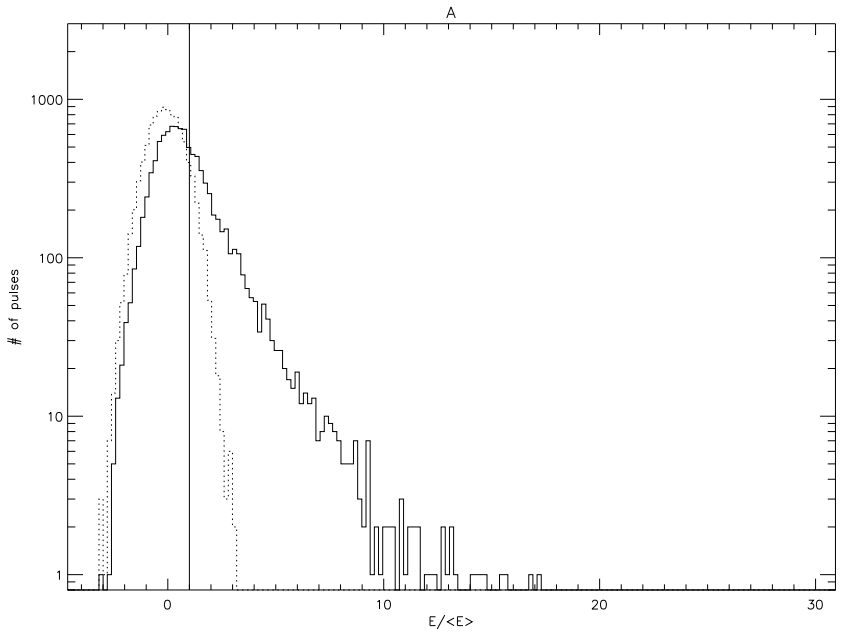

Fig. 6.1.— Pulse energy distribution for PSR B1534+12. The number of pulses for a given energy E are plotted against the pulse energy. The energy axis is in units of the mean pulse energy, $< E >= 7.6$ mJy. The dotted line shows the distribution of comparison energies, while the solid line displays the distribution for the pulsed emission. The solid vertical line represents the mean pulse energy.

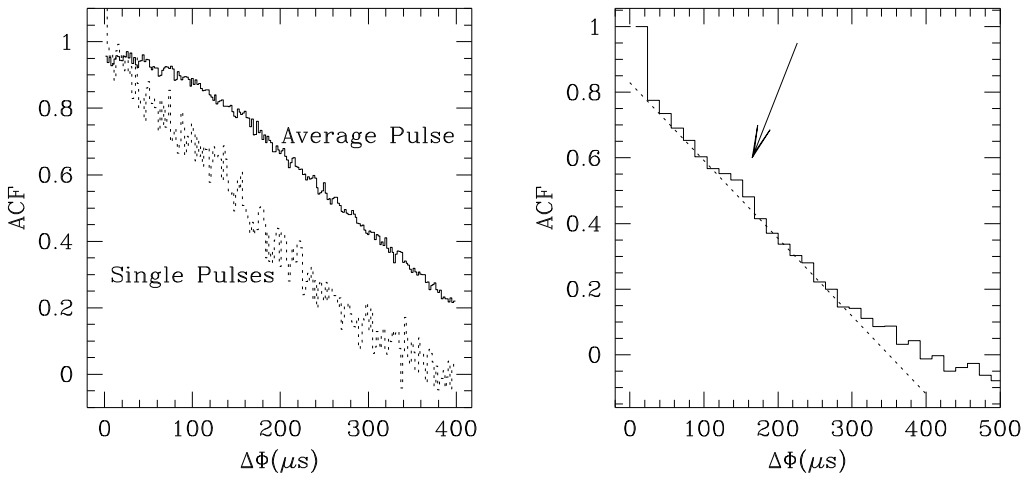

Fig. 6.2.— ACF of individual pulses from PSR B1534+12. The autocorrelation function is displayed for both the individual pulses (dotted line) and the average pulse (solid line) in the first panel. The individual pulses are narrower than the average, but no features are seen on short time scales to indicate that microstructure scales with pulse period. The second panel displays the ACF of the individual pulses at lower resolution, and exhibits a feature at $\sim 150\mu$s.

lower resolution. There is some evidence for an excess at about 150 μs, indicating a possible characteristic time for the emission.

6.5 Analysis of PSR B1937+21

The two windows for the pulse, interpulse, and comparison ranges were combined to produce one energy *vs.* time series for each. These raw time series, $E^R_{[P,IP,C]}(t)$, contain gaps, since we only have profiles for 7 out of 12 periods. The raw series for the OFF window was smoothed, and this baseline level was removed from the series for the other windows, after normalization to energy per bin.

$$E_{[P,IP,C]}(t) = \frac{E^R_{[P,IP,C]}(t)}{N_P} - \frac{< E^R_{Off}(t) >_{\Delta t}}{N_{Off}}$$

The off energy series was smoothed over 4001 data points in the series, corresponding to a time Δt of about 10 seconds. This procedure allows removal of the off-pulse level which slowly varies due to the changing zenith angle of the source during the observation. In addition, an interstellar gain factor was calculated by smoothing the series for the pulse plus interpulse over a similar time scale, $G_{ISS} = a/\overline{a}$ with $a =< E_P(t) + E_{IP}(t) >_{\Delta t}$. This was used to eliminate the slow variations present in the data and expected to be due to interstellar scintillation.

We now consider four observations, taken on four separate days, containing a total of the 757,876 pulses. For each of these observations, the corrected energies, $E^C_{[P,IP,C]} = E_{[P,IP,C]}/G_{ISS}$ were used to determine the mean and rms (distribution width) for each energy series, in addition to the modulation index. The *rms* of the comparison distribution relative to the mean main pulse energy, $\sigma_c/\overline{E}_P$ ranges from 1.1 to 1.4. This means that the signal to noise of the observations is generally low, but somewhat variable. The average interpulse energy is $\overline{E}_{IP} = 0.6\overline{E}_P$ in all cases.

The modulation index $m_{P,IP}$ of a series pulse or interpulse energies $E_{[P,IP]}(t)$ is given by equation 1.1, and reflects the variability in the time series. In slow pulsars, those which have high modulation indices typically have energy distributions which extend to higher energies than those with smaller modulation indices. For the observations discussed here, $m_P \sim .51 - .55$, $m_{IP} \sim .59 - .65$. Thus the interpulse emission is more modulated than that from the main pulse, and the overall level of modulation is less than 100 %. If the early and late halves of the emission are treated individually, we find $m_{P_1} \sim .57 - .59$, $m_{P_2} \sim 1 - 1.5$, $m_{IP_1} \sim .67 - .73$, and $m_{IP_2} \sim 1.4 - 1.5$. Thus more of the fluctuations take place in the late half of the pulse emission.

The corrected energies were used to create a histogram of number *vs.* energy for each observation. Figure 6.3 displays the energy histogram for 757,876 pulses of

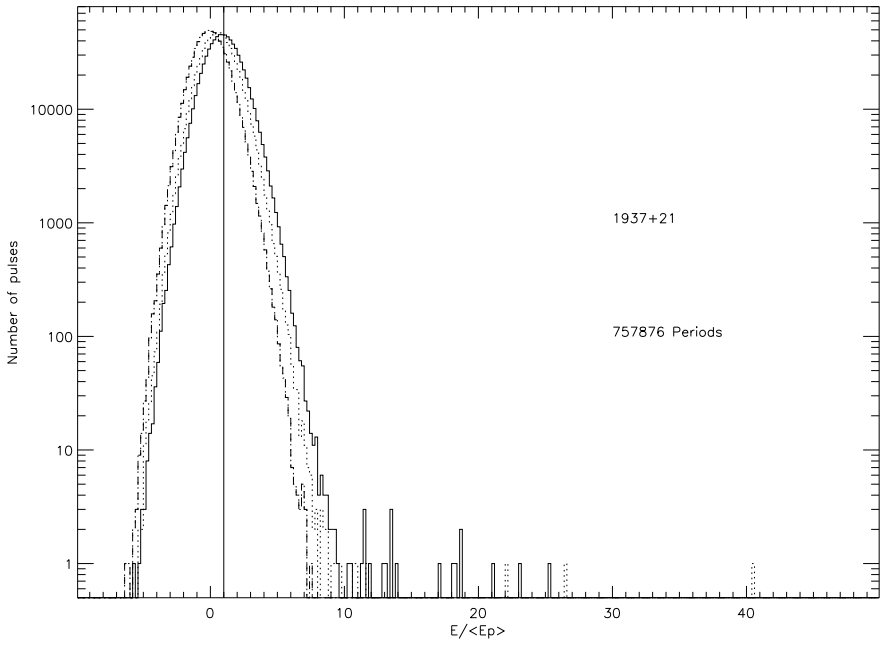

Fig. 6.3.— Probability density distribution of pulse energies. The Number of pulses *vs.* Pulse energy is displayed for 757 876 pulses of data for PSR B1937+21. The energy axis is in units of the average energy in the main pulse. The dashed line shows the distribution of comparison energies, indicating the distribution of noise. The main pulse and interpulse distributions are indicated by the solid and dotted lines, respectively.

data for PSR B1937+21, which includes information from four separate observations. The energy axis is in units of the average energy in the main pulse. This allows the intensity variations from day to day due to ISS to be removed. They will, however, have an effect on the width of the comparison distributions for the four observations relative to this energy scale. In addition, the number of 6 sigma pulses will vary for the four observations, at least in part because the cutoff is different in terms of the mean energy. The dashed line shows the distribution of energies in the comparison region (which is centered on zero energy, as expected by construction, since $E_C \sim E_{Off}$), while the solid and dotted lines display the energy distributions of the main pulse and interpulse respectively. The width of the comparison distribution is an indication of the noise present in our energy determinations.

It is clear that the SNR is poor, in that the average main pulse energy is significantly less than the width of the comparison distribution. This implies that a typical single pulse cannot be observed. The energy distribution for the pulse and interpulse emission is, however, broader than the comparison distribution, and is shifted from zero, due to the presence of pulsed emission. This portion of the distribution extends

to energies about 10 times the average pulse energy. There are, however, several main pulses and interpulses which are much stronger than the typical ones. Individual pulses of this strength are seen only here and in the Crab pulsar. Note that the energy scale is in units of $\overline{E}_P$. This means that the strong interpulses are stronger by a factor of 1.67 relative to the average interpulse energy $\overline{E}_{IP}$. There are 23 main pulses and 12 interpulses with energies more than 6 sigma above the mean energy for their respective observations (after correction for interstellar scintillation). Of these, 21 main pulses and 10 interpulses met the threshold for output during processing, and so were extracted and examined. One each of these strong pulses and interpulses are displayed in Figure 6.4, along with the average for the observation which included the strong pulse. The vertical lines on the average profile indicate the limits of the windows used to analyze the energies. Strikingly, the strong pulses are always located at the trailing edge of the average pulse components. Thus we found it necessary to ensure that this region was included in the windows used to calculate the energies, although little of the average pulse energy is contained in this region.

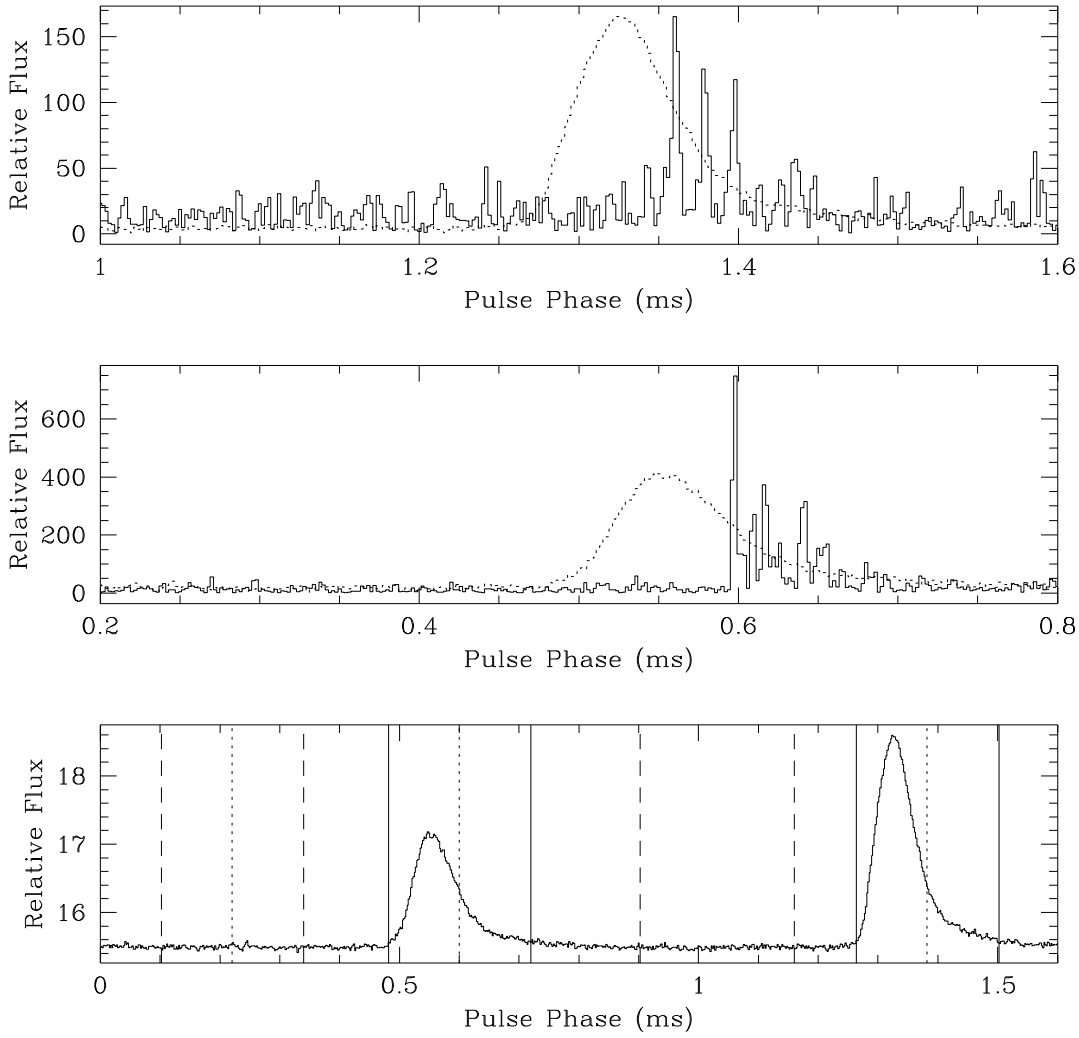

Fig. 6.4.— Very strong main pulse and interpulse from PSR B1937+21. The bottom panel displays the average pulse profile, containing 196 868 pulses. The solid vertical lines indicate the boundaries of the *ON* windows in the pulse and interpulse regions. The dashed vertical lines indicate the boundaries of the comparison region and the region used to determine values off the pulse. The dotted vertical lines indicate the separation of the pulse, interpulse, and comparison windows into two halves, as discussed in the text. The top panel shows one of the very strong pulses, while the middle panel displays a very strong interpulse. The Relative Flux scale is the same for the three panels. In each of the top two panels, the dotted line shows the location of the average pulse profile relative to the individual pulses, although here the average profile is no longer on the same flux density scale.

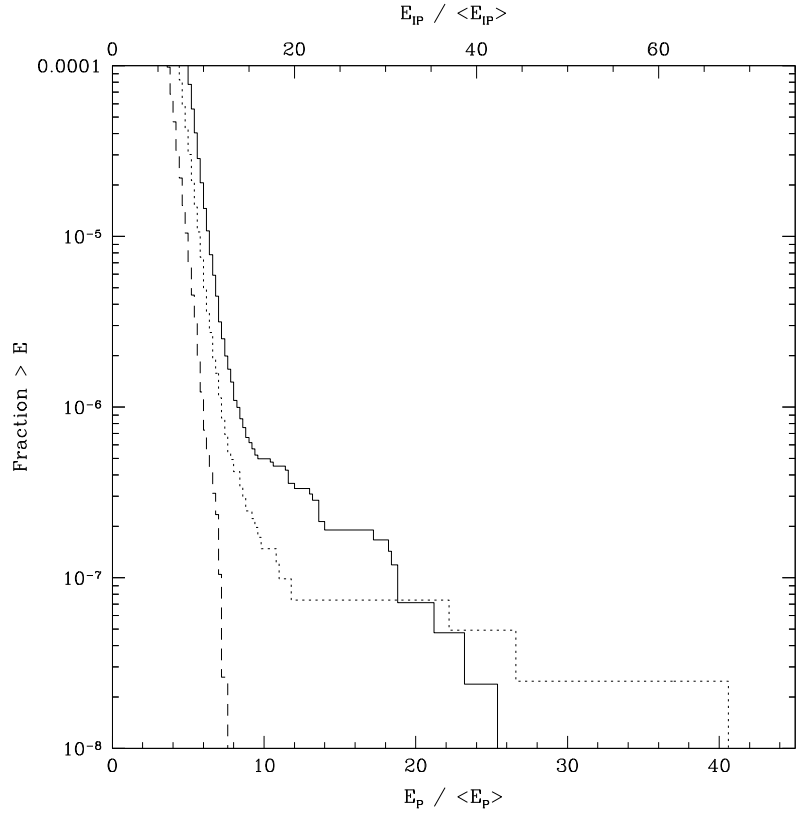

Fig. 6.5.— Integrated probability density distribution for Very strong pulses. The cumulative Number of Pulses *vs.* Energy is displayed for 757 876 pulses of data. The bottom axis is in units of the average main pulse energy, while the top axis is in units of the average interpulse energy. Solid, dotted, and dashed lines display the main pulse, interpulse, and comparison distributions.

6.5.1 Giant Pulses

The strong pulses, like the average profile, are broadened by interstellar scattering. The impulse response of the interstellar medium (ISM) is given by the one-sided exponential in equation 1.19, for a simple single thin screen model of scattering. The presence of the strong pulses only in this exponential scattering tail due to the interstellar medium raises the possibility that they are not intrinsic to the pulsar, but due to some propagation mechanism in the ISM. But this cannot be the case. There is no pulse to pulse energy correlation at the 1 percent level, and no correlation between main pulse and preceding or following interpulse energies at the 2 percent level. Inspection of the strong pulses also revealed that the giant main and interpulses occur independently. This means that the effect has a time scale of less than one pulse period, or approximately 1.6 ms, which is much shorter than any time scale on which the ISM is expected to vary. The time scale for the diffraction pattern to change is many seconds at 430 MHz, for example (Cordes *et al.* 1990).

Figure 6.5 displays the cumulative fraction of pulses with energy $E < \overline{E}$. The scale on the bottom axis is in terms of $\overline{E}_P$, while that on the top axis is in terms of $\overline{E}_{IP}$. There are 46 main pulses which occur with energy $E_P > 8\overline{E}_P$, 21 with $E_P > 10\overline{E}_P$, and 13 with $E_P > 13\overline{E}_P$. There are no main pulses with energies $E_P > 26\overline{E}_P$. In the interpulse distribution, on the other hand, there are 3 interpulses with energies $E_{IP} > 30\overline{E}_{IP}$. There are 20 interpulses with energies $E_{IP} > 13\overline{E}_{IP}$. The interpulse distribution becomes significantly contaminated by the comparison distribution below this point. It seems, however, that more strong interpulses occur at this level than do strong pulses, and that the interpulse distribution extends to higher energies. The fact that $m_{IP} > m_P$ is consistent with this picture. If much of the modulation is due to these strong pulses or interpulses, the larger modulation index for interpulses implies either that there are more large interpulses, or that they occur with larger energies, or both. This behaviour is not confirmed by the larger data set of Cognard *et al.* (1996, who find that the fractional rate of occurrences are the same for both the main pulse and the interpulse.

The strong pulses shown in Figure 6.4 occur tens of microseconds later than the peak of the average pulse emission. This behavior is consistent in all the strong pulses studied. Because the strong pulses occur only in the exponential scattering tail of the average profile, they are actually much stronger relative to the average energy in that portion of the profile than is apparent in the energy scale of Figure 6.3. This makes their energies hundreds of times that of the average. This is shown in Figure 6.4, as all profiles are on the same relative flux scale.

Since these giant pulses only occur late relative to the average emission, they should produce extra modulation in the second half of the emission. This is consistent with the 100 % modulation for this portion of the emission region which was found earlier. These pulses evidently cause a significant fraction of the energy modulation for this window.

The phase of the 21 and 10 very strong main pulses and interpulses relative to the arrival of the average pulse was determined by cross correlating their profiles with the appropriate average profile. The strong pulses associated with the main pulse occur with a delay of $48 \pm 4.4\mu$s, while the strong interpulses occur with a delay of $66 \pm 4.6\mu$s. Both these delay values are larger than those quoted by Cognard *et al.* (1996), although the difference is $> 3\sigma$ only for the interpulse. Inspection of Figure 2 of Wolszczan *et al.* (1984) indicates that at 1384 MHz the strongest main pulses appear to arrive latest, with the strongest displayed pulse offset $45 - 50\mu$s from the average. It is intriguing that the delays between the average profile and the strong main pulses correspond to the location of the small secondary maxima in the average 1410-MHz main pulse and interpulse profile displayed in Figure 3.25. These

secondary maxima are also visible as shoulders in the 800-MHz profile displayed in that figure. Any such features in the average 575-MHz profile are hidden by the exponential scattering tail.

The averages of the very large main pulses (21) and interpulses (10) were generated. This was done by determining the relative phases of the averages for the four observations by cross-correlation. The individual pulses from the four observations were then shifted relative to each other by these same amounts, and then averaged. No attempt was made to further align the individual pulses. Several attempts were made to fit these average profiles by simple functions. The impulse response of the interstellar medium discussed earlier suggests use of a one-sided exponential, $exp(-t/t_{exp})$. A fit made by requiring the area of the pulse (or interpulse) average to equal the area of this exponential, and requiring the same decay time for both (since they pass through the same ISM) is shown in the top panel of Figure 6.6. This simple model works remarkably well. The interstellar broadening time $t_{exp} \sim 52\mu$s found here is somewhat longer than $\sim 30\mu$s time scale for broadening τ_B expected for this pulsar (Cordes *et al.* 1990). This simple model cannot, however, account for emission on the leading edge of the average. Such emission must be due either to the fact that the ISM is not a thin screen, or that the intrinsic average pulsar emission for these pulses is not an impulse. A simple addition to the thin screen model involves two thin screens. The appropriate fitting function is then the convolution of two exponentials, and is of the form $exp(-t/t_2)[1-exp(-t/t_1)]$. (unless $t_1 = t_2$, then the form is $t\ exp(-t/t_1)$). This model of the ISM yields the fit shown in Figure 6.6, with $t_1 \sim 14\mu$s and $t_2 \sim 36\mu$s. This does a better job of matching the emission on the leading edge, and drops to $1/e$ of its maximum value approximately 47μs past the peak. Fitting using a smoothed one-sided exponential approximates the effect of individual pulses having exponential shapes (each one being intrinsically an impulse), but with some dither in phase from pulse to pulse. Individual pulse studies of slow pulsars have revealed that the phases of individual pulses do vary within the pulse window, indicating that this is a reasonable model. A reasonable fit here is obtained with $t_{exp} \sim 42\mu$s, and rectangular smoothing lengths of 30μs and 18μs for main pulse and interpulse, respectively. Once again, the leading edge emission is accounted for, as can be seen in Figure 6.6. The value of t_{exp} found for this model is closest to the expected $\tau_B \sim 30\mu$s. These last two models are better fits to the data than the simple exponential, and produce similar reduced chi squared values. These values are not one, because the average profiles are quite noisy. The portion of the chi squared value associated with the interpulse average is significantly larger, which is not surprising given that it appears noisier. These averages are noisy because they contain a small number of strong pulses, each of which contains sharp structure on short time scales. In contrast to these results,

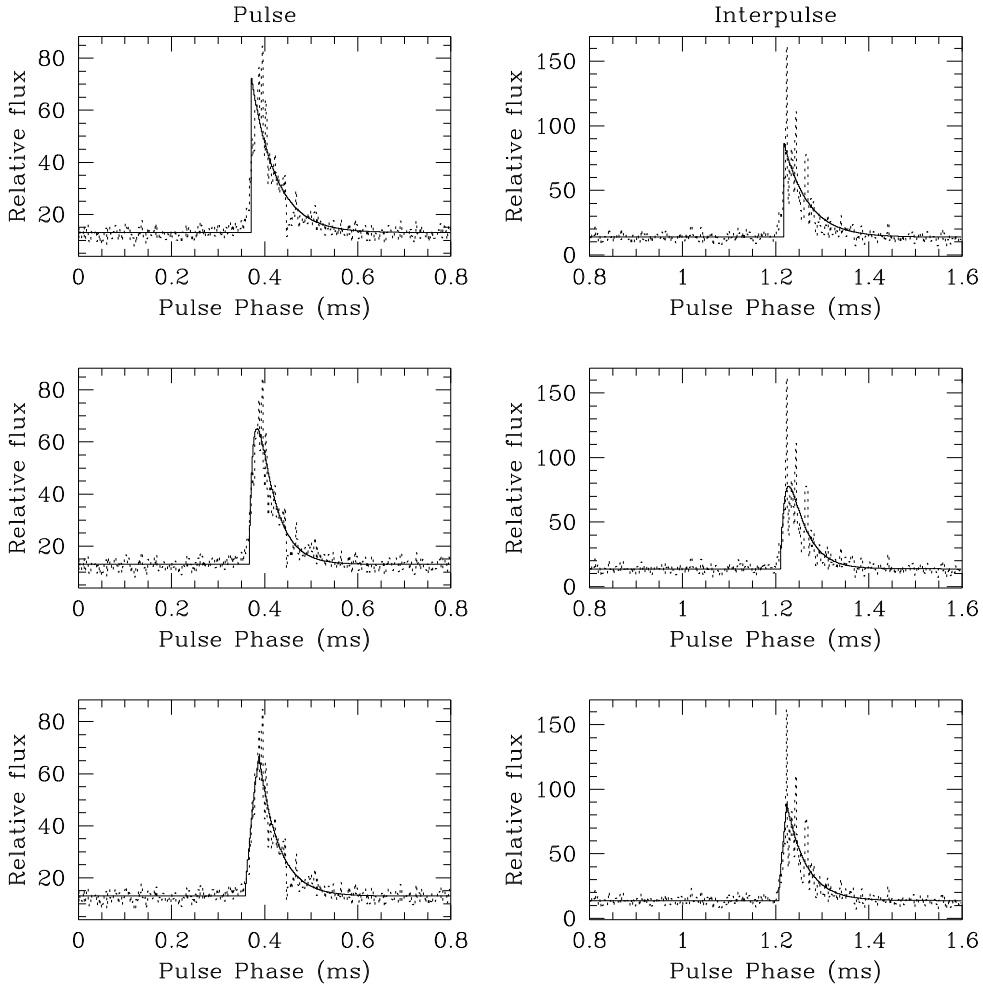

Fig. 6.6.— Shape of very strong pulses in PSR B1937+21. The dashed lines for all panels on the left hand side display the average profile for 21 very strong main pulses. The dashed lines for all panels on the right hand side display the average profile for 10 very strong interpulses. The solid lines in the top two panels are for the best fitting model of the form $e^{-\frac{t}{t_{exp}}}$. In the middle two panels, the solid lines are for the best fitting model for the convolution of two exponentials, while the bottom two panels contain the model for exponentials with smoothing.

Cognard *et al.* (1996) found no evidence for jitter in giant pulse arrival times; their giant pulse average has a rise time of 5 μs, and their exponential decay time of 25μs is comparable to the expected value. More giant pulses were included in their averages, which may account for some of the discrepancy.

6.5.2 Temporal variations

The very strong pulses discussed above show extremely sharp features. From the impulse response of the ISM we expect an exponential envelope, plus noise with the number of degrees of freedom related to the time-bandwidth product, $\sqrt{Bt}$, here

corresponding to intensity modulations of 71%. This is in general agreement with the observations. Emission intrinsic to the pulsar could be even stronger, and as sharp as a microsecond. If this were true, it would argue that microstructure scales with period, and is thus largely an angular effect. Alternatively, most of the structure shown could be due to amplified system noise.

A reasonable model of pulsed emission is the amplitude modulated noise (AMN) model of Rickett (1975). In this model, the pulsar field $g(t)$ is given by $g(t) = a(t)n(t)$, where $a(t)$ is a real amplitude modulation, containing any subpulse or micropulse time variations, and $n(t)$ is an uncorrelated noise process. Then the intensity $I(t)$ is given by $I(t) = [\eta T_{sys} + |g(t)|^2]$, and contains the fluctuations of $a(t)^2$. But the error ΔI in our estimation of $I(t)$ is proportional to $I(t) = [\eta T_{sys} + |g(t)|^2]$, which contains a contribution due to the source (pulsar). When $a(t)$ is large, *ie* the pulsar is extremely strong, ΔI is also large. So for extremely strong pulses, sharp fluctuations may be due either to system noise amplified by the source, or to intrinsic fluctuations of the pulsar.

The main pulse shown in Figure 6.4 contains a remarkable triple feature. It is possible that these are all due to one impulse from the pulsar, separated due to varying propagation paths in the ISM. The exponential envelope expected for the impulse response of the ISM is based on the Gaussian probability of scattering into an angle theta, and is thus true only in a time averaged sense. Instantaneously, individual paths with different scattering delays and amplitudes may be relevant. This would also lead to fluctuations in the pulse profile that don't appear noise-like.

A classic test for microstructure is to calculate the autocorrelation function (ACF) of the pulse profile data. Changes in the slope of the ACF at a given lag $t_\circ$ indicate the existence of significant structure on time scales $\lesssim t_\circ$. Here, however, we don't really have the signal to noise to test for microstructure in this fashion. We must find another way to determine the significance of the sharp fluctuations in our data.

Are the sharp fluctuations in our strong pulses due to real variations in $a(t)$, or are they consistent with amplified system noise? If they are consistent with amplified system noise, then there is some true underlying 'smooth' distribution, with a realization of system noise superimposed upon it. Let $< I(t) >_{\Delta t}$ be a running mean of $I(t)$ calculated over Δt, and $I_n(t, \Delta t) = I(t)/ < I(t) >_{\Delta t}$. Then if $< I(t) >_{\Delta t}$ is the true underlying distribution, and any extra fluctuations are due to system noise, then the probability density function (PDF) of $I_n(t, \Delta t)$ in the region of the pulse will be the same as the PDF of the system noise in a region off the pulse. If Δt is 2μs, however, then $< I(t) >_{\Delta t} = I(t)$, and $I_n(t, \Delta t) = 1$, so its PDF is a delta function, and very unlike the PDF of the off pulse system noise. If Δt is large compared with the time scale of true fluctuations in $a^2(t)$, then the PDF of $I_n(t, \Delta t)$ will contain an

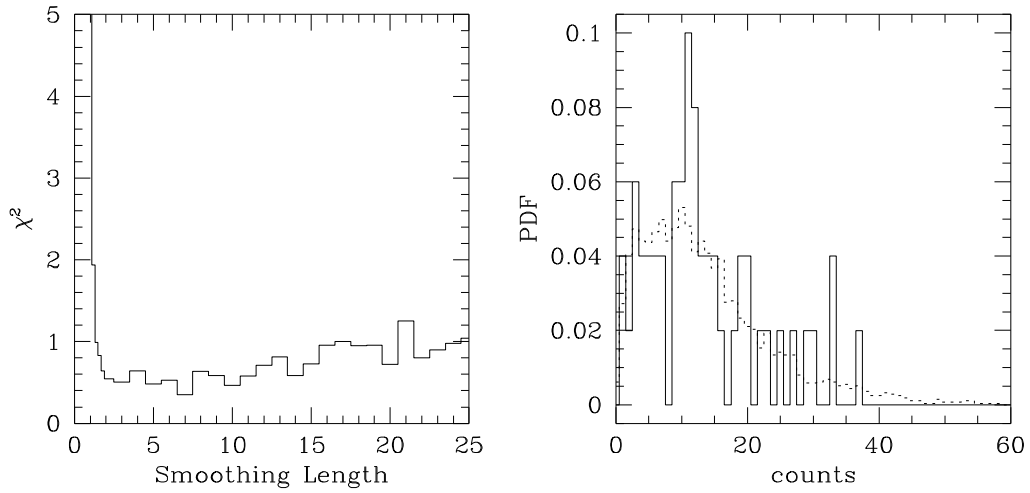

Fig. 6.7.— χ^2 of PDF for a very strong pulse. A running mean of the data for this pulse was calculated over Δt, and this was used to normalize the data at each point. The probability density function of the resulting values in a region centered on the pulse was compared to the corresponding PDF for a region away from the pulsed emission. The first panel displays the χ^2 quantity of this comparison for a variety of smoothing lengths Δt. A distinct minimum for a given Δt would indicate emission with that characteristic time scale. The second panel displays the PDF for the on-pulse region (solid line) and the PDF for the off-pulse region (dotted line) for the smoothing length with the smallest χ^2.

excess at large values relative to that of the off pulse system noise. So comparison (in a χ^2 sense) of the PDF of $I_n(t, \Delta t)$ with the off pulse PDF for a variety of Δt values will produce a minimum in the chi squared distribution at Δt equal to the time scale of fluctuations in $a^2(t)$. This is similar to analysis performed by Bartel and Hankins (1982). They compared the PDF of I_n to the expected exponential distribution e^{-I_n} for noise. Here, we compute the off PDF explicitly.

For several strong pulses and interpulses, the above procedure was performed for a variety of smoothing lengths. A typical example of the results is shown in Figure 6.7. The expected peak in the chi squared distribution at a smoothing length of one bin (2μs) is clear, but there is no well defined minimum. This implies that we are unable to detect any intrinsic variations on these times scales. It is still possible that there are intrinsic variations on time scales shorter than can be resolved.

This result, coupled with the fact that the average of the strong pulses is consistent with the impulse response of the interstellar medium plus phase jitter, indicates that these very strong pulses are extremely sharp; narrower than our 2μs resolution.

6.6 Discussion of Giant Pulses

6.6.1 Comparison to the Crab Giant Pulses

Giant pulses have been found only in this pulsar and the Crab pulsar. Many of their properties are similar, while others are strikingly different. The delayed nature of the giant pulses in PSR B1937+21 is very different from the observed behaviour of the Crab giant pulses. Lundgren (1994) finds no offset between the Crab giant pulses and the average, although Friedman & Boriakoff (1990) find that the giant pulses may occur *earlier* in this object.

The giant pulses in the Crab pulsar are energetically important, as was discussed in Chapter 5, contributing a larger fraction of the total energy at higher frequencies. For the 1937+21 data presented here, the main pulses with energy $E_P > \overline{1}0E_P$ contribute less than 0.05% of the total main pulse energy. This is insignificant, despite the fact that each pulse is very large relative to the average at its phase. The interpulses with energy $E_{IP} > 13\overline{E}_{IP}$ contribute about 0.05% of the total interpulse energy. Thus it seems as though the strong interpulses are slightly more important energetically, but still insignificant at 430 MHz. They may be more important at higher frequencies, however, if they behave as do the giant pulses in the Crab.

Cognard *et al.* (1996) noted that the giant pulses occur at similar rates in the two pulsars. Their data, and Figure 6.3 suggest that the giant pulses may form a separate distribution in this object, just as they do in the Crab pulsar (Lundgren *et al.* 1995). No correlations have been found between adjacent or nearby pulses or interpulses for either pulsar. The time scale of the effect producing the large pulses is extremely short, less than one spin period.

The pulse-interpulse morphology of the average PSR B1937+21 profile is similar to that of the multi-wavelength components in the Crab profile. Any conclusions drawn based on this similarity are highly speculative, especially since these two components of the Crab may be produced in a different location in the magnetosphere than the radio precursor. For either pulsar, attempts at profile classification using the methods successful for normal pulsars encounter difficulties.

6.6.2 Models of the Emission Beam

One of the most striking features of the strong pulses in PSR B1937+21 is that they are delayed relative to the average of the weaker pulses. As noted above, the shape of the pulse profile in the Crab pulsar does not change for the giant pulses. However, shape changes with intensity have been reported for some slow pulsars.

Krishnamohan and Downs (1983) reported shape changes with intensity in the Vela pulsar, in which the stronger pulses arrived progressively earlier. They modelled these shape changes as due to the presence of a number of components which fluctuate independently (and are allowed to drift in position with intensity). They concluded that each component is produced at a different distance from the neutron star, and that these distances may vary with the intensity of the component. This model, combined with the rotating vector model for each component, correctly explains the changes in polarization position angle with pulse intensity. In this view, emission altitude is related to pulse intensity.

McKinnon and Hankins (1993) found shape variations with intensity in PSR 0329+54. Once again, the stronger pulses arrive earlier. For this pulsar, the assumptions of Krishnamohan & Downs (1983) would result in components whose emission altitudes conflicted with that expected from Rankin's (1990) classification of the pulsar, if emission fills the open field line region. Instead, McKinnon and Hankins interpreted the data as an indication of a 'hot' spot on the surface with a varying location. The strong core component is more aligned along the line of sight when it appears earlier in the pulse profile, and so appears more intense. In this model the hot spot moves by less than 43 m, where the diameter of the polar cap is 240 m. Thus correlations between pulse intensity and pulse phase have been explained in two very different ways in the above two cases.

In the case of PSR B1937+21, we have an offset between the large pulses and the average profile, implying a different emission location for the large pulses. The temporal offset could be due either to different altitudes of emission, horizontal separation at a constant altitude, or a combination of the two effects. A temporal offset of 50μs corresponds to a difference in altitude of $c\Delta t/(1+\sin\alpha) \sim 7.5$km $\sim R_{NS}$, about one neutron star radius. The light cylinder for this pulsar is at a distance of only 75 km $\sim 5R_{NS}$. Thus a change in altitude of 7.5 km for the two types of emission is a significant fraction of the distance to the light cylinder. Such a change is altitude would be somewhat surprising since Cordes and Stinebring (1984) used multifrequency measurements to determine that all emission from this pulsar arises from the same altitude to within ± 2 km. The same 50μs offset could be explained by a separation of about 11° in phase. This corresponds to $2-3$ km on the neutron star surface, and is well within the size of the polar cap predicted by the last open field line. If this were the case, then the $\sim 30\mu$s jitter between various large pulses corresponds to ~ 1.5 km motion of this region.

The fact that the giant pulses in the Crab pulsar appear to come from a separate distribution implies that there is a different emission mechanism, or different emission location within the magnetosphere, or possibly both of the above, for the giant and

weaker pulses. However, lack of an offset in the timing residuals between giant pulses and the average pulse profile suggests that the emission region is the same.

The temporal offset of the large pulses in PSR B1937+21 strongly suggests a different emission location for these pulses, as discussed above. If the large pulses come from a different location, they may also be produced via a somewhat different emission mechanism. Their narrowness and temporal offset perhaps point to some sort of maser mechanism.

Due to the temporal separation, these strong pulses cannot simply be due to a temporal modulation of the pulsar beam. It is possible, however, that the very strong pulses are due to a separate narrow component with some temporal modulation. In this case, the emission is clearly in a high state for less than one pulse period. The above analysis of the sharp rise in the giant pulse profile indicated that the width of the large pulses is only a few μs (the width of the interstellar scattering tail makes it difficult to be precise), and perhaps much less. The average size of the beam corresponding to this component is reflected in the arrival time jitter between pulses. The 3σ arrival time variation among these pulses is about 15μs, while the model using pulse jitter and the ISM indicates such variations could be as much as 30μs. If each large pulse is broadened solely due to interstellar propagation, then the high state duration is only a few microseconds, and is smaller than this average beam size. If, on the other hand, the width of the individual large pulses is approximately the same as the jitter between pulses, the high state duration lasts at least as long as this $15 - 30\mu$s, and possibly almost as long as a period.

If these individual pulses are due to an angular modulation, then the measured width of their average corresponds to a beam less than $\sim 20\mu$s wide (as determined from the rise time of the giant pulse average), and possibly much smaller. For giant pulses with beam width $w_{\rm gp}$, occurring a fraction f of the time, the wobble perpendicular to the trajectory of the line of sight (in the ϕ direction) is $w_{\rm gp}/(Pf)$. Then a jitter of 30 μs $\sim 6.75^\circ$ along the observer's line of sight implies that for the same jitter in the ϕ direction, giant pulses would be observed much more frequently than is the case. For a 1 μs beam, about 1 of every 30 pulses is expected to be giant! This cannot be reconciled with the observed low occurrence (of order 1/10000) of giant pulses for a circular beam, unless the beam width is less than 0.003μs. This corresponds to a region with a radius of only 3 cm on the neutron star surface.

Thus the strong pulses in PSR B1937+21 are probably produced in a different region than the average weaker pulses, possibly in a temporally modulated separate component. It is intriguing that similar effects are found in the main pulse and in the interpulse, since these are supposedly two separate poles. On the other hand, the main pulse and interpulse features of the Crab pulsar are believed to originate high in

the magnetosphere, with both components resulting from emission from a single pole (Romani & Yadigaroglu 1995), and some authors believe this model may be extended to other young radio pulsars (Manchester 1996). If the emission does originate from two poles, then the mechanism is stimulated in both places by the properties of the pulsar. It is surprising, however, that such a phenomenon could produce not only strong pulses in both poles, but the similar relative delays. These relative delays are not equal, however, so the two poles need not be identical.

6.6.3 Further Studies

Since the very strong pulses discussed in this paper occur in the scattering tail, data at higher frequencies such as 1400 MHz would make possible better measurements of the individual pulse widths, which would help to constrain the models for the emission of these strong pulses, as well as clarifying the relationship between these very strong pulses and the narrow trailing components visible in the average pulse profile. In addition, if these events are related to the Giant Pulses in the Crab pulsar, they may become energetically more important at higher frequencies, and thus be easier to study. However, inspection of archival data taken in Arecibo showed no evidence for giant pulses at 1400 MHz, at the level of about 30 times the average pulse energy (corresponding to energies ~ 100 times the average energy on the trailing edge of the pulse).

Similar studies of other millisecond pulsars can tell us if these events are isolated to this object, or whether they are common in millisecond pulsars. Some millisecond pulsars have profiles with sharp features similar to that of this pulsar, while others contain emission spreading over much of a pulse period (as would be expected from the width of the last open field lines for these short period objects). Perhaps the presence of these events in PSR 1937+21 is related to the unexpected sharpness of its components. Cognard *et al.* (1996) suggest that the unique properties of the Crab pulsar and PSR B1937+21 may be due to the large strength of the magnetic field at the light cylinder, $B_{LC} \sim 10^6$ Gauss. All other pulsars have weaker B_{LC}. Pulsar B1957+20 has the next strongest B_{LC}, of $\sim 4 \times 10^5$ Gauss. Early analysis of some 430-MHz data on PSR 1957+20 revealed no similar features, although this object is significantly weaker, and strong pulses with energies above 125 times the average energy would be required for such events to appear. Pulsar J0437−4715 is nearby and very strong. Single pulse studies have revealed that the strongest individual pulses are very narrow, and preferentially located within the average profile, resulting in profile variations with intensity (Anderson *et al.* 1996, Ables *et al.* 1997). No truly giant pulses have been seen, nor is there any evidence for microstructure or a preferred time scale for the emission (Jenet *et al.* 1998).

6.7 Conclusions

Single pulse observations of two millisecond pulsars were presented in this chapter. The giant pulses of PSR B1937+21 are similar to those found in the Crab pulsar. They are, however, *delayed* relative to the average pulse profile, and correspond to features on the trailing edges of the components in high frequency average pulse profiles. This suggests that they come from a different emission region, and perhaps are due to a somewhat different emission mechanism. The observations are difficult to explain with a simple randomly wobbling circular beam. It is possible that giant pulses occur due to temporal modulation of a separate component of emission. No pulse to pulse or pulse-interpulse energy correlations were found, indicating that the phenomenon occurs on extremely short time scales. The delay of these pulses to a location relative to the average profile where the emission is significantly less than the peak average emission implies that they have energies hundreds of times that of the average emission in that region, although they are too rare to be energetically important at this frequency. The average pulse profile of these strong pulses is consistent with the exponential impulse response of the interstellar medium, coupled with some phase jitter between strong pulses. No giant pulses were seen in this object at 1400-MHz, and they occur uniquely in PSR B1937+21 and the Crab pulsar. The single pulses presented for PSR B1534+12 are correlated on time scales of a few periods, with no periodicities evident in the power spectrum. The pulse energy histogram extends to slightly higher energies than is typical in slow pulsars, but is otherwise similar. No evidence for microstructure which scales with period are seen.

I see my journey rolling out in front of me
It reaches on ahead far as the eye can see
"I See My Journey" by Eileen McGann

Chapter 7

Conclusions

The observations in this thesis were undertaken to investigate the current and magnetic field structure in the magnetospheres of millisecond pulsars, and to shed light on the processes responsible for radio emission in pulsars.

Part I

Normal pulsars, with spin periods near 1 second and surface magnetic fields near 10^{12} Gauss, have been successfully classified based on multi-frequency observations of their intensity profiles and polarization properties. The pulse profile morphology, coupled with the available polarization position angle information, suggests that the emission is produced in a hollow cone filling the open field line region around the magnetic axis. Shorter-period pulsars, with periods between 1 and 50 milliseconds and magnetic fields of $\sim 10^9$ Gauss, have remarkably similar emission properties. This is due to the fact that the accelerating voltage, believed to play an important role in the emission process, is proportional to B/P^2 and is therefore similar for the two classes of objects. Millisecond pulsars do not, however, fit into the classification scheme developed for canonical pulsars.

The magnetospheric configurations of millisecond and normal pulsars can be quite different. The open field line region above the polar cap scales with $P^{-1/2}$, and is therefore much larger in the short-period objects. An emission beam filling this region should therefore be much broader. In addition, the distance to the light cylinder (which scales with P) is much less in these objects. The radio emission is more likely to originate at an altitude which is significant fraction of the light cylinder radius. Rotational sweep-back of the magnetic field and relativistic effects are also likely to be more important.

Careful polarimetric observations have been presented for nine millisecond pulsars at 575 MHz, 820 MHz, and 1410 MHz. This high resolution multi-frequency data set is the first of its kind. A few additional objects have been studied at a single frequency. As has been noted in other studies, the component widths for these objects are typically narrower than expected based on the observed distribution for slower pulsars. The relationship between core component width and pulse period that is true

for long-period pulsars does not explain the observations for these objects. To further complicate matters, the dependence of conal component widths on pulse period is poorly understood for all pulsars. The classification of pulse components into core and cone components remains uncertain, as several components which might otherwise be considered core components have flat spectra. As a result, millisecond pulsar pulse intensity profiles do not develop with frequency in the same way as do those for normal pulsars. Component separations and pulse widths change very little with radio frequency, indicating that the emission region is very compact. For radiation which fills the open field lines, only a very narrow range in altitude is consistent with the observations.

The polarization profiles of millisecond pulsars exhibit many of the features that are seen for normal pulsars: significant linear and circular polarization under some pulse components, well-defined polarization position angle curves, and orthogonal mode transitions accompanied by a decrease in the linearly polarized radiation. The radiation does not depolarize at high frequencies, however, contrary to the canonical behaviour. In addition, the distribution of slopes of the polarization position angle curves in normal pulsars has a wider range than the distribution for millisecond pulsars. Although this effect has been attributed to magnetic field distortions, a simple geometric $P^{-1/2}$ scaling of the open field line region explains the observations.

Intensity profile variations have been discovered in several millisecond pulsars. These occur on longer time scales than the traditional 'moding' behaviour exhibited by slow pulsars. The fraction of objects exhibiting profile variations may, however, be similar. In contrast, temporal variations of the fractional polarization appear to be much more common in millisecond pulsars.

The classification of millisecond pulsars is still uncertain, within the canonical models. A larger multi-frequency data set of polarization profiles for low-period objects would be useful. In particular, detailed observations of pulsars with intermediate periods of about 100 milliseconds might help to define the transition between the emission properties of the two classes of objects. Polarization data at both higher and lower frequencies could prove useful. The steep spectra of these objects makes high-frequency polarimetry difficult, and scattering effects at low radio frequencies may limit their usefulness. Observations taken with a larger telescope would assist the investigation of short-term temporal variations in the intensity and polarization profiles of these pulsars. The long-term temporal variations could be studied in more detail through intensive monitoring with a telescope of modest size.

Part II

Single pulse measurements of normal pulsars have revealed the presence of microstructure, on times scales of $\sim 10 - 100\mu$s. If this phenomenon is due to an angular effect, it should scale with pulsar period. High time-resolution observations of the single pulses of millisecond pulsars would then show a characteristic time scale of at most a few μs in these objects. If microstructure is due to a temporal variation in the emission beam, then it should be visible on the same time scales in millisecond pulsars.

The giant pulses of the Crab pulsar are unusual, since at some radio frequencies these rare pulses dominate the emission. Simultaneous observations of this object at 610 MHz and 1400 MHz revealed that the emission mechanism is broadband on this time scale. The arrival times of the giant pulses are tightly correlated between the two radio frequencies, limiting the effects of frequency dependent propagation in the magnetosphere. An emission bandwidth of at least 0.8 GHz at 1 GHz constrains models of the emission process to those which can explain its broadband nature. Both angular and temporal origins for the energy modulation are possible: we cannot distinguish between the effects of a randomly wobbling intense beam and an intrinsic change in the intensity of the emission. The pulse shapes at 1400 MHz are complex, and suggest the possibility that a single giant pulse is multiply imaged in the surrounding nebular material. These observations occurred during an epoch of extreme scattering in the nebula. A study of these pulse shapes at epochs with reduced scattering will reveal whether their characteristics are constant, or vary with the nebular scattering.

The fastest millisecond pulsar, PSR B1937+21, also exhibits the phenomenon of giant pulses, although they do not contribute as large a fraction of the radio pulse energy as is true for the Crab giant pulses. These giant pulses occur on extremely short time scales, and are unexpectedly delayed relative to the peaks in the average pulse profile. They probably coincide with the sharp trailing features seen in the 1410-MHz pulse profile. Their properties are difficult to explain with a randomly wobbling beam. A separate emission component with temporal modulation may be the origin of these pulses. Simultaneous dual-frequency observations of these giant pulses could help constrain the emission process, but will be difficult. No other pulsar is known to emit pulses which can be classified as giant. Single pulse measurements of the millisecond pulsar PSR B1534+12 show no evidence for microstructure which scales with pulse period. Characteristic time scales less than about 2μs would not, however, be seen in our data. Broadband data recorders are now being used to investigate single pulses with higher time resolution.

Many aspects of millisecond pulsar emission remain puzzling. Nonetheless, average polarization profiles and single-pulse investigations of these objects provide valuable constraints on pulsar emission geometries and processes.

References

Ables, J. G., McConnell, D., Deshpande, A. A., & Vivekanand, M. 1997, ApJ, 475, L33

Anderson, S. B., Jenet, F. A., Kaspi, V. M., Prince, T. A., Sandhu, J. S., & Unwin, S. C. 1996, in Proc. IAU Colloq. 160, *Pulsars: Problems and Progress*, ed. S. Johnston, M. A. Walker & M. Bailes (San Francisco: ASP), 211

Ardavan, H. 1992, in Proc. IAU Colloq. 128, *Magnetospheric Structure and Emission Mechanisms of Radio Pulsars*, ed. T. H. Hankins, J. M. Rankin & J. A. Gil (Poland: Pedagogical University Press), 316

Ardavan, H. 1994, MNRAS, 268, 361

Argyle, E., & Gower, J. F. R. 1972, ApJ, 175, L89

Arons, J. 1992, in Proc. IAU Colloq. 128, *The Magnetospheric Structure and Emission Mechanisms of Radio Pulsars*, ed. T. H. Hankins, J. M. Rankin & J. A. Gil (Poland: Pedagogical University Press), 56

Arons, J. 1993, ApJ, 408, 160

Arons, J. 1996, Space Sci. Rev., 75, 235

Arons, J. 1997, in Proc. of *Neutron Stars and Pulsars: Thirty Years After the Discovery*, held in Kyoto, Japan, Nov. 1997, in press

Arons, J., & Scharlemann, E. T. 1979, ApJ, 231, 854

Arzoumanian, Z., Phillips, J. A., Taylor, J. H., & Wolszczan, A. 1996, ApJ, 470, 1111

Asséo, E. 1993, MNRAS, 264, 940

Baade, W., & Zwicky, F. 1934, in Proc. Natl. Acad. Sci. USA, 20, 254

Backer, D. C. 1970, Nature, 228, 1297

Backer, D. C. 1971, Ph.D. Thesis, Cornell University

Backer, D. C. 1976, ApJ, 209, 895

Backer, D. C. 1989 in NATO ASI series C, Vol 262, *Timing Neutron Stars*, ed. H. Ögelman & E. P. J. van den Heuvel (Dordrecht: Kluwer), 3

Backer, D. C. 1995, JApA, 16, 165

Backer, D. C. 1996 in IAU Symp. 165, *Compact Stars in Binaries*, ed. E. P. J. van den Heuvel & Erik Kuulkers (Dordrecht: Kluwer), 197

Backer, D. C. 1998, ApJ, 493, 873

Backer, D. C., Rankin, J. M., & Campbell, D. B. 1975, ApJ, 197, 481.

Backer, D. C., Rankin, J. M., & Campbell, D. B. 1976, Nature, 263, 202.

Backer, D. C., & Rankin, J. M. 1980, ApJS, 42, 143

Backer, D. C., Kulkarni, S. R., Heiles, C., Davis, M. M., & Goss, W. M. 1982, Nature, 300, 615

Backer, D. C., Foster, R. S., & Sallmen, S. 1993, Nature, 365, 817

Backer, D. C., Hama, S., van Hook, S., & Foster, R. S. 1993, ApJ, 404, 636

Backer, D. C., & Wong, T. 1996, in Proc. IAU Colloq. 160, *Pulsars: Problems and Progress*, ed. S. Johnston, M. A. Walker & M. Bailes (San Francisco: ASP), 87

Backer, D. C., Dexter, M., Zepka, A., Ng, D., Wertheimer, D. J., Ray, P. S., & Foster, R. S. 1997, PASP, 109, 61

Backer, D. C., & Sallmen, S. 1997, AJ, 114, 1539

Bailes, M., Johnston, S., Bell, J. F., Lorimer, D. J., Stappers, B. W., Manchester, R. N., Lyne, A. G., Nicastro, L., d'Amico, N., & Gaensler, B. W. 1997, ApJ, 481, 386

Barnard, J. J. 1986, ApJ, 302, 120

Barnard, J. J., & Arons, J. 1986, ApJ, 302, 138

Bartel, N., Kardashev, N. S., Kuzmin, A. D., Nikolaev, N. Ya., Popov, M. V., Sieber, W., Smirnova, T. V., Soglasnov, V. A., & Wielebinski, R. 1981, A&A, 93, 85

Bartel, N., & Hankins, T. H. 1982, ApJ, 254, L35

Bartel, N., Morris, D., Sieber, W., & Hankins, T. H. 1982, ApJ, 258, 776

Bell, J. F., Kulkarni, S. R., Bailes, M., Leitch, E. M., & Lyne, A. G. 1995, ApJ, 452, L121

Bell, J. F., Bailes, M., Manchester, R. N., Lyne, A. G., Camilo, F., & Sandhu, J. S. 1997, MNRAS, 286, 463

Beskin, V. S. 1990, Pis'ma Ast. Zh., 16, 665 (Sov. Ast. Lett., 16)

Beskin, V. S., Gurevich, A. V., & Istomin, Ya. N. 1986. Soviet Phys. –Uspekhi, 29, 946

Beskin, V. S., Gurevich, A. V., & Istomin, Ya. N. 1988. Ap&SS, 146, 205

Bhattacharya, D. 1996, in Proc. IAU Colloq. 160, *Pulsars: Problems and Progress*, ed. S. Johnston, M. A. Walker & M. Bailes (San Francisco: ASP), 547

Biggs, J. D. 1990, MNRAS, 245, 514

Biggs, J. D. 1992, ApJ, 394, 574

Biggs, J. D., Lyne, A. G., Hamilton, P. A., McCulloch, P. M., & Manchester, R. N. 1988, MNRAS, 235, 255

Blaskiewicz, M., 1991, Ph.D. Thesis, Cornell University

Blaskiewicz, M., Cordes, J. M., & Wasserman, I. 1991, ApJ, 370, 643

Boriakoff, V. 1983, ApJ, 272, 687

Boriakoff, V. 1992 in Proc. IAU Colloq. 128, *The Magnetospheric Structure and Emission Mechanisms of Radio Pulsars*, ed. T. H. Hankins, J. M. Rankin & J. A. Gil (Poland: Pedagogical University Press), 343

Boriakoff, V. 1996, in Proc. IAU Colloq. 160, *Pulsars: Problems and Progress*, ed. S. Johnston, M. A. Walker & M. Bailes (San Francisco: ASP), 187

Boriakoff, V., & Ferguson D. C. 1981, in IAU Symp. 95, *Pulsars, 13 years of Research on Neutron Stars*, ed. W. Sieber & R. Wielebinski (Dordrecht: D. Reidel), 191

Buschauer, R., & Benford, G. 1976, MNRAS, 177, 109

Buschauer, R., & Benford, G. 1977, MNRAS, 179, 189

Camilo, F. 1995, Ph.D. Thesis, Princeton University

Camilo, F. *et al.* 1998, in preparation

Camilo, F., Foster, R. S., & Wolszczan, A. 1994, ApJ, 437, L39

Camilo, F., Nice, D. J., Shrauner, J. A., & Taylor, J. H. 1996, ApJ, 469, 819

Campbell, D. B., Heiles, C., & Rankin, J. M. 1970, Nature, 225, 527

Chen, K., & Ruderman, M. 1993a, ApJ, 408, 179

Chen, K., & Ruderman, M. 1993b, ApJ, 402, 264

Cheng, A. F., & Ruderman, M. A. 1977, ApJ, 212, 800

Cheng, A. F., & Ruderman, M. A. 1979, ApJ, 229, 348

Cheng, K. S., Ho, C., & Ruderman, M. 1986, ApJ, 300, 500

Cognard, I., Shrauner, J. A., Taylor, J. H., & Thorsett, S. E. 1996, ApJ, 457, L81

Comella, J. M., Craft, H. D., Lovelace, R. V. E., Sutton, J. M., & Tyler, G. L. 1969, Nature, 221, 453

Cordes, J. M. 1978, ApJ, 222, 1006

Cordes, J. M. 1981, in IAU Symp. 95, *Pulsars: 13 Years of Research on Neutron Stars*, ed. W. Seiber & R. Weilebinski (Dordrecht: D. Reidel), 115

Cordes, J. M., & Hankins, T. H. 1977, ApJ, 218, 484

Cordes, J. M., Rankin, J., & Backer, D. C. 1978, ApJ, 223, 961

Cordes, J. M., Weisberg, J. M., & Boriakoff, V. 1983, ApJ, 268,370

Cordes, J. M., & Stinebring, D. R. 1984, ApJ, 277, L53

Cordes, J. M., Wasserman, I., & Blaskiewicz M. 1990, ApJ, 349, 546

Cordes, J. M., Weisberg, J. M., & Hankins, T. H. 1990, AJ, 100, 1882

Cordes, J. M., Wolszczan, A., Dewey, R. J., Blaskiewicz, M., & Stinebring, D. R. 1990, ApJ, 349, 245

Cordes, J. M., Hankins, T. H., & Moffett, D. 1998, in preparation

da Costa, A. A., & Kahn, F. D. 1985, MNRAS, 215, 701

Daugherty, J. K., & Harding, A. K. 1982, ApJ, 252, 337

Davies, J. G., Lyne, A. G., Smith, F. G., Izvekova, V. A., Kuzmin, A. D., & Shitov, Yu. P. 1984, MNRAS, 211, 57

Durdin, J. M., Large, M. I., Little, A. G., Manchester, R. N., Lyne, A. G., & Taylor, J. H. 1979, MNRAS, 196, 39P

Eilek, J. A. 1996, in Proc. IAU Colloq. 160, *Pulsars: Problems and Progress*, ed. S. Johnston, M. A. Walker & M. Bailes (San Francisco: ASP), 155

Eilek, J. A., Hankins T. H., & Moffett, D. A. 1998, in preparation

Ferguson, D. C., & Seiradakis, J. H. 1978, A&A, 64, 27

Foster, R. S., & Backer, D. C. 1990, ApJ, 361, 300

Foster, R. S., Fairhead, L., & Backer, D. C. 1991, ApJ, 378, 687

Foster, R. S., Wolszczan, A., & Camilo, F. 1993, ApJ, L91

Friedman, J., & Boriakoff, V. 1990, in Proc. IAU Colloq. 128, *The Magnetospheric Structure and Emission Mechanisms of Radio Pulsars*, ed. T. H. Hankins, J. M. Rankin & J. A. Gil (Poland: Pedagogical University Press), 347

Fruchter, A. S., Berman, G., Bower, G., Convery, M., Goss, W. M., Hankins, T. H., Klein, J. R., Nice, D. J., Ryba, M. F., Stinebring, D. R., Taylor, J. H., Thorsett, S. E., & Weisberg, J. M. 1990, ApJ, 351, 642

Gangadhara, R. T. 1996, A&A, 314, 853

Gil, J. A. 1986, ApJ, 309, 609

Gil, J. A. 1987, ApJ, 314, 629

Gil, J. A. 1991, A&A, 243, 219

Gil, J. A., & Snakowski, J. K. 1990a, A&A, 234, 237

Gil, J. A., & Snakowski, J. K. 1990b, A&A, 234, 269

Gil, J. A., Snakowski, J. K., & Stinebring, D. R. 1991, A&A, 242, 119

Gil, J. A., Lyne, A. G., Rankin, J. M., Snakowski, J. K., & Stinebring, D. R. 1992, A&A, 255, 181

Gil, J. A., & Kijak, J. 1993, A&A, 273, 563

Gil, J. A., Kijak, J., & Seiradakis, J. H. 1993, A&A, 272, 268

Gil, J. A., & Han, J. L. 1996, ApJ, 458, 265

Gil, J. A., & Krawczyk, A. 1996, MNRAS, 280, 143

Goldreich, P., & Julian, W. H. , 1969, ApJ, 157, 869

Goldstein, S. J., & Meisel, D. D. 1969, Nature, 224

Gould, D. M., & Lyne, A. G., 1997, MNRAS, submitted

Gwinn, C. R., Ojeda, M. J., Britton, M. C., Reynolds, J. E., Jauncey, D. L., King, E. A., McCulloch, P. M., Lovell, J. E. J., Flanagan, C. S., Smits, D. P., Preston, R. A., & Jones, D. L. 1997, ApJ, 483, L53

Hankins, T. H. 1971, ApJ, 169, 487

Hankins, T. H., & Rickett, B. J. 1975, Meth. in Comp. Phys., 14, 55

Hankins, T. H., & Fowler, L. A. 1986, ApJ, 304, 256

Hankins, T. H., & Rickett, B. J. 1986, ApJ, 311, 684

Heiles, C., Campbell, D. B., & Rankin, J. M. 1970, Nature, 226, 529.

Heiles, C., & Rankin, J. M. 1971, Nature, Physical Science, 231, 97

Helfand, D. J., Manchester, R. N., & Taylor, J. H. 1975, ApJ, 198, 661

Hesse, K. H., & Wielebinski, R. 1974, A&A, 31, 409

Hewish, A., Bell, S. J., Pilkington, J. D. H., Scott, P. F., & Collins, R. A. 1968, Nature, 217, 709

Holloway, N. J. 1973, Nature, Physical Science, 246, 6

Hulse, R. A., & Taylor, J. H. 1975, ApJ, 201, L55

Jenet, F., Anderson, S. B., Kaspi, V. M., Prince, T. A., & Unwin, S. C. 1998, submitted

Jones, P. B. 1980, ApJ, 236, 661

Jones, P. B. 1986, MNRAS, 218, 477

Kapadia, A. A., Rabaey, J. M., Backer, D. C., Wertheimer, D. J., & Dexter, M. R. 1993, in Proc. *Fourth International Conference on Signal Processing Applications and Technology; ICSPAT '93*, (Newton, MA: DSP Associates), vol. 1, 71

Kaspi, V. M. 1995, in ASP Conf. Ser. 72, *Millisecond Pulsars: A Decade of Surprise*, ed. A. S. Fruchter, M. Tavani & D. C. Backer (San Francisco: ASP), 345

Kazbegi, A. Z., Machabeli, G. Z., & Melikidze, G. I. 1991, MNRAS, 253, 377

Kazbegi, A., Machabeli, G., Melikidze, G., & Shukre, C. 1991, A&A, 309, 515

Kijak, J., & Gil, J. 1997, MNRAS, 288, 631

Kijak, J., Kramer, M., Wielebinski, R., & Jessner, A. 1997, A&A, 318, L63

Komesaroff, M. M. 1970, Nature, 225, 612

Kossl, D., Wolff, R. G., Muller, E., & Hillebrandt, W. 1988, A&A, 205, 347

Kramer, M. 1994, A&AS, 107, 527

Kramer, M. 1995, Ph.D. Thesis, Max-Planck-Institut für Radioastronomie

Kramer, M., Wielebinski, R., Jessner, A., Gil, J. A., & Seiradakis, J. H. 1994, A&AS, 107, 515

Kramer, M., Xilouris, K. M., Jessner, A., Wielebinski, R., & Timofeev, M. 1996, A&A, 306, 867

Kramer, M., Xilouris, K. M., Jessner, A., Lorimer, D. R., Wielebinski, R., & Lyne, A. G. 1997, A&A, 322, 846

Kramer, M., Xilouris, K. M., Lorimer, D. R., Doroshenko, O., Jessner, A., Wielebinski, R., Wolszczan, A., & Camilo, F. 1998, ApJ, 501, in press

Krause-Polstorff, J., & Michel, F. C. 1985, MNRAS, 213, 43

Krishnamohan, S., & Downs, G. S. 1983, ApJ, 265, 372

Kuzmin, A. D. 1992, in Proc. IAU Colloq. 128, *The Magnetospheric Structure and Emission Mechanisms of Radio Pulsars*, ed. T. H. Hankins, J. M. Rankin, & J. A. Gil (Poland: Pedagogical University Press), 288

Kuzmin, A. D., & Losovsky, B. Ya. 1994, A&A, 308, 91

Kuzmin, A. D., Izvekova, V. A., Shitov, Yu. P., Sieber, W., Jessner, A., Wielebinski, R., Lyne, A. G., & Smith, F. G. 1997, A&AS, 127, 355

Lorimer, D. R., Nicastro, L., Lyne, A. G., Bailes, M., Manchester, R. N., Johnston, S., Bell, J. F., D'Amico, N., & Harrison, P. A. 1995a, ApJ, 439, 933

Lorimer, D. R., Yates, J. A., Lyne, A. G., & Gould, D. M. 1995b, MNRAS, 273, 411

Lundgren, S. C. 1994, Ph.D. Thesis, Cornell University

Lundgren, S., Cordes, J. C. Cordes, Ulmer, M., Foster, R., & Hankins, T. H. 1995, ApJ, 453, 433

Luo, Q., & Melrose, D. B. 1992, MNRAS, 258, 616

Luo, Q., & Melrose, D. B. 1995, MNRAS, 276, 372

Lyne, A. G., & Ashworth, M. 1983, MNRAS, 204, 519

Lyne, A. G., Biggs, J. D., Brinklow, A., Ashworth, M., & McKenna, J. 1988, Nature, 332, 45

Lyne, A. G., & Manchester, R. N. 1988, MNRAS, 234, 477

Lyne, A. G., Pritchard, R. S., Graham-Smith, F., & Camilo, F. 1996, Nature, 381, 497

Machabeli, G. Z., & Usov, V. V. 1979, Sov. Astron. Lett., 5, 238

Malofeev, V. M., Gil, J. A., Jessner, A., Malov, I. F., Seiradakis, J. H., Sieber, W., & Wielebinski, R. 1994, A&A, 285, 201

Manchester, R. N. 1971, ApJS, 23, 283

Manchester, R. N. 1996, in Proc. IAU Colloq. 160, *Pulsars: Problems and Progress*, ed. S. Johnston, M. A. Walker & M. Bailes (San Francisco: ASP), 193

Manchester, R. N., Huguenin, G. R., & Taylor, J. H. 1972, ApJ, 174, L19

Manchester, R. N., Taylor, J. H., & Huguenin, G. R. 1973, ApJ, 179, L7

Manchester, R. N., Taylor, J. H., & Huguenin, G. R. 1975, ApJ, 196, 83

McKinnon, M. M. 1993, ApJ, 413, 317

McKinnon, M. M. 1994, *Polarization Calibration of the NRAO 140-ft Telescope with Feed Rotation*, National Radio Astronomy Observatory Memo

McKinnon, M. M. 1997, ApJ, 475, 763,

McKinnon, M. M., & Hankins, T. H. 1993, A&A, 269, 325

Melrose, D. B. 1978, ApJ, 225, 557

Melrose D. B. 1992, in Proc. IAU Colloq. 128, *The Magnetospheric Structure and Emission Mechanisms of Radio Pulsars*, ed. T. H. Hankins, J. M. Rankin, & J. A. Gil (Poland: Pedagogical University Press), 306

Melrose D. B. 1996, in Proc. IAU Colloq. 160, *Pulsars: Problems and Progress*, ed. S. Johnston, M. A. Walker & M. Bailes (San Francisco: ASP), 139

Michel, F. C. 1982, Rev. Mod. Phys., 54, 1

Moffett, D. A. 1997, Ph.D. Thesis, New Mexico Institute of Technology

Moffett, D. A., & Hankins, T. H. 1996, ApJ, 468, 779

Morris, D., Sieber, W., Ferguson, D. C., & Bartel, N. 1980, A&A, 84, 260

Morris, D., Graham, D. A., & Sieber, W. 1981, A&A, 100, 107

Morris, D., Graham, D. A., Sieber, W., Bartel, N., & Thomasson, P. 1981, A&AS, 46, 421

Muslimov, A. G., & Tsygan, A. I. 1990, Soviet Ast., 34, 133

Muslimov, A. G., & Tsygan, A. I. 1992, MNRAS, 255, 61

Narayan, R., & Vivekanand, M. 1982, A&A, 113, L6

Narayan, R., & Vivekanand, M. 1983, A&A, 122, 45

Navarro, J., & Manchester, R. N. 1996, in Proc. IAU Colloq. 160, *Pulsars: Problems and Progress*, ed. S. Johnston, M. A. Walker & M. Bailes (San Francisco: ASP), 249

Neuhauser, D., Koonin, S. E., & Langanke, K. 1987, Phys. Rev. A., 36, 4163

Nicastro, L., Lyne, A. G., Lorimer, D. R., Harrison, P. A., Bailes, M., & Skidmore, B. D. 1995, MNRAS, 273, L68

Ostriker, J. P., & Gunn, J. E. 1969, ApJ, 157, 1395

Pacini, F. 1967, Nature, 216, 567

Phillips, J. A. 1992, ApJ, 385, 282

Phillips, J. A., & Wolszczan, A. 1992, ApJ, 385, 273

Phinney, S., & Taylor, J. H. 1977, Nature, 277, 117

Radhakrishnan, V., & Cooke, D. J. 1969, ApJ, 3, 225

Radhakrishnan, V., & Rankin, J. M. 1990, ApJ, 352, 258

Rankin, J. M. 1983a, ApJ, 274, 333

Rankin, J. M. 1983b, ApJ, 274, 359

Rankin, J. M. 1986, ApJ, 301, 901

Rankin, J. M. 1988, ApJ, 325, 314

Rankin, J. M. 1990, ApJ, 352, 247

Rankin, J. M. 1993, ApJ, 405, 285

Rappaport, S., Podsiadlowski, P., Joss, P. C., Di Stefano, R., & Han, Z. 1995, MNRAS, 273, 731

Rathnasree, N., & Rankin, J. M. 1995, ApJ, 452, 814

Rathnasree, N., & Rankin, J. M. 1996, in Proc. IAU Colloq. 160, *Pulsars: Problems and Progress*, ed. S. Johnston, M. A. Walker & M. Bailes (San Francisco: ASP), 265

Rickett, B. J. 1975, ApJ, 197, 185

Rickett, B. J., Hankins, T. H., & Cordes, J. M. 1975, ApJ, 201, 425

Romani, R., & Yadigaroglu, I. -A. 1995, ApJ, 438, 314

Rots, A. H., Jahoda, K., Macomb, D. J., Kawai, N., Saito, Y., Kaspi, V. M., Lyne, A. G., Manchester, R. N., Backer, D. C., Somer, A. L., Marsden, D., & Rothschild, R. E. 1998, ApJ, in press

Rowe, E. T. 1995, A&A, 296, 275

Ruderman M. 1991a, ApJ, 382, 576

Ruderman M. 1991b, ApJ, 382, 587

Ruderman, M. A., & Sutherland P. G. 1975, ApJ, 196, 51

Saito, Y., Kawai, N., Kamae, T., Shibata, S., Dotani, T., & Kulkarni, S. R. 1997, ApJ, 477, L37

Sallmen, S., & Backer, D. C. 1995, in ASP Conf. Ser. 72, *Millisecond Pulsars: A Decade of Surprise*, ed. A. S. Fruchter, M. Tavani & D. C. Backer (San Francisco: ASP), 340

Sallmen, S., Backer, D. C & Kramer, M. 1997, BAAS, 189, 74.08

Scharlemann, E. T., Arons, J., & Fawley, W. M. 1978, ApJ, 222, 297

Segelstein, D. J., Rawley, L. A., Stinebring, D. R., Fruchter, A. S., & Taylor, J. H. 1986, Nature, 322, 714

Sieber, W. 1997, A&A, 321, 519

Smirnova, T. V., & Shishov, V. I., 1989, Soviet Ast., L15, 191

Staelin, D. H., & Reifenstein, E. C. 1968, Science, 162, 1481

Staelin, D. H., & Sutton, J. M. 1970, Nature, 226, 69

Stinebring, D. S., 1982, Ph.D. Thesis, Cornell University.

Stinebring, D. R., Cordes, J. M., Rankin, J. M., Weisberg, J. M., Boriakoff, V. 1984a, ApJS, 55, 247

Stinebring, D. R., Cordes, J. M., Weisberg, J. M., Rankin, J. M., Boriakoff, V. 1984b, ApJS, 55, 279

Sturrock, P. A. 1971, ApJ, 164, 529

Sutton, J. M., Staelin, D. H., & Price, R. M. 1971, in IAU Symp. 46, *The Crab Nebula*, ed. R. D. Davies & F. G. Smith (Dordrecht: Reidel), 97

Taylor, J. H. 1994, Rev. Mod. Phys., 66, 711

Taylor, J. H. 1995, JApA, 16, 307

Taylor, J. H. 1996, in Proc. IAU Colloq. 160, *Pulsars: Problems and Progress*, ed. S. Johnston, M. A. Walker & M. Bailes (San Francisco: ASP), 65

Taylor, J. H., & Weisberg, J. M. 1989, ApJ, 345, 434

Taylor, J. H., & Cordes, J. M. 1993, ApJ, 411, 674

Taylor, J. H., Manchester, R. N., & Lyne, A. G. 1993, ApJS, 88, 529

Taylor, J. H., Manchester, R. N., Lyne, A. G., & Camilo, F. 1995, unpublished (available at ftp://pulsar. princeton. edu/pub/catalog)

Thorsett, S. E. 1991, ApJ, 377, 263

Thorsett, S. E., & Stinebring, D. R. 1990, ApJ, 361, 664

van den Heuvel, E. P. J. 1995, JApA 16, 255

van Kerkwijk, M. H., Bergeron, P., & Kulkarni, S. R. 1996, ApJ, L89

von Hoensbroech, A., & Xilouris, K. M. 1997a, A&A, 324, 981

von Hoensbroech, A., & Xilouris, K. M. 1997b, A&A, 126, 121

Weatherall, J. C. 1997, ApJ, 483, 402

Weatherall, J. C., & Eilek, J. A. 1997, ApJ, 474, 407

Weisberg, J. M., Romani, R. W., & Taylor, J. H. 1989, ApJ, 347, 1030

Weisberg, J. M., Cordes, J. M., Lundgren, S. C., Dawson, B. R., Despotes, J. T, Morgan, J. J., Weitz, K. A., Zink, E. C., & Backer, D. C. 1998, ApJS, submitted

Wolszczan, A., Cordes, J. M., & Stinebring, D. R. 1984, in *Millisecond Pulsars Workshop*, ed. S. Reynolds & D. Stinebring (NRAO: Green Bank), 63

Wolszczan, A., & Cordes, J. M. 1987, ApJ, 320, L35

Xilouris, K. M. 1991, A&A, 248, 323

Xilouris, K. M., Kramer, M., Jessner, A., & Wielebinski, R. 1994, A&A, 288, L17

Xilouris, K. M., Seiradakis, J. H., Gil, J., Sieber, W., & Wielebinski, R. 1995, A&A, 293, 153

Xilouris, K. M., Kramer, M., Jessner, A., Wielebinskis, R., & Timofeev, M. 1996, A&A, 309, 481

Xilouris, K. M., Kramer, M., Jessner, A., von Hoensbroech, A., Lorimer, D., Wielebinski, R., Wolzczan, A., & Camilo, F. 1998, ApJ, 501, in press